



HAL
open science

Optically active luminescent nanocrystals complexed with chiral silica nanoribbons

Peizhao Liu

► **To cite this version:**

Peizhao Liu. Optically active luminescent nanocrystals complexed with chiral silica nanoribbons. Other. Université de Bordeaux; Kyōto daigaku, 2021. English. NNT : 2021BORD0220 . tel-03811563

HAL Id: tel-03811563

<https://theses.hal.science/tel-03811563>

Submitted on 12 Oct 2022

HAL is a multi-disciplinary open access archive for the deposit and dissemination of scientific research documents, whether they are published or not. The documents may come from teaching and research institutions in France or abroad, or from public or private research centers.

L'archive ouverte pluridisciplinaire **HAL**, est destinée au dépôt et à la diffusion de documents scientifiques de niveau recherche, publiés ou non, émanant des établissements d'enseignement et de recherche français ou étrangers, des laboratoires publics ou privés.



THESIS UNDER DOUBLE-DEGREE AGREEMENT

To Obtain

DOCTORAL DEGREE

Of

UNIVERSITY OF BORDEAUX

DOCTORAL SCHOOL OF CHEMICAL SCIENCES

And

KYOTO UNIVERSITY

GRADUATE SCHOOL OF ENERGY SCIENCE

By

Peizhao LIU

OPTICALLY ACTIVE LUMINESCENT NANOCRYSTALS COMPLEXED

WITH CHIRAL SILICA NANORIBBONS

Under Supervision of

Dr. Reiko ODA and Dr. Takashi SAGAWA

Defended on 21 September 2021

Jury Members

Dr. Hiroataka IHARA	Professor, Kumamoto University	Reviewer
Dr. Thomas BUERGI	Professor, University of Geneva	Reviewer
Dr. Yann BATTIE	Professor, University of Lorraine	Examiner
Dr. Keiichi ISHIHARA	Professor, Kyoto University	Examiner
Dr. Rika HAGIWARA	Professor, Kyoto University	Invited
Dr. Takashi SAGAWA	Professor, Kyoto University	Thesis Supervisor
Dr. Reiko ODA	Research Director, CNRS	Thesis Supervisor

Optically active luminescent nanocrystals complexed with chiral silica nanoribbons

Chiral materials exist everywhere in our world at various scales and play an important role in biopharmaceutics. Also, it shows promising applications in chiral catalysis, recognition, sensing, and spintronics *etc.* Inorganic materials such as luminescent nanocrystals (NCs) exhibited excellent optical properties and high resistance to photo-oxidation compared with organic optical materials. NCs have been widely used in lighting, display, solar cells, photodetectors, and so on. The chiral optical properties will involve more advanced applications to NCs if chirality is induced to NCs. Recently, more and more attentions are focused on the study of endowing chirality to NCs. Generally, there are four ways to endow chirality to NCs, 1) NCs capped with chiral ligands, 2) NCs prepared with chiral lattice, 3) NCs prepared with chiral shape, 4) NCs chiral self-organization. In this thesis, we focus on endowing chirality to NCs to achieve chiral NCs with high dissymmetric g-factor by their chiral self-organization on the surface of inorganic chiral silica ribbons and preparing the chiral shaped NCs inside of hollow chiral silica ribbons. 1). NCs chiral self-organization. The NCs grafted on the surface of inorganic chiral silica ribbons don't show any optically active properties in suspension state, while it exhibits strong optically active properties upon drying as film states. These results are different from the gold nanoparticle grafted on the surface of organic or inorganic templates which show strong chirality induction in suspension state. And then we systematically studied the CdSe based nanocrystals grafted on chiral silica nanoribbons to investigate the mechanism of chirality induction by their chiral self-organization. The effects of grafting CdSe nanocrystals with different grafting densities, sizes, crystal structures, and shape were investigated. The ensemble of the observation gives us powerful hints for designing efficient chiroptical nano-systems based on inorganic silica-QD components. 2). The chiral shaped NCs growth inside of hollow silica ribbons. The chiral shaped perovskite nanocrystals (PNCs) with right- or left-handed chiral shape structure was first presented *via* a simple supersaturation recrystallization method. The handedness of PNCs are determined by the handedness of hollow silica templates. The right-handed PNCs show positive CPL signals, while the left-handed PNCs show negative CPL signals with dissymmetric g-factor up to $\pm 2 \times 10^{-2}$. Also, the right- and left-handed PNCs show strong mirror CD images which exhibit dissymmetric g-factor ($\pm 1.5 \times 10^{-2}$). The tremendous g-factor of chiral shaped PNCs prepared inside of hollow silica ribbons enrich the chiral group of PNCs which can benefit their applications.

Key words: Chiral silica ribbons, semiconductor nanocrystals, optical activity, chiral self-organization, chiral shape

Nanocristaux luminescents optiquement actifs formés *via* des nanorubans de silice chiraux

Les matériaux chiraux existent partout dans notre monde à différentes échelles et jouent un rôle important dans la biopharmaceutique, la catalyse chirale, la reconnaissance moléculaire, la détection ou la spintronique. Les matériaux inorganiques tels que les nanocristaux luminescents (NC) présentent d'excellentes propriétés optiques et une résistance élevée à la photo-oxydation par rapport aux matériaux optiques organiques. Les NC ont été largement utilisés dans l'éclairage, l'affichage, les cellules solaires, les photodétecteurs, *etc.* Si une chiralité est induite aux NC, des applications plus avancées peuvent être envisagées. C'est pourquoi de plus en plus d'études se concentrent sur l'étude de la chiralité endossée aux NC. En général, il existe quatre façons de doter de chiralité des NC : 1) les NC recouverts de ligands chiraux, 2) les NC préparés avec un réseau chiral, 3) les NC préparés avec une forme chirale, 4) l'auto-organisation chirale des NC. Dans cette thèse, nous nous concentrons sur l'attribution de chiralité aux NC pour obtenir des NC chiraux avec un facteur g dissymétrique élevé par leur auto-organisation chirale à la surface des rubans de silice chirale inorganiques et la préparation des NC en forme chirale à l'intérieur des rubans de silice chirale creuse. 1) Auto-organisation chirale de NCs. Les NC greffés à la surface des rubans de silice chirale ne présentent aucune propriété chiro-optique à l'état de suspension. Cependant, lorsque les suspensions sont séchées sous forme de film, de fortes propriétés chiro-optiques apparaissent. Ces résultats sont différents de la nanoparticule d'or greffée à la surface de structures organiques ou inorganiques qui montrent une forte induction de chiralité en état de suspension. Dans le but d'étudier le mécanisme d'induction de la chiralité par auto-organisation chirale, une étude systématique a été effectuée sur des NCs de type CdSe. Les effets du greffage des NCs avec différentes densités, tailles, structures cristallines et formes ont été étudiés. L'ensemble des observations nous donne des indices puissants pour concevoir des nano-systèmes chiro-optiques efficaces basés sur des composants inorganiques silice-QD.

2) NCs de forme chirale. Les nanocristaux de pérovskite (PCN) de forme hélicoïdale droite ou gauche ont été élaborés *via* une méthode simple de recristallisation par supersaturation. La synthèse a lieu à l'intérieure de la double paroi des hélices de silice. Les hélices de PNC droites montrent des signaux CPL positifs, tandis que les PNC gauches montrent des signaux CPL négatifs avec un facteur g dissymétrique allant jusqu'à $\pm 2 \times 10^{-2}$. En outre, les PNC droite et gauche montrent de forts CD opposés avec un facteur g dissymétrique ($\pm 1,5 \times 10^{-2}$). Les grandes valeurs de ces facteurs g enrichit considérablement le domaine des PNCs chiraux utiles pour des applications spécifiques.

Mots-clés : Rubans de silice chiraux, nanocristaux semi-conducteurs, activité optique, auto-organisation chirale, morphologie chirale

List of Abbreviations

NCs	Nanocrystals
SNCs	Semiconduction nanocrystals
PNCs	Perovskite nanocrystals
NPs	Nanoparticles
GNPs	Gold nanoparticles
NPLs	Nano-platelets
QDs	Quantum dots
QRs	Quantum rods
VB	Valence band
CB	Conduction band
CPL	Circularly polarized luminescence
L-CP Light	Left-handed circularly polarized light
R-CP Light	Right-handed circularly polarized light
CP-EL	Circularly polarized electroluminescence
CD	Circular dichroism
DRCD	Diffuse reflection circular dichroism
VCD	Vibrational circular dichroism
CB	Circular birefringence
LD	Linear dichroism
LPL	Linear polarized light
OA	Optical activity
OR	Optical rotation
ORD	Optical rotatory dispersion
ICD	Induced circular dichroism
ICPL	Induced circularly polarized luminescence
PEM	Photoelastic modulator
PLQY	Photoluminescence quantum yield

FITC	Fluorescein isothiocyanate
IR	Infrared
FTIR	Fourier transform infrared
APTES	(3-aminopropyl)triethoxysilane
TEOS	Tetraethoxysilane
MPA	3-mercaptopropionic acid
LGAm	<i>N,N</i> -bis(octadecyl)- <i>L</i> -glutamic diamide
DGAm	<i>N,N</i> -bis(octadecyl)- <i>D</i> -glutamic diamide
CISS	Chiral-induced spin selectivity
COS	Chiral optical scattering
MeCys	<i>D</i> - or <i>L</i> -cysteinemethylester hydrochloride
DT	1-dodecanethiol
TGA	Thioglycolic acid
OLA	Oleylamine
OA	Oleic acid
TOP	Tri- <i>n</i> -octyl phosphine
TOPO	Trioctylphosphine oxide
TDPA	Tetradecylphosphonic acid
HPA	Hexyl phosphonic acid
ODE	Octadecene
DMF	Dimethylformamide
PMMA	Poly(methyl methacrylate)
SEM	Scanning electron microscope
STEM	Scanning transmission electron microscope
TEM	Transmission electron microscopy
Cryo-EM	Cryogenic electron microscopy
XRD	X-ray diffraction
GIXS	Grazing incident X-ray scattering
SAXS	Small-angle X-ray scattering
GISAXS	Grazing-incidence small angle X-ray scattering

GIWAXS	Grazing-incidence wide angle X-ray scattering
3D	Three dimensional
m	Mass
L	Length
ρ	Density
LEDs	Light-emitting diodes
HI	Hot injection
LARP	Ligand-assisted re-precipitation
rpm	Revolutions per minute
BEM	Boundary element method
CDM	Coupled dipole method
GMRES	Generalized minimal residual method
BZ	Brillion zone
SHG	Second-harmonic generation
FWHM	Full width at half maximum
SILAR	Successive ion layer adsorption and reaction
ee	Enantiomeric excess

Contents

Chapter 1. Introduction	2
1. Introduction of chirality	2
1.1 Organic chiral materials vs inorganic chiral materials.....	3
1.1.1 Chiral organic molecules and intrinsic chiral inorganic nanomaterials (chiral shape and chiral lattice).....	3
1.1.2 Organic chiral molecules chiral self-assembly and inorganic chiral nanomaterials chiral self-organization.....	5
1.1.3 Organic achiral molecular chiral self-assembly vs Inorganic achiral nanomaterials chiral self-organization.....	6
1.2 Chirality characterization	8
1.2.1 Circular dichroism and linear dichroism	8
1.2.2 Circularly polarized luminescence	10
2. Introduction of semiconductor NCs.....	10
2.1 Properties of luminescent semiconductor NCs	12
2.1.1 Surface effect and size confinement.....	12
2.1.2 Excellent optical properties.	13
2.1.3. The surface functionalization of NCs	14
2.2 Applications of chiral luminescent semiconductor NCs.....	17
2.2.1 Chiral-induced spin selectivity (CISS)	17
2.3 How to introduce chirality to inorganic semiconductor NCs	19
2.3.1 Chirality induced by chiral ligand	20
2.3.2 Chirality induced by chiral lattice.....	24
2.3.3 Chirality induced by the chiral shape of individual particle.....	26
2.3.4 Chirality induced by chiral self-organization.....	28
3. Conclusion	35
4. Reference	36
Chapter 2. Research design	47
1. Research design	47
2. Preparation of chiral silica ribbons and its basic properties	48
2.1 Synthesis of chiral silica ribbons and its surface modification with (3-aminopropyl)triethoxysilane (APTES).....	48

2.2 Evaluation of dispersity and mass concentration	50
2.3 Calculation of surface area.....	51
3. The complexation between luminescent NCs and silica ribbons.....	53
3.1 Functionalized luminescent NCs combined with amine-modified silica ribbons	54
3.2 Ligands exchanged of luminescent NCs by amine modified silica ribbons.....	55
3.3 In-situ growth of luminescent nanocrystals outside or inside of silica ribbons	55
3. Conclusion	56
4. Reference	58

Chapter 3. Chiral optical scattering from silica helical and twisted ribbons

.....	60
1. Introduction.....	60
2. Theoretical analysis	61
3. Results and discussions.....	63
3.1 Silica nanoribbons deposited on substrates	63
4. Experiment section.....	74
4.1 Silica nanoribbons preparation and Quartz slides substrate preparation	74
4.2 Silica nanoribbons film preparation.....	74
4.3 CD and LD measurement	75
5. Conclusion	75
6. Reference	77

Chapter 4. Optically active perovskite nanocrystals helically arranged on inorganic silica helical ribbons

.....	81
1. Introduction.....	81
2. Synthesis of perovskites nanocrystals.....	83

2.1 Synthesis at high temperature	84
2.2 Synthesized at room temperature	85
3. In-situ growth of CsPbBr ₃ nanocrystals on the surface of silica helical ribbons.....	86
4. PNCs grafted on the silica helical ribbons by ligands exchange method	90
4.1 Results in suspension	91
4.1.1 PNCs prepared at low temperature with silica helical ribbons.....	91
4.1.2 PNCs prepared at high temperature with silica helical ribbons	96
4.2 Results in drying state	102
4.2.1 Solvent evaporation temperature effect	106
4.2.2 The kinetic drying effect of the PNCs-silica helical ribbons	114
4.2.3 Temperature stability	116
4.2.4 Theoretical simulation	118
5. CONCLUSION.....	120
6. Experimental section.....	121
6.1 Materials and instruments.....	121
6.2 CsPbBr ₃ perovskites nanocrystals (PNCs) prepared at room temperature ..	122
6.3 In-situ growth of CsPbBr ₃ on the surface of silica helical ribbons	122
6.4 CsPbBr ₃ perovskites nanocrystals (PNCs) prepared at high temperature	123
6.5 Grafting of CsPbBr ₃ PNCs on the surface of silica helical ribbons by ligand exchange methods	124
6.6 Coupled dipole method simulation	125
7. Reference	128

Chapter 5. Chirality induction to CdSe nanocrystals self-organized on silica nanoribbons tuning chiroptical properties.....

1. Introduction.....	133
2. Quantum dots size and molar concentration calculations.....	135
3. Result and discussion.....	138
3.1 Grafting density effects.....	139
3.2 Concentration, temperature, and solvent effect	143
3.3 CdSe-silica helical ribbons annealing	145

3.4 CdSe-silica helical ribbons PMMA film.....	146
3.5 Size and crystal structure effect	147
3.6 The effect of the chiral morphologies: Helical vs twisted ribbons.....	153
3.7 Core-shell structured QDs with silica helical ribbons	158
3.8 Quantum rods shape effect	160
4. Conclusion	166
5. Experiment section.....	167
5.1 Chemical and reagents.....	167
5.2 Cubic crystal structured CdSe QDs synthesise and purification.....	168
5.3 Hexagonal crystal structured CdSe QDs synthesise and purification.....	168
5.4 CdSe/CdS quantum rods (QRs) synthesise and purification	169
5.5 Grafting of QDs and QRs on the surface of silica helices by ligand exchange methods	169
5.6 Optical properties simulations by CDM	170
6. Reference	173

Chapter 6. Chiral shaped perovskite nanocrystals growth inside

chiral hollow silica nanoribbons.....	177
1. Introduction.....	177
2. Result and discussion.....	178
2.1 One-step method.....	180
2.1.1 Effect of concentration.....	180
2.1.2 Effect of annealing condition	182
2.2 Two-step method	183
2.2.1 Effect of concentration.....	183
2.2.2 Effect of solvent evaporation	184
2.2.3 Effect of annealing condition	185
2.2.4 Effect of halide composition	186
3. Conclusion	187
4. Experiment section.....	188
4.1 Materials and instruments.....	188

4.2 Silica ribbons and ions precursors.....	188
5. Reference	190
Chapter 7. Conclusion and perspectives.....	194
List of publications	200
Acknowledgment	202

Chapter 1. Introduction	2
1. Introduction of chirality	2
1.1 Organic chiral materials vs inorganic chiral materials	3
1.1.1 Chiral organic molecules and intrinsic chiral inorganic nanomaterials (chiral shape and chiral lattice).....	3
1.1.2 Organic chiral molecules chiral self-assembly and Inorganic chiral nanomaterials chiral self-organization	5
1.1.3 Organic achiral molecules chiral self-assembly vs Inorganic achiral nanomaterials chiral self-organization	6
1.2 Chirality characterization	7
1.2.1 Circular dichroism and linear dichroism.....	8
1.2.2 Circularly polarized luminescence.....	10
2. Introduction of semiconductor NCs.....	10
2.1 Properties of luminescent semiconductor NCs.....	12
2.1.1 Surface effect and size confinement	12
2.1.2 Excellent optical properties.....	13
2.1.3 The surface functionalization of NCs.....	14
2.2 Applications of chiral luminescent semiconductor NCs	17
2.2.1 Chiral-induced spin selectivity (CISS)	17
2.3 How to introduce chirality to inorganic semiconductor NCs	19
2.3.1 Chirality induced by chiral ligand	20
2.3.2 Chirality induced by chiral lattice	24
2.3.3 Chirality induced by the chiral shape of individual particle	26
2.3.4 Chirality induced by chiral self-organization	28
3. Conclusion	35
4. Reference	36

Chapter 1. Introduction

1. Introduction of chirality

Chirality means the geometric property which cannot be superimposed on its mirror image by any combination of rotations and translations.¹ Chirality is commonly observed in nature and life, which exists at all length scales, from the subatomic, atomic, and molecular level (*e.g.* the single left- or right-handed amino acid) to the supramolecular level (*e.g.* the right-handed double helix of DNA), and up to macro-biomaterialized materials (*e.g.* tendril and snail shells) and macroscopic scales (galaxy) (Figure 1-1).² Why life is chiral has puzzled scientists for over a century until Louis Pasteur discovered molecular chirality in his meticulous experiment in 1848.³ He separated the mirror-image forms of salts of tartaric acid manually and found that their solutions rotate the plane-polarized light in opposite directions. After that, the studies of chirality are thriving and the chiral molecules play an important role in drugs or drug candidates since their enantiomers exhibit marked differences in their pharmacodynamics, pharmacokinetic, and toxicological properties.^{4, 5} Beyond that, chiral materials also used in chiral catalysis, recognition, sensing, and spintronics.⁶⁻¹¹

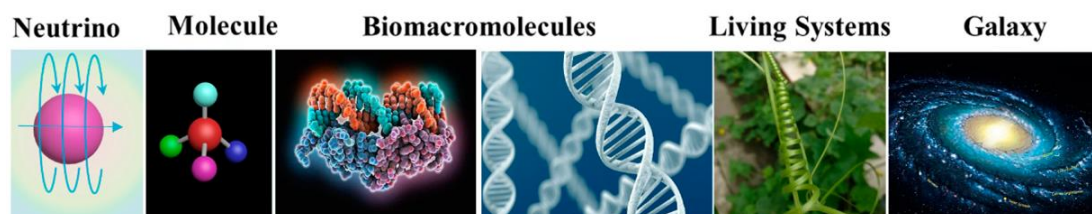


Figure 1-1. Chiral architectures at various scales, from neutrino to enantiomeric molecules, proteins and DNA biomacromolecules, macroscopic living systems, and galaxy.

Generally, chirality could be classified into organic and inorganic chiral systems. Compared with the organic molecular system, inorganic nanocrystals (NCs) possess stronger and tunable light absorption or emission, and remarkable resistance to

chemical and photo-degradation which have attracted considerable attentions in recent years.^{12, 13} In this thesis, the chirality induction to inorganic semiconductor NCs by their chiral self-organization or growth with chiral shape assisted by chiral silica ribbons were systematic studied. As we all know, most bottom-up methods to prepare inorganic chiral materials were obtained by chiral organic molecules (such as chiral ligands) or organic chiral supramolecular templates (NCs and chiral lipid co-assembly).¹² That means the chirality of inorganic materials is tightly related to chiral organic materials. In this chapter, firstly, the organic and inorganic chiral materials will be compared. Secondly, the advantageous properties and promising applications of inorganic semiconductor NCs will be discussed. Thirdly, endowing chirality to inorganic semiconductor NCs by chiral organic ligands, chiral lattice and shape, chiral self-organization will be discussed in detail. Last but not least, the surface of NCs and silica ribbons will be introduced which is helpful for their combination.

1.1 Organic chiral materials vs inorganic chiral materials

Organic chiral materials have been widely studied for over a hundred years, while inorganic chiral materials thriving in recent several decades. Similar to the organic chiral system from small molecules to hierarchal supramolecular chiral self-assembly, the inorganic materials also exhibited chirality from intrinsic chirality (isolated NCs) to hierarchical chiral self-organization. Here, some examples are shown for the contrast of organic and inorganic chirality in small chiral organic molecule *vs* isolated inorganic chiral NCs, chiral organic molecules chiral self-assembly *vs* chiral NCs chiral self-organization, and achiral organic molecular chiral self-assembly *vs* achiral NCs chiral self-organization.

1.1.1 Chiral organic molecules and intrinsic chiral inorganic nanomaterials (chiral shape and chiral lattice)

Small organic molecule chirality has long fascinated chemists and provided an

intellectually challenging exercise for selective chemical synthesis and catalysis. Generally, the chirality of the small molecules could arise from the point, axial, helical, propeller inherent, mechanical, and planar chirality (Figure 1-2 (a)).¹¹ Isolated inorganic NCs chirality can arise from chiral lattice¹⁴⁻²¹ or chiral shape²²⁻²⁹. As shown in Figure 1-2 (b), the chiral shaped gold nanohelix show strong mirror circular dichroism (CD) images with left-handed and right-handed helicity.³⁰ The chiral lattice and chiral shaped isolated NCs will be discussed in section of 2.3.2 and 2.3.3.

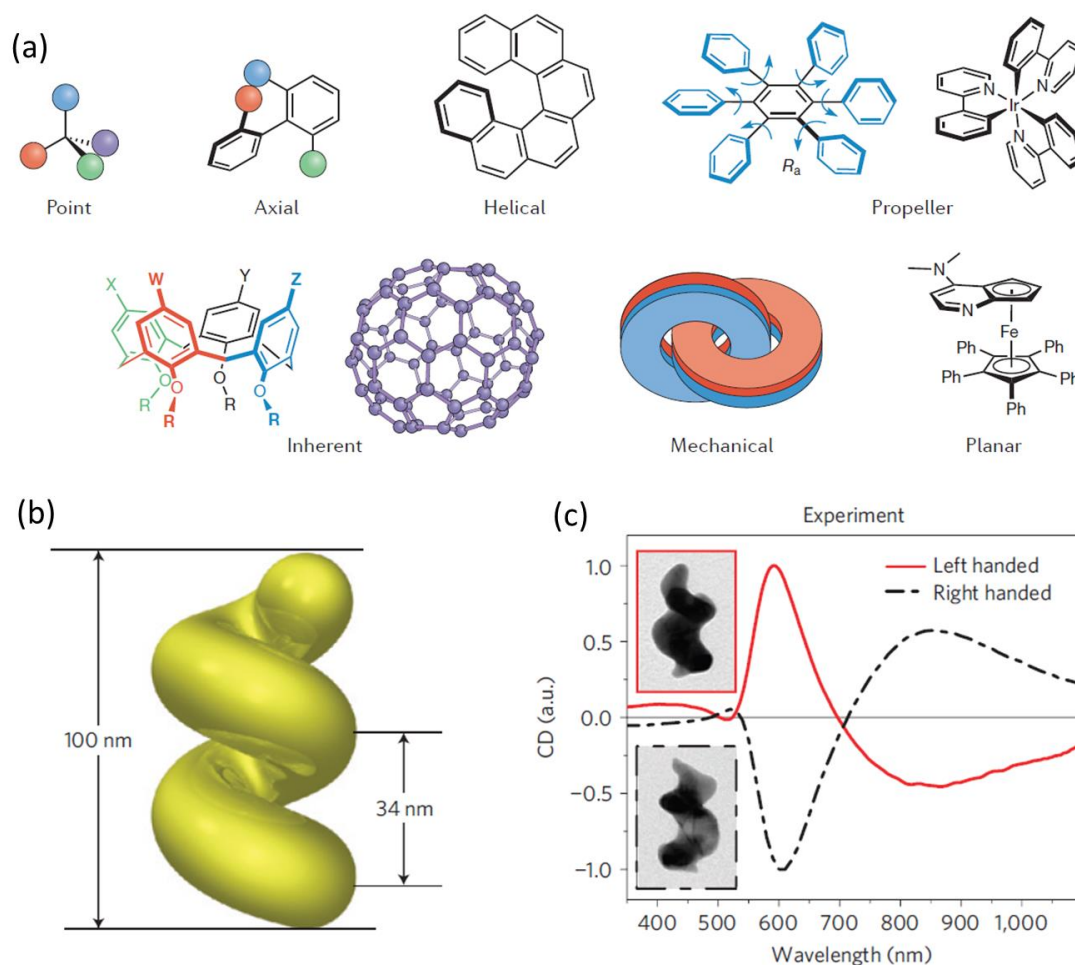


Figure 1-2. (a) Small chiral molecules classification. (b) Model two-turn gold nanohelix showing critical dimensions. (c) Normalized CD spectra of left- and right-handed helices. Inset: TEM images of grown structures with left (top) and right (bottom) chirality.

1.1.2 Organic chiral molecules chiral self-assembly and inorganic chiral nanomaterials chiral self-organization

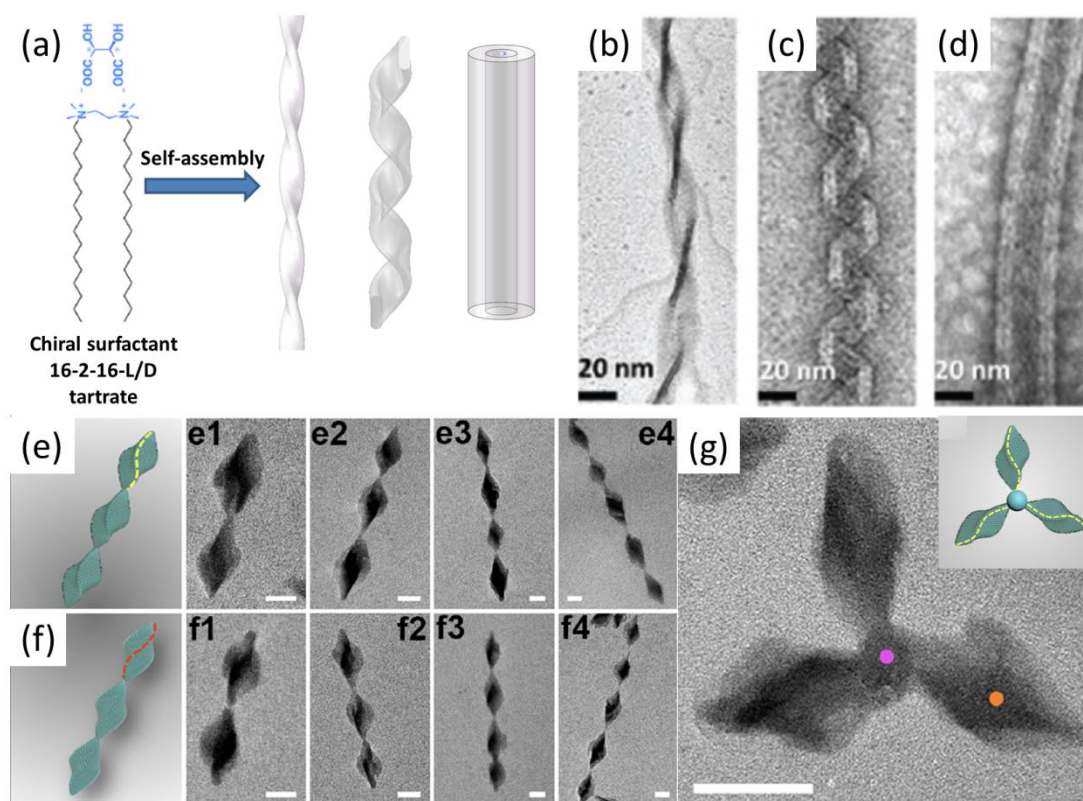


Figure 1-3. (a) Schematic of the chemical structure of 16-2-16 D-tartrate self-assembles into twisted ribbons, helical ribbons, and tubules. TEM images of the schematic representation of twisted ribbons (b), helical ribbons (c), and tubules (C) of 16-2-16 D-tartrate. (e, f) Models of a chain assembled from left- and right-handed NCs, respectively. (e1-e4, f1-f4) TEM images of left-handed and right-handed chains with different n , respectively. (g) Typical TEM image and model (inset picture) of a propeller. The three blades and central domain are pure HgS and alloyed $\text{Hg}_{0.64}\text{Ag}_{0.36}\text{S}$ respectively.

Organic chiral molecules chiral self-assembly have been widely reported and many excellent review papers have given good summarization.³¹⁻³³ For example, Oda's group has studied the chiral surfactant self-assembly since 1999.³⁴ This chiral amphiphilic molecules can self-assemble into twisted, helical ribbons, and tubules (Figure 1-3) with different Gemini tartrate aging time, and the different chiral

morphologies correspond to different CD spectra.³⁵⁻³⁷ Similarly, the chiral shape of inorganic NCs could self-organized with different morphologies as shown in Figure 1-3 (e-g).¹⁸ Cinnabar HgS NCs with chiral lattice and morphology can form two well-defined chiral superstructures, collinear chains (Figure 1-3 (e)) and propellers (Figure 1-3 (g)). The chiroptical responses of the superstructures are found to uniquely depend on the intrinsic chirality of building blocks and their coupling. The cooperative chirality at different length scales by tailoring both crystallographic, morphological handedness and also building blocks in a superstructure would offer a unique platform for understanding the hierarchical chirality.

1.1.3 Organic achiral molecules chiral self-assembly vs Inorganic achiral nanomaterials chiral self-organization

Apart from the self-assembly of the chiral molecules, achiral molecules chiral self-assembly by chiral additives,³⁸ chiral solvents,³⁹ circularly polarized light illumination,⁴⁰⁻⁴² spin coating,⁴³ rotational and magnetic forces,⁴⁴ and vortex flow⁴⁵⁻⁵³ also have been widely reported. For example, dendritic zinc porphyrin solution without stirring was CD silent, while it became optically active upon mechanical rotary stirring (Figure 1-3 a-b).⁴⁸ The CD spectra reversed with stirring clockwise direction or counterclockwise directions which were supposed to be caused by the partial orientation of the molecules chiral and achiral assemblies during the stirring process. The artificial CD spectra were supposed to be originated from the convective flow based on linear dichroism and vortex flow based on linear dichroism and linear birefringence.⁴⁷ Oriol found that the induced chirality in stirred solutions originates from the chiral supramolecular nanofibers with J-aggregation.⁵² Based on experimental Mueller matrix analysis, the inversion of the induced chirality with reversed stirring directions (clockwise and counterclockwise) does not show a significant difference in the linear birefringence and linear dichroism spectra. This indicates that the vortex flow direction can play an essential role in the induction of supramolecular chirality (Figure 1-4 b).⁵⁴ Inorganic achiral NCs such as plasmonic

gold and silver NCs, semiconductor NCs with the chiral organization could be easily obtained by chiral soft templates.⁵⁵⁻⁶² For example, quantum dots (QDs) capped with 3-mercaptopropionic acid (MPA) ligands co-assembly with organic lipid gelator *N,N*-bis(octadecyl)-*L*-glutamic diamide (LGAm), and its enantiomer DGAm show circularly polarized luminescence (CPL) as shown in Figure 1-4 (c-e).⁵⁸ More NCs chiral organization systems would be discussed in the chirality induction's part (section of 2.3.4).

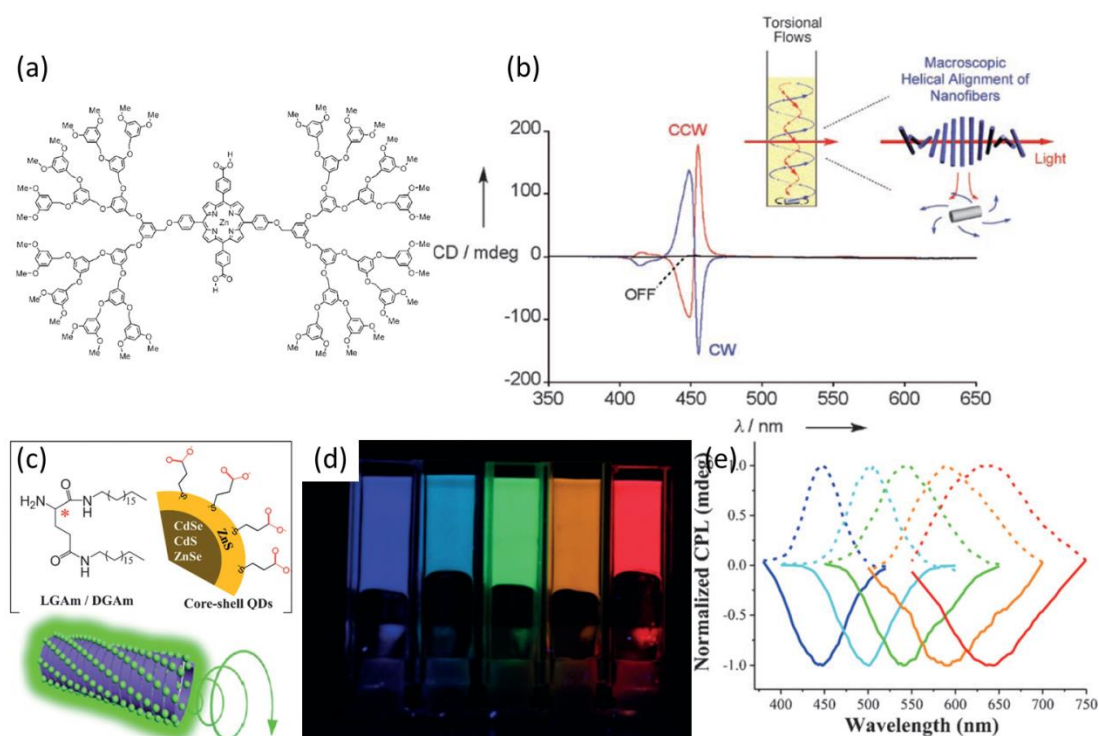


Figure 1-4. (a) The dendritic zinc porphyrin molecule structure. (b) Circular dichroism spectra of a benzene solution of assemblies of dendritic zinc porphyrin upon rotary stirring in clockwise and counterclockwise directions, and without stirring. The insets show the schematic illustration of torsional flows and macroscopic helical alignment of nanofibers generated upon counterclockwise rotary stirring. (c) Molecular structure of the gelators (chiral templates) and core-shell structured QDs with same ZnS shell but different cores (CdSe, CdS, and ZnSe), and the QDs and gelator co-assembly system gels model. (d) the QDs and gelator co-assembly gels under UV light. (e) the mirror images of CPL spectra of the corresponding co-gels.

1.2 Chirality characterization

Chiral materials attracted lots of attention due to their optically active properties. The first chiroptical phenomenon was observed with optical rotation (OR) and its wavelength dependence, which is named as optical rotatory dispersion (ORD). The optically active properties could also be evaluated by refraction, scattering, absorption, and emission-based circular dichroism. Lots of books and review papers have already given a nice introduction to circular dichroism.⁶³⁻⁶⁶ In this thesis, the scattering, absorption, and emission-based circular dichroism are discussed. Here, electron transition circular dichroism (CD) and circularly polarized luminescence (CPL) will be briefly introduced. Besides, linear dichroism is also discussed which significantly affects the CD and CPL measurement results.

1.2.1 Circular dichroism and linear dichroism

As it is well known that the linear polarized light (LPL) could be divided into two orthogonal LPL with the same amplitude and phase. And the circularly polarized light could be obtained by shifting the two orthogonal LPL phase with $\pm 90^\circ$ as shown in Figure 1-5 (a). Generally, the linear polarized and circularly polarized light (CP Light) could be obtained by a nature light pass through a polarizer and photoelastic modulator (PEM). The direction of linear polarized and handedness of CP Light could be controlled by the PEM as shown in Figure 1-5 (b).

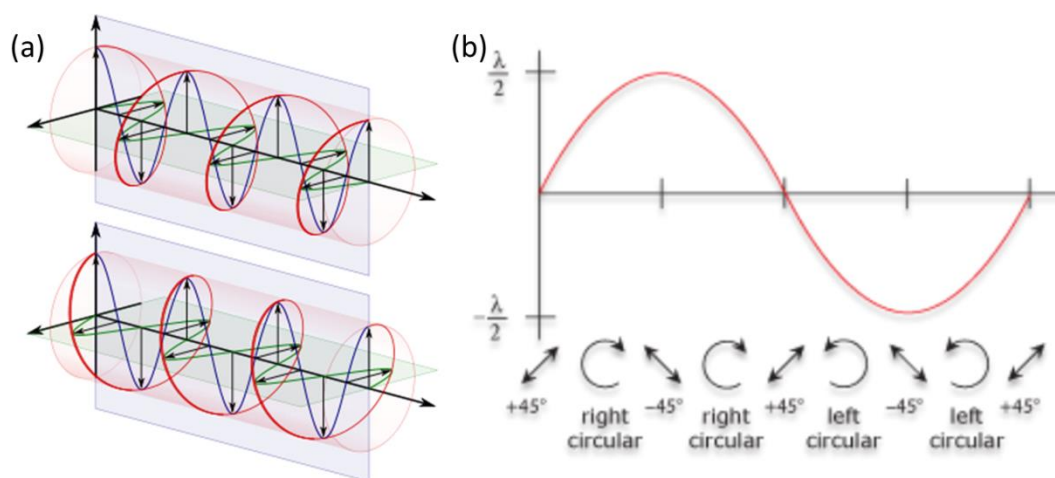


Figure 1-5. (a) Left- and right-handed circularly polarized light. (b) Linear polarized

light and circularly polarized light are generated after passing through a PEM with a different phase shift.

Circular dichroism (CD) is the difference in the absorption of left-handed circularly polarized light (L-CP Light) and right-handed circularly polarized light (R-CP Light).

$CD = \Delta A(\lambda) = A(\lambda)_{L-CP\ Light} - A(\lambda)_{R-CP\ Light}$, where λ represent the wavelength

Normally, the measurement of CD is ellipticity (θ) and the ellipticity is defined as:

$$\tan(\theta) = (E_{R-CP\ Light} - E_{L-CP\ Light}) / (E_{R-CP\ Light} + E_{L-CP\ Light})$$

The E is the electric field for each CP Light and the θ is in radians small enough, the equation could be approximated as:

$$\begin{aligned} \theta &\approx (E_{R-CP\ Light} - E_{L-CP\ Light}) / (E_{R-CP\ Light} + E_{L-CP\ Light}) \\ &= (I_{R-CP\ Light}^{1/2} - I_{L-CP\ Light}^{1/2}) / (I_{R-CP\ Light}^{1/2} + I_{L-CP\ Light}^{1/2}) \approx \Delta A * (\ln 10 / 4) \end{aligned}$$

The I is the intensity of L-CP Light and R-CP Light, and the unit of θ is mdeg, so the θ (mdeg) is:

$$\theta(\text{mdeg}) = \Delta A * (\ln 10 / 4) * (180 / \pi) * 1000 \approx 32980 * \Delta A$$

The dissymmetric g-factor is the ratio of circular dichroism to conventional absorption defined as:

$$g = \Delta \epsilon / \epsilon = \Delta A / A = \theta(\text{mdeg}) / (32980 * A)$$

Linear dichroism is the difference in the absorption of parallel and perpendicular linearly polarized light to an orientation axis.

$LD = \Delta A(\lambda) = A(\lambda)_{//} - A(\lambda)_{\perp}$, where λ represent the wavelength

The CD and LD measurement could be briefly described as shown in Figure 1-6. For the CD, the same density of L-CP Light and R-CP Light pass through the optically active medium result in different absorption of L-CP Light and R-CP Light, while for the LD, the same density of vertical and horizontal polarized light passing through the optically active medium result in different absorption of vertical and horizontal polarized light.

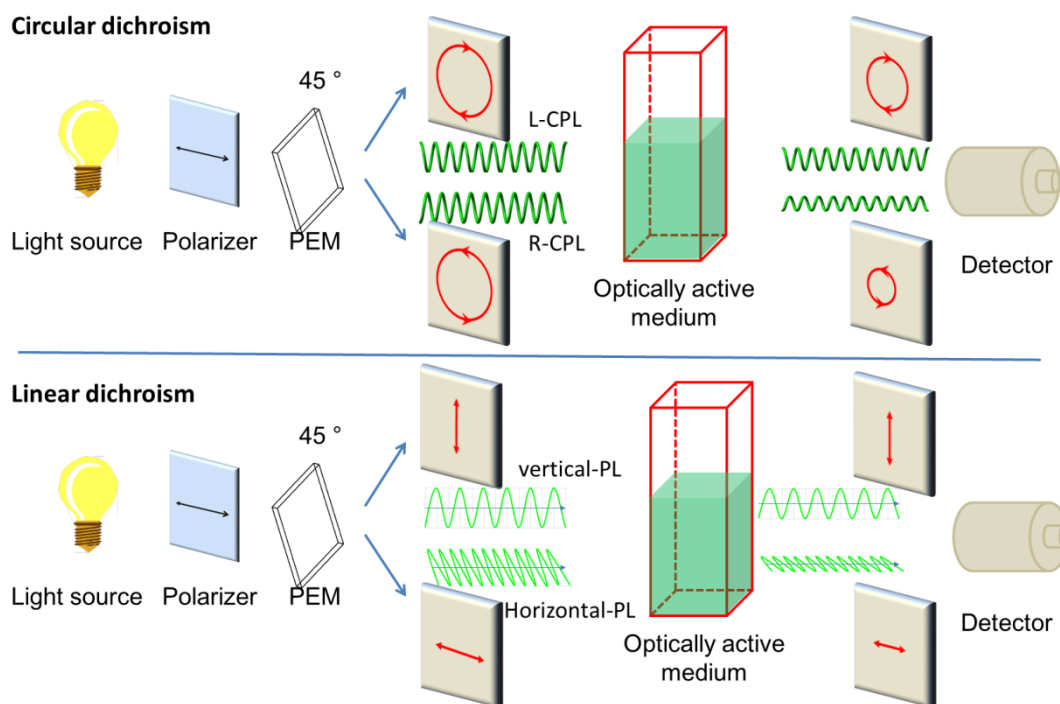


Figure 1-6. Schematic of CD and LD spectroscopy.

1.2.2 Circularly polarized luminescence

Circularly polarized luminescence (CPL) is the different emission of L-CP Light and R-CP Light. Generally, the chiral luminescent materials excited by non-polarized light emit circularly polarized light as shown in Figure 1-7. Similarly, the dissymmetric g -factor is defined as $g_{lum} = [CPL / (32980 / \ln 10)] / DC$

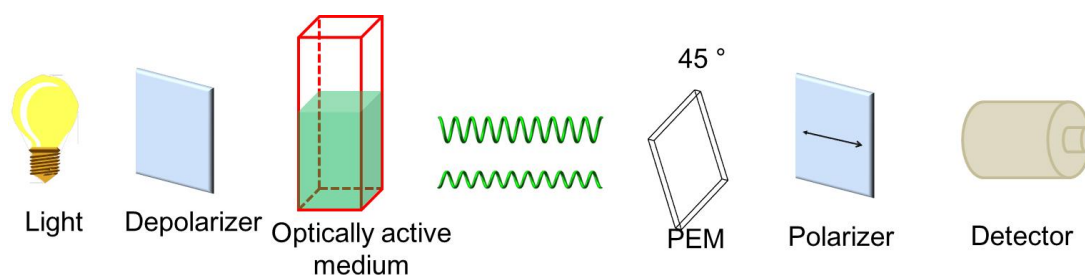


Figure 1-7. Schematic of CPL spectroscopy.

2. Introduction of semiconductor NCs

Nanoscience and nanotechnology are changing our daily life (such as computer chips)

since 21 century in response to the demands for energy and the concerns of global warming and climate change.⁶⁷ The nanomaterials are gradually used in solar energy conversion, optoelectronics, nanophotonics, spintronics, smart coatings, smart catalysts, biomedical applications, *etc.*⁶⁸ Nanomaterials exhibit size-dependent physical and chemical properties which makes it possible to engineer the material properties not only by defining their chemical compositions but also by tailoring their size and shape, and manipulating individual atoms or small nanoparticles building blocks.⁶⁹⁻⁷¹ For example, the band gap of the bulk of semiconductor materials is determined by their chemical compositions (Figure 1-8 (a)). When the size decreased smaller than their exciton Bohr radius, they show a strong size confinement effect increasing the band gap energy with size decreasing. Figure 1-8 (b) shows a typical CdSe quantum dots (QDs) model which is made of several hundred atoms and capped with ligands to keep their colloidal stability.⁷¹ Different semiconductor NCs exhibit different absorption and emission spectra range tailored by their size which can be used in different areas and applications (Figure 1-8 (c)).⁷²

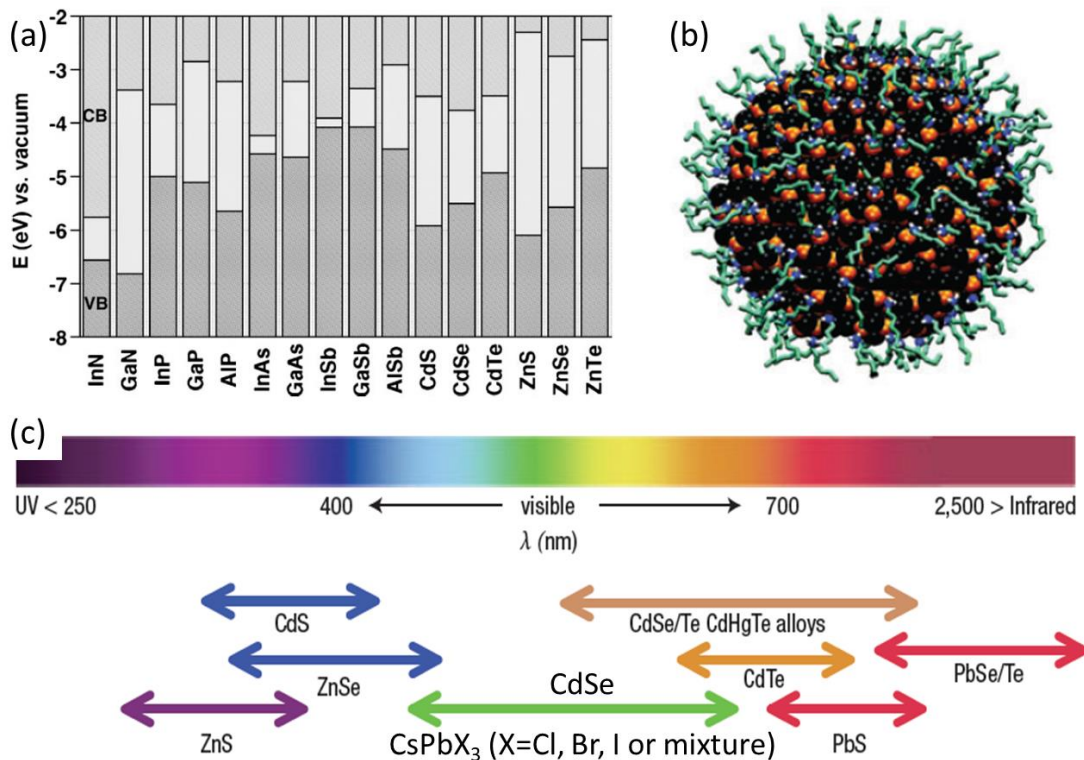


Figure 1-8. (a) Electronic energy levels of selected III-V and II-VI bulk semiconductors using the valence band offsets (VB: valence band, CB: conduction

band). (b) Molecular simulation snapshot of a colloidal CdSe NC capped by hexylamine molecules. Colour coding: black, Se; orange, Cd, light blue, C; dark blue, N; white, H; yellow, S; brown, P; red, O. (c) Representative semiconductor NCs core materials scaled as a function of their emission wavelength superimposed over the spectrum.

2.1 Properties of luminescent semiconductor NCs

2.1.1 Surface effect and size confinement

Semiconductor NCs such as CdSe QDs are composed of several hundred to several thousand atoms. As nanomaterials size decreases, the number of atoms is gradually reduced, while the fraction of atoms located at the surface increases as shown in Figures 1-9 (a-b).⁷³ The surface-to-volume ratio increases as its size decreases are essentially called the scaling effect. The increase in the surface-to-volume ratio has a dramatic impact on its physic and chemical properties since surface atoms have fewer neighbors than their interior counterparts, and therefore possess unsatisfied chemical bonds (dangling bonds). These unshared atomic orbitals give rise to energy levels within the band gap of the NCs which impair the photoluminescence quantum yield (PLQY) of the NCs due to their non-radiative recombination of the exciton.⁷¹ Surface passivation is necessary to eliminate dangling bonds from the surface of semiconductor NCs by overgrowing a shell of wider band gap semiconductor or by coating the surface with suitable organic ligands.

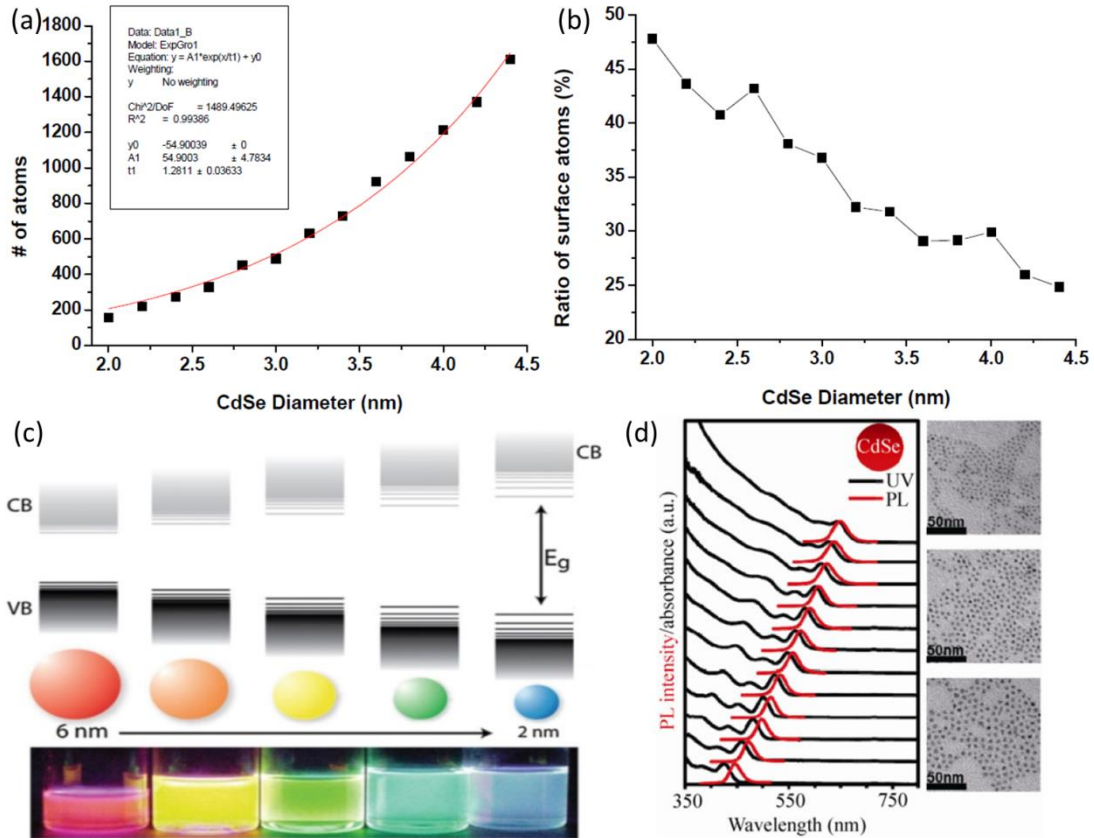


Figure 1-9. The number of atoms (a) and the ratio of surface atoms (b) in a CdSe quantum dot with zinc blend structure, estimated by using Materials Studio software (c) Schematic representation of the quantum confinement effect on the energy level structure of semiconductor material. The lower panel shows colloidal suspensions of CdSe NCs of different sizes under CV excitation. (d) UV-vis, PL spectra, and TEM images of CdSe NCs with different sizes.

Besides, the band gap of a semiconductor NC becomes larger with decreasing size due to the raised discrete energy levels (with decreasing atoms numbers) of both the conduction band and valence band as shown in Figure 1-9 (c). It means that the optical band gap of QDs can be tuned by simply changing their size. For example CdSe QDs with increasing size, the absorption and emission spectra show red shift (Figure 1-9 (d)).

2.1.2 Excellent optical properties.

Compared with organic fluorophores, QDs exhibit excellent optical properties such as high PLQY, broad absorption spectrum, size-tunable emission, high resistance to photo-oxidation, and good color saturation. As shown in Figures 1-10, the organic fluorophores have narrow absorption and broad emission result in overlap of excitation and emission spectrum, while the inorganic QDs show broad absorption and narrow symmetric emission spectra.⁷⁴ The full width at half maximum could be less than 12 nm and the multicolor NCs of different sizes can be excited by a single wavelength which is shorter than their emission wavelength. Besides, inorganic QDs are not prone to photo-bleaching⁷⁵ and produce two to eleven times brighter fluorescence than organic fluorophores due to the large molar extinction coefficients (10-50 times greater).^{76, 77}

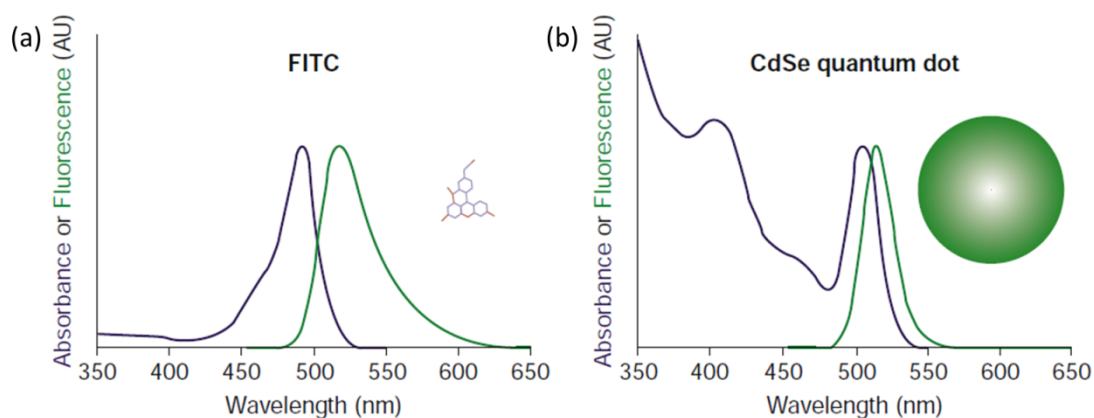


Figure 1-10. Comparison of absorption (blue) and emission (green) spectra between FITC (Fluorescein isothiocyanate) (a) and a CdSe QD (b).

The aforementioned excellent optical properties relate mostly to the inorganic nature of QD provide promising potential applications in light conversion materials such as lighting and display, biology, solar cells, photodetectors *etc.* There will be more promising applications if the NCs exhibit optically active properties.

2.1.3. The surface functionalization of NCs

It is important to know the surface properties of NCs and hard templates to combine them and realize NCs chiral self-organization. In this thesis, the semiconductor NCs

and chiral silica ribbons were used for the project study. The silica ribbons have been studied for more than ten years in our group and the surface can be functionalized with the amine active group by (3-aminopropyl)triethoxysilane (APTES). The surface of NCs will be briefly inducted to explore how to combine them with silica ribbons.

NCs have surface ligands to keep their colloidal stability and generally, the ligands could be modified as the anchor for the functional materials. It is better to understand the NC-ligand bond first to manipulate the surface of NCs. The ligands are defined as L-, X- or Z-type depending on the number of electrons that the neutral ligand contributes to the NC-ligand bond (2, 1, or 0 respectively) according to covalent bond classification.⁷⁸⁻⁸⁰ As shown in Figure 1-11 (a), L-type ligands are neutral two-electron donors with a lone electron pair that actively coordinates surface metal atoms. Ligands such as amines, phosphines, and phosphine oxides are L-type ligands. X-type ligands such as carboxylates, thiolates, and phosphonates, as well as inorganic ions (halides, InCl_4^- , AsS_3^{3-} etc.) have an odd number of valence-shell electrons, requiring one electron from the NC surface site to form a two-electron covalent bond. Nucleophilic (electron-rich) L- and X-type ligands bind to electron-deficient (electrophilic) surface sites with pronounced Lewis acidity, typically undercoordinated metal ions at the NC surface. The surface of metal chalcogenides, oxides, and another compound NCs also exposes electron-rich Lewis basic sites. These sites can interact with Z-type ligands, such as $\text{Pb}(\text{OOCR})_2$ or CdCl_2 which bind through the metal atom as two-electron acceptors.⁷⁸ Charge balancing requirements restrict ligand exchange reaction in a polar solvent as shown in Figure 1-11 (b). The ligand exchange processes are governed by the adsorption enthalpy and acidity differences which hampering exchange for weaker binding and less acidic ligands.⁷⁹ The X-type ligands exhibited reversible and irreversible ligands exchange for different active anchor group ligands. As shown in Figure 1-11 (c), the carboxylic acid ligands with different lengths could be exchanged reversibly and can be replaced by phosphonic acid and thiol, but not reversibly.⁸¹ Also the active anchor group adsorption energy is related to its carbon-carbon length, for the carboxylate, hydroxyl,

and amine molecules, the adsorption energy of the ligand molecule with a long carbon chain is weaker than that of a smaller molecule with the same active anchor group (Figure 1-11 (d)).⁸² Those ligands exchange rules would guide us to modify the surface of NCs towards functional materials.

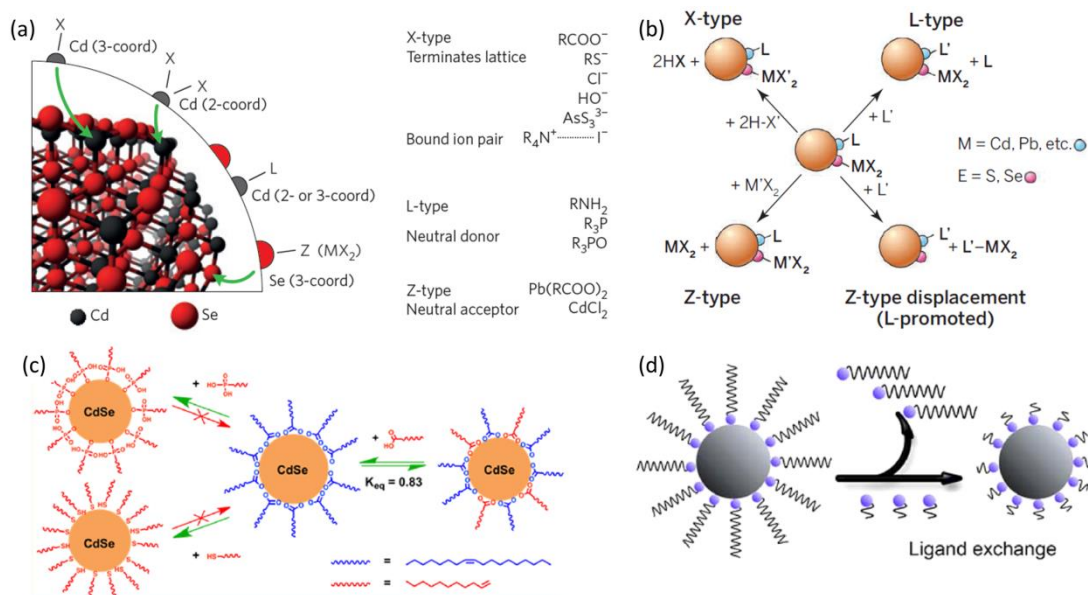


Figure 1-11. (a) Classification of ligand binding motifs at the surface of CdSe NCs. Anionic X-type ligands bind to surface cations imparting electroneutrality to metal-rich NC facets. Neutral L-type electron donor ligands attach to electrophilic metal sites on stoichiometric NC facets. Neutral Z-type electron acceptor ligands bind to electron-rich undercoordinated Se atoms. Green arrows highlight examples of such atoms at the surface of a CdSe NC model. (b) Examples of several ligand exchange reactions are shown. (c) Scheme of the ligands exchange between carboxylic acid, phosphonic acid, and thiol. (d) Scheme of the ligands exchange between molecules with long and short carbon chains.

The NCs and silica can be modified with a functional group like amine, carboxylate, and thiol.^{72, 83-87} In our group, the silica can be well modified with amine, the synthesized NCs are capped with oleylamine, oleic acid, or phosphonic acid. Generally, there are two ways to graft NCs on the surface of silica ribbons, one way is the use of the NCs modified with 3-mercaptopropionic acid (MPA) with carboxylate anchor group which can combine with silica surface amine; another way is the

process in which the silica surface amine replaces NCs surface amine ligands and is directly combined with NCs surface atoms. The latter method is just like a ligands exchange in case the silica surface amine carbon chain is shorter than the NCs surface amine ligand carbon chain.

2.2 Applications of chiral luminescent semiconductor NCs

Chiral luminescent materials showed different absorption and emission of left- and right-handed circularly polarized light which are related to the electron spin. Transducing information encoded within electron spins into photons is an attractive route toward realizing smaller, faster, and more energy-efficient technologies for memory storage,⁸⁸ quantum computation for information processing,⁸⁹ and electronic-magnetic- or temperature-based sensors.⁹⁰ Organic chiral materials have already been used in chiral catalysis,⁹¹ chiral separations,⁹² 3D display⁹³, and spintronics.⁹⁴ Endowing chirality to inorganic semiconductor NCs would expand their applications widely. Indeed, the chiral semiconductor NCs have exhibited potential applications in biology, chemistry, and physics fields. In Biology, the chiral semiconductor NCs have been used in chiral drug and amino acid detection,^{95,96} cytotoxicity mediation⁹⁷, and gene editing.⁹⁸ In chemistry, they could be used in chiral catalysis,⁹⁹ enantiomeric detection¹⁰⁰, and separation.¹⁰¹ In physics, they could be used in CPL detector¹⁰ and spintronics due to their chiral-induced spin selectivity effects.¹³

2.2.1 Chiral-induced spin selectivity (CISS)

Chirality-induced spin selectivity (CISS) effect was first reported in 1999¹⁰² and recently, the field has been expanded fast in both extensive experimental and theoretical studies which were summarized in several review papers.^{13, 103, 104} The CISS effect is hypothesized to arise from the coupling between the magnetic moment of an electron and effective magnetic fields generated by electron propagation through a stereogenic center or along a molecular helix. This effective magnetic field lifts the spin degeneracy (a result of the Zeeman effect), thereby aligning the electron spin

parallel (right-handed helicity) or antiparallel (left-handed helicity) to the direction of the electron's linear momentum.¹⁰³ As shown in Figure 1-12, the non-polarized electrons pass through the chiral crystals to generate spin-polarized electrons and the spin directions depend on the handedness of the crystals.¹⁰⁵

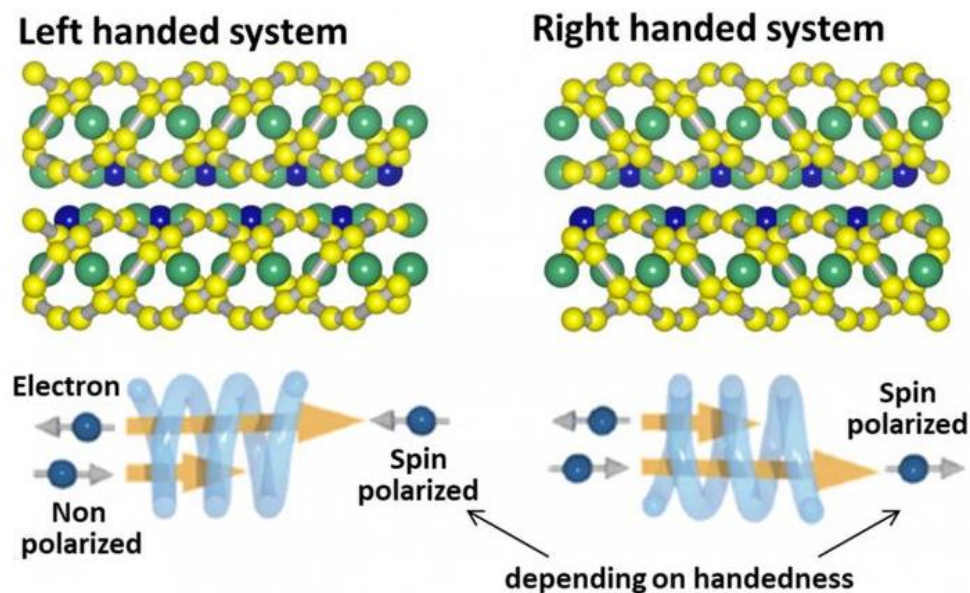


Figure 1-12. Schematic of crystalline structures of chiral crystals CrNb_3S_6 and chirality-induced spin selectivity phenomena in chiral materials.

CISS effect has been used in electrochemical splitting of water into hydrogen and oxygen due to the electron spin orientation could decide the chemical reaction path. Different products can be obtained when the dissociation occurs from a singlet state versus a triplet state has been reported in 1995.¹⁰⁶ The splitting of water process starts from two water molecules which are singlets and ends with two hydrogen molecules (singlets) and an oxygen molecule which is a triplet. Theoretically, this process is spin-forbidden and slow.¹⁰⁷ In fact, this process requires a significant overpotential voltage and accompanied by a byproduct of hydrogen peroxide (singlet). Recent researches indicate that the chiral anode resulted selected spin can decrease the overpotential and suppress the byproduct of hydrogen peroxide (Figure 1-13 (a-b)).¹⁰⁸⁻¹¹⁰ Also the CISS effect can induce circularly polarized luminescence, as shown in Figure 1-13 (c-e), chiral $(R/S\text{-MBA})_2\text{PbI}_4$ can induce selected spin into CsPbI_3 NCs layer and result in circularly polarized electroluminescence (CP-EL).⁹

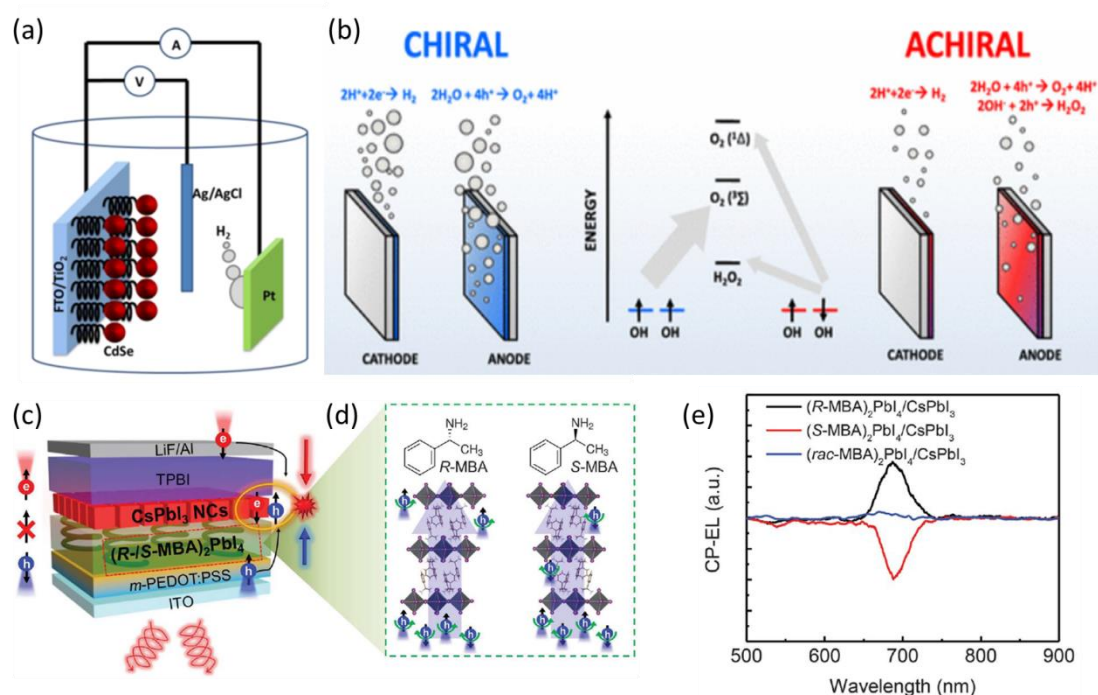


Figure 1-13. (a) Scheme of the photoelectrochemical cell used in the present study for water splitting. CdSe nanoparticles (red) are bound to the TiO₂ nanoparticles through chiral molecules. The TiO₂ nanoparticles are attached to the FTO conduction electrode. On the Pt electrode, the H⁺ ions are reduced to form H₂. (b) Scheme of the water-splitting process in chiral and achiral anode system. (c) Schematic illustration of spin-polarized charge injection and CP-EL emission in spin-LEDs. (d) Chiral 2D layered hybrid perovskites structure of (R-/S-MBA)₂PbI₄ polycrystalline. (e) The CP-EL spectra of spin-LEDs based on CISS layer/CsPbI₃ NCs.

Chiral inorganic NCs have already shown promising and advantaged applications due to their special photoelectric properties. How endowing chirality to inorganic NCs is an emerging and urgent issue.

2.3 How to introduce chirality to inorganic semiconductor NCs

There are various ways to obtain chiral signals from NCs or nanoparticles (NPs). C. Gautier and T. Burgi¹¹¹ have described three categories of chiral metal nanoparticles: (a) chiral ligands are used to stabilize the NCs creating a chiral “footprint” on the surface of the metal, (b) the optical activity arises from an intrinsically chiral

inorganic core shape, (c) the inorganic core can be chiral electrostatic field. This classification is based on the chiral source which has chiral optical activity: particle structure, environment, and surface, respectively.

This was further developed by N. A. Kotov et.al¹¹² in the extensive review describing four types of chemical and physical origins of chirality for nanoparticles based on the differences in the formation process of the chiral particles. (a) NPs with the chiral surface of the inorganic core, which is normally induced through the adsorption of chiral molecules. (b) NPs with a chiral pattern of the surface ligands. (c) the inorganic core of the NP has a chiral shape itself. (d) polarization effects in the inorganic core, which can be induced by chiral molecules or assembly of nanoparticles.

In this section, the chirality of nanoparticles induced by chiral ligands, chiral lattice, the chiral shape of an individual particle, and chiral self-organization (template-free and chiral template self-organization) of achiral particles have been detailed discussed.

2.3.1 Chirality induced by chiral ligand

Chiral ligands have been widely used to endow chirality to NCs of noble metal, such as Au nanocluster^{113, 114}, and Ag nanoparticles¹¹⁵. In 2005¹¹⁶, the pair of gold nanocluster enantiomers was first reported; The gold nanoclusters capped with D- or L-penicillamine show mirror images CD spectra, and their dissymmetry g-factor decreased with increasing gold nanocluster size. The mechanism of chirality induction by chiral ligands is supposed to be chiral footprint or local chiral distortion of the surface atoms. To have a better understanding of the chirality induction, the binding model between chiral ligands and Au nanoparticles has been studied by infrared (IR) and vibrational circular dichroism (VCD) spectra^{117, 118}. The authors have shown that thiols and carboxylic acid group co-interact with the gold particle lead to the chiral footprint which is the origin of the observed optical activity.

Meanwhile, semiconductor NCs such as quantum dots (QDs) capped with chiral ligands also attract lots of attention due to their excellent absorption and emission

properties. In 2007¹¹⁹, Gun'ko first reported optically active properties of CdS QDs capped with D- or L-penicillamine. Subsequently, many reports can be found for the investigation of the mechanism of chirality induction from chiral ligands to QDs. In 2009¹²⁰, Nakashima *et al.* reported CdS, CdSe and CdTe QDs capped with D- or L-cysteinemethylester hydrochloride. Interestingly, neither CdSe nor CdTe QDs showed a CD signal in the range of the first exciton peak (CdSe at 470 nm and CdTe at 540 nm). It indicates that the observed CD signals cannot be attributed to the first excitonic transition in QDs cores but attributed to the surface Cd atoms coordinated by ligands S atoms. The chirality of QDs is supposed to be originated from the distorted Cd-S-ligands surfaces. Furthermore, the chirality of the NC surface was maintained even after ligands were exchanged from chiral with an achiral thiol, providing a chiral memory effect as shown in Figure 1-14 (a).

In 2015¹²¹, Gun'ko proposed that the CdSe/ZnS QDs have intrinsic chirality caused by the presence of natural chiral defects even they are prepared without using chiral ligands. As shown in Figure 1-14 (b), the TEM images of as-prepared QDs show the possible presence of left- and right-handed screw dislocations. The QDs are supposed to compose of the racemic mixture of left- and right-handed QDs and also non-chiral QDs. They have shown that the racemic mixture of such NCs can be separated using water-soluble chiral ligands mixed with oil-soluble QDs through the phase transfer method.

In 2016¹²², Balaz found that the CD signals could be inversed only by alteration of the structure of the chiral ligand. The QDs combined with only two ligands slightly different both having levorotatory (L) (Acetyl-L-cysteine vs L-cysteine) configuration show mirror CD images (Figure 1-13 (c)). It was demonstrated that the CD signals are determined not only by the absolute configuration but also by the binding modes between the chiral ligands and the QDs surface. An inversion of CD signals of HgS QDs upon heating with N-acetyl-L-cysteine also reported¹²³. This inversion was explained by Fourier transform infrared (FTIR) and theoretical calculation as the result of the modification of the coordination between chiral ligands and the surface of QDs upon heating. Gun'ko¹²⁴ then reported that the binding mode of cysteine on

CdSe/CdS QDs strongly depends on the concentration of the ligands (Figure 1-14 (d)). In lower cysteine concentration, the cysteine combined with QDs surface with tridentate mode with enhanced CD signals whilst, at higher cysteine concentration, the tridentate coordination mode changed to bidentate coordination mode result in a decrease in the CD signals. Indeed, the chiral ligands have a big influence on the chirality induction process.

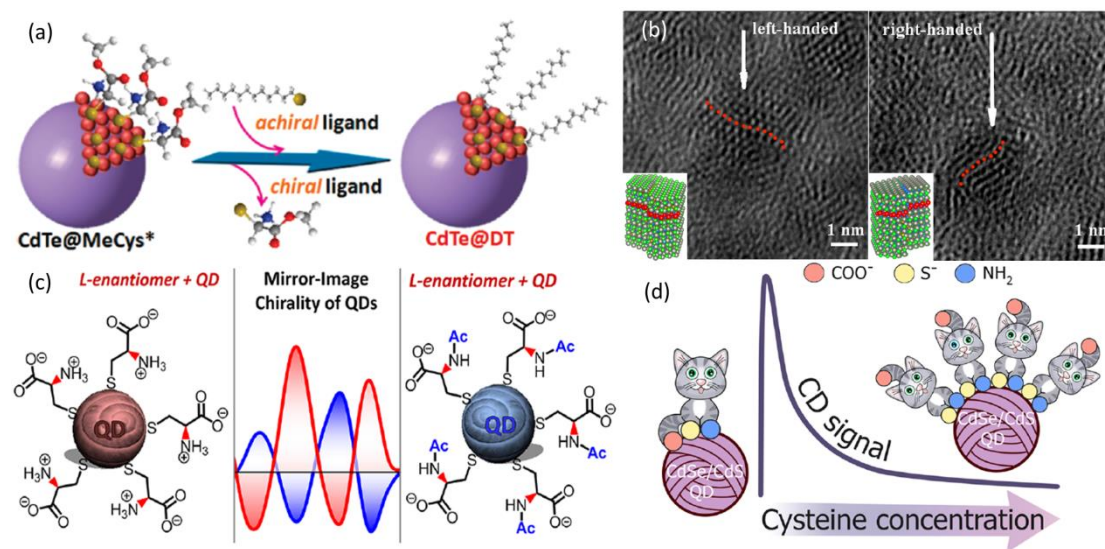


Figure 1-14. (a) Schematic of chiral memory effect by a ligand-exchange reaction from chiral ligands D- or L-cysteinemethylester hydrochloride (MeCys) to 1-dodecanethiol (DT). (b) TEM images of the CdSe/ZnS QDs. The arrows indicate possible screw dislocation and the red dotted lines indicate the direction of the dislocations. The insert pictures indicate the atomistic models of CdSe/ZnS QDs with right and left screw dislocations and the dislocations are set in the (010) plane of CdSe core of NCs with (-) Burgers vector and (+) Burger vector. (c) Same configuration but different binding arrangements of N-acetyl-L-cysteine and L-homocysteine-QDs result in mirror CD images. (d) The strong influence of the concentration of a chiral amino acid (cysteine) on its binding modes upon the surface of CdSe/CdS QDs, resulting in varying QDs chiroptical activity and corresponding CD signals.

The physical and chemical properties of NCs are determined by their size, shape, and

crystal structure. Beyond the chirality induction based on the effect of the chiral ligand, the inherent structural properties of NCs such as their sizes, shapes, and crystal structures also show a great impact on the chirality induction. In 2011, Tang¹²⁵ and Markovich¹²⁶ reported simultaneously that CdSe QDs combined with chiral ligands show optical activity size dependence effect. As shown in Figure 1-15 (a), the dissymmetry g-factor (g_{abs}) decreased with increasing the size of QDs which is likely due to the decreasing of surface-to-volume ratio. In 2017¹²⁷, Tang reported that the CdSe rods with different aspect ratios combined with L/D cysteine show dissymmetry g-factor of shape dependence effect. The g-factor increases with an increasing aspect ratio (sphere to the rod) and reaches a saturated value with an aspect ratio at about 3.7 based on the theoretical calculations. Recently, CdSe/CdS with various morphologies such as quantum rods, nanoflowers, tadpoles, tetrapods also has been reported¹²⁸⁻¹³⁰. In 2018¹³¹, Tang reported that the CdSe nanoplatelets having wurtzite (hexagonal) and zincblende (cubic) crystal structure shown different behaviors in terms of chirality induction from their L/D cysteine ligands as shown in Figure 1-15 (c). CdSe NPLs with hexagonal crystal structure showed 10 times higher CD spectra compared to those having cubic crystal structure. This was explained as the results of their different dipole moment and polarization.

In general, bare core QDs suffer lower photoluminescence quantum yield (PLQY) due to their surface traps. QDs with core-shell structures like CdSe core and CdS shell could boost the PLQY which could be widely used in lighting and display. As shown in Figure 1-15 (d), the QDs with CdSe/CdS core-shell structure showed dissymmetry g-factor and PLQY which depended on the CdS shell thickness; PLQY increased with CdS shell thickness increasing, while the g-factor decreased due to the increased distance between chiral ligands and CdSe core.¹³²

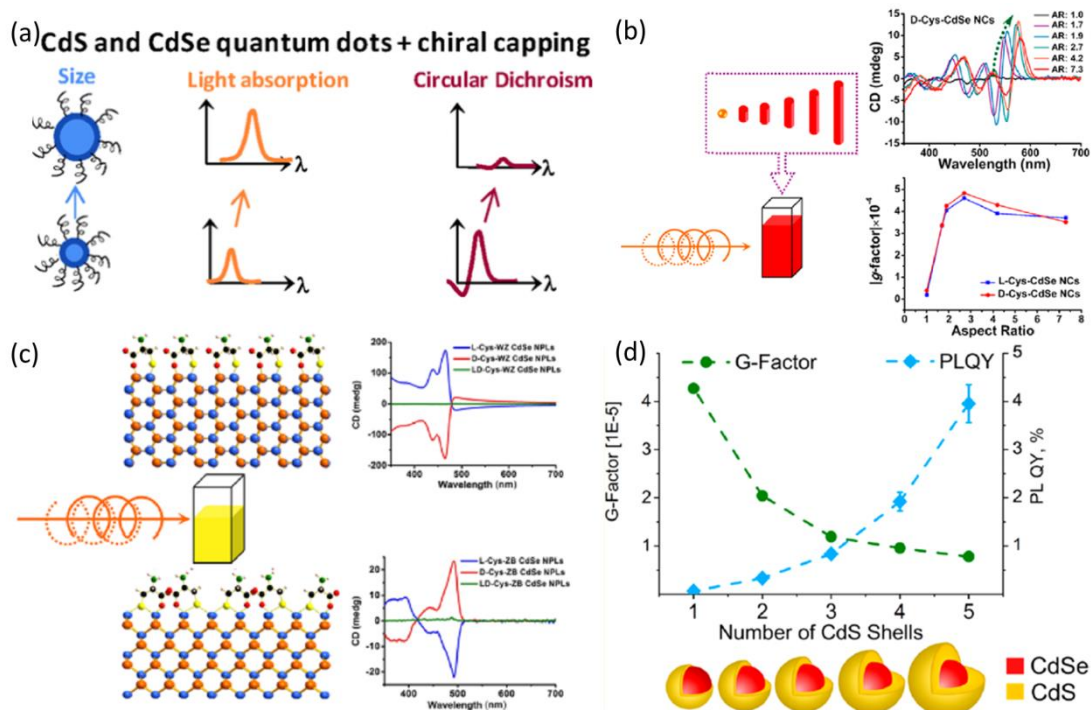


Figure 1-15. (a) Size effect of optical activity properties of CdSe and CdS QDs induced by chiral ligands. The increasing size of QDs results in stronger and red shift absorption but lower CD signals. (b) Shape effect of optical activity properties of CdSe quantum rods induced by chiral ligands. Dissymmetric g-factor increased with increasing rods aspect ratio and then reached a plateau. (c) Crystal structure effect of optical activity properties of CdSe nano-platelets (NPLs). The hexagonal crystal structured CdSe NPLs capped with L- or D-cysteine ligands show distinguished CD shape and much stronger CD signal compared with cubic crystal structured CdSe NPLs. (d) Shell-thickness effect of optically active properties of CdSe/CdS core-shell structured QDs induced by chiral ligands. The increased shell thickness results in enhanced fluorescence but lower induced dissymmetric g-factor.

Recently, perovskite NCs combined with chiral ligands also show promising CD and CPL properties.^{10, 13, 133, 134} The best dissymmetry g-factor can reach 0.02 which is the highest among the NCs chiral ligands system.

2.3.2 Chirality induced by chiral lattice

Apart from crystals of synthetic chiral organic molecules and natural biomolecules, there are also many chiral crystals inorganic materials.^{15, 17, 135} Recently, the inorganic semiconductor NCs with chiral lattice attracted lots of attention due to their excellent electronic, magnetic, and optical properties.^{14, 16, 18, 21} The chiral lattice of α -HgS NCs with right- or left-handed lattice could be prepared by the thiolated chiral biomolecules as shown in Figures 1-16 (a-c). The enantiomeric excess could be decided by the configuration of chiral biomolecules.¹⁴ The enantiopurity of chiral HgS NCs could be enhanced by the Ostwald ripening process to achieve a higher g-factor up to 0.02 as shown in Figure 1-16 (d).¹⁶ Besides, the chiral lattice of HgS NCs could be grown into a chiral shape or a different achiral shape with cooperative chirality.²⁰ Similar to the hierarchical assembly of chiral biomolecules, the chiral crystals HgS NCs could be self-organized with certain conditions as shown in Figure 1-16 (c).¹⁸ The chiroptical responses of the self-organization system are found to uniquely depend on intrinsic chirality of building blocks and their coupling. In addition to the chiral lattice of HgS, the chiral lattice of Se and Te nanostructure also could be synthesized assisted by chiral biomolecules.²²

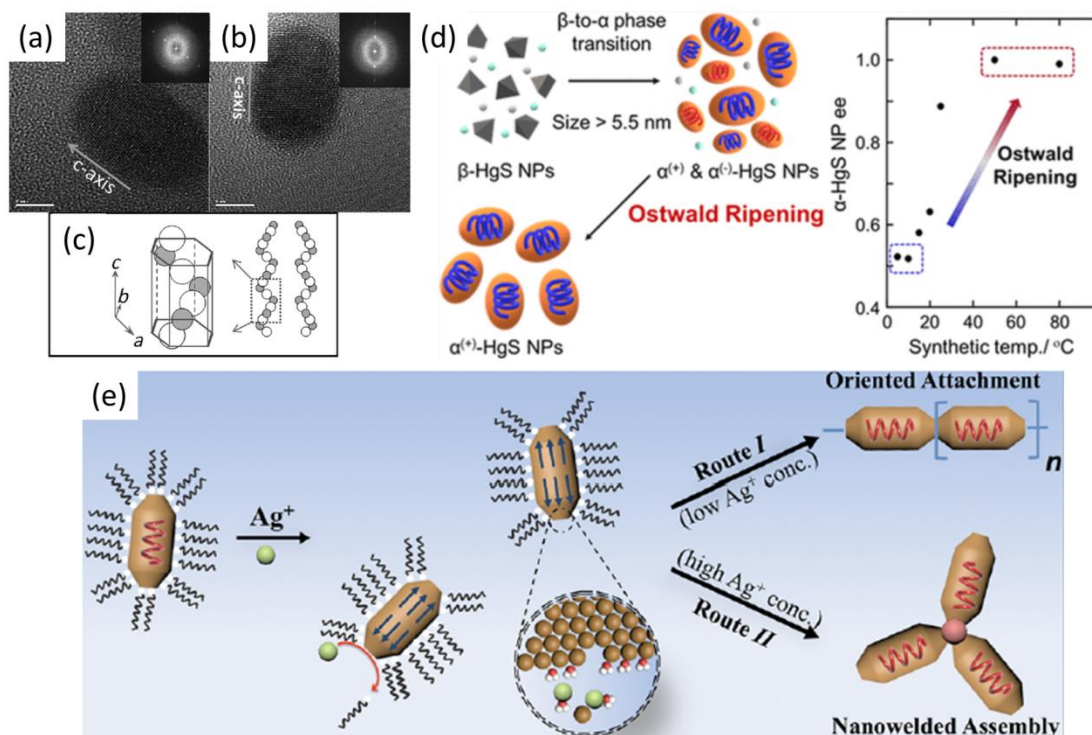


Figure 1-16. (a) and (b) High-resolution TEM images of individual HgS NCs; blue arrows mark the c-axis direction of the NC. Scale bars are 5 nm. (c) Schematic

illustration of the opposite spirals of atoms with a fraction of one spiral reconstructed inside the frame of the hexagonal unit cell. (d) Schematic of pure enantiomeric of HgS growth process and the ee value of HgS with different synthesis temperature. (e) Schematic illustration of Ag ions assisted assembly of chiral HgS NCs for inorganic chiral building block system.

2.3.3 Chirality induced by the chiral shape of individual particle

Many reports can be found on the chiral shapes of inorganic materials obtained by soft templates such as SiO_2 ^{35, 136-138}, TiO_2 ¹³⁹, CdS ¹⁴⁰ helices, or chiral shapes induced by chiral molecules such as ZnO ¹⁴¹, Ag ¹⁴² films, and CuO nanoflowers.¹⁴³ Such inorganic NCs having morphologically chiral shape, while it is very challenging to achieve them, are very efficient in chirality induction and many applications due to their excellent physical and chemical properties can be envisaged. In 2014²², tellurium and selenium nanoparticles having chiral shape were synthesized assisted by chiral thiolated biomolecules with dissymmetry g-factor up to 0.03. Figures 1-17 (g) and (h) show the dark-field scanning transmission electron microscopy (STEM) images and tomographic reconstruction of the tellurium particle respectively. Also, the chiral tellurium nanostructures were transformed into chiral morphology of gold and silver telluride nanostructures with dissymmetry g-factor up to 0.015. In 2017^{18, 20}, chiral morphology of HgS was synthesized assisted with chiral ligands. As shown in Figure 1-17 (a), the α -HgS NCs with achiral morphology are applied as seeds, followed by successive ion layer adsorption and reaction (SILAR) method to epitaxial growth HgS with twisted bipyramid morphology. The prevailing morphology from epitaxial growth is determined by the chiral molecules utilized during the epitaxial growth and is independent of the crystallographic chirality of the seed nanoparticles. Figures 1-17 (b) and (c) show the right- and left-handed twisted bipyramid nanostructures with D- or L-penicillamine molecules as chiral morphology modifiers during the epitaxial growth process respectively. In 2018²⁸, chiral gold nanoparticles were synthesized by using chiral amino acids and peptides to control the handedness which shows strong

optical activity with a large dissymmetry g -factor of 0.2. As shown in Figure 1-17 (d), the L- and D-cysteine were used to synthesize right- and left-handed helicoid cube which shows mirror CD images. Figures (e) and (f) show the SEM image of right-handed and left-handed helicoid cubes respectively. Several reports on the chiral gold NPs followed since then.²⁴⁻²⁷ Also, the chiral morphology of palladium nanoparticles was obtained by the same protocol as shown in Figures (g-h).²⁹

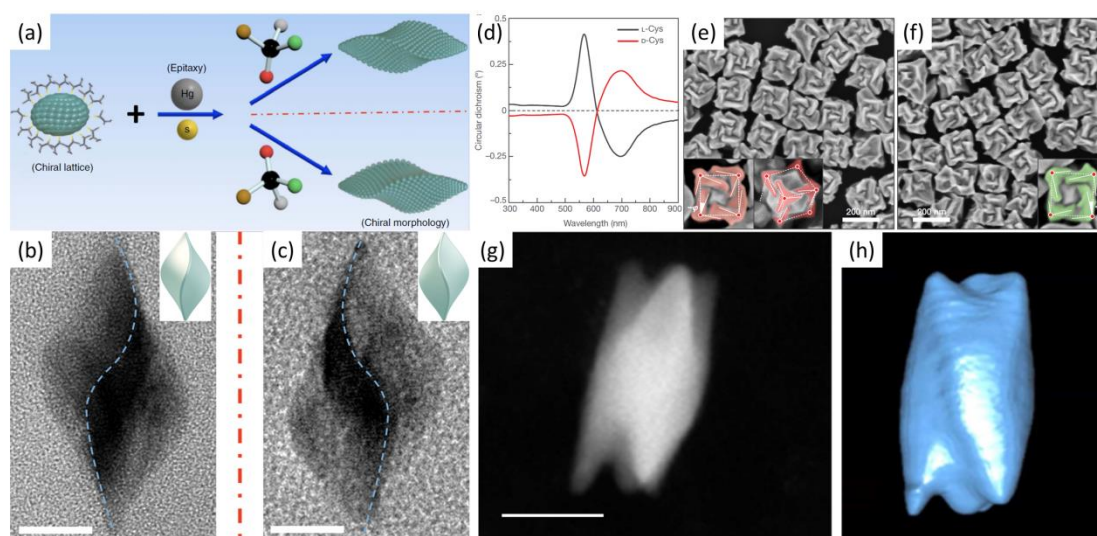


Figure 1-17. (a) Schematic of the growth process based on epitaxial principle with involvement of chiral molecule to tailor the chirality of morphology. (b) and (c) Typical TEM images of prevailing individual twisted triangular bipyramid nanostructures. Blue dashed curves are added to guide the eyes for different twisting orientations in the chiral nanostructure. Scale bar, 20 nm. Inset pictures indicate the structural models of two mirrored nanostructures. (d) Circular dichroism spectra of chiral nanoparticles synthesized using L-cysteine (black) and D-cysteine (red). (e) SEM image of L-cysteine nanoparticles. The highlighting in the insets illustrates the fact that the edges (solid lines) are tilted by an angle $-\phi$ concerning the vertices (red dots) and cubic outline (dashed lines), as viewed along the [110] (left) and [111] (right) directions. (f) SEM image of D-cysteine nanoparticles. The inset highlights the tilted edges (solid lines), cubic outline (dashed lines), and tilt angle ($+\phi$). (g) Dark-field STEM image and (h) tomographic reconstruction of the tellurium particle. Scale bar, 100 nm.

The inorganic materials having a chiral shape exhibited promising potential applications due to their big dissymmetry g-factor. Designing fluorescent NCs with having chiral shapes represents the new change with extremely promising applications.

2.3.4 Chirality induced by chiral self-organization

Recently, complex superstructures obtained from the self-assembly of NCs have been widely explored due to their unique optic, electronic, and magnetic properties. Similar to the organic molecular self-assemblies, the inorganic NCs can also be self-assembled into superstructures by their various inter-particle force, such as van der Waals force, electrostatic force, magnetic interaction, molecular surface force, and entropic effects^{144, 145}. Chiral superstructure could also be obtained under certain conditions.

In 2010¹⁴⁶, Kotvo *et al.* showed that the CdTe NCs self-assemble into twisted ribbons by visible light illumination. This chiral self-assembly is driven by the balancing force between attraction and electrostatic repulsion of the inter-nanoparticles. However, the self-assembled twisted ribbons are racemic with equal right-handed and left-handed twisted ribbons due to the absence of a chiral source. To get higher enantiomeric excess (ee) value, right- or left-handed circularly polarized light (CP-Light) was applied to obtain right- or left-handed twisted ribbons¹⁴⁷. As shown in Figure 1-18 (a), the CdTe QDs stabilized with achiral capping agent thioglycolic acid (TGA) could self-assemble into predominantly right- or left-handed twisted ribbons under the right- or left-CP-light illumination with ee value at 0.3. Figure 1-18 (b) shows the 3D tomographic reconstruction and SEM images of right- and left-twisted ribbons separately with a pitch around 800 nm.

Recently, gold NPs chiral self-assembly driven by CP-light illumination also reported¹⁴⁸. Subsequently, nanoparticle self-assembly has been optimized to get much higher ee values. CdTe with chiral ligands could be self-assembled into twisted ribbons by controlling the pH¹⁴⁹. The pH can control the repulsive interaction between

CdTe nanoparticles and result in chiral self-assembly. Higher ee value of twisted ribbons could be obtained due to the nanoparticle surface chiral ligands interactions. Also, the chiral assembly could be controlled by inducing polar solvent methanol¹⁵⁰. Interestingly, the CdTe nanoparticles have a chiral self-sorting effect. The racemic mixture of D- and L-cysteine CdTe assembled structures contained both left- and right-handed helices and there are no straight ribbons observed (conglomerate-type mixture), i.e. the CdTe nanoparticles trend self-assembly with NPs of the same chirality. The geometry of helices has been precisely controlled by solvent, pH, chiral ligand density, and coordination bridges between nanoparticles¹⁵¹. Those helical ribbons obtained by CdTe NCs self-assembly can show dissymmetric g-factor up to 6×10^{-2} as shown in Figures 1-18 (e) and (f).

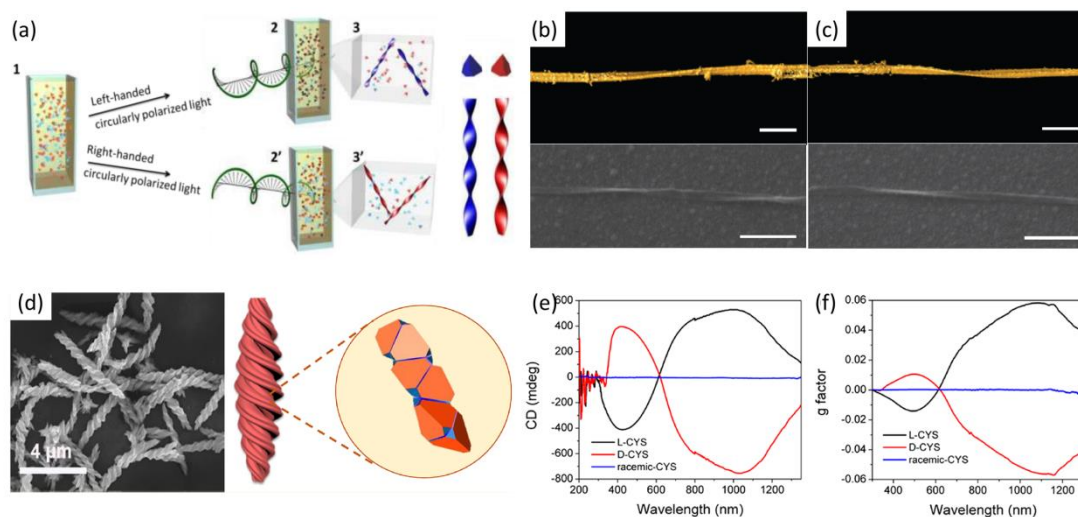


Figure 1-18. (a) Schematics of the CPL-induced self-assembly process. 1. Racemic mixture of CdTe QDs capped with L- and D-cysteine is prepared. 2. Left-handed CP-light selectively activates left-handed NPs. 2'. Right-handed CP-light activates right-handed NPs. 3. The excited left-handed NPs are self-assembled into left-handed nanoribbons. 3'. Right-handed NPs are self-assembled into right-handed nanoribbons. (b) and (c) show the surface rendering of 3D TEM tomographic reconstruction and SEM images of single left-handed and right-handed nanoribbons separately. (d) SEM image of CdTe helical superstructure by self-assembly (left) and the origin of enantiopurity in NP assembly into helices (right). (e) and (f) show the CD and g-factor of CdTe helical superstructure self-assembled by L-cys-CdTe NPs, D-cys-CdTe NPs,

and racemic cys-CdTe NPs.

The above chiral assemblies are mainly related to the chiral source such as chiral ligands or CP-light. Here, some interesting chiral assembly happened without any chiral source. In 2014¹⁵², Klajn reported the helical self-assembly of magnetite Fe₃O₄ nanocubes at air/liquid interfaces (Figure 1-19 (a)). These Fe₃O₄ NPs have a cubic shape with an average edge length around 13 nm and have axes [111] crystallographic direction. Without external magnetic fields, the NPs self-assemble into belts due to the shape anisotropy (favoring face-to-face interactions). When an external magnetic field is applied, the magnetite NCs self-assemble into helical superstructure due to the competition between the shape anisotropy and magnetocrystalline anisotropy (favoring corner-to-corner interactions). Figure 1-19 (b) shows the shapes of Fe₃O₄ NPs affect the morphologies of the self-assembly under external magnetic fields, truncated octahedral self-assembly into belts, while rounded cubes and Fe₃O₄-Ag heterodimeric NCs self-assembly into helical superstructures. This helical self-assembly also has self-sorting effects, but the handedness of assembled helices is random with a different batch of experiments. The CdSe nanoplatelets (NPLs) also can similarly self-assembly into chiral ribbons by adding the achiral ligands oleic acid¹⁵³ as shown in Figure 1-19 (e).

To conclude this section, an interesting report in which Xia *et al.* showed that spherical polystyrene beads with particle size around several hundred nanometers also could organize into helical structures when they are confined in the V-shaped grooves¹⁵⁴ (Figure 1-19 (g)). The authors reported that the helical organization of these spherical particles was observed when the ratio between the width of the V-grooves and the diameter of the colloids falls between 2.7-2.85. And the handedness could be controlled by the relative orientation of capillary force concerning the longitudinal axis of the helices, while the capillary force is created by the meniscus of the liquid during the filling of the particles in aqueous suspension into the grooves. As shown in Figure 1-19 (g), the capillary force oriented to the right direction (region B) result in left-handed helical self-assembly, while the capillary

force oriented to left direction (region D) result in right-handed helical self-assembly. Meanwhile, the capillary force oriented to the middle part (region C), both right- and left-handed helical ribbons could be observed.

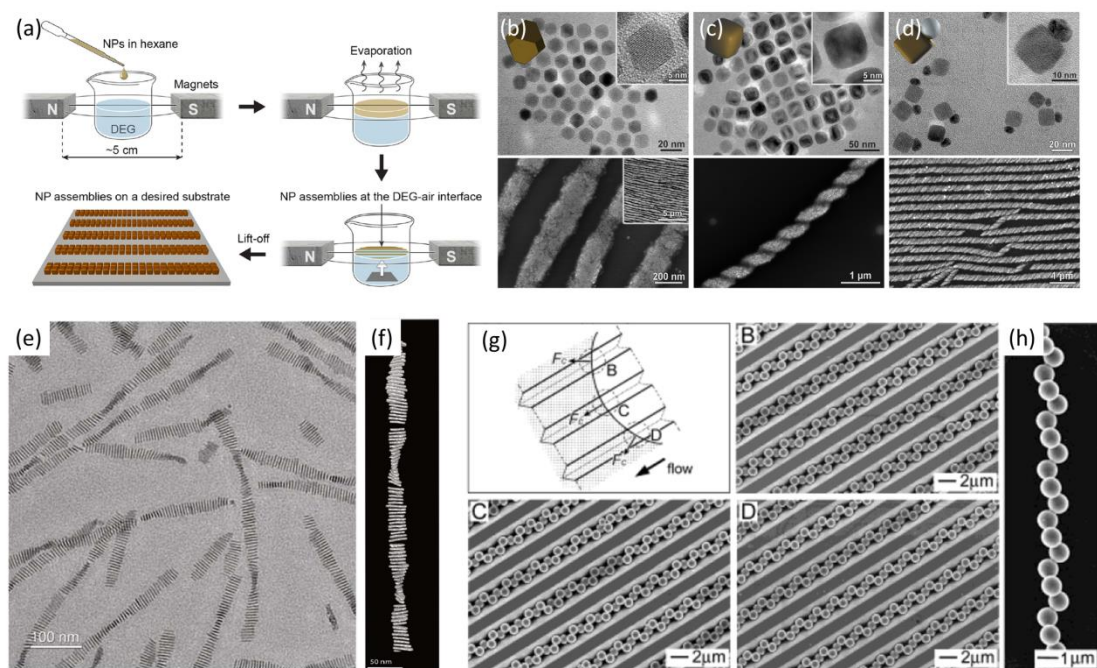


Figure 1-19. (a) Schematic representation of the experimental setup for self-assembly of magnetic Fe₃O₄ NCs. (b) TEM images of truncated octahedral (top) and SEM images of 1D belts as they assemble (bottom). (c) TEM images of rounded cubes (top) and an SEM image of the resulting helix (bottom). (d) TEM images of Fe₃O₄-Ag heterodimeric NCs (top) and an SEM image of an ensemble of helices (bottom). (e) TEM images of twisted ribbons of self-assembled CdSe NPLs. (f) 3D model from the tomographic reconstruction of a twisted ribbon. (g) SEM images of helical chains with different chiralities were obtained with the capillary forces oriented toward different directions relative to the longitudinal axis of the V-grooves. (h) The SEM image of a free-standing helical aggregate after it had been welded by thermal annealing and subsequently released from the original V-grooves.

Template-free chiral self-assembly as presented above has been developed with amazing progress, a higher ee value of chiral superstructure and a stronger

dissymmetric g-factor has been achieved. However, no CPL reported until now, it might be due to the quench of fluorescence with the strict condition for the chiral self-assembly. There is no doubt that higher CD and CPL properties will be achieved and widely used in different fields in the future.

Chiral assemblies by soft templates for the NCs, such as gold NPs^{57, 59, 60, 62, 155-157}, and silver NPs¹⁵⁸ have been widely reported. Gold nanorods (NRs) self-organized in three-dimensional (3D) chiral fibers structure made by anthraquinone-based oxalamide (Figure 1-20 (a)).⁵⁷ NRs are preferentially aligned along the longitudinal direction of the fibers through non-covalent interactions. The CD spectra between 300 to 500 nm correspond to the supramolecular fibers, while the CD between 600 to 900 nm corresponds to the chiral arrangement of the NRs associated with the longitudinal localized surface-plasmon resonance (LSPR) yielding a g-factor of 0.02. For the gold nanospheres combined with these chiral fibers, no optical activity was observed at the LSPR wavelength range. However, gold NPs with spherical shape self-organized with DNA origami could show strong CD signals in the LSPR wavelength as shown in Figure 1-20 (b).^{62, 157} Also, the gold NPs or NRs and liquid crystal molecules could co-crystallize into right- or left-handed helical alignment which also shows CD images as shown in Figure 1-19 (c).^{55, 155} Similarly, the QDs can co-assembly with chiral lipid *N,N*-bis(octadecyl)-*L*-glutamic diamide (LGAm) or DGAm into helical alignment which results in big optically active properties as shown in Figure 1-20 (d).^{56, 58} Chiral lipids can form a gel with chiral assembly, by adding PNCs, they can co-assemble to form cogel. The doped PNCs follow the chirality of the gel structure to produce a chiral packing that could lead to the induced chirality of PNCs. By heating or cooling the cogel, the induced CPL could be switched off. The chiral self-assembly by chiral soft templates exhibits strong optically active properties, however, it suffers bad stability due to the fragile of the soft templates which are easy to be destroyed by changing temperature, pH, and impurity which hinders future applications.

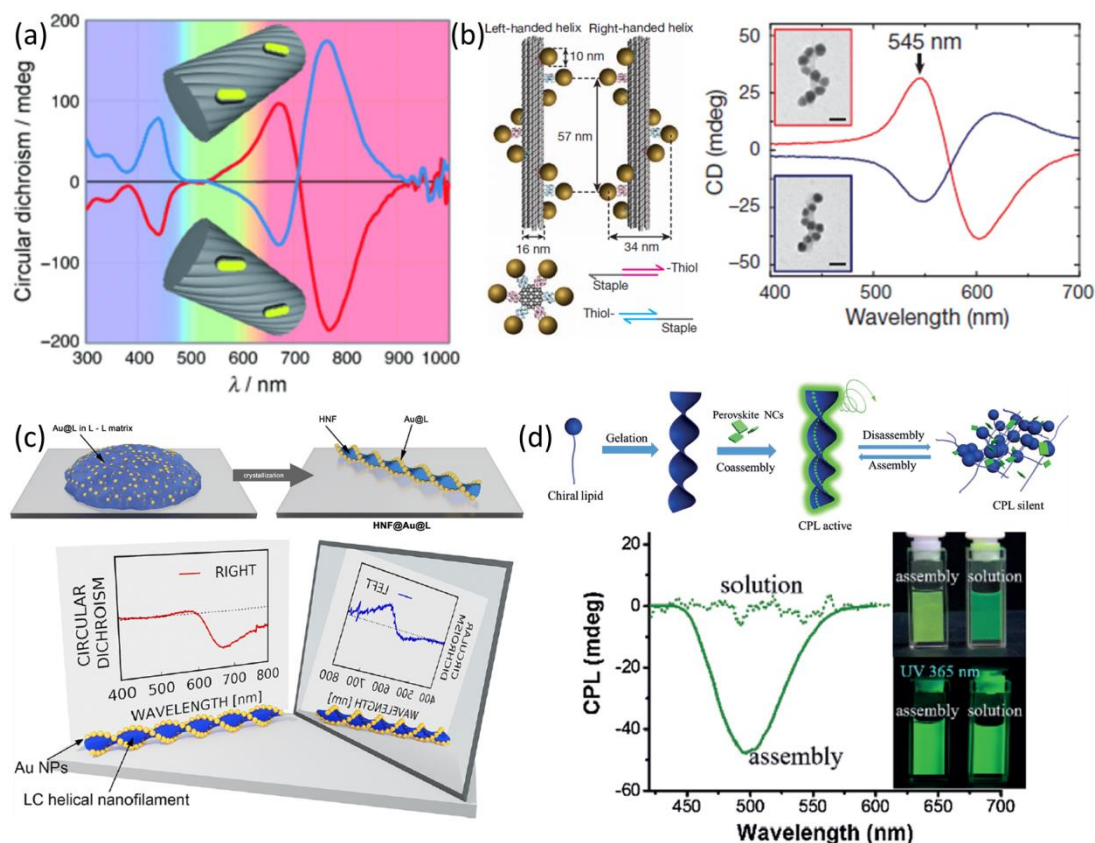


Figure 1-20. (a) General sketch of the Au NRs positioned onto the surface of a cylinder of fiber backbone with chiral morphology, the orientation of each particle is defined so that its long axis is tangential to a helical curve of 3 μm pitch. (b) Left- and right-handed nanohelices (diameter 34 nm, helical pitch 57 nm) are formed by nine gold nanoparticles with the diameter of 10 nm that are attached to the surface of DNA origami 24-helix bundles (each of diameter 16 nm) and typical CD spectra of the chiral self-organized NPs-helix. (c) Scheme of the formation of Au NPs helical assemblies templated by liquid crystals and the corresponded CD spectra with right or left-handed assemblies. (d) Illustration of the possible co-assembly induced chirality of perovskite NCs in chiral gels. The co-assembly system could be destroyed by changing the temperature.

Compared with fragile soft templates, hard templates such as chiral silica ribbons are much stable which would be more useful to design functionalized materials. In 2013, Che reported chirality introduction by metal ions or metal oxides chiral arrangement along with the chiral mesoporous silica due to the molecular imprinting (Figure 1-21

(a)).¹⁵⁹ Also in our group, gold NPs electrostatically adsorbed or covalently grafted on the surface of silica helical ribbons also have shown strong CD signals from the plasmonic resonance as shown in Figure 1-21 (b).^{160, 161}

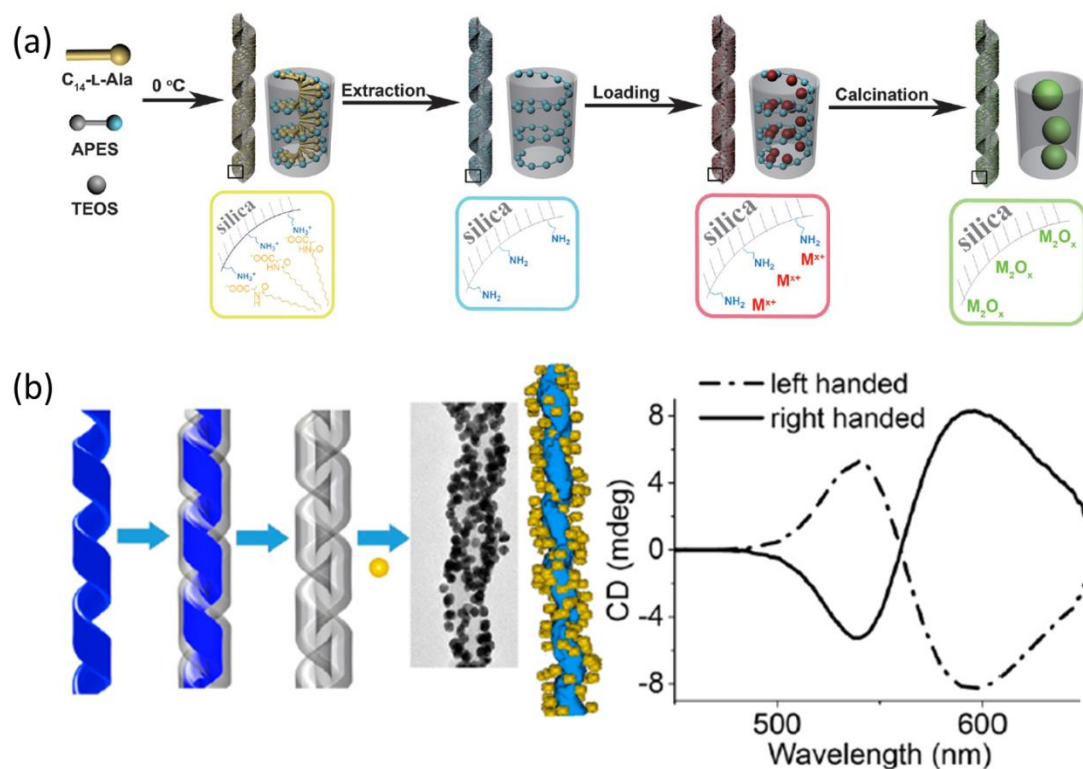


Figure 1-21 (a) Schematic of nanoparticle self-organized in the side of silica helices. (b) Gemini surfactant self-assemble to form nanometric helices and is used as the template for sol-gel condensation to obtain silica nanohelices. The functionalized silica nanorhelices are decorated with gold NPs. The right picture shows typical CD spectra of gold NPs-R/L-silica nanorhelices.

Compared with soft templates, hard templates show promising applications. While the study of gold NPs chiral self-organization by hard templates is reported to a limited extent. The yield dissymmetric g-factor ranges from magnitudes of 10^{-4} to 10^{-3} which is lower than that with self-organization assisted by soft templates (10^{-2}). The difference of the g-factor might be caused by the different gold NPs self-organization due to the different interactions of NPs with hard templates and soft templates. The

study of luminescent semiconductor NCs chiral self-organization by hard templates is still lacking. Besides, chiral luminescent NCs with CPL would benefit their applications. So there is still a long road for the development of the NCs chiral self-assembly with hard templates.

3. Conclusion

In this chapter, it introduced that chirality widely exists in our world and emphasized its importance in our life. The organic and inorganic chirality from molecular chirality to hierarchical chirality has been discussed and compared one to one correspondence. Compared with organic optical materials, inorganic optical materials exhibit excellent optical properties and stability. The chirality of inorganic materials especially NCs attract more and more attentions recently. Inorganic chiral NCs exhibited promising applications in spintronics, catalysis, detector *etc.* The general way to endow chirality to NCs has been summarized. Chirality induced by chiral ligands exhibited a small dissymmetric g-factor and result in lower fluorescence. Chirality induced by chiral lattice and chiral shape show big dissymmetric g-factor but with limited materials have been reported. Chirality induced by chiral self-organization also shows a big dissymmetric g-factor. The chiral self-organization by chiral organic templates or templates free has been widely reported, while the reported chiral self-organization by chiral inorganic templates is still limited. In this thesis, the aim is to obtain optically active inorganic NCs by chiral self-organization on the surface of inorganic templates or preparation of chiral shaped NCs inside hollow silica ribbons. At last, the surface of NCs and ligands exchange has been introduced to guide us on how to combine the NCs with inorganic silica ribbons.

4. Reference

1. Liu, K. S.; Tian, D. L.; Jiang, L., Frontier of Inorganic Synthesis and Preparative Chemistry (I) Biomimetic Synthesis. In *Modern Inorganic Synthetic Chemistry*, 2017; pp 687-721.
2. Cheng, X.; Miao, T.; Qian, Y.; Zhang, Z.; Zhang, W.; Zhu, X., Supramolecular Chirality in Azobenzene-Containing Polymer System: Traditional Postpolymerization Self-Assembly Versus In Situ Supramolecular Self-Assembly Strategy. *Int J Mol Sci* **2020**, *21* (17).
3. Pasteur, L., Mémoire sur la relation qui peut exister entre la forme cristallines et la composition chimique, et sur la cause de la polarisation rotatoire. *C. R. T. Academie des science* **1848**, *26*, 535-539.
4. Brooks, W. H.; Guida, W. C.; Daniel, K. G., The significance of chirality in drug design and development. *Curr Top Med Chem* **2011**, *11* (7), 760-70.
5. Smith, S. W., Chiral toxicology: it's the same thing...only different. *Toxicol Sci* **2009**, *110* (1), 4-30.
6. Chen, Z.; Wang, Q.; Wu, X.; Li, Z.; Jiang, Y. B., Optical chirality sensing using macrocycles, synthetic and supramolecular oligomers/polymers, and nanoparticle based sensors. *Chem Soc Rev* **2015**, *44* (13), 4249-63.
7. Pu, L., Fluorescence of organic molecules in chiral recognition. *Chem Rev* **2004**, *104* (3), 1687-716.
8. Xia, Y.; Zhou, Y.; Tang, Z., Chiral inorganic nanoparticles: origin, optical properties and bioapplications. *Nanoscale* **2011**, *3* (4), 1374-82.
9. Kim, Y. H.; Zhai, Y.; Lu, H.; Pan, X.; Xiao, C.; Gaubing, E. A.; Harvey, S. P.; Berry, J. J.; Vardeny, Z. V.; Luther, J. M.; Beard, M. C., Chiral-induced spin selectivity enables a room-temperature spin light-emitting diode. *Science* **2021**, *371* (6534), 1129-1133.
10. Chen, C.; Gao, L.; Gao, W.; Ge, C.; Du, X.; Li, Z.; Yang, Y.; Niu, G.; Tang, J., Circularly polarized light detection using chiral hybrid perovskite. *Nat Commun* **2019**, *10* (1), 1927.
11. Brandt, J. R.; Salerno, F.; Fuchter, M. J., The added value of small-molecule chirality in technological applications. *Nature Reviews Chemistry* **2017**, *1* (6).
12. Gao, X.; Han, B.; Yang, X.; Tang, Z., Perspective of Chiral Colloidal Semiconductor Nanocrystals: Opportunity and Challenge. *J Am Chem Soc* **2019**, *141* (35), 13700-13707.
13. Long, G.; Sabatini, R.; Saidaminov, M. I.; Lakhwani, G.; Rasmita, A.; Liu, X.; Sargent, E. H.; Gao, W., Chiral-perovskite optoelectronics. *Nature Reviews Materials* **2020**, *5* (6), 423-439.
14. Ben-Moshe, A.; Govorov, A. O.; Markovich, G., Enantioselective synthesis of intrinsically chiral mercury sulfide nanocrystals. *Angew Chem Int Ed Engl* **2013**, *52* (4), 1275-9.
15. Dryzun, C.; Avnir, D., On the abundance of chiral crystals. *Chem Commun (Camb)* **2012**, *48* (47), 5874-6.
16. Kuno, J.; Miyake, K.; Katao, S.; Kawai, T.; Nakashima, T., Enhanced Enantioselectivity in the Synthesis of Mercury Sulfide Nanoparticles through Ostwald Ripening. *Chemistry of Materials* **2020**, *32* (19), 8412-8419.
17. Flack, H. D., Chiral and Achiral Crystal Structures. *Helvetica Chimica Acta* **2003**, *86* (4), 905-921.
18. Wang, P. P.; Yu, S. J.; Ouyang, M., Assembled Suprastructures of Inorganic Chiral Nanocrystals and Hierarchical Chirality. *J Am Chem Soc* **2017**, *139* (17), 6070-6073.
19. Kuznetsova, V.; Gromova, Y.; Martinez-Carmona, M.; Purcell-Milton, F.; Ushakova, E.; Cherevko, S.; Maslov, V.; Gun'ko, Y. K., Ligand-induced chirality and optical activity in semiconductor nanocrystals: theory and applications. *Nanophotonics* **2020**, *10* (2), 797-824.
20. Wang, P. P.; Yu, S. J.; Govorov, A. O.; Ouyang, M., Cooperative expression of atomic chirality in

- inorganic nanostructures. *Nat Commun* **2017**, *8*, 14312.
21. Yang, L.; Liu, J.; Sun, P.; Ni, Z.; Ma, Y.; Huang, Z., Chiral Ligand-Free, Optically Active Nanoparticles Inherently Composed of Chiral Lattices at the Atomic Scale. *Small* **2020**, *16* (24), e2001473.
22. Ben-Moshe, A.; Wolf, S. G.; Bar Sadan, M.; Houben, L.; Fan, Z.; Govorov, A. O.; Markovich, G., Enantioselective control of lattice and shape chirality in inorganic nanostructures using chiral biomolecules. *Nat Commun* **2014**, *5*, 4302.
23. Huffaker, D. L.; Eisele, H.; Tepliakov, N. V.; Baimuratov, A. S.; Baranov, A. V.; Fedorov, A. V.; Rukhlenko, I. D., Analytical study of optical activity of chiral-shape nanocrystals. In *Quantum Dots and Nanostructures: Growth, Characterization, and Modeling XIV*, 2017.
24. Cho, N. H.; Byun, G. H.; Lim, Y. C.; Im, S. W.; Kim, H.; Lee, H. E.; Ahn, H. Y.; Nam, K. T., Uniform Chiral Gap Synthesis for High Dissymmetry Factor in Single Plasmonic Gold Nanoparticle. *ACS Nano* **2020**, *14* (3), 3595-3602.
25. Karst, J.; Cho, N. H.; Kim, H.; Lee, H. E.; Nam, K. T.; Giessen, H.; Hentschel, M., Chiral Scatterometry on Chemically Synthesized Single Plasmonic Nanoparticles. *ACS Nano* **2019**, *13* (8), 8659-8668.
26. Kim, H.; Im, S. W.; Cho, N. H.; Seo, D. H.; Kim, R. M.; Lim, Y. C.; Lee, H. E.; Ahn, H. Y.; Nam, K. T., gamma-Glutamylcysteine- and Cysteinylglycine-Directed Growth of Chiral Gold Nanoparticles and their Crystallographic Analysis. *Angew Chem Int Ed Engl* **2020**, *59* (31), 12976-12983.
27. Yuan, C.; Jiang, J.; Wang, D.; Hu, Y.; Liu, M., In Situ Growth of Chiral Gold Nanoparticles in Confined Silica Nanotube. *J Nanosci Nanotechnol* **2019**, *19* (5), 2789-2793.
28. Lee, H. E.; Ahn, H. Y.; Mun, J.; Lee, Y. Y.; Kim, M.; Cho, N. H.; Chang, K.; Kim, W. S.; Rho, J.; Nam, K. T., Amino-acid- and peptide-directed synthesis of chiral plasmonic gold nanoparticles. *Nature* **2018**, *556* (7701), 360-365.
29. Cho, N. H.; Lee, H. E.; Ahn, H. Y.; Lee, Y. Y.; Im, S. W.; Kim, H.; Nam, K. T., Cysteine Induced Chiral Morphology in Palladium Nanoparticle. *Particle & Particle Systems Characterization* **2019**, *36* (5).
30. Mark, A. G.; Gibbs, J. G.; Lee, T. C.; Fischer, P., Hybrid nanocolloids with programmed three-dimensional shape and material composition. *Nat Mater* **2013**, *12* (9), 802-7.
31. Liu, M.; Zhang, L.; Wang, T., Supramolecular Chirality in Self-Assembled Systems. *Chem Rev* **2015**, *115* (15), 7304-97.
32. Wang, Y.; Xu, J.; Wang, Y.; Chen, H., Emerging chirality in nanoscience. *Chem Soc Rev* **2013**, *42* (7), 2930-62.
33. Mateos-Timoneda, M. A.; Crego-Calama, M.; Reinhoudt, D. N., Supramolecular chirality of self-assembled systems in solution. *Chem Soc Rev* **2004**, *33* (6), 363-72.
34. Oda, R.; Huc, I.; Schmutz, M.; Candau, S.; MacKintosh, F., Tuning bilayer twist using chiral counterions. *Nature* **1999**, *399* (6736), 566-569.
35. Delclos, T.; Aime, C.; Pouget, E.; Brizard, A.; Huc, I.; Delville, M. H.; Oda, R., Individualized silica nanohelices and nanotubes: tuning inorganic nanostructures using lipidic self-assemblies. *Nano Lett* **2008**, *8* (7), 1929-35.
36. Gao, J.; Okazaki, Y.; Pouget, E.; Nlate, S.; Kauffmann, B.; Artzner, F.; Buffeteau, T.; Oda, R., Slow kinetic evolution of nanohelices based on gemini surfactant self-assemblies with various enantiomeric excess; chiral segregation towards a racemic mixture. *Materials Chemistry Frontiers* **2021**, *5* (7), 3021-3028.
37. Oda, R.; Artzner, F.; Laguerre, M.; Huc, I., Molecular Structure of Self-Assembled Chiral Nanoribbons and Nanotubules Revealed in the Hydrated State. *Journal of the American Chemical*

Society **2008**, *130* (44), 14705-14712.

38. Huang, S.; Chen, Y.; Ma, S.; Yu, H., Hierarchical Self-Assembly in Liquid-Crystalline Block Copolymers Enabled by Chirality Transfer. *Angew Chem Int Ed Engl* **2018**, *57* (38), 12524-12528.

39. Jiang, S.; Zhao, Y.; Wang, L.; Yin, L.; Zhang, Z.; Zhu, J.; Zhang, W.; Zhu, X., Photocontrollable induction of supramolecular chirality in achiral side chain Azo-containing polymers through preferential chiral solvation. *Polymer Chemistry* **2015**, *6* (23), 4230-4239.

40. Wang, L.; Yin, L.; Zhang, W.; Zhu, X.; Fujiki, M., Circularly Polarized Light with Sense and Wavelengths To Regulate Azobenzene Supramolecular Chirality in Optofluidic Medium. *J Am Chem Soc* **2017**, *139* (37), 13218-13226.

41. Iftime, G.; Labarthe, F. L.; Natansohn, A.; Rochon, P., Control of Chirality of an Azobenzene Liquid Crystalline Polymer with Circularly Polarized Light. *Journal of the American Chemical Society* **2000**, *122* (51), 12646-12650.

42. Choi, S. W.; Kawauchi, S.; Ha, N. Y.; Takezoe, H., Photoinduced chirality in azobenzene-containing polymer systems. *Phys Chem Chem Phys* **2007**, *9* (28), 3671-81.

43. Yamaguchi, T.; Kimura, T.; Matsuda, H.; Aida, T., Macroscopic spinning chirality memorized in spin-coated films of spatially designed dendritic zinc porphyrin J-aggregates. *Angew Chem Int Ed Engl* **2004**, *43* (46), 6350-5.

44. Micali, N.; Engelkamp, H.; van Rhee, P. G.; Christianen, P. C.; Monsu Scolaro, L.; Maan, J. C., Selection of supramolecular chirality by application of rotational and magnetic forces. *Nat Chem* **2012**, *4* (3), 201-7.

45. D'Urso, A.; Randazzo, R.; Lo Faro, L.; Purrello, R., Vortexes and nanoscale chirality. *Angew Chem Int Ed Engl* **2010**, *49* (1), 108-12.

46. Spada, G. P., Alignment by the convective and vortex flow of achiral self-assembled fibers induces strong circular dichroism effects. *Angew Chem Int Ed Engl* **2008**, *47* (4), 636-8.

47. Wolffs, M.; George, S. J.; Tomovic, Z.; Meskers, S. C.; Schenning, A. P.; Meijer, E. W., Macroscopic origin of circular dichroism effects by alignment of self-assembled fibers in solution. *Angew Chem Int Ed Engl* **2007**, *46* (43), 8203-5.

48. Tsuda, A.; Alam, M. A.; Harada, T.; Yamaguchi, T.; Ishii, N.; Aida, T., Spectroscopic Visualization of Vortex Flows Using Dye-Containing Nanofibers. *Angewandte Chemie* **2007**, *119* (43), 8346-8350.

49. Okano, K.; Taguchi, M.; Fujiki, M.; Yamashita, T., Circularly Polarized Luminescence of Rhodamine B in a Supramolecular Chiral Medium Formed by a Vortex Flow. *Angewandte Chemie International Edition* **2011**, *50* (52), 12474-12477.

50. Tsujimoto, Y.; Ie, M.; Ando, Y.; Yamamoto, T.; Tsuda, A., Spectroscopic Visualization of Right- and Left-Handed Helical Alignments of DNA in Chiral Vortex Flows. *Bulletin of the Chemical Society of Japan* **2011**, *84* (10), 1031-1038.

51. Okano, K.; Arteaga, O.; Ribo, J. M.; Yamashita, T., Emergence of chiral environments by effect of flows: the case of an ionic oligomer and Congo Red dye. *Chemistry* **2011**, *17* (34), 9288-92.

52. Arteaga, O.; Canillas, A.; Purrello, R.; Ribo, J. M., Evidence of induced chirality in stirred solutions of supramolecular nanofibers. *Opt Lett* **2009**, *34* (14), 2177-9.

53. Ribo, J. M.; Crusats, J.; Sagues, F.; Claret, J.; Rubires, R., Chiral sign induction by vortices during the formation of mesophases in stirred solutions. *Science* **2001**, *292* (5524), 2063-6.

54. Merg, A. D.; Boatz, J. C.; Mandal, A.; Zhao, G.; Mokashi-Punekar, S.; Liu, C.; Wang, X.; Zhang, P.; van der Wel, P. C. A.; Rosi, N. L., Peptide-Directed Assembly of Single-Helical Gold Nanoparticle Superstructures Exhibiting Intense Chiroptical Activity. *J Am Chem Soc* **2016**, *138* (41), 13655-13663.

55. Baginski, M.; Tupikowska, M.; Gonzalez-Rubio, G.; Wojcik, M.; Lewandowski, W., Shaping Liquid Crystals with Gold Nanoparticles: Helical Assemblies with Tunable and Hierarchical Structures Via Thin-Film Cooperative Interactions. *Adv Mater* **2020**, *32* (1), e1904581.
56. Shi, Y.; Duan, P.; Huo, S.; Li, Y.; Liu, M., Endowing Perovskite Nanocrystals with Circularly Polarized Luminescence. *Adv Mater* **2018**, *30* (12), e1705011.
57. Guerrero-Martinez, A.; Auguie, B.; Alonso-Gomez, J. L.; Dzolic, Z.; Gomez-Grana, S.; Zinic, M.; Cid, M. M.; Liz-Marzan, L. M., Intense optical activity from three-dimensional chiral ordering of plasmonic nanoantennas. *Angew Chem Int Ed Engl* **2011**, *50* (24), 5499-503.
58. Huo, S.; Duan, P.; Jiao, T.; Peng, Q.; Liu, M., Self-Assembled Luminescent Quantum Dots To Generate Full-Color and White Circularly Polarized Light. *Angewandte Chemie International Edition* **2017**, *56* (40), 12174-12178.
59. Chen, C. L.; Zhang, P.; Rosi, N. L., A new peptide-based method for the design and synthesis of nanoparticle superstructures: construction of highly ordered gold nanoparticle double helices. *J Am Chem Soc* **2008**, *130* (41), 13555-7.
60. Shen, X.; Song, C.; Wang, J.; Shi, D.; Wang, Z.; Liu, N.; Ding, B., Rolling up gold nanoparticle-dressed DNA origami into three-dimensional plasmonic chiral nanostructures. *J Am Chem Soc* **2012**, *134* (1), 146-9.
61. Wang, Y.; Wang, Q.; Sun, H.; Zhang, W.; Chen, G.; Wang, Y.; Shen, X.; Han, Y.; Lu, X.; Chen, H., Chiral transformation: from single nanowire to double helix. *J Am Chem Soc* **2011**, *133* (50), 20060-3.
62. Kuzyk, A.; Schreiber, R.; Fan, Z.; Pardatscher, G.; Roller, E. M.; Hogele, A.; Simmel, F. C.; Govorov, A. O.; Liedl, T., DNA-based self-assembly of chiral plasmonic nanostructures with tailored optical response. *Nature* **2012**, *483* (7389), 311-4.
63. Schellman, J. A., Circular dichroism and optical rotation. *Chemical Reviews* **1975**, *75* (3), 323-331.
64. Rodger, A.; Nordén, B., *Circular dichroism and linear dichroism*. Oxford University Press, USA: 1997; Vol. 1.
65. Berova, N.; Polavarapu, P. L.; Nakanishi, K.; Woody, R. W., *Comprehensive chiroptical spectroscopy: applications in stereochemical analysis of synthetic compounds, natural products, and biomolecules*. John Wiley & Sons: 2012; Vol. 2.
66. Berova, N.; Nakanishi, K.; Woody, R. W., *Circular dichroism: principles and applications*. John Wiley & Sons: 2000.
67. Dai, Q.; Duty, C. E.; Hu, M. Z., Semiconductor-Nanocrystals-Based White Light-Emitting Diodes. *Small* **2010**, *6* (15), 1577-1588.
68. de Mello Donegá, C., *Nanoparticles: workhorses of nanoscience*. Springer: 2014.
69. Alivisatos, A. P., Perspectives on the Physical Chemistry of Semiconductor Nanocrystals. *The Journal of Physical Chemistry* **1996**, *100* (31), 13226-13239.
70. Roduner, E., Size matters: why nanomaterials are different. *Chem Soc Rev* **2006**, *35* (7), 583-92.
71. Donega, C. d. M., Synthesis and properties of colloidal heteronanocrystals. *Chemical Society Reviews* **2011**, *40* (3), 1512-1546.
72. Medintz, I. L.; Uyeda, H. T.; Goldman, E. R.; Mattoussi, H., Quantum dot bioconjugates for imaging, labelling and sensing. *Nature Materials* **2005**, *4* (6), 435-446.
73. Jun, S.; Jang, E., Bright and stable alloy core/multishell quantum dots. *Angewandte Chemie* **2013**, *52* (2), 679-82.
74. Bailey, R. E.; Smith, A. M.; Nie, S., Quantum dots in biology and medicine. *Physica E: Low-dimensional Systems and Nanostructures* **2004**, *25* (1), 1-12.

75. Jaiswal, J. K.; Mattoussi, H.; Mauro, J. M.; Simon, S. M. J. N. b., Long-term multiple color imaging of live cells using quantum dot bioconjugates. *2003*, *21* (1), 47-51.
76. Larson, D. R.; Zipfel, W. R.; Williams, R. M.; Clark, S. W.; Bruchez, M. P.; Wise, F. W.; Webb, W. W., Water-soluble quantum dots for multiphoton fluorescence imaging in vivo. *Science* **2003**, *300* (5624), 1434-6.
77. Gao, X.; Yang, L.; Petros, J. A.; Marshall, F. F.; Simons, J. W.; Nie, S., In vivo molecular and cellular imaging with quantum dots. *Curr Opin Biotechnol* **2005**, *16* (1), 63-72.
78. Boles, M. A.; Ling, D.; Hyeon, T.; Talapin, D. V., Erratum: The surface science of nanocrystals. *Nat Mater* **2016**, *15* (3), 364.
79. De Roo, J.; Van Driessche, I.; Martins, J. C.; Hens, Z., Colloidal metal oxide nanocrystal catalysis by sustained chemically driven ligand displacement. *Nat Mater* **2016**, *15* (5), 517-21.
80. Green, M. L. H.; Parkin, G., Application of the Covalent Bond Classification Method for the Teaching of Inorganic Chemistry. *Journal of Chemical Education* **2014**, *91* (6), 807-816.
81. Knauf, R. R.; Lennox, J. C.; Dempsey, J. L., Quantifying Ligand Exchange Reactions at CdSe Nanocrystal Surfaces. *Chemistry of Materials* **2016**, *28* (13), 4762-4770.
82. You, H.; Wang, W.; Yang, S., A universal rule for organic ligand exchange. *ACS Appl Mater Interfaces* **2014**, *6* (21), 19035-40.
83. Karakoti, A. S.; Shukla, R.; Shanker, R.; Singh, S., Surface functionalization of quantum dots for biological applications. *Adv Colloid Interface Sci* **2015**, *215*, 28-45.
84. Rahman, I. A.; Padavettan, V., Synthesis of Silica Nanoparticles by Sol-Gel: Size-Dependent Properties, Surface Modification, and Applications in Silica-Polymer Nanocomposites—A Review. *Journal of Nanomaterials* **2012**, *2012*, 1-15.
85. Saengdee, P.; Chairiratanakul, W.; Bunjongpru, W.; Sripumkhai, W.; Srisuwan, A.; Jeamsaksiri, W.; Hruanun, C.; Poyai, A.; Promptmas, C., Surface modification of silicon dioxide, silicon nitride and titanium oxynitride for lactate dehydrogenase immobilization. *Biosens Bioelectron* **2015**, *67*, 134-8.
86. Bagwe, R. P.; Hilliard, L. R.; Tan, W., Surface modification of silica nanoparticles to reduce aggregation and nonspecific binding. *Langmuir* **2006**, *22* (9), 4357-62.
87. Mohammed, A. M.; Rahim, R. A.; Ibraheem, I. J.; Loong, F. K.; Hisham, H.; Hashim, U.; Al-Douri, Y., Application of Gold Nanoparticles for Electrochemical DNA Biosensor. *Journal of Nanomaterials* **2014**, *2014*, 1-7.
88. Žutić, I.; Fabian, J.; Das Sarma, S., Spintronics: Fundamentals and applications. *Reviews of Modern Physics* **2004**, *76* (2), 323-410.
89. Awschalom, D. D.; Bassett, L. C.; Dzurak, A. S.; Hu, E. L.; Petta, J. R., Quantum spintronics: engineering and manipulating atom-like spins in semiconductors. *Science* **2013**, *339* (6124), 1174-9.
90. Clevenson, H.; Trusheim, M. E.; Teale, C.; Schröder, T.; Braje, D.; Englund, D., Broadband magnetometry and temperature sensing with a light-trapping diamond waveguide. *Nature Physics* **2015**, *11* (5), 393-397.
91. Heard, A. W.; Goldup, S. M., Synthesis of a Mechanically Planar Chiral Rotaxane Ligand for Enantioselective Catalysis. *Chem* **2020**, *6* (4), 994-1006.
92. Banerjee-Ghosh, K.; Ben Dor, O.; Tassinari, F.; Capua, E.; Yochelis, S.; Capua, A.; Yang, S. H.; Parkin, S. S. P.; Sarkar, S.; Kronik, L.; Baczewski, L. T.; Naaman, R.; Paltiel, Y., Separation of enantiomers by their enantiospecific interaction with achiral magnetic substrates. *Science* **2018**, *360* (6395), 1331-1334.
93. Woods, A. J.; Boher, P.; Holliman, N. S.; Leroux, T.; Bignon, T.; Dodgson, N. A.; Collomb-Patton, V., Multispectral polarization viewing angle analysis of circular polarized stereoscopic 3D displays. In

Stereoscopic Displays and Applications XXI, 2010.

94. Sun, X.; Velez, S.; Atxabal, A.; Bedoya-Pinto, A.; Parui, S.; Zhu, X.; Llopis, R.; Casanova, F.; Hueso, L. E., A molecular spin-photovoltaic device. *Science* **2017**, *357* (6352), 677-680.
95. Delgado-Perez, T.; Bouchet, L. M.; de la Guardia, M.; Galian, R. E.; Perez-Prieto, J., Sensing chiral drugs by using CdSe/ZnS nanoparticles capped with N-acetyl-L-cysteine methyl ester. *Chemistry* **2013**, *19* (33), 11068-76.
96. Han, C.; Li, H., Chiral recognition of amino acids based on cyclodextrin-capped quantum dots. *Small* **2008**, *4* (9), 1344-50.
97. Li, Y.; Zhou, Y.; Wang, H. Y.; Perrett, S.; Zhao, Y.; Tang, Z.; Nie, G., Chirality of glutathione surface coating affects the cytotoxicity of quantum dots. *Angew Chem Int Ed Engl* **2011**, *50* (26), 5860-4.
98. Sun, M.; Xu, L.; Qu, A.; Zhao, P.; Hao, T.; Ma, W.; Hao, C.; Wen, X.; Colombari, F. M.; de Moura, A. F.; Kotov, N. A.; Xu, C.; Kuang, H., Site-selective photoinduced cleavage and profiling of DNA by chiral semiconductor nanoparticles. *Nat Chem* **2018**, *10* (8), 821-830.
99. Shah, E.; Soni, H. P., Inducing chirality on ZnS nanoparticles for asymmetric aldol condensation reactions. *RSC Advances* **2013**, *3* (38).
100. Wei, Y.; Hao, H.; Zhang, J.; Hao, X.; Dong, C., Sensitive and selective detection of l-tryptophan using Mn-ZnS QDs as the ratiometric emission probe. *Analytical Methods* **2014**, *6* (10).
101. Vulugundam, G.; Misra, S. K.; Ostadhossein, F.; Schwartz-Duval, A. S.; Daza, E. A.; Pan, D., (-)/(+)-Sparteine induced chirally-active carbon nanoparticles for enantioselective separation of racemic mixtures. *Chem Commun (Camb)* **2016**, *52* (47), 7513-6.
102. Ray, K.; Ananthavel, S. P.; Waldeck, D. H.; Naaman, R., Asymmetric scattering of polarized electrons by organized organic films of chiral molecules. *Science* **1999**, *283* (5403), 814-6.
103. Abendroth, J. M.; Stemer, D. M.; Bloom, B. P.; Roy, P.; Naaman, R.; Waldeck, D. H.; Weiss, P. S.; Mondal, P. C., Spin Selectivity in Photoinduced Charge-Transfer Mediated by Chiral Molecules. *ACS Nano* **2019**, *13* (5), 4928-4946.
104. Naaman, R.; Paltiel, Y.; Waldeck, D. H., Chiral Induced Spin Selectivity Gives a New Twist on Spin-Control in Chemistry. *Acc Chem Res* **2020**, *53* (11), 2659-2667.
105. Inui, A.; Aoki, R.; Nishiue, Y.; Shiota, K.; Kousaka, Y.; Shishido, H.; Hirobe, D.; Suda, M.; Ohe, J. I.; Kishine, J. I.; Yamamoto, H. M.; Togawa, Y., Chirality-Induced Spin-Polarized State of a Chiral Crystal CrNb₃S₆. *Phys Rev Lett* **2020**, *124* (16), 166602.
106. Wolff, H. J.; Burssher, D.; Steiner, U. E., Spin-orbit coupling controlled spin chemistry of Ru(bpy)₃²⁺ photooxidation: Detection of strong viscosity dependence of in-cage backward electron transfer rate. *Pure and Applied Chemistry* **1995**, *67* (1), 167-174.
107. Chretien, S.; Metiu, H., O₂ evolution on a clean partially reduced rutile TiO₂(110) surface and on the same surface precovered with Au₁ and Au₂: the importance of spin conservation. *J Chem Phys* **2008**, *129* (7), 074705.
108. Mtangi, W.; Kiran, V.; Fontanesi, C.; Naaman, R., Role of the Electron Spin Polarization in Water Splitting. *J Phys Chem Lett* **2015**, *6* (24), 4916-22.
109. Zhang, W.; Banerjee-Ghosh, K.; Tassinari, F.; Naaman, R., Enhanced Electrochemical Water Splitting with Chiral Molecule-Coated Fe₃O₄ Nanoparticles. *ACS Energy Letters* **2018**, *3* (10), 2308-2313.
110. Ghosh, K. B.; Zhang, W.; Tassinari, F.; Mastai, Y.; Lidor-Shalev, O.; Naaman, R.; Möllers, P.; Nürenberg, D.; Zacharias, H.; Wei, J.; Wierzbinski, E.; Waldeck, D. H., Controlling Chemical Selectivity in Electrocatalysis with Chiral CuO-Coated Electrodes. *The Journal of Physical Chemistry C* **2019**, *123* (5),

3024-3031.

111. Gautier, C.; Burgi, T., Chiral gold nanoparticles. *Chemphyschem* **2009**, *10* (3), 483-92.
112. Ma, W.; Xu, L.; de Moura, A. F.; Wu, X.; Kuang, H.; Xu, C.; Kotov, N. A., Chiral Inorganic Nanostructures. *Chem Rev* **2017**, *117* (12), 8041-8093.
113. Schaaff, T. G.; Whetten, R. L., Giant Gold–Glutathione Cluster Compounds: Intense Optical Activity in Metal-Based Transitions. *The Journal of Physical Chemistry B* **2000**, *104* (12), 2630-2641.
114. Gautier, C.; Burgi, T., Chiral inversion of gold nanoparticles. *J Am Chem Soc* **2008**, *130* (22), 7077-84.
115. Li, T.; Park, H. G.; Lee, H.-S.; Choi, S.-H., Circular dichroism study of chiral biomolecules conjugated with silver nanoparticles. *Nanotechnology* **2004**, *15* (10), S660-S663.
116. Yao, H.; Miki, K.; Nishida, N.; Sasaki, A.; Kimura, K., Large Optical Activity of Gold Nanocluster Enantiomers Induced by a Pair of Optically Active Penicillamines. *Journal of the American Chemical Society* **2005**, *127* (44), 15536-15543.
117. Gautier, C.; Burgi, T., Chiral N-isobutyryl-cysteine protected gold nanoparticles: preparation, size selection, and optical activity in the UV-vis and infrared. *J Am Chem Soc* **2006**, *128* (34), 11079-87.
118. Ock, K. S.; Dembereldorj, U.; Park, J.; Ganbold, E. O.; Kim, S.; Shin, H. C.; Joo, S. W., Temperature-dependent structural change of D-penicillamine-capped chiral gold nanoparticles investigated by infrared spectroscopy. *Spectrochim Acta A Mol Biomol Spectrosc* **2013**, *102*, 419-24.
119. Moloney, M. P.; Gun'ko, Y. K.; Kelly, J. M., Chiral highly luminescent CdS quantum dots. *Chem Commun (Camb)* **2007**, (38), 3900-2.
120. Nakashima, T.; Kobayashi, Y.; Kawai, T., Optical activity and chiral memory of thiol-capped CdTe nanocrystals. *J Am Chem Soc* **2009**, *131* (30), 10342-3.
121. Mukhina, M. V.; Maslov, V. G.; Baranov, A. V.; Fedorov, A. V.; Orlova, A. O.; Purcell-Milton, F.; Govan, J.; Gun'ko, Y. K., Intrinsic Chirality of CdSe/ZnS Quantum Dots and Quantum Rods. *Nano Lett* **2015**, *15* (5), 2844-51.
122. Choi, J. K.; Haynie, B. E.; Tohgha, U.; Pap, L.; Elliott, K. W.; Leonard, B. M.; Dzyuba, S. V.; Varga, K.; Kubelka, J.; Balaz, M., Chirality Inversion of CdSe and CdS Quantum Dots without Changing the Stereochemistry of the Capping Ligand. *ACS Nano* **2016**, *10* (3), 3809-15.
123. Kuno, J.; Imamura, Y.; Katouda, M.; Tashiro, M.; Kawai, T.; Nakashima, T., Inversion of Optical Activity in the Synthesis of Mercury Sulfide Nanoparticles: Role of Ligand Coordination. *Angew Chem Int Ed Engl* **2018**, *57* (37), 12022-12026.
124. Kuznetsova, V. A.; Mates-Torres, E.; Prochukhan, N.; Marcaste, M.; Purcell-Milton, F.; O'Brien, J.; Visheratina, A. K.; Martinez-Carmona, M.; Gronnova, Y.; Garcia-Melchor, M.; Gun'ko, Y. K., Effect of Chiral Ligand Concentration and Binding Mode on Chiroptical Activity of CdSe/CdS Quantum Dots. *ACS Nano* **2019**, *13* (11), 13560-13572.
125. Zhou, Y.; Zhu, Z.; Huang, W.; Liu, W.; Wu, S.; Liu, X.; Gao, Y.; Zhang, W.; Tang, Z., Optical coupling between chiral biomolecules and semiconductor nanoparticles: size-dependent circular dichroism absorption. *Angew Chem Int Ed Engl* **2011**, *50* (48), 11456-9.
126. Moshe, A. B.; Szwarcman, D.; Markovich, G., Size dependence of chiroptical activity in colloidal quantum dots. *ACS Nano* **2011**, *5* (11), 9034-43.
127. Gao, X.; Zhang, X.; Deng, K.; Han, B.; Zhao, L.; Wu, M.; Shi, L.; Lv, J.; Tang, Z., Excitonic Circular Dichroism of Chiral Quantum Rods. *J Am Chem Soc* **2017**, *139* (25), 8734-8739.
128. Hao, J.; Li, Y.; Miao, J.; Liu, R.; Li, J.; Liu, H.; Wang, Q.; Liu, H.; Delville, M.-H.; He, T.; Wang, K.; Zhu, X.; Cheng, J., Ligand-Induced Chirality in Asymmetric CdSe/CdS Nanostructures: A Close Look at Chiral

- Tadpoles. *ACS Nano* **2020**, *14* (8), 10346-10358.
129. Cheng, J.; Hao, J.; Liu, H.; Li, J.; Li, J.; Zhu, X.; Lin, X.; Wang, K.; He, T., Optically Active CdSe-Dot/CdS-Rod Nanocrystals with Induced Chirality and Circularly Polarized Luminescence. *ACS Nano* **2018**, *12* (6), 5341-5350.
130. Shao, X.; Wu, Y.; Jiang, S.; Li, B.; Zhang, T.; Yan, Y., Chiral 3D CdSe Nanotetrapods. *Inorg Chem* **2020**, *59* (19), 14382-14388.
131. Gao, X.; Zhang, X.; Zhao, L.; Huang, P.; Han, B.; Lv, J.; Qiu, X.; Wei, S. H.; Tang, Z., Distinct Excitonic Circular Dichroism between Wurtzite and Zincblende CdSe Nanoplatelets. *Nano Lett* **2018**, *18* (11), 6665-6671.
132. Purcell-Milton, F.; Visheratina, A. K.; Kuznetsova, V. A.; Ryan, A.; Orlova, A. O.; Gun'ko, Y. K., Impact of Shell Thickness on Photoluminescence and Optical Activity in Chiral CdSe/CdS Core/Shell Quantum Dots. *ACS Nano* **2017**, *11* (9), 9207-9214.
133. Chen, W.; Zhang, S.; Zhou, M.; Zhao, T.; Qin, X.; Liu, X.; Liu, M.; Duan, P., Two-Photon Absorption-Based Upconverted Circularly Polarized Luminescence Generated in Chiral Perovskite Nanocrystals. *J Phys Chem Lett* **2019**, *10* (12), 3290-3295.
134. He, T.; Li, J.; Li, X.; Ren, C.; Luo, Y.; Zhao, F.; Chen, R.; Lin, X.; Zhang, J., Spectroscopic studies of chiral perovskite nanocrystals. *Applied Physics Letters* **2017**, *111* (15), 151102.
135. Saeva, F. D.; Olin, G. R.; Chu, J. Y. C., Circular Dichroism of Trigonal Selenium Formed in a Chiral Polymer Matrix. *Molecular Crystals and Liquid Crystals* **2011**, *41* (1), 5-9.
136. Paredes, B.; Widera, A.; Murg, V.; Mandel, O.; Folling, S.; Cirac, I.; Shlyapnikov, G. V.; Hansch, T. W.; Bloch, I., Tonks-Girardeau gas of ultracold atoms in an optical lattice. *Nature* **2004**, *429* (6989), 277-81.
137. Che, S.; Garcia-Bennett, A. E.; Yokoi, T.; Sakamoto, K.; Kunieda, H.; Terasaki, O.; Tatsumi, T., A novel anionic surfactant templating route for synthesizing mesoporous silica with unique structure. *Nat Mater* **2003**, *2* (12), 801-5.
138. Sugiyasu, K.; Tamaru, S.-i.; Takeuchi, M.; Berthier, D.; Huc, I.; Oda, R.; Shinkai, S., Double helical silica fibrils by sol-gel transcription of chiral aggregates of gemini surfactants. *Chemical communications* **2002**, (11), 1212-1213.
139. Liu, S.; Han, L.; Duan, Y.; Asahina, S.; Terasaki, O.; Cao, Y.; Liu, B.; Ma, L.; Zhang, J.; Che, S., Synthesis of chiral TiO₂ nanofibre with electron transition-based optical activity. *Nat Commun* **2012**, *3*, 1215.
140. Sone, E. D.; Zubarev, E. R.; Stupp, S. I., Semiconductor Nanohelices Templated by Supramolecular Ribbons. *Angewandte Chemie International Edition* **2002**, *41* (10), 1705-1709.
141. Duan, Y.; Han, L.; Zhang, J.; Asahina, S.; Huang, Z.; Shi, L.; Wang, B.; Cao, Y.; Yao, Y.; Ma, L.; Wang, C.; Dukor, R. K.; Sun, L.; Jiang, C.; Tang, Z.; Nafie, L. A.; Che, S., Optically Active Nanostructured ZnO Films. *Angew Chem Int Ed Engl* **2015**, *54* (50), 15170-5.
142. Ma, L.; Cao, Y.; Duan, Y.; Han, L.; Che, S., Silver Films with Hierarchical Chirality. *Angew Chem Int Ed Engl* **2017**, *56* (30), 8657-8662.
143. Duan, Y.; Liu, X.; Han, L.; Asahina, S.; Xu, D.; Cao, Y.; Yao, Y.; Che, S., Optically active chiral CuO "nanoflowers". *J Am Chem Soc* **2014**, *136* (20), 7193-6.
144. Boles, M. A.; Engel, M.; Talapin, D. V., Self-Assembly of Colloidal Nanocrystals: From Intricate Structures to Functional Materials. *Chem Rev* **2016**, *116* (18), 11220-89.
145. Bishop, K. J.; Wilmer, C. E.; Soh, S.; Grzybowski, B. A., Nanoscale forces and their uses in self-assembly. *Small* **2009**, *5* (14), 1600-30.
146. Srivastava, S.; Santos, A.; Critchley, K.; Kim, K. S.; Podsiadlo, P.; Sun, K.; Lee, J.; Xu, C.; Lilly, G. D.;

Glotzer, S. C.; Kotov, N. A., Light-controlled self-assembly of semiconductor nanoparticles into twisted ribbons. *Science* **2010**, *327* (5971), 1355-9.

147. Yeom, J.; Yeom, B.; Chan, H.; Smith, K. W.; Dominguez-Medina, S.; Bahng, J. H.; Zhao, G.; Chang, W. S.; Chang, S. J.; Chuvilin, A.; Melnikau, D.; Rogach, A. L.; Zhang, P.; Link, S.; Kral, P.; Kotov, N. A., Chiral templating of self-assembling nanostructures by circularly polarized light. *Nat Mater* **2015**, *14* (1), 66-72.

148. Kim, J. Y.; Yeom, J.; Zhao, G.; Calcaterra, H.; Munn, J.; Zhang, P.; Kotov, N., Assembly of Gold Nanoparticles into Chiral Superstructures Driven by Circularly Polarized Light. *J Am Chem Soc* **2019**, *141* (30), 11739-11744.

149. Zhou, Y.; Marson, R. L.; van Anders, G.; Zhu, J.; Ma, G.; Ercius, P.; Sun, K.; Yeom, B.; Glotzer, S. C.; Kotov, N. A., Biomimetic Hierarchical Assembly of Helical Supraparticles from Chiral Nanoparticles. *ACS Nano* **2016**, *10* (3), 3248-56.

150. Feng, W.; Kim, J.-Y.; Wang, X.; Calcaterra, H. A.; Qu, Z.; Meshi, L.; Kotov, N. A., Assembly of mesoscale helices with near-unity enantiomeric excess and light-matter interactions for chiral semiconductors. *Science advances* **2017**, *3* (3), e1601159.

151. Yan, J.; Feng, W.; Kim, J.-Y.; Lu, J.; Kumar, P.; Mu, Z.; Wu, X.; Mao, X.; Kotov, N. A., Self-Assembly of Chiral Nanoparticles into Semiconductor Helices with Tunable near-Infrared Optical Activity. *Chemistry of Materials* **2019**, *32* (1), 476-488.

152. Singh, G.; Chan, H.; Baskin, A.; Gelman, E.; Repnin, N.; Kral, P.; Klajn, R., Self-assembly of magnetite nanocubes into helical superstructures. *Science* **2014**, *345* (6201), 1149-53.

153. Jana, S.; de Frutos, M.; Davidson, P.; Abecassis, B., Ligand-induced twisting of nanoplatelets and their self-assembly into chiral ribbons. *Sci Adv* **2017**, *3* (9), e1701483.

154. Yin, Y.; Xia, Y., Self-assembly of spherical colloids into helical chains with well-controlled handedness. *J Am Chem Soc* **2003**, *125* (8), 2048-9.

155. Szustakiewicz, P.; Kowalska, N.; Grzelak, D.; Narushima, T.; Gora, M.; Baginski, M.; Pocięcha, D.; Okamoto, H.; Liz-Marzan, L. M.; Lewandowski, W., Supramolecular Chirality Synchronization in Thin Films of Plasmonic Nanocomposites. *ACS Nano* **2020**, *14* (10), 12918-12928.

156. Lan, X.; Su, Z.; Zhou, Y.; Meyer, T.; Ke, Y.; Wang, Q.; Chiu, W.; Liu, N.; Zou, S.; Yan, H.; Liu, Y., Programmable Supra-Assembly of a DNA Surface Adapter for Tunable Chiral Directional Self-Assembly of Gold Nanorods. *Angew Chem Int Ed Engl* **2017**, *56* (46), 14632-14636.

157. Schreiber, R.; Luong, N.; Fan, Z.; Kuzyk, A.; Nickels, P. C.; Zhang, T.; Smith, D. M.; Yurke, B.; Kuang, W.; Govorov, A. O.; Liedl, T., Chiral plasmonic DNA nanostructures with switchable circular dichroism. *Nat Commun* **2013**, *4*, 2948.

158. Shemer, G.; Krichevski, O.; Markovich, G.; Molotsky, T.; Lubitz, I.; Kotlyar, A. B., Chirality of Silver Nanoparticles Synthesized on DNA. *Journal of the American Chemical Society* **2006**, *128* (34), 11006-11007.

159. Duan, Y.; Che, S., Electron transition-based optical activity (ETOA) of achiral metal oxides derived from chiral mesoporous silica. *Chemistry* **2013**, *19* (32), 10468-72.

160. Cheng, J.; Le Saux, G.; Gao, J.; Buffeteau, T.; Battie, Y.; Barois, P.; Ponsinet, V.; Delville, M. H.; Ersen, O.; Pouget, E.; Oda, R., GoldHelix: Gold Nanoparticles Forming 3D Helical Superstructures with Controlled Morphology and Strong Chiroptical Property. *ACS Nano* **2017**, *11* (4), 3806-3818.

161. Gao, J.; Wu, W.; Lemaire, V.; Carvalho, A.; Nlate, S.; Buffeteau, T.; Oda, R.; Battie, Y.; Pauly, M.; Pouget, E., Tuning the Chiroptical Properties of Elongated Nano-objects via Hierarchical Organization. *ACS Nano* **2020**, *14* (4), 4111-4121

Chapter 2. Research design

1. Research design	47
2. Preparation of chiral silica ribbons and its basic properties	47
2.1 Synthesis of chiral silica ribbons and its surface modification with (3-aminopropyl)triethoxysilane (APTES)	48
2.2 Evaluation of dispersity and mass concentration	50
2.3 Calculations of surface area	51
3. The complexation between luminescent NCs and silica ribbons.....	53
3.1 Functionalized luminescent NCs combined with amine-modified silica ribbons.....	54
3.2 Ligands exchanged of luminescent NCs by amine modified silica ribbons	55
3.3 NCs in-situ growth inside or outside of silica ribbons	55
3. Conclusion	56
4. Reference	58

Chapter 2. Research design

1. Research design

Based on the first chapter review of the chiral materials and frontier research of our group on chiral silica ribbons, it is easy to design the project by combining achiral nanocrystals (NCs) with silica ribbons to endow chirality to luminescent NCs. In this thesis, two different approaches were used to endow chirality to luminescent NCs by our chiral silica ribbons. First approach is the grafting of luminescent NCs on the surface of silica ribbons. Second approach is the in-situ growth of luminescent NCs in the hollow silica ribbons. As shown in Figure 2-1, first, silica helical/twisted ribbons were prepared by sol-gel reaction of tetraethoxysilane (TEOS) by using helical/twisted ribbon-like molecular assemblies of gemini tartrate as organic template. The surface of the obtained hollow silica helical/twisted ribbons was modified with amine which could be engaged with luminescent NCs. The hollow helical structures offer the opportunity to endow chirality by chiral self-organization of luminescent NCs on the surface of silica ribbons or preparation of chiral shaped luminescent NCs inside hollow silica ribbons. In this thesis, different kinds of NCs, such as perovskite CsPbX_3 ($X = \text{Cl}, \text{Br}, \text{I}$ or their mixture) and CdSe based NCs were prepared. For those two materials, the absorption and emission spectra could cover the whole visible light range by tuning their composition, shape, and size, which show great commercial applications in lighting and display. The magnetic, electrical, and optical properties of NCs are decided by their size, shape, and crystal structure. It would be interesting to study the size, shape, and crystal structure effects on the NCs hierarchical chiral building block system. The chirality is induced by chiral arrangement of NCs, which could be affected by their size, shape, crystal structure resulting in different optically active properties. The luminescent NCs, which synthesized inside the hollow silica ribbons, show a similar helical shape as the original organic template. Different shapes of NCs could be prepared by changing the morphology of organic template (molecular assemblies of Gemini tartrate). Gemini tartrate-L self-assembles into

right-handed silica ribbons, while Gemini tartrate-D self-assembles into left handed silica ribbons. As shown in Figure 2-1, twisted and helical organic templates could be obtained by changing the aging time of Gemini tartrate self-assembly. Hollow silica twisted and helical ribbons could be obtained and finally affect the chiral shape of NCs which result in different optically active properties.

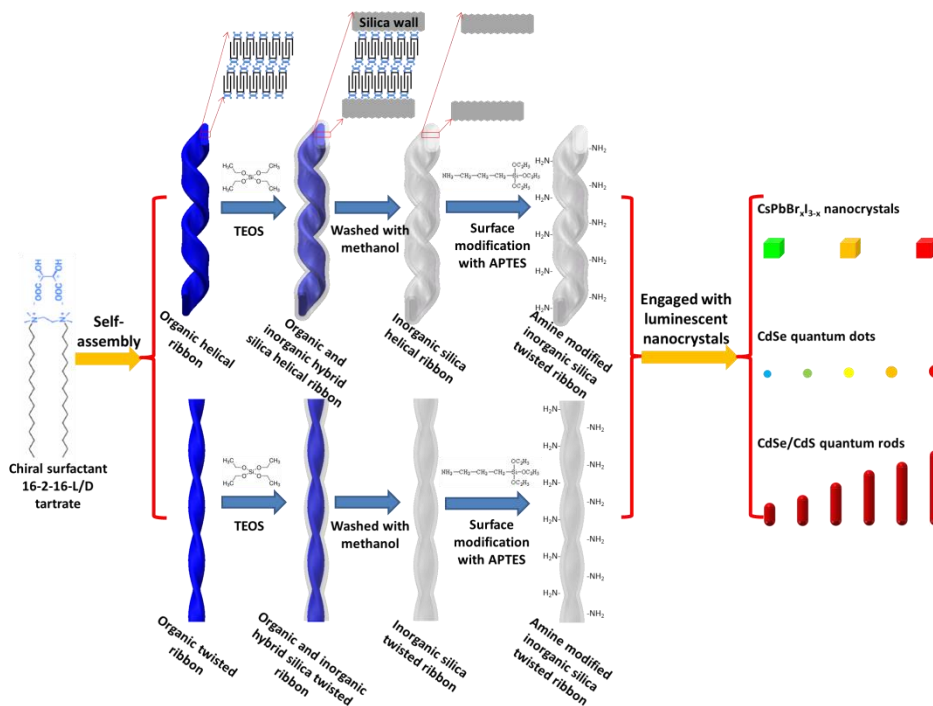


Figure 2-1. Diagram of research designation

2. Preparation of chiral silica ribbons and its basic properties

2.1 Synthesis of chiral silica ribbons and its surface modification with (3-aminopropyl)triethoxysilane (APTES)

The chiral silica ribbons were synthesized as in our previous reports.¹ Typically, 3.6 mg 16-2-16 L- (or D-) tartrate was dissolved into 5 mL Milli-Q water and heated to 60 °C, and kept for 20 min. Then, the clear solution was kept at a 20 °C incubator to let self-assembly aging for 2 hours for twisted ribbons or 3 days for helical ribbons. After that, 5 mL of pre-hydrolyzed tetraethyl orthosilicate (TEOS) aqueous solution (0.5 mL TEOS mixed with 10 mL 0.1 mM aqueous solution of L/D-tartaric acid for 7

h on the roller-mixer) was added to the self-assembly precursors, and the mixture was kept at 20 °C incubator for overnight. The unreacted TEOS and 16-2-16 L/D tartrate template were removed by washing with methanol (twice) and absolute ethanol (three times) by centrifugation at 3893 g for 6 min. Finally, the obtained silica ribbons were dispersed into a 5 mL absolute ethanol solution for further use. As shown in Figures 2-2 (a-c), 2 h aged gel with TEOS transcription, silica twisted ribbons were obtained with pitch around 100 nm and width around 22.5 nm. On the other hand, as shown in Figures 2-2 (d-e), 3 days aged gel with TEOS transcription, silica helical ribbons were obtained with pitch around 60 nm and width around 30 nm.

To combine silica ribbons with luminescent NCs, the surface of silica ribbons was functionalized with amine by APTES modification. Typically, 10 μ L of APTES was added into the 5 mL silica helices (around 1 mg/mL) ethanol solution, and sonicated for 10 min, then the mixture was kept in an oil bath at 80 °C for overnight. The sample was then washed with absolute ethanol (twice) with centrifugation at 10000 g for 10 min. This process was repeated once more to make sure of the good surface modification.

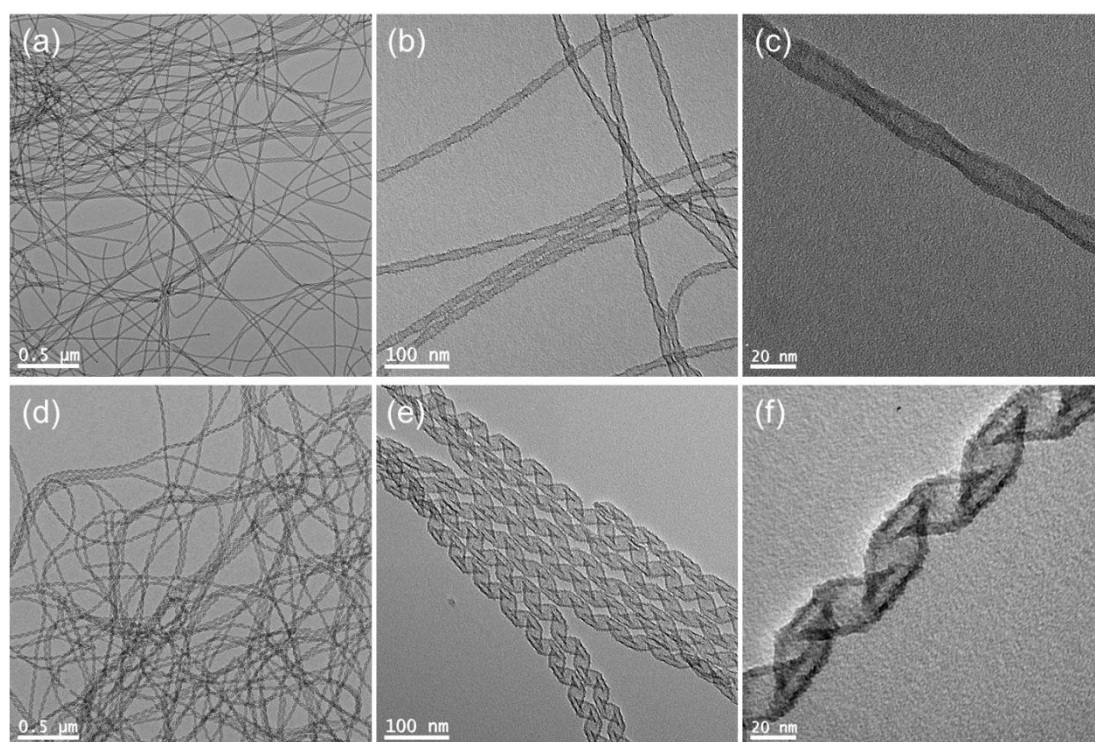


Figure 2-2. TEM images of silica twisted ribbons (a), (b), (c) and silica helical ribbons (d), (e), (f) with different magnification

2.2 Evaluation of dispersity and mass concentration

As shown in Figure 2-2, the gel transcriptions of silica ribbons are long and entangled which is hindering further applications. To obtain individualized and well-dispersed silica ribbons, a tip-sonication is necessary to dis-entangle and fragment the aggregated silica ribbons.

The tip-sonication treatment was carried out using a high-intensity ultrasonic processor (Vibra cell 75186). Typically, 5 mL of silica ribbons ethanol solution (1 mg/mL) in 15 mL tube with ice-water bath, the micro-tip was set at tube 4 mL, 3 mL, 2 mL and 1 mL position in turn. The power was set at 130 W, and sonication for 10 min with pulses of 1 s separated by 1 s pauses for each position. Then the solution was centrifuged at 3984 g for 10 min to precipitate the remaining aggregate part. The supernatant solution was collected for further use.

The mass concentration of silica ribbons was calculated by measuring the mass of dried silica ribbons in solution with a certain volume. Typically, 50 uL solution of silica ribbons was dropped into three aluminum foil containers parallel and dried at 80 °C for 2 h. The mass of silica ribbons was calculated based on the mass of aluminum foil without and with silica ribbons. The average value of the three samples was used as the mass concentration. As shown in Figures 2-3 (a-c), at lower magnification, the prepared silica ribbons are knotted and entangled. After tip-sonication treatment, the knotted and entangled aggregation part could be disentangled and fragmented. As shown in Figures 2-3 (d-f), the well-dispersed silica ribbons are homogeneously dispersed on the surface of the TEM grid.

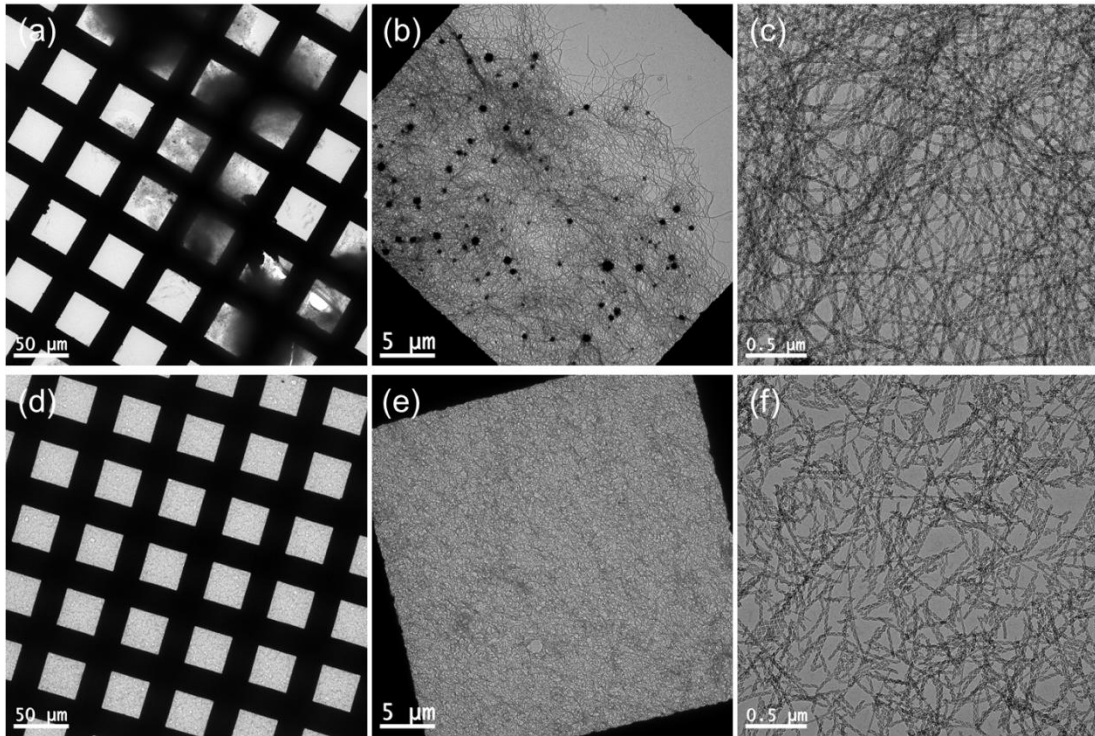


Figure 2-3. TEM images of silica helical ribbons before tip-sonication (a), (b), (c) and after tip-sonication (d), (e), (f) with different magnification

2.3 Calculation of surface area

It is also vital to know the surface area of silica ribbons to design functionalized materials. According to the TEM images of synthesized silica helical ribbons and twisted ribbons and our previous report,¹ the 3D models of silica helical and twisted ribbons were drawn as shown in Figure 2-4. To quantify the surface area of silica helical and twisted ribbons, an approximation was made by stretch the helical and twisted ribbons to be flat. For the flat ribbons, the mass (m) of silica equals to the total length (L) multiplied by the cross-sectional area S and the density ($\rho \approx 2.2 \text{ g/cm}^3$): $m = L * S * \rho$. The surface area of ribbons could be obtained according to the total length of ribbons and the perimeter.

Silica helical ribbons

$$\text{Cross-sectional area } S = 2 * 16.5 * 3.5 + \pi * (6.75^2 - 3.25^2) = 225.5 \text{ nm}^2$$

$$\text{Outer perimeter : } D1 = 16.5 + 16.5 + 2 * \pi * 6.75 = 75.4 \text{ nm}$$

$$\text{Inside perimeter : } D2 = 16.5 + 16.5 + 2 * \pi * 3.25 = 53.4 \text{ nm}$$

Silica twisted ribbons

Cross-sectional area $S' = 2 \cdot 9 \cdot 3.5 + \pi \cdot (6.75^2 - 3.25^2) = 172.9 \text{ nm}^2$

Outer perimeter : $D1' = 9 + 9 + 2 \cdot \pi \cdot 6.75 = 60.4 \text{ nm}$

Inside perimeter : $D2' = 9 + 9 + 2 \cdot \pi \cdot 3.25 = 38.4 \text{ nm}$

Based on the calculation methods and the basic parameters of silica helical and twisted ribbons, the surface area of silica could be approximated calculated as Table 2-1.

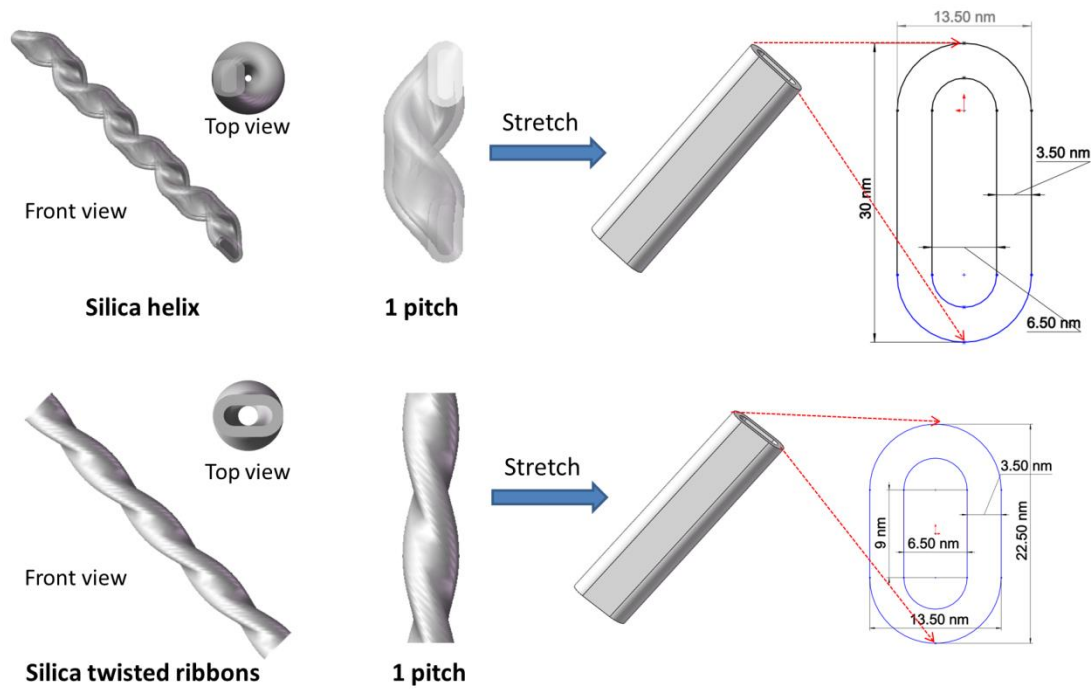


Figure 2-4. Silica helix and twisted ribbons models and their basic parameters

Table 2-1. Calculated parameters of silica helical/twisted ribbons

	Mass	Cross-sectional area	The total length of silica	Outside perimeter	Inside perimeter	Outside surface area	Inside surface area
Helical ribbons	0.5 mg	225.5 nm ²	1.01*10 ¹⁵ nm	75.4 nm	53.4 nm	7.59*10 ¹⁶ nm ²	5.36*10 ¹⁶ nm ²
Twisted ribbons	0.5 mg	172.9 nm ²	1.31*10 ¹⁵ nm	60.4 nm	38.4 nm	7.93*10 ¹⁶ nm ²	5.05*10 ¹⁶ nm ²

Based on the properties of silica ribbons and the possible mechanism of chirality induction to luminescent NCs, there are two possibilities to endow chirality to luminescent NCs complexed with our silica ribbons. First approach is the grafting of luminescent NCs on the outer surface of chiral silica ribbons as shown in Figure 2-5 (a). Second approach is in-situ growth of luminescent NCs in the hollow silica ribbons as shown in Figure 2-5 (b).

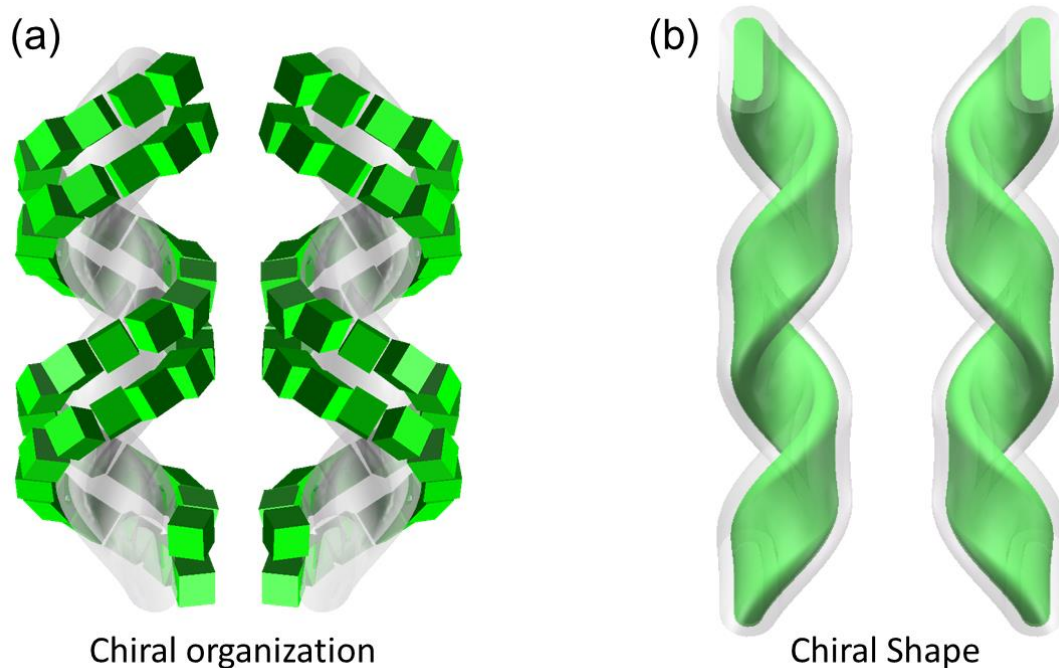


Figure 2-5. Chirality induction to NCs by chiral building block system (a) and confinement growth of NCs with chiral shape (b).

3. The complexation between luminescent NCs and silica ribbons

According to the description above, there are two ways to endow chirality to luminescent NCs. The key point is how to engage them together. The traditional way is to modify the surface of NCs and silica ribbons with an active group such as -COOH and -NH_2 separately. The active group can combine them by electrostatic or covalent bonding. As it is well known, the NCs have surface ligands to keep colloid stability in suspension. So if the amine-modified silica ribbons are acted as one kind of ligands for NCs, there is a possibility to engage them together by sample ligands

exchange methods. In addition, the silica ribbons have a hollow structure with helical or twisted organic templates space structure which would be allowed the growth of the NCs inside with a chiral shape. Here, three ways to engage NCs with silica ribbons to obtain optically active NCs were discussed.

3.1 Functionalized luminescent NCs combined with amine-modified silica ribbons

Silica modified with APTES has been widely reported in the fields of biochemistry, analytical chemistry, catalyst technology, and electronics²⁻⁴. Semiconductor NCs need to be modified with an active group such as carboxylic acid which could form electrostatic or covalent bonding with an amine. Hence, the NCs could be grafted on the surface of silica ribbons. Typically, as shown in Figure 2-6 (a), in the initial oil phase, oleic acid or oleylamine ligands bound to QDs are exchanged with 3-mercaptopropionic acid (MPA) to obtain the aqueous phase of QDs. So the surface of QDs is modified with carboxyl group as shown in Figure 2-6 (b). The carboxyl-modified QDs and amine-modified silica helical ribbons are mixed so that the amine and carboxyl group could be connected by electrostatic or covalent bonding at a certain condition. The QDs can be grafted on the surface of silica helical ribbons. However, the ligands exchange from the oil phase to the aqueous phase result in lower photoluminescence quantum yield (PLQY) which is a drawback for optical applications.⁵⁻⁷

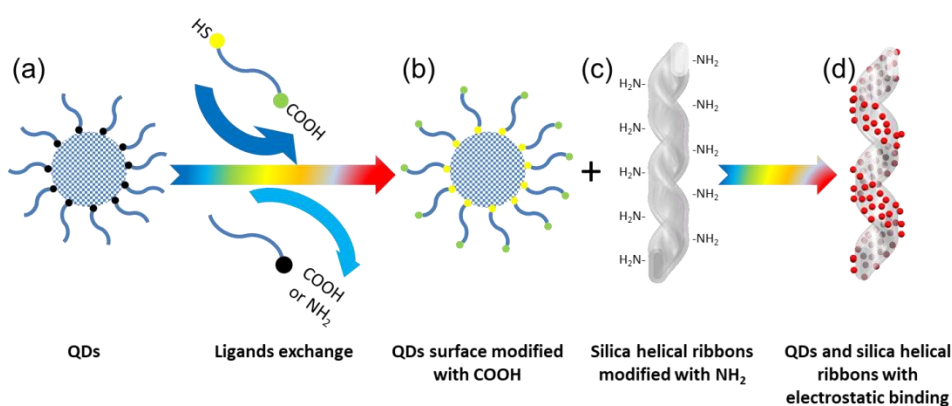


Figure 2-6. Functionalized NCs combined with amine-modified silica ribbons

3.2 Ligands exchanged of luminescent NCs by amine modified silica ribbons

It is well known that amine is general ligand binding on the surface of QDs to keep colloid stability with high photoluminescence quantum yield. If the amine-modified silica ribbons are acted as one kind of “helix amine ligands”, the QDs could be grafted on the surface of silica helical ribbons by “ligands exchanged methods”. Typically, the QDs surface has amine ligands such as oleylamine which show dynamic equilibrium bonding on the QDs surface atoms as shown in Figures 2-7 (a) and (b). When the QDs and amine-modified silica ribbons are mixed, the silica ribbons “helix amine ligands” could be a substitute for the initial oleylamine ligands. Therefore, the QDs could be grafted on the surface of silica ribbons. This grafting method doesn't need phase transfer from the oil phase to an aqueous phase which could maintain the photoluminescence as much as possible.

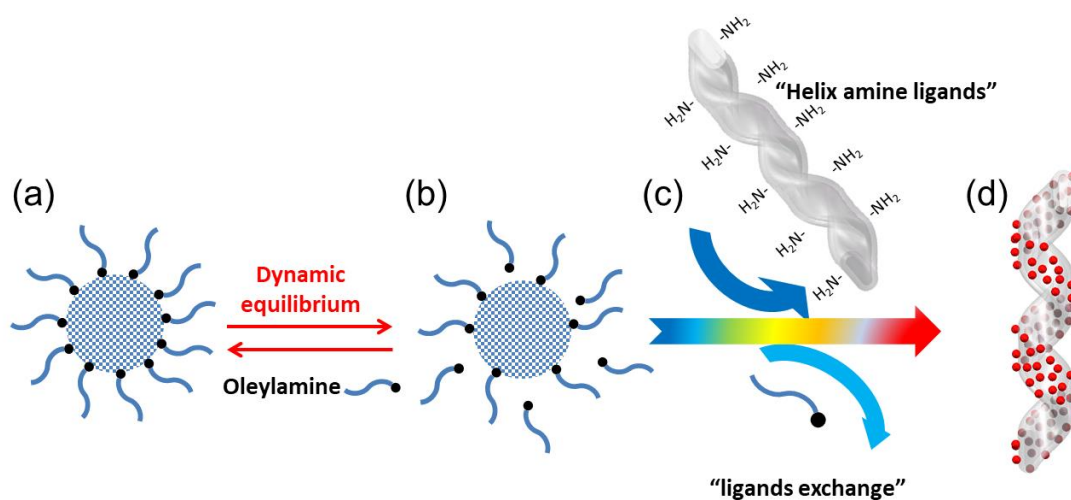


Figure 2-7. NCs grafted on the surface of silica ribbons by “ligands exchange methods”.

3.3 In-situ growth of luminescent nanocrystals outside or inside of silica ribbons

Generally, the NCs were synthesized by combining cations, anions, and ligands in certain conditions. If the amine-modified silica ribbons are acted as a kind of amine

ligands, in a certain condition, the NCs could be grown on the surface of silica ribbons as shown in Figure 2-8 upward picture. Besides, the silica ribbons are a mesoporous structure after remove the organic templates. The hollow matrixes could be used to synthesis templating of semiconducting NCs for II–VI, III–V, and perovskite compounds in the last two decades.⁸⁻¹² As shown in Figure 2-8 downward picture, the mixture solution of cations, anions, and hollow silica ribbons, in a certain condition, the NCs could grow inside of silica ribbons. In this way, chiral shape NCs could be obtained and its chiral shape is determined by the handedness of silica ribbons.

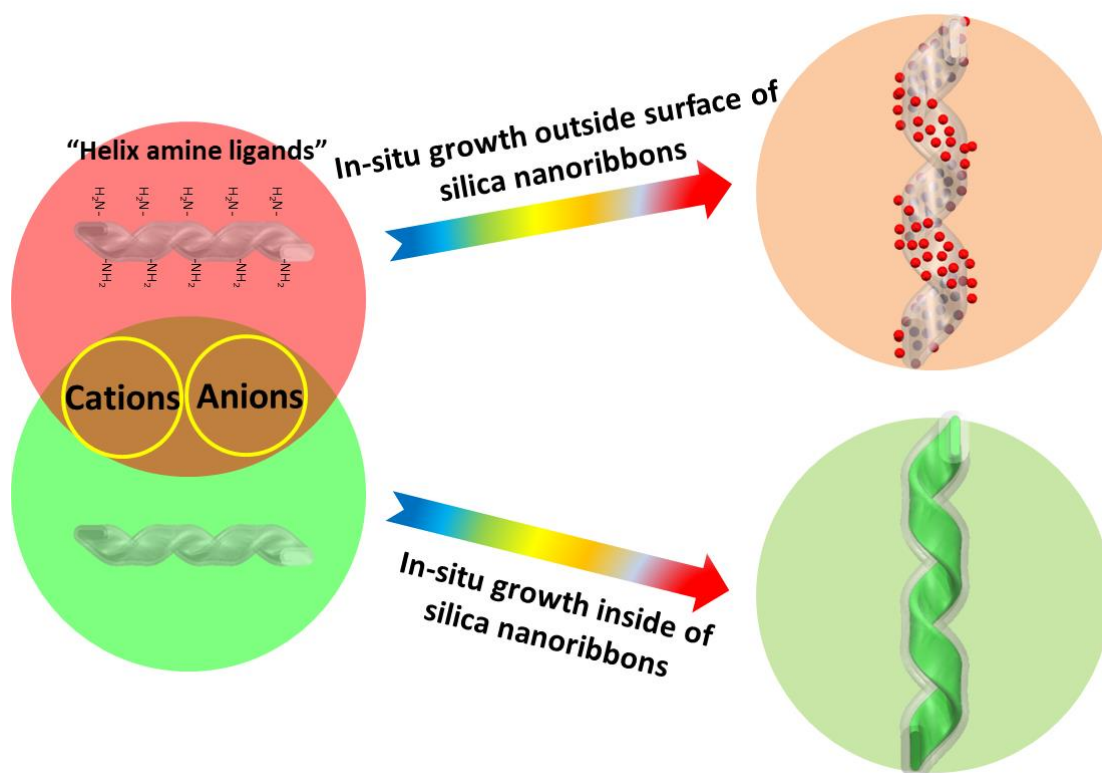


Figure 2-8. NCs engaged with silica ribbons by in-situ growth outside surface (upward) or inside of silica ribbons (downward).

3. Conclusion

In this chapter, two possible ways to endowing chirality to NCs assisted by the inorganic chiral hollow silica ribbons were discussed. The silica ribbons replicated the

organic helical Gemini tartrate shape which has chiral helical and hollow structure. The helical and hollow structures offer the opportunity to endow chirality by the NCs' chiral self-organization on the surface of silica ribbons or preparation of chiral shape of NCs inside of hollow silica ribbons. The synthesis and surface modification process of silica helical and twisted ribbons was presented. Also, related parameters of silica ribbons are approximately calculated for the preparation of NCs complexed with the silica ribbons. Then three possible methods for grafting NCs on the surface of the silica ribbons are discussed in detail. A general way to grow NCs inside the hollow silica ribbons has also been presented in this thesis.

4. Reference

1. Okazaki, Y.; Cheng, J.; Dedovets, D.; Kemper, G.; Delville, M.-H.; Durrieu, M.-C.; Ihara, H.; Takafuji, M.; Pouget, E.; Oda, R., Chiral Colloids: Homogeneous Suspension of Individualized SiO₂ Helical and Twisted Ribbons. *ACS Nano* **2014**, *8* (7), 6863-6872.
2. Saengdee, P.; Chairiratanakul, W.; Bunjongpru, W.; Sripumkhai, W.; Srisuwan, A.; Jeamsaksiri, W.; Hruanun, C.; Poyai, A.; Promptmas, C., Surface modification of silicon dioxide, silicon nitride and titanium oxynitride for lactate dehydrogenase immobilization. *Biosens Bioelectron* **2015**, *67*, 134-8.
3. Rahman, I. A.; Padavettan, V., Synthesis of Silica Nanoparticles by Sol-Gel: Size-Dependent Properties, Surface Modification, and Applications in Silica-Polymer Nanocomposites—A Review. *Journal of Nanomaterials* **2012**, *2012*, 1-15.
4. Bagwe, R. P.; Hilliard, L. R.; Tan, W., Surface modification of silica nanoparticles to reduce aggregation and nonspecific binding. *Langmuir* **2006**, *22* (9), 4357-62.
5. Gao, X.; Chan, W. C.; Nie, S., Quantum-dot nanocrystals for ultrasensitive biological labeling and multicolor optical encoding. *Journal of biomedical optics* **2002**, *7* (4), 532-538.
6. Osaki, F.; Kanamori, T.; Sando, S.; Sera, T.; Aoyama, Y., A quantum dot conjugated sugar ball and its cellular uptake. On the size effects of endocytosis in the subviral region. *Journal of the American Chemical Society* **2004**, *126* (21), 6520-6521.
7. William, W. Y.; Chang, E.; Drezek, R.; Colvin, V. L., Water-soluble quantum dots for biomedical applications. *Biochemical and biophysical research communications* **2006**, *348* (3), 781-786.
8. Martin, C. R., Nanomaterials: a membrane-based synthetic approach. *Science* **1994**, *266* (5193), 1961-6.
9. Agger, J. R.; Anderson, M. W.; Pemble, M. E.; Terasaki, O.; Nozue, Y., Growth of Quantum-Confined Indium Phosphide inside MCM-41. *The Journal of Physical Chemistry B* **1998**, *102* (18), 3345-3353.
10. Moller, K.; Bein, T., Inclusion Chemistry in Periodic Mesoporous Hosts. *Chemistry of Materials* **1998**, *10* (10), 2950-2963.
11. Li, Y.; Xu, D.; Zhang, Q.; Chen, D.; Huang, F.; Xu, Y.; Guo, G.; Gu, Z., Preparation of Cadmium Sulfide Nanowire Arrays in Anodic Aluminum Oxide Templates. *Chemistry of Materials* **1999**, *11* (12), 3433-3435.
12. Parala, H.; Winkler, H.; Kolbe, M.; Wohlfart, A.; Fischer, R. A.; Schmechel, R.; Seggern, H. v., Confinement of CdSe Nanoparticles Inside MCM-41. *Advanced Materials* **2000**, *12* (14), 1050-1055.

Chapter 3. Chiral optical scattering from silica helical and twisted ribbons

1. Introduction.....	60
2. Theoretical analysis	61
3. Results and discussions.....	63
3.1 Silica nanoribbons deposited on substrates.....	63
4. Experiment section.....	74
4.1 Silica nanoribbons preparation and Quartz slides substrate preparation.....	74
4.2 Silica nanoribbons film preparation	74
4.3 CD and LD measurement	75
5. Conclusion	75
6. Reference	77

Chapter 3. Chiral optical scattering from silica helical and twisted ribbons

1. Introduction

The investigation of the chirality of solid materials has been the focus of intensive studies. While they have been performed mainly on crystalline and/or periodic structures,¹⁻¹⁴ non-crystalline (non-ordered and non-periodic structures) materials also have the potential to show promising chiral properties.¹⁵ An interesting example is that of amorphous (non-crystalline) chiral silica synthesized by the sol-gel condensation of silica alkoxide in the presence of chiral organic molecular assemblies as templates. This approach was first reported by Shinkai *etc.*¹⁶ After this report, numerous helical (morphologically chiral) nano-materials have been synthesized and been studied for their chiroptical properties.¹⁷⁻²¹

In general, the optical activity (OA) observed from solid materials could be classified into three contributions. i) Absorption and emission based OA^{9, 22-24}, ii) Refraction based OA²⁵ and iii) Elastic scattering or Non-Elastic Raman scattering based OA.²⁶⁻³⁶ Absorption and emission based OA is the difference of absorption or emission of left-handed (LH) and right-handed (RH) circular polarized (CP) light. Absorption based OA (circular dichroism: CD) has been widely studied, such as gold and silver metal plasmonic absorption OA, electronic transition OA and vibrational OA. Emission based OA corresponds to circularly polarized luminescence (CPL). Refraction based OA (circular birefringence) comes from the difference of the velocities of LH-CP light and RH-CP light which pass through the OA medium, which is determined by the different refractive indices of the material for the RH- and LH-CP light. In contrast to electron transitions such as light absorption and emission, light scattering from nanometric or submicrometric materials shows interesting optical properties such as elastic light scattering and fadeless coloring in the UV-vis region.³⁷⁻³⁹ The scattering based OA comes from the scattering at the surfaces having different refractive indexes from the surrounding media and having chiral structure. Due to the no-energy loss process, it can lead to a number of promising applications.

Meanwhile, scattering based OA observed from solid particles which typically have the high refractive indexes is mixed with absorbance based OA, therefore, the contribution of the two needs to be separated. Indeed, it is important to note that in the transmission mode of UV-vis and CD spectrometers which detect the number of (or the difference of the number of) photons which reaches the detector after passing through the samples, the variation of the photon number through absorbance or scattering mechanisms cannot be distinguished.

Our group have previously shown that helical (or twisted) nano silica can be obtained by sol-gel reaction of tetraethoxysilane (TEOS) using molecular assemblies of chiral surfactant (having the formula $C_2H_4-1,2-((CH_3)_2N^+C_{16}H_{33})_2$ with a tartrate counterion) as organic template.⁴⁰⁻⁴² When L-tartrate is used as counterion, RH-nanohelices are obtained and D-tartrate is used, LH-nanohelices are obtained. These nanohelices show strong vibrational circular dichroism (VCD) signals at Si-O-Si asymmetric stretching vibrational band even after removal of organics by calcination.²¹ Meanwhile, when dried, these chiral silica nanoribbons show strong scattering in the UV range due to the higher refractive index of silica than that of air. Therefore, it is very important to understand how the scattering aspect affects the chiroptical signals, in particular when measuring the electronic CD signals. In this chapter, the optically active absorbance and scattering of the helical/twisted silica nanoribbons were investigate by using CD spectrometer with or without integration sphere, and compare with the results obtained by the simulation.

2. Theoretical analysis

The extinction and scattering cross section of individual silica helices and twist ribbons are simulated according to the boundary element method (BEM).⁴³ This method requires discretizing the surface of the nanostructure. More than 5000 vertices are used to define each nanostructure surface. The dielectric function of silica is given by Palik⁴⁴ while air is used as the ambient medium. As illustrated in Figure 1, the

incident light is parallel or perpendicular to the helices/twist ribbons orientation. The extinction (σ_{ext}) and scattering (σ_{scat}) cross sections are simulated for LH- and RH-circular polarizations. The extinction and scattering cross sections of nanostructures for non-polarized light are calculated from the following equation:

$$\sigma_{ext/scat} = \frac{\sigma_{ext/scat,L} + \sigma_{ext/scat,R}}{2}, \quad (1)$$

with $\sigma_{ext/scat,L}$ and $\sigma_{ext/scat,R}$ are the extinction or scattering cross obtained for LH- and RH- circular polarization, respectively. The circular dichroism (CD_{ext}) is deduced from the following equation:

$$CD_{ext} = \sigma_{ext,L} - \sigma_{ext,R}. \quad (2)$$

CD_{ext} is the sum of two contributions:

$$CD_{ext} = CD_{scat} + CD_{abs}. \quad (3)$$

The first term of equation 3 is the dichroism induced by the chiral scattering (CD_{scat}) while the second term is related to the difference in the absorption of LH- and RH- CP light (CD_{abs}). The g-factor is estimated from the ratio between the CD_{ext} and the extinction cross section σ_{ext} .

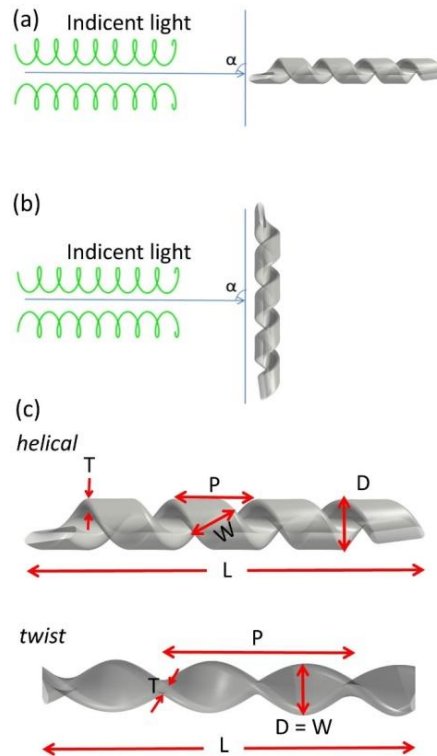


Figure 3-1. The diagram of the scattering based OA of silica nanoribbons depend on

the alignment of silica nanoribbons, (a) helix is out-of-plane and is parallel to the incident light. (b) helix is in-plane and is perpendicular to the incident light. (c) Scheme showing the various dimensions for helical and twisted ribbons; pitch (P), width of the ribbons (W), diameter (D), length (L), thickness (T).

3. Results and discussions

3.1 Silica nanoribbons deposited on substrates

To investigate the effect of the scattering and absorbance of individualized silica nanohelices, their suspension was submitted to ultrasonication to create homogeneous suspension of short nanohelices in ethanol⁴¹. The suspension was then drop-casted on a $2 \times 2 \text{ cm}^2$ quartz substrate. These silica helices were then submitted to calcination at $900 \text{ }^\circ\text{C}$ directly on the quartz plate for 2 hours. For the quantitative evaluation of morphologies, each 200 points of various dimensions (width, total thickness, pitch, length, and diameter) were measured from TEM images. As our group previously reported²¹, the silica nanohelices undergo shrinkage after calcination and the dimensions are shown in Table 3-1.

Table 3-1. Dimensions of the helical and twisted silica nanoribbons. Some values were taken from our previous publications.^{21, 41} To obtain the dimensions of the twist ribbons after calcination which is difficult to clearly determine due to their small size, same shrinking ratios are taken as helical ribbons for the width, thickness pitch and length respectively and applied to the sizes before the calcination.

	Width	Thickness	Pitch	Length	Diameter
Twist before					19.4 ± 3.8 nm
calc.	19.4 ± 3.8 nm	12.2 ± 2.3 nm	88.6 ± 14.0 nm	500 nm	(= Width)
Twist after					16.7 ± 3.3 nm
calc. at 900 °C	16.7 ± 3.3 nm*	12.0 ± 2.2 nm*	69.2 ± 10.9 nm*	390 nm	(= Width)
Ratio				78.1%	86.3%
after/before	86.3%	98.2%	78.1%	(= Pitch)	(= Width)
Helical before					
calc.	26.2 ± 2.4 nm	11.4 ± 1.4 nm	58.0 ± 12.4 nm	500 nm	27.1 ± 4.2 nm
Helical after					
calc. at 900 °C	22.6 ± 2.2 nm	11.2 ± 1.0 nm	45.3 ± 8.8 nm	390 nm	24.4 ± 3.4 nm
Ratio				78.1%	
after/before	86.3%	98.2%	78.1%	(= Pitch)	90.0%

Figures 3-2 (a-d) show the 3D illustrations of helical and twisted silica nanoribbons as well as the TEM images of RH- helical and twisted nanoribbons before and after the calcination. As discussed above, the signals of absorbance and CD measured from the CD apparatus in transmission mode are in fact based on the extinction which includes both scattering and absorbance contribution, which called extinction and CD_{ext} respectively hereafter.

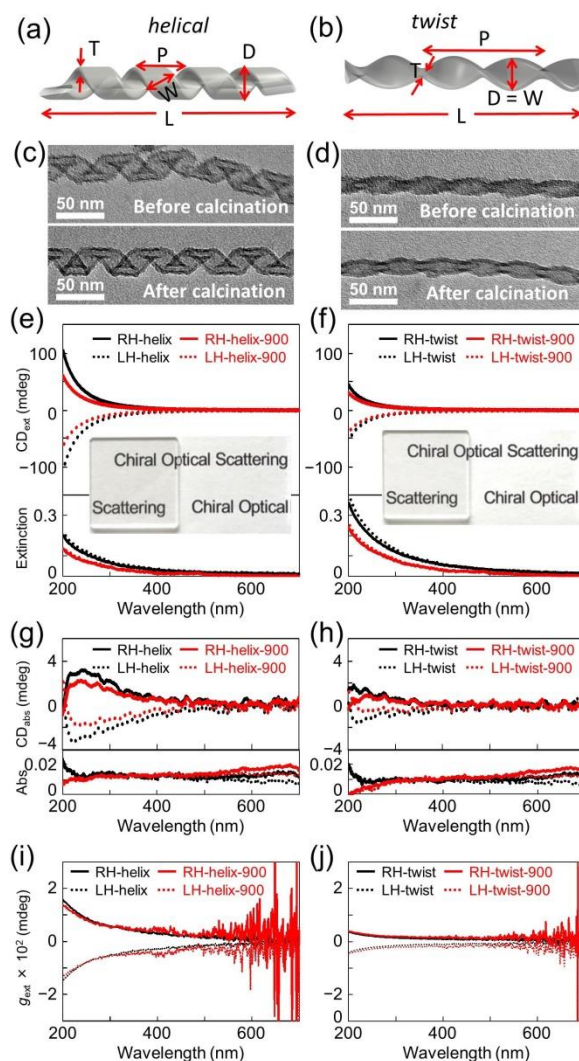


Figure 3-2. 3D illustrations of (a) helical and (b) twisted silica nanoribbons. TEM images of RH- (c) helical and (d) twisted silica nanoribbons before and after calcination. CD_{ext} (top) and extinction (bottom) spectra of drop-casted films ($50 \mu\text{g cm}^{-2}$) of (e) helical and (f) twisted silica nanoribbons. The insert images are the photos of the films before and after calcination. CD_{abs} (top) and absorption (bottom) spectra of drop-casted films ($50 \mu\text{g cm}^{-2}$) of (g) helical and (h) twisted silica nanoribbons. (i) and (j) are g -factors calculated from CD_{ext} and extinction of helical and twisted silica, respectively (e and f).

When the silica nanohelices are dispersed in ethanol, the extinction increases in the UV range below 300 nm, meanwhile, no CD_{ext} is observed (Figure 3-3). When they are drop-casted on the quartz substrates, the obtained transparent films showed strong extinction and CD_{ext} . In Figures 3-2 (e-f), it show the extinction and CD_{ext} observed

from helical and twisted silica nanoribbons both for RH- and LH-ribbons and both before and after calcination at 900 °C. The extinction tails towards the wavelength up to 600 nm. Mirror image CD_{ext} signals were observed for RH- (positive) and LH-nanohelices (negative). All the CD_{ext} signals of the films were obtained by the mean data of the CD_{ext} measured by two angles with 0° and 90° and LD signals (less than 5×10^{-4}) were measured in parallel (Figures 3-4). Both extinction and CD_{ext} signals decrease upon calcination of the substrate at 900 °C. Helical nanoribbons CD_{ext} signals are higher than that of twisted nanoribbon whilst they have lower extinction.

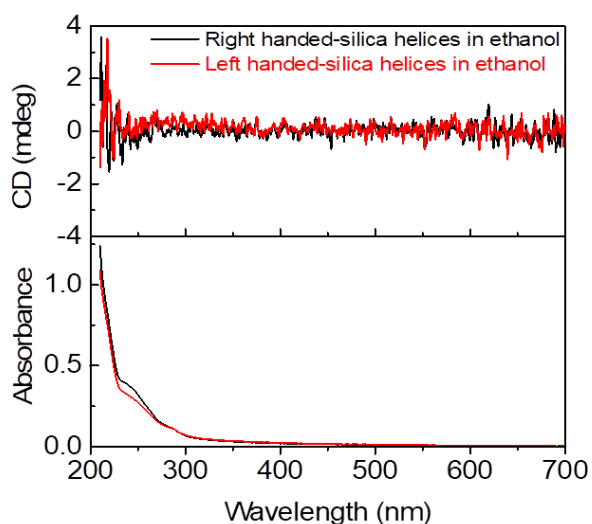


Figure 3-3. CDext (top) and extinction (bottom) spectra of helical silica nanoribbon in ethanol.

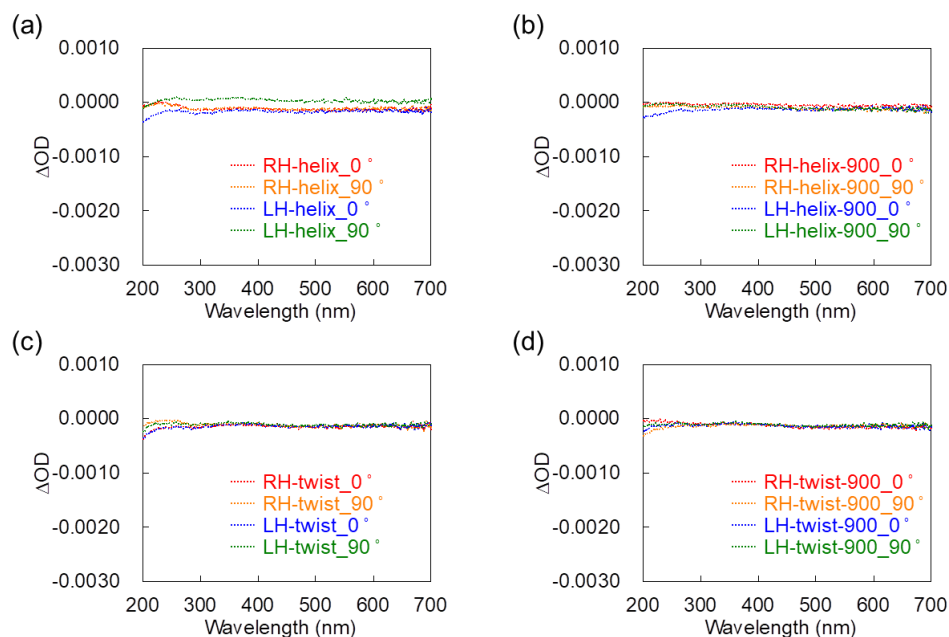


Figure 3-4. LD spectra of silica helical nanoribbon films (a) before and (b) after calcination at 900 °C. LD spectra of silica twisted nanoribbon films (c) before and (d) after calcination at 900 °C. All spectra were recorded by CD spectrometer on the transmission mode. All films were measured at two angles (0° and 90°) rotated around the light beam axis.

To quantify the contribution of the (chiral) scattering and absorbance from silica nanohelices separately, CD_{abs} measurements of drop-casted silica helix films were performed with diffuse reflection CD (DRCD) mode for which the scattered light is collected using integration sphere on the CD apparatus. The results of DRCD (CD_{abs}) and absorbance of RH- and LH-helical silica nanoribbons as well as RH- and LH-twisted silica nanoribbons are shown in Figure 3-2 (g-h) respectively. Small CD_{abs} signals were observed at around 200-250 nm, which corresponds to the impurities (e.g., OH or dissolved O_2 molecules) and nonstoichiometric vacancies (e.g., oxygen).²⁶ Although our previous report on the VCD spectral measurements strongly supported the existence of such a chiral information in molecular level from siloxane structure of helical/twisted silica nanohelices²¹, the amplitudes of the absorbance and CD_{abs} intensities in the UV range are much smaller ($\sim 1/10$ and $\sim 1/33$ respectively) than that of the extinction and CD_{ext} respectively, clearly indicating that the scattering

and the chiral optical scattering (COS) signals are the dominant origin of the extinction and CD_{ext} . Again, upon calcination at 900 °C, both absorbance and CD_{abs} decreased.

Hereafter, the scattering intensity and COS are discussed in detail. As it can be seen from the Table 1, both the helical or twisted nanoribbons shrink after calcination, which is directly reflected to the decrease of the scattering intensity. This means that along with the decrease of the pitches, the diameter and the length of the helices also decrease, therefore totally the scattering intensity decreases. In order to investigate how this shrinking affects the COS, the g-factors which correspond to the normalization by the CD_{ext} divided by the extinction were compared. For both helical and twist ribbons, the g-factors before and after the calcination are shown in Figures 3-2 (i-j). No significant modification was observed both for helical and twisted ribbons after the calcination. For both morphologies they showed continuous decrease with increasing wavelength, for helical ribbons showing g-factor ~ 0.015 (at 200 nm) and ~ 0.0035 (at 200 nm) for twisted ribbons, respectively.

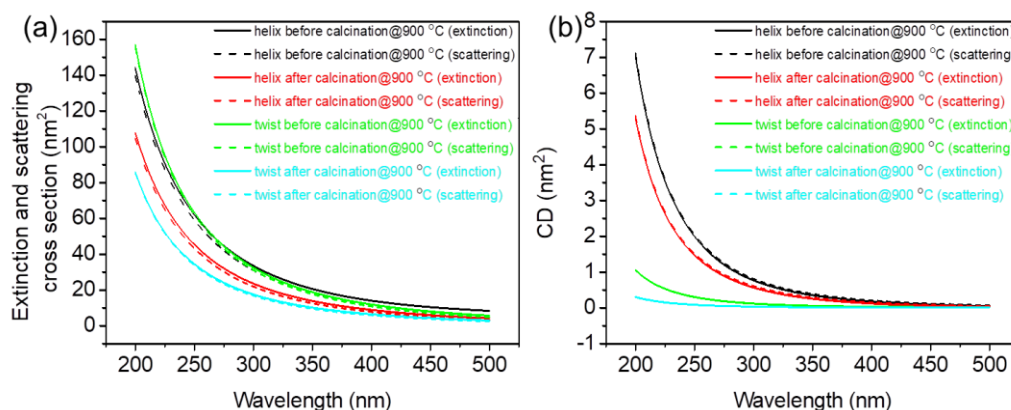


Figure 3-5. Simulation data of extinction and CD_{ext} as well as scattering cross section and CD_{scat} values of helical and twisted ribbons before and after calcination at 900 °C.

Then simulation has been done for the extinction and CD_{ext} as well as scattering cross section and CD_{scat} values (Figure 3-5) for helical and twisted ribbons before and after the calcination using the measured values shown in Table 3-1. The simulations are performed by considering that the light beam is perpendicular to the helix/twist ribbon

(in-plane configuration in Figure 3-1, (b)). CD_{ext} and extinction cross section are very close to CD_{scat} and scattering cross section, respectively (Figure 3-5). This results confirmed that the contribution of absorbance and CD_{abs} is negligible comparing the scattering and CD_{scat} . Thus, in the following discussion, CD_{ext} is assimilated to CD_{scat} . It was also observed that the cross section and CD_{scat} decrease for the calcined helices. Scattering and CD_{scat} for helical ribbons are stronger than those for twisted ribbons in good agreement with the experimental observation. How the modification of pitch and the length of the ribbons affect the scattering intensities were also investigated by simulation, the CD_{ext} values as well as the g-factors are shown in Figure 3-6 (a).

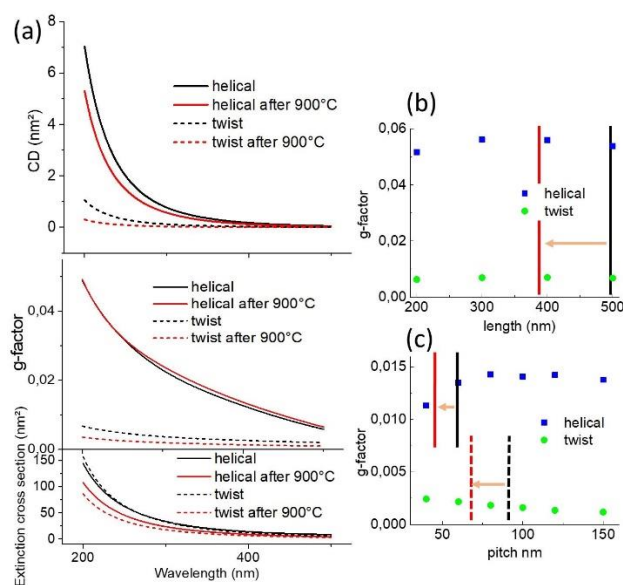


Figure 3-6. (a) Simulated extinction cross section, CD_{ext} , g-factors of helical and twisted silica nanoribbons. Variation of g-factors of helical and twisted nanoribbons as a function of (b) ribbons' length at a fixed diameter and pitches, and (c) pitches at a fixed length and diameter.

Figures 3-6 (b-c) show the simulation of how g-factors at a wavelength of 200 nm evolves with the length (at a fixed pitch and diameter) and the pitch (at a fixed length and diameter) respectively of a single helical or twisted ribbon. The corresponding extinction and CD_{ext} values are shown in Figure 3-7. The incident light is perpendicular to the helix orientation.

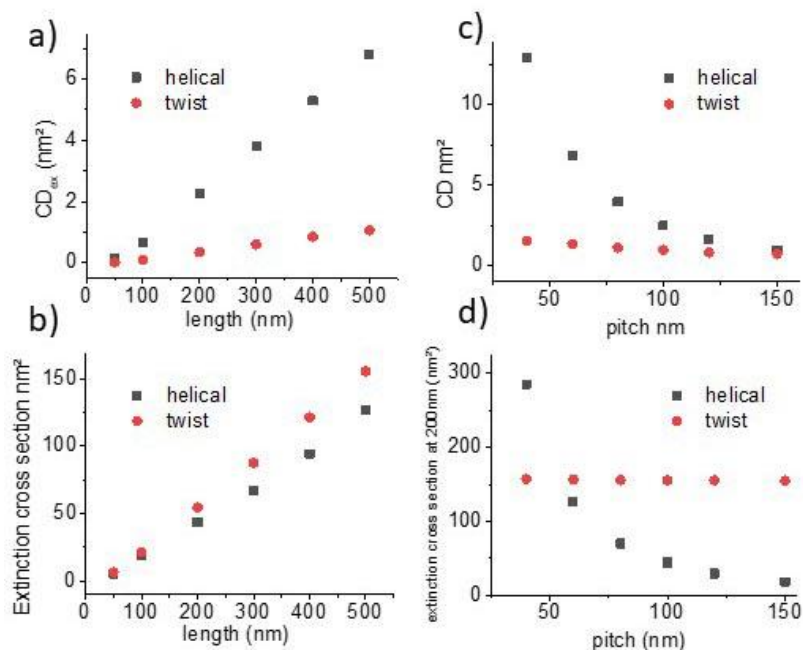


Figure 3-7 Simulated extinction and CD_{ext} at a wavelength of 200 nm as a function of the length (at a fixed pitch and diameter) and the pitch (at a fixed length and diameter) respectively of a single helical or twisted ribbon

It is clearly observed that for the pitches and the lengths in the range of helical and twisted ribbons observed for the present system (Pitches: 25 - 150 nm. Lengths: 200 - 500 nm), the g-factors of COS signals do not vary much. As shown in Figure 3-7, when the dimensions decrease during the calcination, both CD_{ext} and extinction vary in the same direction (CD_{ext} ↑ and extinction ↑ for increasing length, whereas both CD_{ext} ↓ and extinction ↓ for increasing pitch) compensating the variation of each other.

As a whole, all these simulated data are in very good agreement with the experimental ones. Slight difference between the simulation and the experimental results is likely due to the fact that 1) the simulation is done on one helix whereas the measurements are done for the closely packed samples (figure 3-8) with large polydispersities on the dimensions in particular for the length of the helices. 2) The inter-helix scattering is not taken into account, and 3) variation in refractive index of silica before and after the calcination which is not taken into account in the simulation. Indeed, the refractive

index should depend on the density of helices.

Finally, the effect of the quantity of silica nanoribbons on the substrates was compared. As shown in Figure 3-8, $25 \mu\text{g cm}^{-2}$, $50 \mu\text{g cm}^{-2}$, $100 \mu\text{g cm}^{-2}$, $150 \mu\text{g cm}^{-2}$, and $200 \mu\text{g cm}^{-2}$ of silica nanoribbons films were prepared on the $2 \times 2 \text{ cm}^2$ quartz substrates and the extinction and CD_{ext} were measured. While the intensity of the extinction increased linearly with the quantity of silica nanoribbons (Figure 3-8 (a)), CD_{ext} intensity increased much more slowly beyond $50 \mu\text{g cm}^{-2}$ of silica nanohelices (Figure 3-8 (b)) and the g-factor in this range decreased (Figure 3-8 (c)). From scanning electron microscope (SEM) images, it confirmed that $25 \mu\text{g cm}^{-2}$ of silica nanoribbons was enough to homogeneously cover the quartz surface of the substrate (Figure 4 (d)). To understand the decrease in the COS signal at the larger quantities of silica helices, the effect of the orientation (in plane or out of plane) of a helix on the COS signal by simulation was investigated. As shown in Figure 3-8 (f), out-of-plane helix showed opposite CD_{ext} signal from that of in-plane helix. Although similar coverage of surfaces were observed for the top views of all the films, cross-section SEM images of these films showed clear difference of their thicknesses. In the case of $25 \mu\text{g cm}^{-2}$ and $50 \mu\text{g cm}^{-2}$ films, thickness of silica layer was around $0.18 \mu\text{m}$ and $0.35 \mu\text{m}$ respectively, which is thinner than the average length of silica nanohelices. On the other hands, in the case of $200 \mu\text{g cm}^{-2}$ film, the thickness of silica layer was about $3.2 \mu\text{m}$, which is much larger than the average length of silica nanohelices. These results indicate that in the thinner layer ($< 50 \mu\text{g cm}^{-2}$), the in-plane orientation of silica nanohelices are dominant whilst in the thicker layers ($> 100 \mu\text{g cm}^{-2}$), in-plane and out-of-plane orientation of silica nanohelices (Figure 3-8 (e)) can co-exist. Also, electromagnetic interaction between helices in the thicker layers of helices and the multiple scattering can perturb the polarizations of the scattered light. These results can also be compared with the measurement from the drop-cast film of cut silica nanoribbons and non-cut nanoribbons (Figure 3-9). Non-cut silica nanoribbons show smaller COS. In both cases either for the highly concentrated drop-casted film or non-cut film, silica nanohelices are strongly aggregated in 3D direction.

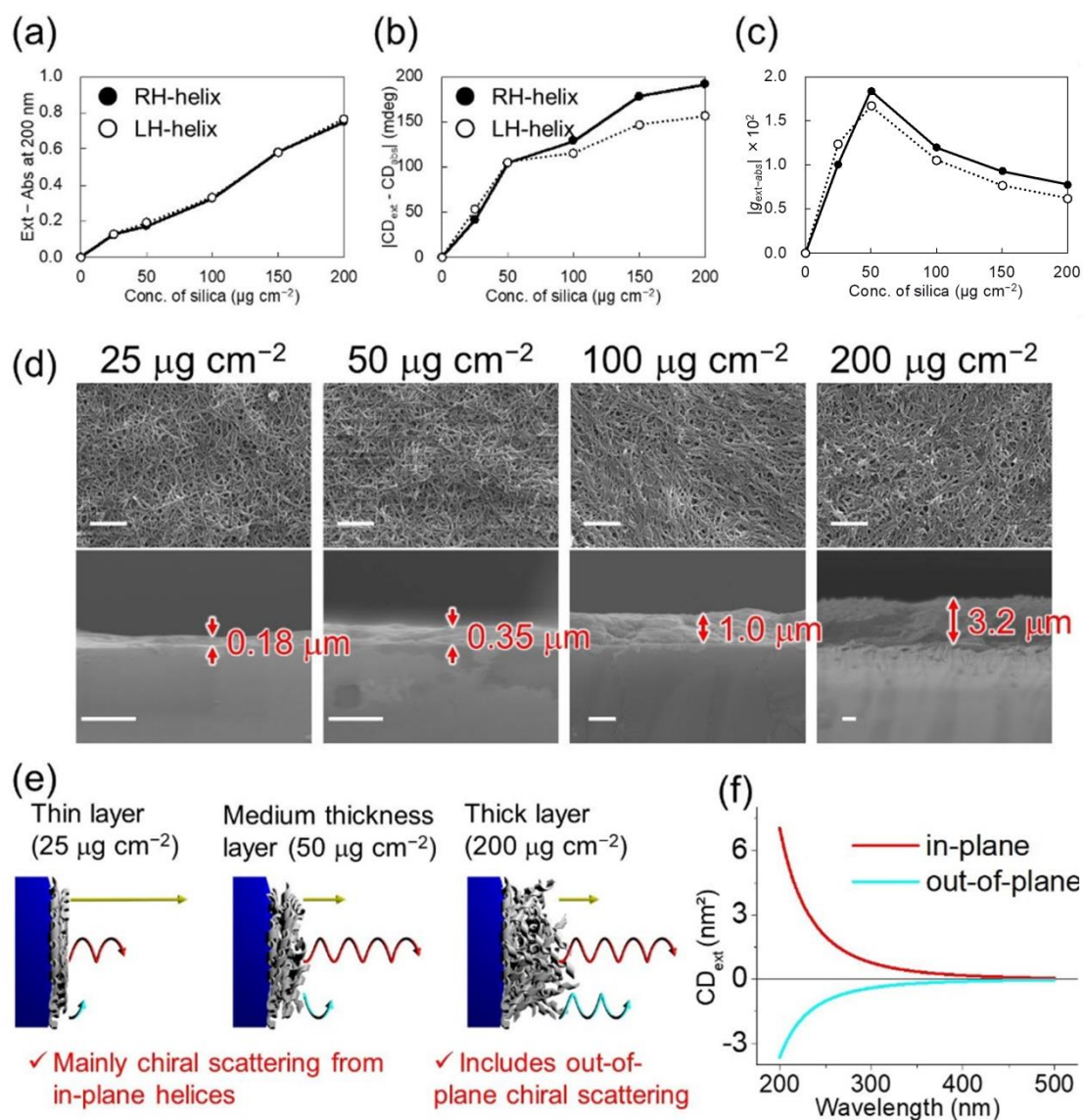


Figure 3-8. Concentration dependences of silica nanohelices films on (a) total scattering ($\text{Ext} - \text{Abs}$) at 200 nm, (b) chiral optical scattering ($\text{CD}_{\text{ext}} - \text{CD}_{\text{abs}}$) at 200 nm, and (c) g -factor of chiral optical scattering ($g_{\text{ext-abs}}$). (d) SEM images of surface (top) and cross-section (bottom) of helical silica nanoribbon films with different quantities. (e) Plausible mechanisms of COS from silica nanohelices film with different thickness. Dark blue rectangle indicates quartz substrate. Yellow, red, and blue arrows indicate nonchiral optical scattering light from quartz substrate, chiral scattering from in-plane helices, and opposite-handed chiral scattering from out-of-plane helices, respectively. (f) Simulated CD_{ext} of a helical nanoribbon oriented in-plane (red line) and out-of-plane (blue line).

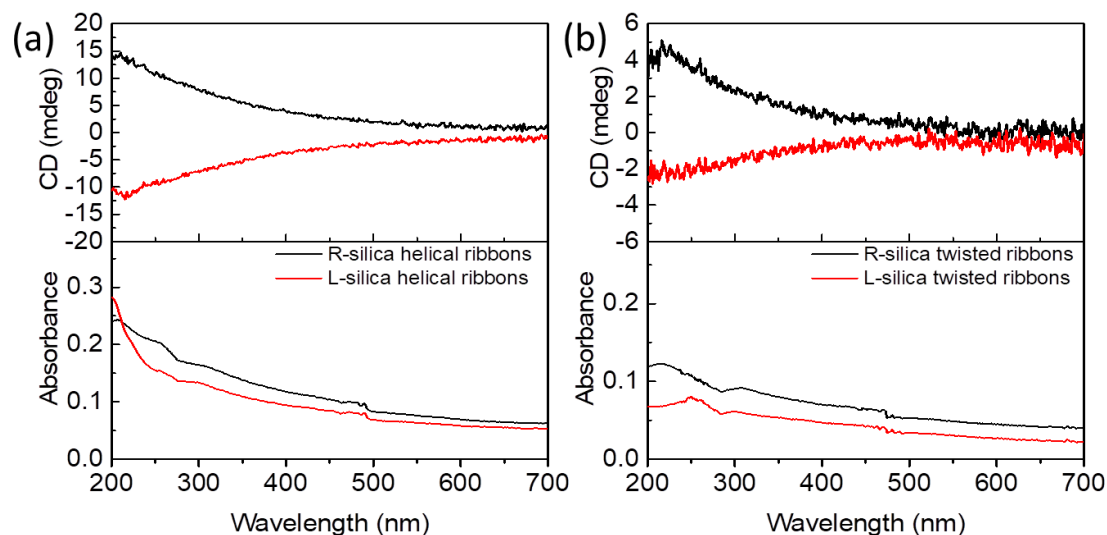


Figure 3-9. CD_{ext} (top), and extinction (bottom) spectra of non-cut (a) helical and (b) twisted silica nanoribbon films.

As chapter 2 mentioned, the main project of this program is endowing optically active properties to luminescent nanocrystals by engaging QDs with silica nanoribbons, so it is important to know how the scattering based OA of silica nanoribbons affects the luminescent nanocrystals. Herein, the CdSe/ZnS quantum dots (QDs) and silica helical nanoribbons without amine modification were selected for the study. In this case, the QDs and silica helices are isolated, not combined by electrostatic or covalent bonding. Firstly, as shown in Figure 3-10 (a) insert picture, the QDs, and silica helical ribbons were drop-casted on the same side of the quartz substrate. For only silica helical ribbons films, it shows small scattering absorbance and big CD signals (black curve). When the QDs were drop-casted and mixed with the silica helical ribbons, the absorbance increased due to the absorption of QDs, while no CD signals are corresponding to the QDs absorption. At the same time, the CD signals due to the scattering of the silica helical ribbons decreased, and this reduction of scattering CD is supposed to be impregnated with QDs which might weaken the chiral structure. Also, the film was measured by flip 180° , and it has no influence on the CD spectra. Secondly, the silica helical ribbons film and QDs were drop-casted on the different sides of quartz substrate as shown in Figure 3-10 (b) insert picture. The QDs were drop-casted on the other side of the quartz substrate, and no significant changes

observed on the CD spectra. These results will help us to understand the difference of QDs-silica helices with or without grafting.

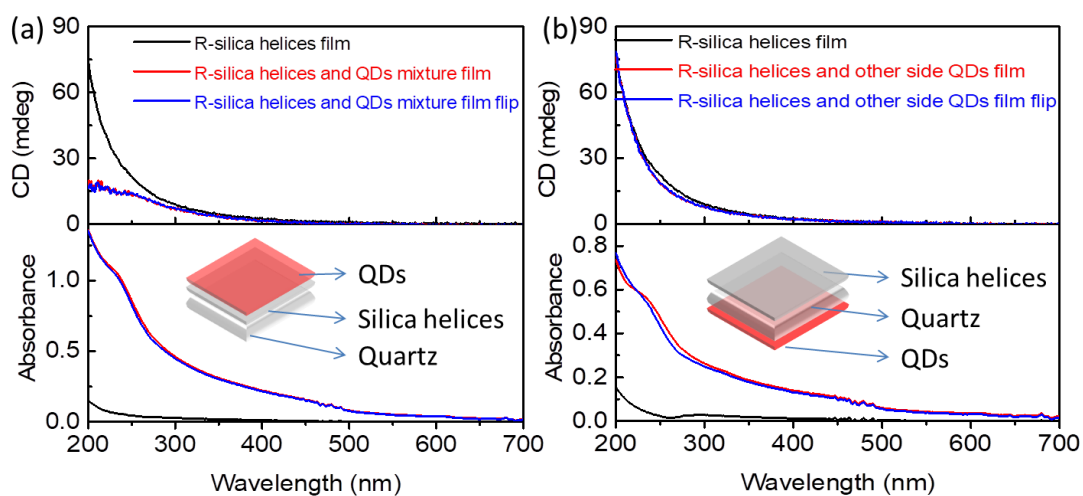


Figure 3-10. CD and absorption spectra of R-silica helical ribbons film and R-silica helical ribbons QDs mixture film with front side and back side measurement (a), insert picture show the film structure; CD and absorption spectra of R-silica helical ribbons film, R-silica helical ribbons and QDs in different side of quartz substrate film with front side and back side measurement (b), insert picture show the structure film.

4. Experiment section

4.1 Silica nanoribbons preparation and Quartz slides substrate preparation

The well-dispersed silica helical/twisted ribbons ethanol solution (1 mg/mL) was prepared by usual methods as shown in chapter 2. Then the quartz slides were cut into 1 cm*1cm and washed with Milli-Q water, acetone, and isopropanol in turn with sonication for 30 min. The washed quartz slides were kept in isopropanol for further use.

4.2 Silica nanoribbons film preparation

Typically, for 50 ug silica nanoribbons film, 50 uL silica nanoribbons (1 mg/mL) ethanol solution was drop-casted on the surface of quartz substrate and drying at room temperature.

For 100 ug silica nanoribbons film, 50 uL silica nanoribbons (1 mg/mL) ethanol solution were drop-casted again on the surface of 50 ug silica nanoribbons film and drying at room temperature.

For the silica nanoribbons film calcination, the temperature was increased from 25 °C to 900 °C with 9 hours and kept at 900 °C for 2 h.

For the silica nanoribbons film and QDs, first, 50 ug silica nanoribbons films were prepared, then QDs solution drop-casted on the silica nanoribbons side or another side of the quartz substrate.

4.3 CD and LD measurement

All the samples were measured with two angles (0 ° and 90 °), the final CD spectra were obtained by the mean values of data measured at 0 ° and 90 ° to eliminate the contribution of linear dichroism. The LD is also measured with two angles (0 ° and 90 °) to know whether LD affects the CD or not.

5. Conclusion

This chapter investigated the chiral optical scattering from nanometric helical and twisted silica nanoribbons deposited on substrates. By using a CD spectrometer in both transmission mode and diffuse reflection mode, it demonstrates that the contribution of the absorbance and absorbance-based CD are present but negligible compared to the scattering and COS. Helical ribbons show larger COS and g-factors compared to twisted ribbons. For the both morphologies, after calcination and shrinkage, COS intensities decreased but when normalized by the scattering intensity, the variations of g-factors were negligible. All these results are in good agreement with the simulation performed on a single helix oriented perpendicular to the incoming light. The simulation of the COS on a helix oriented parallel to the incoming light shows the opposite signal from that of the helix oriented perpendicular to the incoming light, which is likely the origin of the decrease of COS for the aggregated helices which contain the helices oriented out of plane. The g-factors

observed for helical ribbons are of the order of 10^{-2} which is surprisingly high for materials made from silica alone. Thus the strategy shown here represents a very promising method to create fadeless circular polarizers with one of the most abundant inorganic atoms Si and O by simple coating of silica helices on the transparent films.

6. Reference

1. Pasteur, L., Sur les relations qui peuvent exister entre la forme cristalline, la composition chimique et le sens de la polarisation rotatoire. *Ann. Chim. Phys.* **1848**, *24*, 442-459.
2. Bunn, C. W.; Howells, E. R., Structures of Molecules and Crystals of Fluoro-Carbons. *Nature* **1954**, *174* (4429), 549-551.
3. Kipping, F. S.; Pope, W. J., LXIII.—Enantiomorphism. *Journal of the Chemical Society, Transactions* **1898**, *73* (0), 606-617.
4. Matsuura, T.; Koshima, H., Introduction to chiral crystallization of achiral organic compounds Spontaneous generation of chirality. *Journal of Photochemistry and Photobiology C: Photochemistry Reviews* **2005**, *6* (1), 7-24.
5. Vogl, O., Chiral crystallization and the origin of chiral life on earth: Creation of Chirality. *Journal of Polymer Science Part A: Polymer Chemistry* **2011**, *49* (6), 1299-1308.
6. Akagi, K., Helical Polyacetylene Synthesized with a Chiral Nematic Reaction Field. *Science* **1998**, *282* (5394), 1683-1686.
7. Maeda, K.; Matsushita, Y.; Ezaka, M.; Yashima, E., Layer-by-layer assembly of charged poly(phenylacetylene)s with induced macromolecular helicity. *Chemical Communications* **2005**, (33), 4152.
8. Gautier, C.; Burgi, T., Chiral inversion of gold nanoparticles. *J Am Chem Soc* **2008**, *130* (22), 7077-84.
9. Ma, W.; Xu, L.; de Moura, A. F.; Wu, X.; Kuang, H.; Xu, C.; Kotov, N. A., Chiral Inorganic Nanostructures. *Chemical Reviews* **2017**, *117* (12), 8041-8093.
10. Mukhina, M. V.; Maslov, V. G.; Baranov, A. V.; Fedorov, A. V.; Orlova, A. O.; Purcell-Milton, F.; Govan, J.; Gun'ko, Y. K., Intrinsic Chirality of CdSe/ZnS Quantum Dots and Quantum Rods. *Nano letters* **2015**, *15* (5), 2844-51.
11. Moshe, A. B.; Szwarcman, D.; Markovich, G., Size dependence of chiroptical activity in colloidal quantum dots. *ACS Nano* **2011**, *5* (11), 9034-43.
12. Ben-Moshe, A.; Wolf, S. G.; Bar Sadan, M.; Houben, L.; Fan, Z.; Govorov, A. O.; Markovich, G., Enantioselective control of lattice and shape chirality in inorganic nanostructures using chiral biomolecules. *Nature communications* **2014**, *5*, 4302.
13. Duan, Y.; Liu, X.; Han, L.; Asahina, S.; Xu, D.; Cao, Y.; Yao, Y.; Che, S., Optically active chiral CuO "nanoflowers". *J Am Chem Soc* **2014**, *136* (20), 7193-6.
14. Lee, H. E.; Ahn, H. Y.; Mun, J.; Lee, Y. Y.; Kim, M.; Cho, N. H.; Chang, K.; Kim, W. S.; Rho, J.; Nam, K. T., Amino-acid- and peptide-directed synthesis of chiral plasmonic gold nanoparticles. *Nature* **2018**, *556* (7701), 360-365.
15. Simonyi, M.; Bikádi, Z.; Zsila, F.; Deli, J., Supramolecular exciton chirality of carotenoid aggregates: Supramolecular Exciton Chirality. *Chirality* **2003**, *15* (8), 680-698.
16. Ono, Y.; Nakashima, K.; Sano, M.; Kanekiyo, Y.; Inoue, K.; Shinkai, S.; Sano, M.; Hojo, J., Organic gels are useful as a template for the preparation of hollow fiber silica. *Chemical Communications* **1998**, (14), 1477-1478.
17. Marx, S.; Avnir, D., The Induction of Chirality in Sol–Gel Materials. *Accounts of Chemical Research* **2007**, *40* (9), 768-776.
18. Qiu, H.; Che, S., Chiral mesoporous silica: Chiral construction and imprinting via cooperative self-assembly of amphiphiles and silica precursors. *Chem. Soc. Rev.* **2011**, *40* (3), 1259-1268.

19. van Bommel, K. J. C.; Friggeri, A.; Shinkai, S., Organic Templates for the Generation of Inorganic Materials. *Angewandte Chemie International Edition* **2003**, *42* (9), 980-999.
20. Kelly, J. A.; Giese, M.; Shopsowitz, K. E.; Hamad, W. Y.; MacLachlan, M. J., The Development of Chiral Nematic Mesoporous Materials. *Accounts of Chemical Research* **2014**, *47* (4), 1088-1096.
21. Okazaki, Y.; Buffeteau, T.; Siurdyban, E.; Talaga, D.; Ryu, N.; Yagi, R.; Pouget, E.; Takafuji, M.; Ihara, H.; Oda, R., Direct Observation of Siloxane Chirality on Twisted and Helical Nanometric Amorphous Silica. *Nano letters* **2016**, *16* (10), 6411-6415.
22. Gao, X.; Han, B.; Yang, X.; Tang, Z., Perspective of Chiral Colloidal Semiconductor Nanocrystals: Opportunity and Challenge. *J Am Chem Soc* **2019**, *141* (35), 13700-13707.
23. Tanaka, H.; Inoue, Y.; Mori, T., Circularly Polarized Luminescence and Circular Dichroisms in Small Organic Molecules: Correlation between Excitation and Emission Dissymmetry Factors. *ChemPhotoChem* **2018**, *2* (5), 386-402.
24. Yan, J.; Feng, W.; Kim, J.-Y.; Lu, J.; Kumar, P.; Mu, Z.; Wu, X.; Mao, X.; Kotov, N. A., Self-Assembly of Chiral Nanoparticles into Semiconductor Helices with Tunable near-Infrared Optical Activity. *Chemistry of Materials* **2019**, *32* (1), 476-488.
25. Moxon, J. R. L.; Renshaw, A. R.; Tebbutt, I. J., The simultaneous measurement of optical activity and circular dichroism in birefringent linearly dichroic crystal sections. II. Description of apparatus and results for quartz, nickel sulphate hexahydrate and benzil. *Journal of Physics D: Applied Physics* **1991**, *24* (7), 1187-1192.
26. Bustamante, C.; Tinoco, I., Jr.; Maestre, M. F., Circular differential scattering can be an important part of the circular dichroism of macromolecules. *Proc Natl Acad Sci U S A* **1983**, *80* (12), 3568-72.
27. Ottaway, C. A.; Wetlaufer, D. B., Light-scattering contributions to the circular dichroism of particulate systems. *Archives of Biochemistry and Biophysics* **1970**, *139* (2), 257-264.
28. Robbie, K.; Broer, D. J.; Brett, M. J., Chiral nematic order in liquid crystals imposed by an engineered inorganic nanostructure. *Nature* **1999**, *399* (6738), 764-766.
29. Schellman, J. A., Circular dichroism and optical rotation. *Chemical Reviews* **1975**, *75* (3), 323-331.
30. Shopsowitz, K. E.; Qi, H.; Hamad, W. Y.; MacLachlan, M. J., Free-standing mesoporous silica films with tunable chiral nematic structures. *Nature* **2010**, *468* (7322), 422-5.
31. van Popta, A. C.; Sit, J. C.; Brett, M. J., Optical properties of porous helical thin films. *Appl Opt* **2004**, *43* (18), 3632-9.
32. Wu, T.; Li, G.; Kapitán, J.; Kessler, J.; Xu, Y.; Bouř, P., Two Spectroscopies in One: Interference of Circular Dichroism and Raman Optical Activity. *Angewandte Chemie International Edition* **2020**, *59* (49), 21895-21898.
33. Li, G.; Kessler, J.; Cheramy, J.; Wu, T.; Poopari, M. R.; Bouř, P.; Xu, Y., Transfer and Amplification of Chirality Within the "Ring of Fire" Observed in Resonance Raman Optical Activity Experiments. *Angewandte Chemie International Edition* **2019**, *58* (46), 16495-16498.
34. Bohren, C. F., Light scattering by an optically active sphere. *Chemical Physics Letters* **1974**, *29* (3), 458-462.
35. Awan, Z. A.; Seetharamdoo, D., Scattering characteristics of a metasurface covered chiral sphere. *Appl. Opt.* **2020**, *59* (19), 5670-5679.
36. Crassous, J.; Amon, A.; Crassous, J., Circular differential scattering of polarized light by a chiral random medium. *Physical Review A* **2012**, *85* (2), 023806.
37. Hu, T.; Hong, J., Anisotropic Effective Mass, Optical Property, and Enhanced Band Gap in BN/Phosphorene/BN Heterostructures. *ACS Applied Materials & Interfaces* **2015**, *7* (42), 23489-23495.

38. Iwata, M.; Teshima, M.; Seki, T.; Yoshioka, S.; Takeoka, Y., Bio-Inspired Bright Structurally Colored Colloidal Amorphous Array Enhanced by Controlling Thickness and Black Background. *Advanced Materials* **2017**, *29* (26), 1605050.
39. Takeoka, Y.; Yoshioka, S.; Takano, A.; Arai, S.; Nueangnoraj, K.; Nishihara, H.; Teshima, M.; Ohtsuka, Y.; Seki, T., Production of Colored Pigments with Amorphous Arrays of Black and White Colloidal Particles. *Angewandte Chemie International Edition* **2013**, *52* (28), 7261-7265.
40. Delclos, T.; Aimé, C.; Pouget, E.; Brizard, A.; Huc, I.; Delville, M.-H.; Oda, R., Individualized Silica Nanohelices and Nanotubes: Tuning Inorganic Nanostructures Using Lipidic Self-Assemblies. *Nano letters* **2008**, *8* (7), 1929-1935.
41. Okazaki, Y.; Cheng, J.; Dedovets, D.; Kemper, G.; Delville, M.-H.; Durrieu, M.-C.; Ihara, H.; Takafuji, M.; Pouget, E.; Oda, R., Chiral Colloids: Homogeneous Suspension of Individualized SiO₂ Helical and Twisted Nanoribbons. *ACS Nano* **2014**, *8* (7), 6863-6872.
42. Sugiyasu, K.; Tamaru, S.-i.; Takeuchi, M.; Berthier, D.; Huc, I.; Oda, R.; Shinkai, S., Double helical silica fibrils by sol-gel transcription of chiral aggregates of gemini surfactants. *Chemical communications* **2002**, (11), 1212-1213.
43. Hohenester, U.; Trügler, A., MNPBEM – A Matlab toolbox for the simulation of plasmonic nanoparticles. *Computer Physics Communications* **2012**, *183* (2), 370-381.
44. Palik, E. D., *Handbook of Optical Constants of Solids*. 1985; Vol. 1.

Chapter 4. Optically active perovskite nanocrystals helically arranged on inorganic silica helical ribbons

Chapter 4. Optically active perovskite nanocrystals helically arranged on inorganic silica helical ribbons

1. Introduction.....	81
2. Synthesis of perovskites nanocrystals.....	83
2.1 Synthesis at high temperature	84
2.2 Synthesized at room temperature	85
3. In-situ growth of CsPbBr ₃ nanocrystals on the surface of silica helical ribbons.....	86
4. PNCs grafted on the silica helical ribbons by ligands exchange method	90
4.1 Results in suspension	91
4.1.1 PNCs prepared at low temperature with silica helical ribbons.....	91
4.1.2 PNCs prepared at high temperature with silica helical ribbons	96
4.2 Results in drying state	102
4.2.1 Solvent evaporation temperature effect	106
4.2.2 The kinetic drying effect of the PNCs-silica helical ribbons.....	113
4.2.3 Temperature stability	116
4.2.4 Theoretical simulation	118
5. CONCLUSION.....	119
6. Experiment section.....	121
6.1 Materials and instruments	121
6.2 CsPbBr ₃ perovskites nanocrystals (PNCs) prepared at room temperature	122
6.3 In-situ growth of CsPbBr ₃ on the surface of silica helical ribbons	122
6.4 CsPbBr ₃ perovskites nanocrystals (PNCs) prepared at high temperature.....	123
6.5 Grafting of CsPbBr ₃ PNCs on the surface of silica helical ribbons by ligand exchange methods.....	124
6.6 Coupled dipole method simulation.....	125
7. Reference	128

Chapter 4. Optically active perovskite nanocrystals helically arranged on inorganic silica helical ribbons

1. Introduction

Perovskite nanocrystals (PNCs) show outstanding optoelectronic properties^{1, 2} which have great promising applications in lighting, light-emitting diodes (LEDs)^{3, 4}, and solar cells^{5, 6} in response to the demands for energy and the concerns of global warming and climate change. Recently, the optically active properties of semiconductor nanocrystals (SNCs) have attracted large attention due to the outstanding properties of SNCs and prospective applications in chiral separation and recognition, chiral catalysis, and 3 D display technologies.⁷⁻⁹ Generally, there are four ways to endow chirality to SNCs: i) Combination with chiral ligands;^{10, 11} ii) chiral shape of the individual NC;¹² iii) formation of a chiral lattice;¹³ and iv) chiral arrangement in the presence of chiral building blocks.^{14, 15} In the past decades, SNCs with chiral ligands have been widely reported for the induction of circular dichroism (CD) signals,¹⁶⁻¹⁹ whereas a much more limited number of reports can be found for the induction of circularly polarized luminescence (CPL)^{20, 21} due to the lower photoluminescence quantum yield (PLQY) after ligand exchange.²²⁻²⁴ Core-shell structure SNCs could boost the PLQY, but the outer shell decreases the chirality induction resulting in a lower dissymmetric g-factor.²⁵ The typical absorption and luminescence dissymmetric factors (g) were reported in the range of 10^{-5} to 10^{-3} . Only with the chiral lattice of HgS SNCs synthesized with chiral ligands, dissymmetric factors as large as 10^{-2} was achieved.²⁶ From the chiral lattice formation or chiral shape of SNCs, only induced CD (ICD) and no induced CPL (ICPL) were reported so far.

SNCs could be self-organized directly into chiral superstructure driven by chiral ligands, oxidation, pH controlling, or under circularly polarized light illumination.²⁷⁻²⁹ SNCs self-organization could also happen with chiral organic molecular self-assembly as soft templates, big CPL could be observed.^{14, 15} However, such SNCs chiral self-organization could be easily destroyed by changing the temperature due to the

fragile nature of the organic molecular self-assembly. Inorganic chiral templates offer more robust and promising alternatives. For example, Che reported chirality introduction by metal ions or metal oxides chiral arrangement with the chiral mesoporous silica due to molecular imprinting.³⁰ In our previous work,^{31, 32} gold nanoparticles electrostatically adsorbed or covalently grafted on the surface of silica helical ribbons also showed strong CD signals from their plasmonic resonance. The constituents of these systems were inorganic, allowing them to be dispersed in a large range of solvents, withstand drying, and be organized by the flow induction, enhancing the optical properties of the system.

In this chapter, perovskite CsPbBr_3 nanocrystals (PNCs) and pure enantiomer (right- or left-handed) inorganic silica helical ribbons are chosen for the study of the inorganic building block. First, the surface of silica helical ribbons is modified with amine by 3-aminopropyl-triethoxysilane (APTES). Then the PNCs are grafted on the surface of silica helices by the in-situ growth method or ligand exchange method. The grafted PNCs-silica helical ribbons in suspension show three results according to different conditions. 1) The PNCs grafted on silica helical ribbons do not show any observable CD signals or CPL signals due to the randomly arranged of PNCs in suspension. 2) After the incubation, the grafted PNCs grow by oriented attachment results in chiral arrangement or chiral surface due to the cylindrical curvature of silica helical ribbons, which shows small mirror-image CD signals. 3) Further growth of PNCs for full coverage on the silica surface, strong linear dichroism (LD) dominates due to the strong alignment of PNCs with silica helical ribbons. In suspension, the first result was mostly obtained. However, surprisingly strong CD and CPL signals are observed after the suspension of helical ribbons with PNCs is drop cast to create a dry film. The organization of the PNCs on the silica helical ribbons both in dried film and in suspension, are evaluated with grazing incidence X-ray scattering (GIXS), tomography electron microscopy, and cryo-EM. Closely packed and helically arranged PNCs are observed for the dried film whereas loosely attached PNCs with much less coherent periodic organization likely due to the ligand solvation was observed for the solvated silica helical ribbons. Simulations based on the coupled

dipole method (CDM), demonstrate that the CD is related to the dipolar interaction between PNCs assembled into a chiral structure. These results indicate that closely packed and helically arranged PNCs on the silica helical ribbons formed during the drying process lead to the strong optically active properties in the film state whereas optically active properties are not observable for the solvated loosely packed PNCs with larger mean distances on helical ribbons as the electromagnetic interaction between PNCs fades away quickly with the inter-particle distances. Such observation can help to achieve optically active functional materials with an all-inorganic building block system. The temperature stability of the PNCs-silica helical ribbons film has also been evaluated. The CD dissymmetric g-factor is unchanged upon heating to 80 °C.

2. Synthesis of perovskites nanocrystals

Nanocrystals synthesis approaches could be broadly classified into two categories: “top-down” and “bottom-up”. Top-down routes comprise of fragmentation and structuring of macroscopic solids, such as ball-milling³³ or chemical exfoliation³⁴. The bottom-up strategies start with molecules and ions and proceed *via* gas- or liquid-phase chemical reactions. For the perovskite nanocrystals synthesis, the bottom-up liquid-phase approach is the best way for the fabrication of high-quality colloidal PNCs.³⁵ The most two developed liquid-phase methods for the PNCs synthesis are the hot injection (HI) method and the ligand-assisted re-precipitation (LARP) method. In short, the HI method requires high temperatures and an inert atmosphere which increases the cost and limits the scale-up synthesis.² The LARP method could overcome these two limitations with the cost-effective alternative in an ambient atmosphere at room temperature.¹ However, the LARP method suffers from poor optical properties and stability due to the polar solvent used during the synthesis process.

2.1 Synthesis at high temperature

The first HI method was developed for the synthesis of cadmium chalcogenide NCs. Typically, one precursor is injected rapidly into a hot solution of another precursor, ligands, and a high boiling solvent. The NCs' size, size distribution, crystal structure, composition, and shape could be controlled by the ratio of surfactants to the precursors, the injection temperature, the reaction time, and also the concentration of precursors. All-inorganic or hybrid PNCs (CsPbX_3 , hybrid MAPbX_3 , FAPbX_3 ; $\text{X} = \text{Cl}$, Br , I , or their mixture) could be prepared by the HI method. Typically, for the synthesis of CsPbBr_3 , as shown in Figure 4-1 (a), the hot solution (solvent, ligands, and PbBr_2) was degassed and with nitrogen flow to get inert atmosphere, then the precursor Cs-oleic acid was injected rapidly, after 5 seconds growth, the solution was cooled down with ice-water bath.² As shown in Figure 4-1 (b), the CsPbBr_3 NCs show good size distribution with around 8 nm. In addition, the bandgap could be tuned by the size and composition of halide, as shown in Figure 4-1 (c), the PNCs solution shows different emission colors under a UV lamp at 365 nm. The HI method results in high-quality PNCs with narrow size distribution, high photoluminescence quantum yield (PLQY), and stability. However, the HI method needs high temperature and an inert atmosphere requires heating mantle, vacuum system, and nitrogen which increasing the cost. Besides, it is hard to scale up the synthesis because the large quantities of the injected precursor at a high temperature result in a remarkable drop in the temperature and also inhomogeneous nucleation.

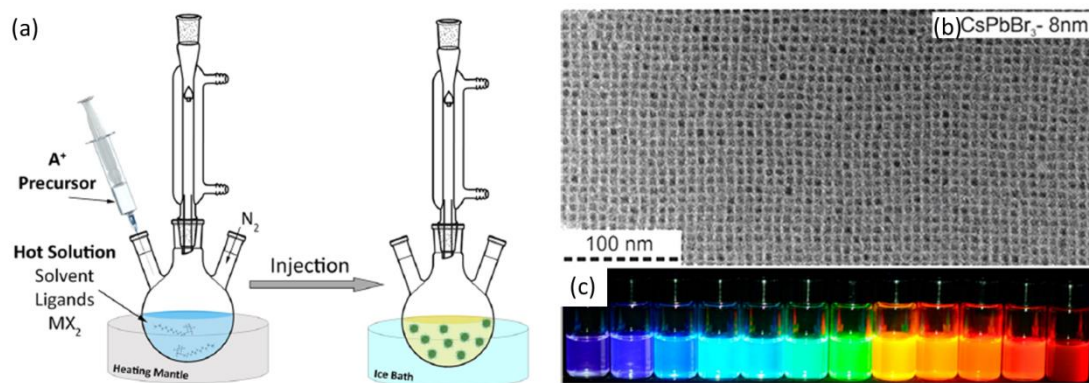


Figure 4-1. Sketch of the HI method used for the synthesis of colloidal PNCs. (b) a typical TEM image of CsPbBr₃ NCs obtained with the HI method. (c) Colloidal PNCs with different sizes and halide composition in toluene solvent under a UV lamp with 365 nm.

2.2 Synthesized at room temperature

The supersaturated recrystallization process consists of dissolving the desired ions in a solvent with an equilibrium concentration; the equilibrium state could be broken to reach a supersaturated state by decreasing the temperature, evaporating the solvent, or adding a miscible co-solvent decreasing the solubility of the ions. If this process contains ligands as shown in Figure 4-2 (a), it is called “ligand-assisted reprecipitation” (LARP). Colloidal NCs could be synthesized with different sizes and also different halide compositions.¹ As shown in Figures 4-2 (b-c), the LARP method synthesized PNCs shows tunable absorption and emission spectra by tuning their size and halide composition. This LARP method could be operated at room temperature under an air atmosphere. Also, it can scale up synthesis easily, which can overcome the drawback of HI methods. As it is well known, the PNCs are very sensitive to polar solvents. Polar solvents such as DMF, DMSO are normally used in the LARP method which can easily degrade and even dissolve the PNCs result in poor optical properties and stability.

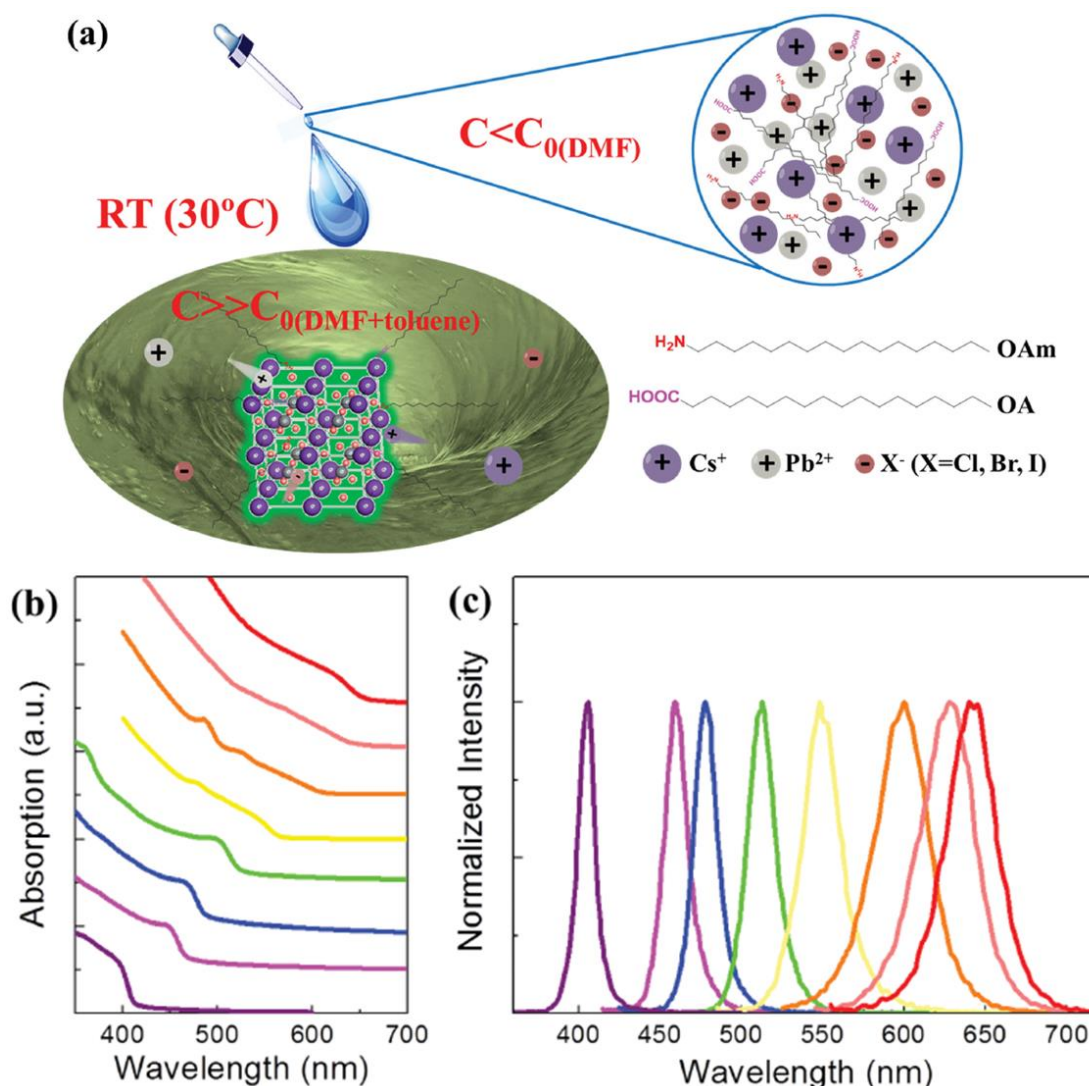


Figure 4-2. (a) The schematic of the LARP method used for the synthesis of PNCs at room temperature. The normalized absorption spectrum (b) and emission spectrum (c) of PNCs synthesized with different halide compositions.

3. In-situ growth of CsPbBr_3 nanocrystals on the surface of silica helical ribbons

PNCs can be synthesized by the ligand-assisted reprecipitation method, the ligand is oleic acid (OA) and oleylamine (OLA) as shown in Figure 4-3 upward picture. Also, the carboxyl and amine ligands could be tuned with different lengths and configurations.³⁶ Interestingly, our silica helical ribbons could be modified with APTES which is a kind of amine ligand, and the APTES amine ligand could be used

in the PNCs synthesis^{37, 38}. So the amine-modified silica helical ribbons could play as a kind of amine ligand (helix amine ligand) for the PNCs synthesis. If the ligand of initial amine oleylamine, is partially or completely replaced by a helix amine ligand as shown in Figure 4-3 downward picture, the PNCs would grow on the surface of silica helical ribbons. In this way, the PNCs could be in-situ grown on the surface of silica helical ribbons.

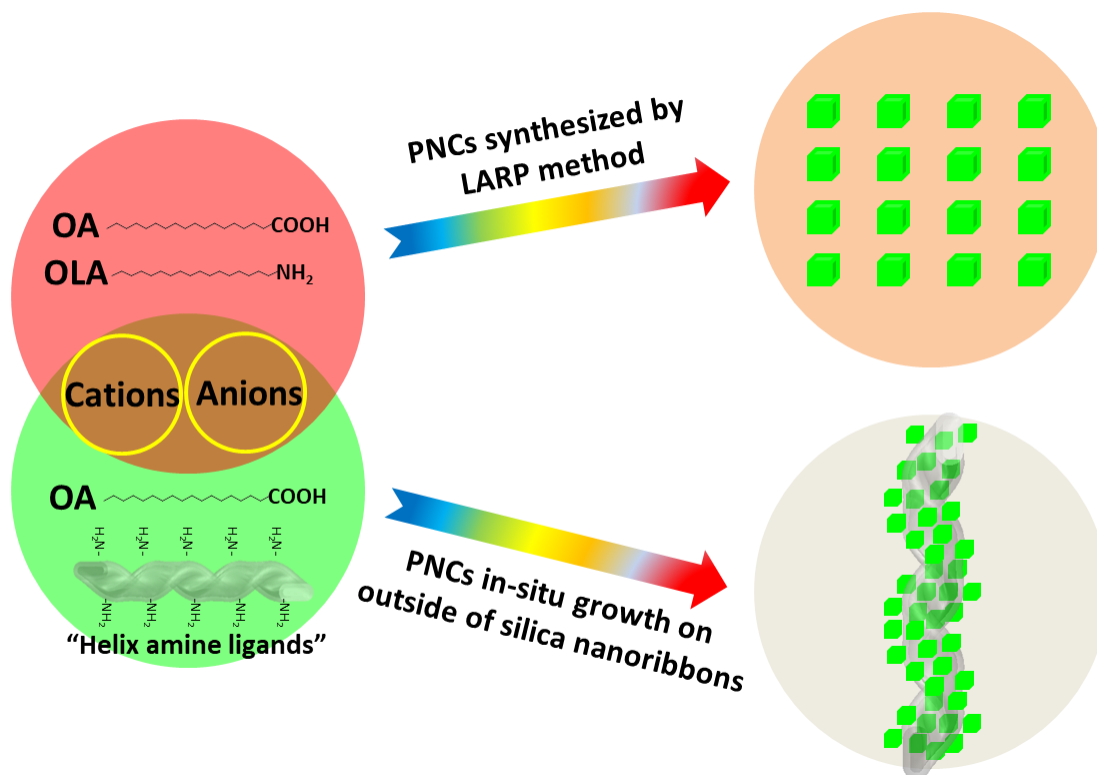


Figure 4-3. Schematic of the PNCs synthesis and PNCs in-situ growth on the surface of silica helical ribbons

Firstly, the CsPbBr₃ PNCs were synthesized by the LARP method and the TEM image shows PNCs have a cubic shape with a size around 10.5 nm as shown in Figure 4-4 (a). When oleylamine were replaced by helix amine ligand and no extra amine added, some PNCs could be grown only on the surface of silica helical ribbons due to the silica ribbons surface amine could be acted as a ligand as shown in Figure 4-4 (b). However, the in-situ growing PNCs have a large size distribution with inhomogeneous shapes. In addition, the density of surface PNCs on the silica helical ribbons is quite low indicating that fewer PNCs were synthesized due to the lack of

extra amine ligand to act as the important ligand binding PNCs and silica ribbons surface. To obtain better results of in-situ growing PNCs on the surface of silica helical ribbons, an extra amine ligand was added. The ions with OA, helix amine ligand, and APTES mixture were injected into toluene solution, PNCs also grow on the surface of silica helical ribbons as shown in Figures 4-4 (c-f). With extra amine APTES increasing, the size of PNCs is decreased which is consistent with the previous report.³⁸ The PNCs are well growing on the surface of silica helical ribbons, while no observed CD could be detected as shown in Figure 4-5 (a). It should be noted that the in-situ grow method results in PNCs in-situ growth on surface of silica helical ribbons and also some un-grafted PNCs with larger sizes. It is hard to separate the free large size of PNCs and PNCs-silica helical ribbons. The turbid suspension shows strong scattering absorption spectra and the emission spectra which exhibits blue shift with increasing the addition of extra APTES as shown in Figure 4-5 (b). The inset pictures show the PNCs-silica helical ribbons in toluene under natural light and a UV lamp at 365 nm.

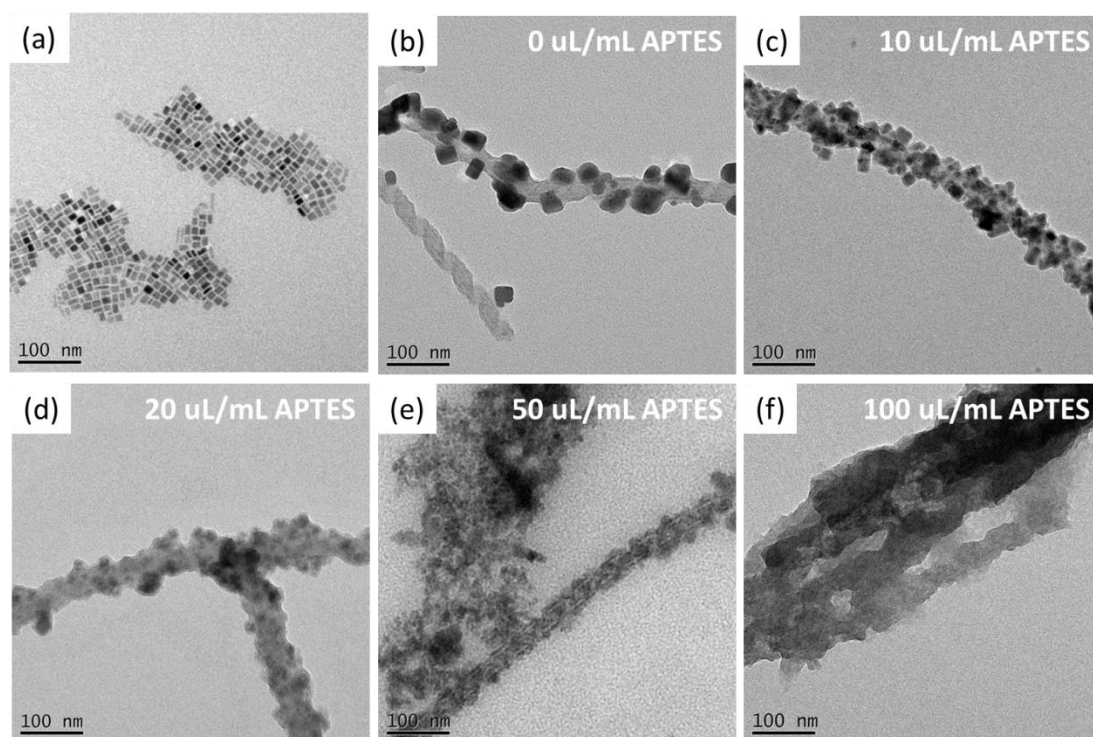


Figure 4-4. The TEM images of CsPbBr₃ NCs (a) and CsPbBr₃ NCs in-situ growth on the surface of silica helical ribbons (b-f) with different amounts of additional amine APTES adding.

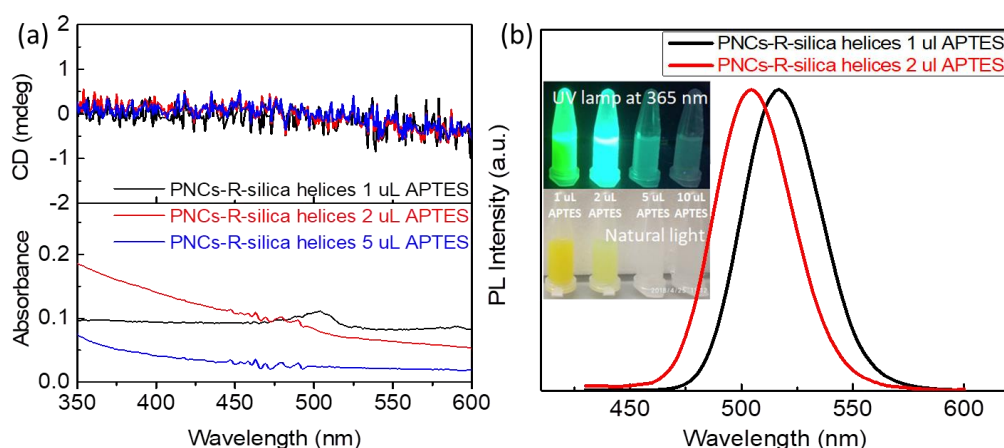


Figure 4-5. (a) CD and absorption spectra of PNC in-situ growth on the surface of right-handed silica helical ribbons with different APTES adding. (b) The photoluminescence of PNCs in-situ growth on the surface of right-handed silica helical ribbons. Inset pictures show the PNCs-R-silica helical ribbons solution irradiation under a UV lamp at 365 nm or natural light with different APTES adding.

With extra APTES adding, the PNCs have better grown on the surface of silica helical ribbons. Another amine ligand oleylamine is also applied as shown in Figure 4-6. With the different amounts of OLA adding, the PNCs are also well grown on the surface of silica helical ribbons, however, still, no CD signals were observed.

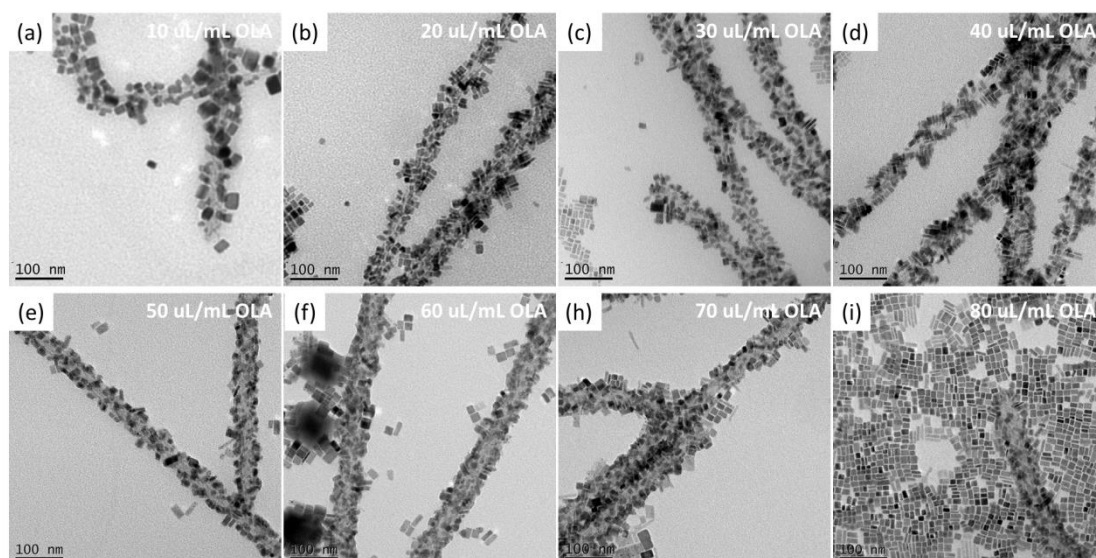


Figure 4-6. TEM images of PNCs in-situ growth on the surface of silica helical ribbons with different OLA adding (a-i).

The in-situ growth of PNCs on the silica helices is a very effective way for the binding of PNCs and silica helical ribbons, while no chirality induction is observed. The grafted PNCs exhibit inhomogeneous size and shape which might hinder their helical alignment. To align the PNCs on the surface of silica helical ribbons, the easiest way is the nanocrystals oriented attachment which has been widely studied in the past several decades.³⁹⁻⁴³ Oriented attachment involves the spontaneous self-organization of adjacent nanocrystals, resulting in crystal growth by the addition of solid particles that share a common crystallographic orientation. The PNCs oriented attachment can happen due to their strong ionic nature.⁴⁴⁻⁴⁶ How to realize the PNCs helical organized on the surface of silica helical ribbons would be the key factor for the chirality induction.

4. PNCs grafted on the silica helical ribbons by ligands exchange method

Inspired by the oriented attachment, the combination way between PNCs and silica helical ribbons was modified. The surface of colloidal nanocrystals is covered with ligands that are in equilibrium with those in the solution.⁴⁷ The PNCs in toluene suspension as used in this study are covered with two types of ligands: oleic acid (bound to cations of Cs or Pb) and oleylamine (bound to halide anions). This bonding between ligands and PNCs also shows a dynamic equilibrium as depicted in Figures 4-7 (a) and (b). When the synthesized PNCs (Figure 4-8 (a)) and amine-modified silica helical ribbons (Figure 4-8 (b)) were mixed, the PNCs could be grafted homogeneously on the surface of silica helical ribbons as shown in Figures 4-8 (c). This is likely due to the ligands exchange between the oleylamine and “helix amine ligands” as shown in Figures 4-7 (b-d). The ligands exchange method needs to purify the PNCs before mixed with amine-modified silica helical ribbons. The purification of PNCs will remove the free ligands and also reduce partial surface bonding ligands which will benefit the PNCs grafting by ligand exchange method. In addition to the

surface bonding, ligands reduction will facilitate the oriented attachment of PNCs. Hence, this ligand exchange method is more suitable for the PNCs oriented attachment.

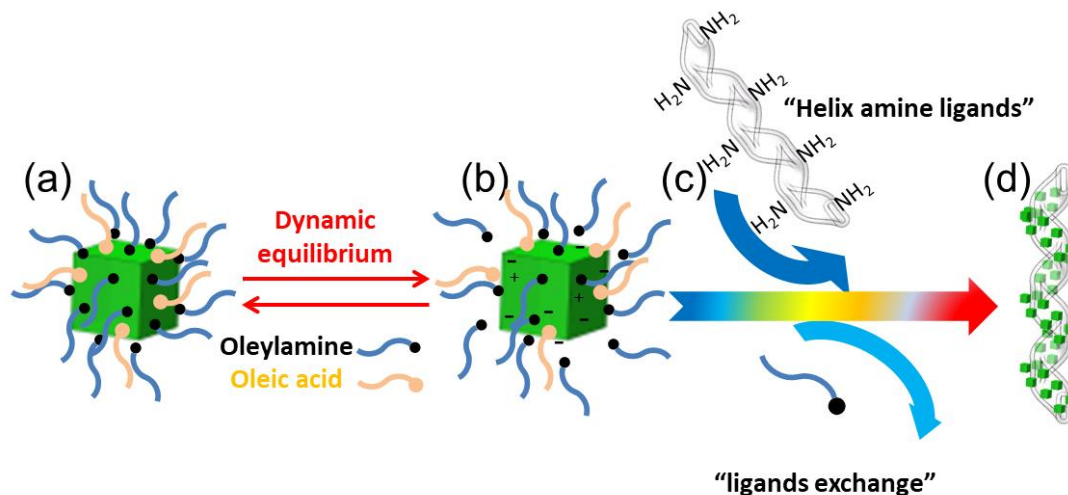


Figure 4-7. Scheme of the ligands exchanges grafting method as discussed in the text.

4.1 Results in suspension

4.1.1 PNCs prepared at low temperature with silica helical ribbons

Figure 4-8 (a) shows the TEM image of PNCs synthesized by the LARP method after purification and size separation. As shown in Figure 4-8 (a) inset picture, the average size of PNCs is around 10.5 nm. The purified PNCs show a strong absorption peak at around 475 nm but do not show any CD signals which indicate achiral PNCs (Figure 4-2 (d)). After grafting by ligand exchange method, homogeneous grafting is observed as shown in Figure 4-8 (c). While no CD signals were observed and the absorption peak shows a little red shift at around 490 nm (Figure 4-9 (e)). The absorption peak redshift (15 nm) might be caused by two possible factors; One is the decrease inter-distance of two adjacent PNCs after grafting on the silica helical ribbons results in strong exciton coupling; Another is the PNCs size increased due to the oriented attachment. While no CD was observed, the redshift might be due to the exciton coupling between two closed PNCs.

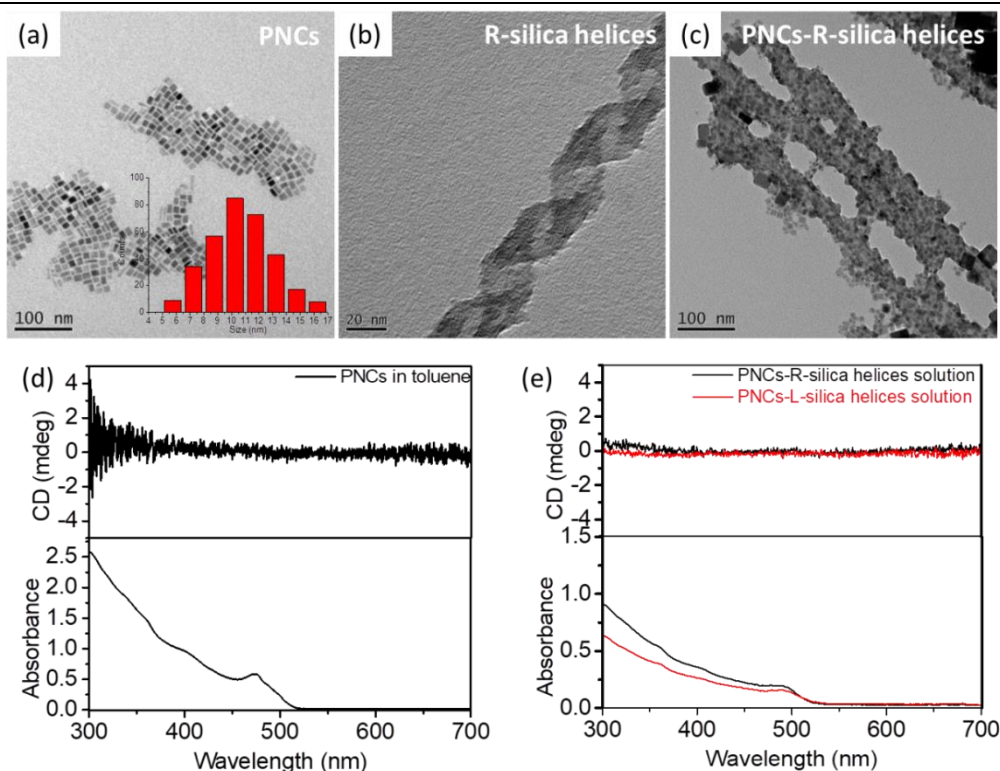


Figure 4-8. (a) TEM image of PNCs synthesized with LARP method. The inset picture shows the size distribution spectra of PNCs. (b) TEM image of typical right-handed silica helical ribbons. (c) TEM images of PNCs-R-silica helical ribbons with ligands exchange grafting method. CD and absorption spectra of PNCs in suspension (d) and PNCs-R/L-silica helical ribbons in suspension (e).

With the experiment repeating, different results were observed as shown in Figure 4-9 (a). The PNCs with right- or left-handed silica helical ribbons show small mirror CD images, and also the absorption peak has a bigger redshift (27 nm) compared with the PNCs before grafting. It should be noticed that the LD is less than 10^{-3} which shows negligible effects on the CD measurement (Figure 4-9 (b)). The PNCs size is bigger than before grafting as shown in Figures 4-9 (c-d). Figure 4-9 (e) shows the size distribution of the PNCs with an average size around 13.5 nm after grafted on the silica helical ribbons. The PNCs volume can be approximately calculated by the cube of the cubic length. Before grafting and after grafting, the volume is 10.5^3 (1157) nm^3 and 13.5^3 (2460) nm^3 separately. The volume of PNCs after grafting is almost double of the PNCs before grafting which indicates two isolated PNCs oriented attachment

happened. The observed mirror CD images are supposed to be the helical alignment of PNCs on the surface of silica helical ribbons due to the adjacent PNCs oriented attachment.

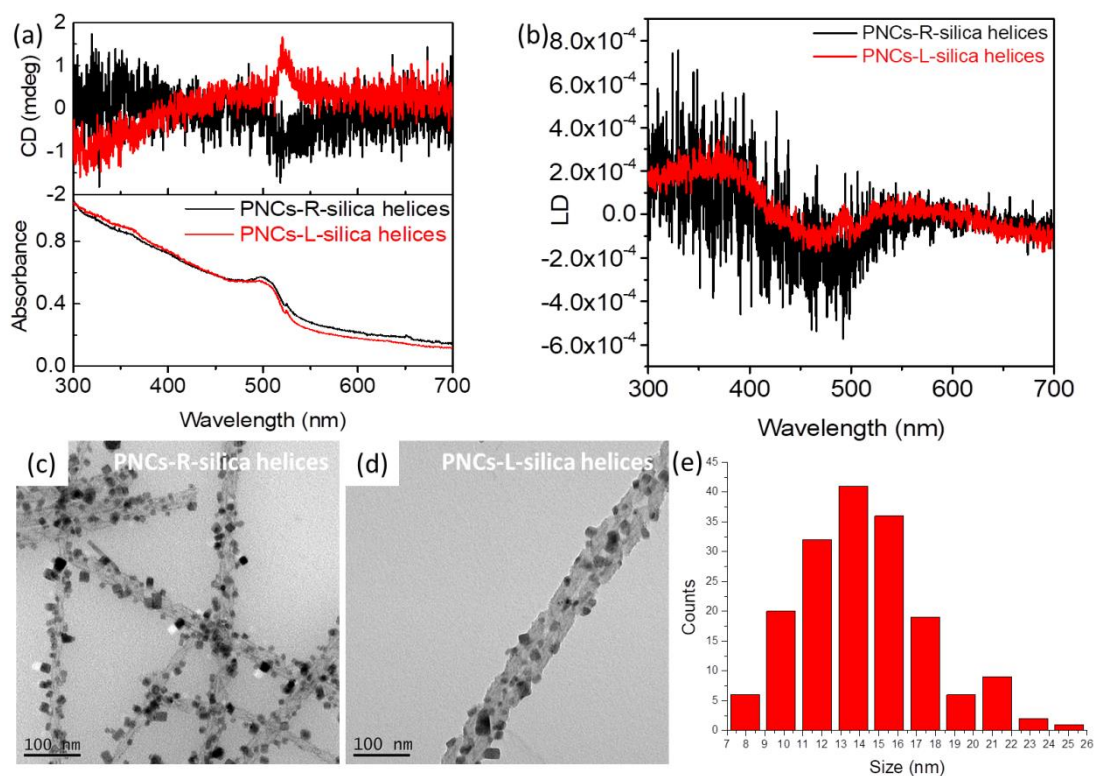


Figure 4-9. CD and absorption spectra (a), LD spectra (b) of PNCs-R/L-silica helical ribbons solution. TEM images (c), (d), and grafted PNCs size distribution (e) of PNCs-R/L-silica helical ribbons.

To understand what happened for the mixture of PNCs and silica helical ribbons, the CD and absorption spectra were monitored for the aged mixture of the purified PNCs toluene solution and amine-modified silica helical ribbons. Firstly, the CD and absorption spectra of PNCs toluene solution were measured. After aging for 10 mins, 20 μ g silica helical ribbons were added to the PNCs solution, the CD and absorption spectra were measured every half an hour. As shown in Figures 4-10 (a) and (d), before adding silica helical ribbons, no CD was observed at 520 nm. After adding silica helical ribbons, still no CD was observed in the first one hour. After that, negative CD signal appeared for right-handed silica helical ribbons and positive CD

signal appeared for left-handed silica helical ribbons. Also as shown in Figures 4-10 (b) and (e), the shoulder absorption peak at around 510 nm appeared when the CD appeared. The shoulder absorption peak corresponds to the increased PNCs size which is supposed to be the oriented attachment of adjacent PNCs after grafted on the surface of silica helical ribbons. The NCs oriented attachment results in large size while lower NCs molar concentration which decreases the absorbance.^{48, 49} This is consistent with our observed results as shown in Figures 4-10 (b) and (e). Figures 4-10 (c) and (f) show the CD peak values evolution with time. After around 2 h, the CD peak values are saturated indicates the grafted PNCs oriented attachment finished. On the other hand, the absorption spectra are still decreased with time, which might be due to the free PNCs oriented attachment happened slowly.

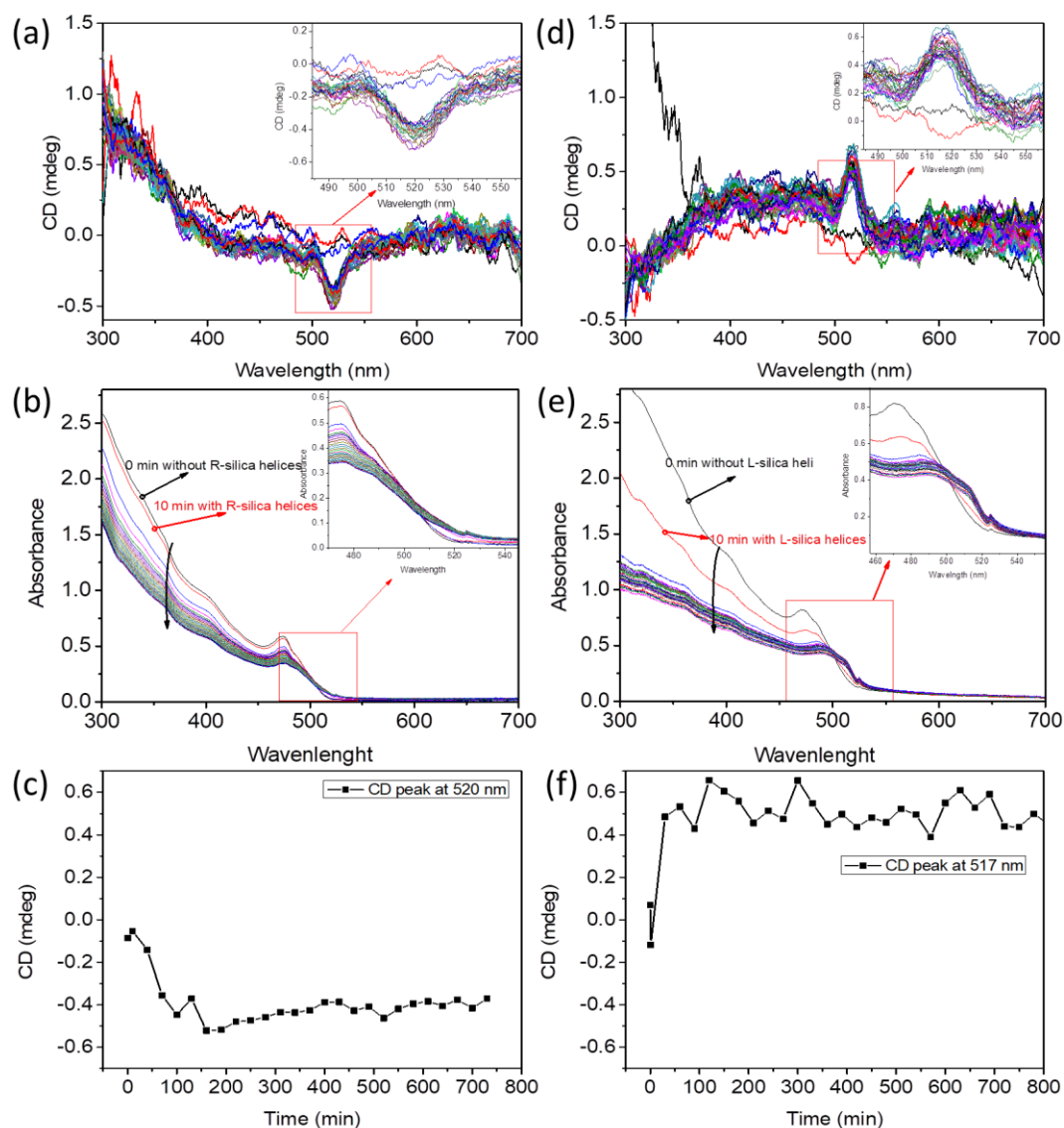


Figure 4-10. Time course of CD (a) and absorption (b), and CD peak at 520 nm spectra (c) of PNCs mixed with right-handed silica helical ribbons. Time course of CD (d) and absorption (e), and CD peak at 520 nm spectra (f) of PNCs mixed with left-handed silica helical ribbons.

In general, PNCs grafted on the silica helical ribbons prepared by the LARP method show two kinds of results in suspension. No CD signals were observed for the PNCs-R/L-silica helical ribbons with small absorption peak redshifted (without oriented attachment), while mirror CD images were detected for the samples with bigger absorption peak redshifted (with oriented attachment). However, PNCs suffers

poor optical properties and stability prepared by the LARP method. It would be interesting to study the PNCs prepared at high temperatures combined with silica helical ribbons.

4.1.2 PNCs prepared at high temperature with silica helical ribbons

Firstly, the PNCs was prepared at high temperature and purified with ethyl acetate and acetonitrile. The TEM image shows good quality of PNCs with a uniform size around 8.8 nm as shown in Figures 4-11 (a-c). As it is well known that the PNCs purification process will decrease the surface of the bonding ligand which results in lower stability.^{50, 51} The fewer surface ligands of PNCs will facilitate the PNCs grafting and oriented attachment. The PNCs were first washed with ethyl acetate to remove unreacted precursors and high boiling solvent. After that, the PNCs were washed with acetonitrile once labeled as 1 PNCs and washed with acetonitrile twice labeled as 2 PNCs. As shown in Figures 4-12 (a) and (b), the purified PNCs 1 and 2 grafted on the silica helical ribbons both show mirror CD images. All the LD values are less than 10^{-3} with negligible effect on CD. Also, the absorption peaks show a big redshift corresponding to the oriented attachment of PNCs.

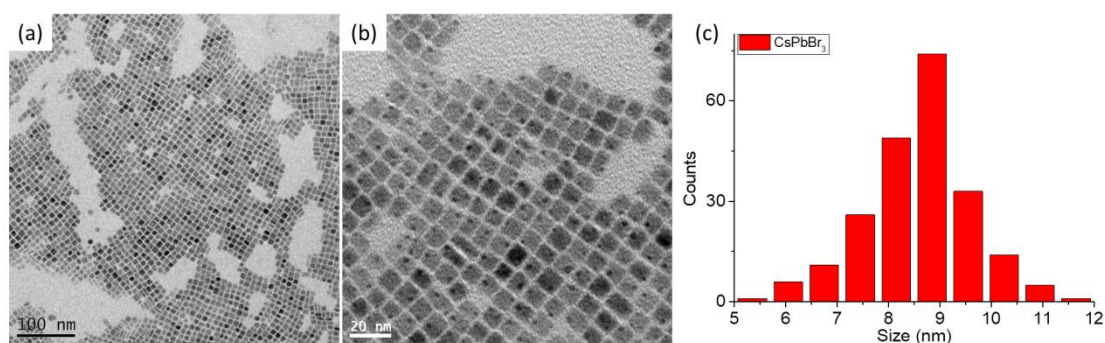


Figure 4-11. (a) and (b) TEM images of PNCs with different magnification. (c) the size distribution of PNCs.

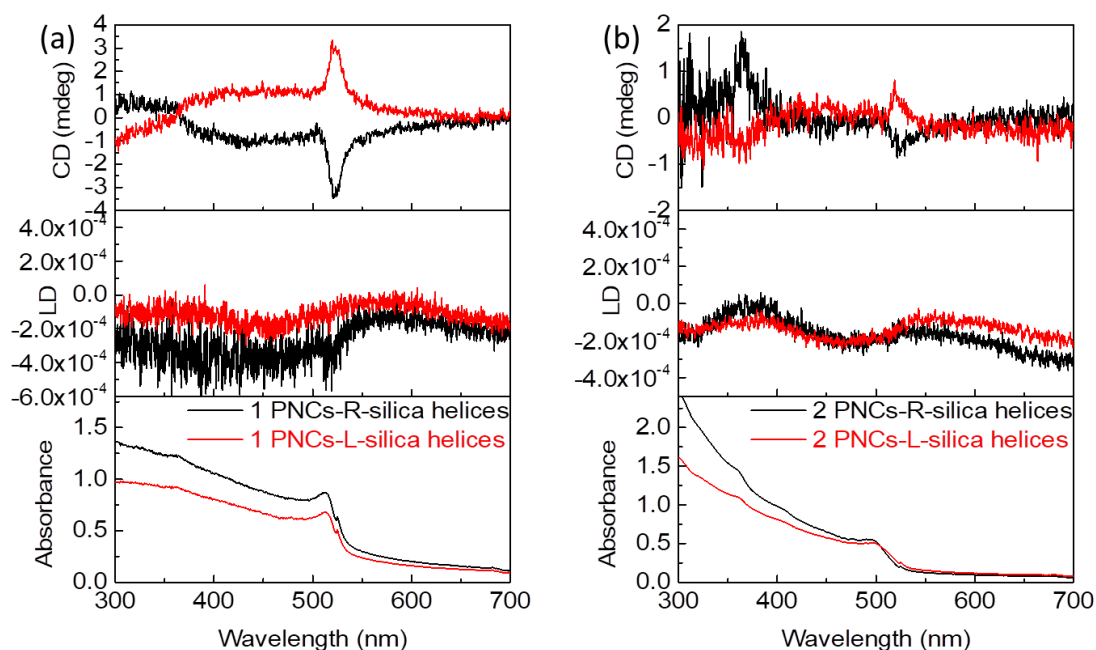


Figure 4-12. CD, LD and absorption spectra of PNCs washed with acetonitrile once grafted on the surface R/L-silica helical ribbons (a) and PNCs washed with acetonitrile twice grafted on the surface R/L-silica helical ribbons (b).

With different purification times, different morphologies of PNCs-silica helical ribbons were observed as shown in Figures 4-13 (a-d). Interestingly, after grafted on the surface of silica helical ribbons, the isolated 1 PNCs show big size, while the 2 PNCs show the smaller size and look like smeared on the surface of silica helical ribbons. As shown in Figures 4-12 (a-b), 1 PNCs-silica helical ribbons absorption peak shows a bigger redshift compared with 2 PNCs. Also, the big and isolated 1 PNCs look like merged on the surface of silica helices which results in cylindrical curvature face of PNCs. The curvature shape of PNCs might be another possible mechanism that leads to the mirror CD images. The 2 PNCs show high-density grafting and look smeared on the surface of silica helical ribbons. However, it shows smaller CD signals compared with 1 PNCs, this might be due to the almost full coverage of silica helical ribbons behaving as nanowire which weaken the PNCs chiral arrangement. Furthermore, the 1 and 2 PNCs-R/L-silica helical ribbons do not show any CPL signals.

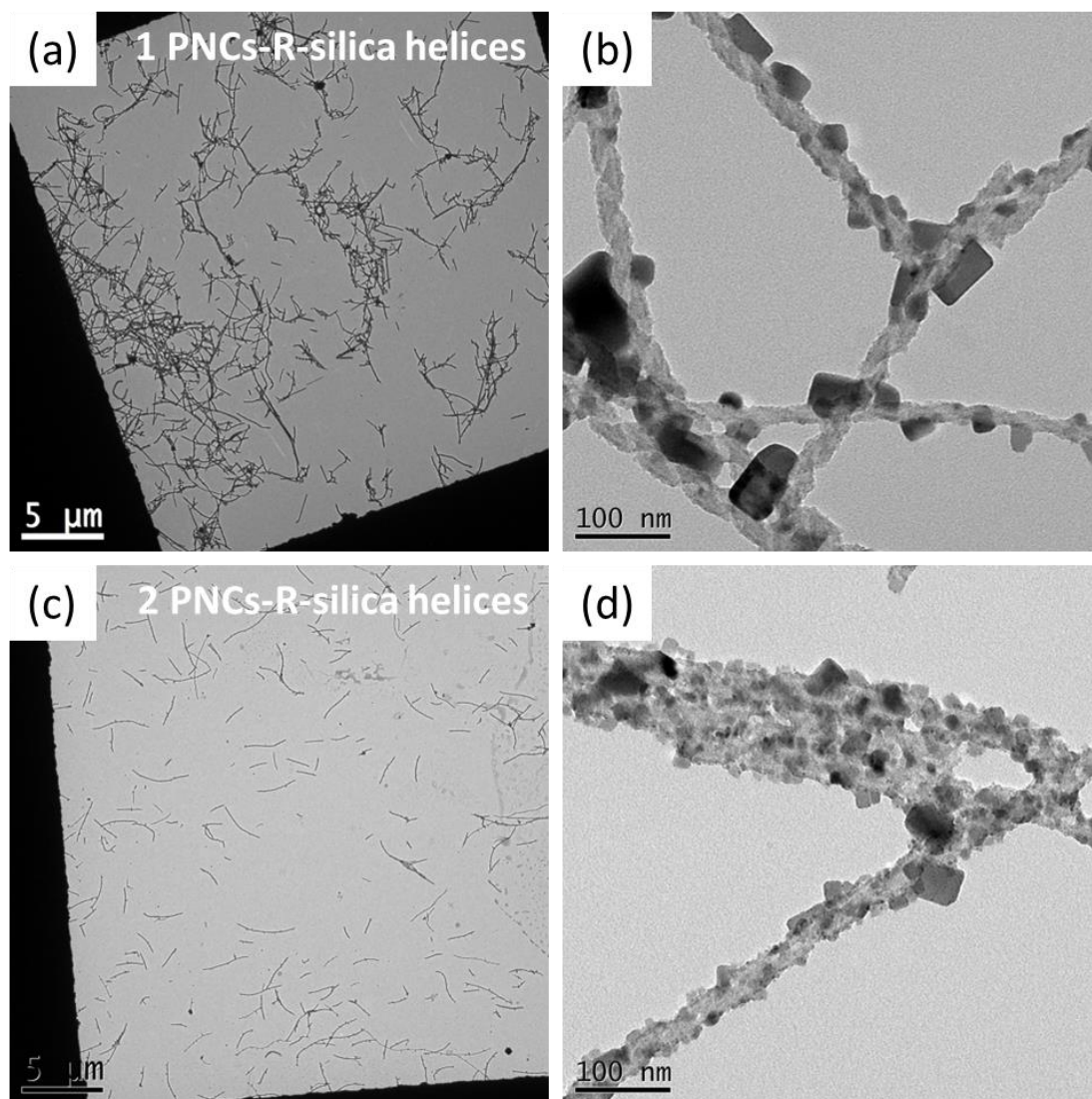


Figure 4-13. TEM images of PNCs washed with acetonitrile once grafted on the surface R/L-silica helical ribbons (a) and PNCs washed with acetonitrile twice grafted on the surface R/L-silica helical ribbons (b).

To understand how the oriented attachment of PNCs affects the induced chirality, the experiments are repeated. However, different and intriguing results were observed as shown in Figures 4-14 (a-b). Stronger but always same shapes of CD spectra were detected for PNCs-R/L-silica helical ribbons. Also, CPL signals always show strong and negative signals for both right- and left-handed samples. The TEM image shows more smeared grafting and is very similar to the 2 PNCs-silica helical ribbons discussed above as shown in Figure 4-14 (c). Also, the CD shapes are similar to the 2 PNCs-R-silica helical ribbons with a negative CD peak at 522 nm and a positive peak

at 365 nm. The strong but same shape of CD and CPL signals are supposed to be affected by the LD. Indeed, they show big LD with 10^{-2} which is 10 times bigger than before.

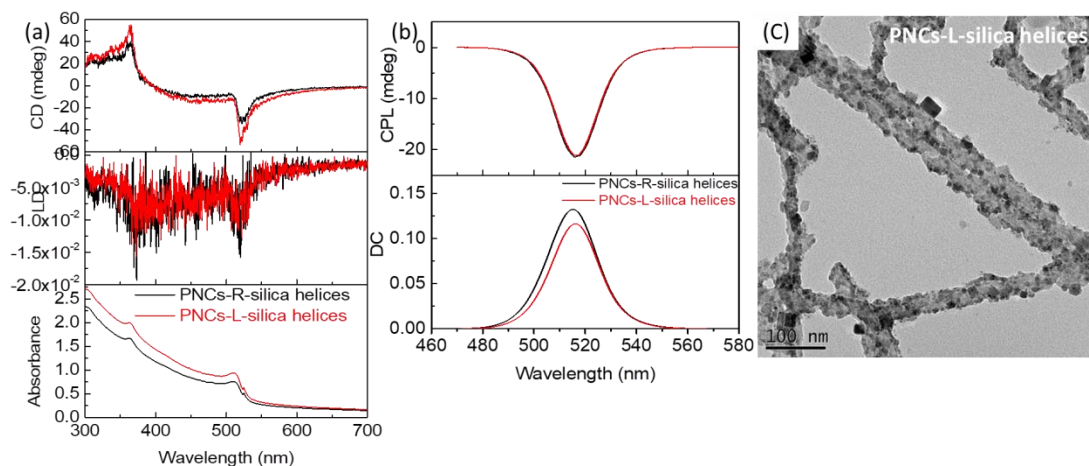


Figure 4-14. CD, LD, and absorption spectra (a) and CPL, DC spectra (b) of PNCs-R/L-silica helical ribbons in toluene solution. (c) TEM image of PNCs-L-silica helical ribbons.

The apparent CD and CPL signals might be affected by the LD. But based on our best knowledge, the LD with 10^{-2} is impossible to result in such strong CD and CPL signals. The strong apparent CD and CPL might also be affected by the vortex flow during the stirring. Also, the samples show some kind of alignment in toluene observed by our naked eye as shown in Figure 4-15 (b) inset picture. The alignment could be affected by the stirring with vortex and convective flow.^{52, 53} So the partial alignment of PNCs-R/L-silica helical ribbons might behave with chiral orientation, and the chiral morphology is decided by the stirring speed and directions. The CD of PNCs-R- (or L-) silica helical ribbons were measured with different stirring speeds. As shown in Figure 4-15 (a), without stirring or stirring at 100 revolutions per minute (rpm), the CD peak at around 520 nm is positive, when the stirring speed increasing, the CD at around 520 nm split into two peaks, positive peak at 513 nm and strong negative peak at 528 nm. The new CD peaks are supposed to be caused by the vortex flow. Figure 4-15 (b) shows the CD values evolution at 365 nm and 528 nm with

different stirring speeds. The maximum value appears at 400 rpm and then decreased a little and keeps stable above 600 rpm. The difference of CD signals might be due to the different morphology of the alignment of the samples due to different vortex flow. Practically, the CD should be measured with opposite stirring direction to know how the CD evolves. Unfortunately, we didn't make it done.

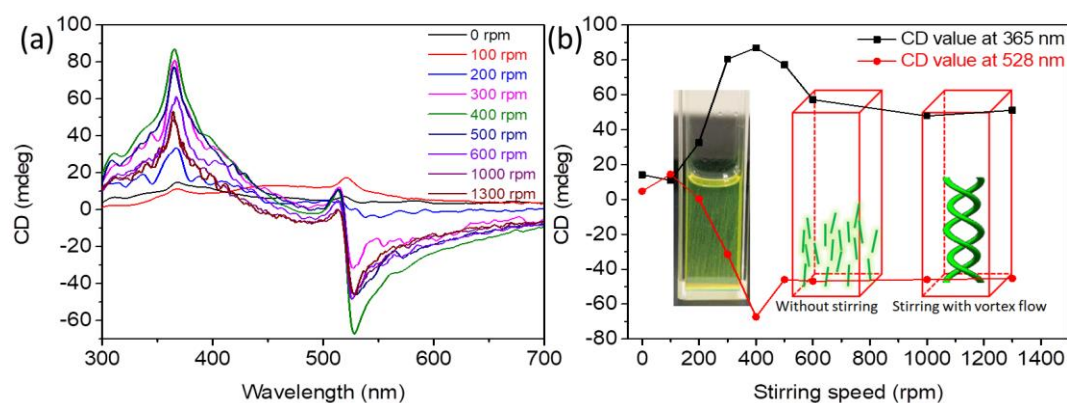


Figure 4-15. CD spectra (a) and CD values evolution at 365 nm and 528 nm separately (b) of PNCs-R-(or L-) silica helical ribbons in toluene solution. The inset picture shows the photograph of PNCs-silica helical ribbons toluene solution in cuvette cell without stirring and two modes show how the samples align in solution with or without stirring.

In conclusion, the chiroptical properties of CsPbBr₃ PNCs combined with right- or left-handed silica helical ribbons in suspension have been studied. Three different results were observed as shown in Figures 4-16. TEM images observation along with CD measurements indicate that when PNCs were grafted randomly on the surface of left- and right-handed silica helices (Step 1), no CD was observed as shown in Figure 4-16 (b). After the incubation, grafted PNCs (Step 2) grow along with the silica helical ribbons, mirror-image CD signals were observed from PNCs-R/L-silica helical ribbons (Figure 4-16 (c)). Further growth of PNCs for full coverage on the silica surface (Step 3) results in partial alignment of PNCs-R/L-silica helical ribbons, strong apparent CD signals were observed due to the LD and vortex flow (Figure 4-16 (d)).

It should be noted that the results of step 1 and step 3 are reproducible, while step 2 has a problem of reproducibility. A long time and great effort have been spent on the reproducibility of step 2, while most of the results are as shown in step 1 and the remaining results are as shown in step 3. Anyhow, inspired by the previous results, it confirms that the NCs' alignment on the surface of silica helical ribbons is vital for chirality induction. To realize the alignment of PNCs on the surface of silica helical ribbons, the study of PNCs oriented attachment were investigated. The controlling of grafting aging time, the crystal structure of PNCs, polar solvent or addition of surfactant during the grafting process, and annealing in solution *etc.* have been applied, still, the results only show step 1 or step 3. For the annealing effect study, the annealing of PNCs-R/L-silica helical ribbons has been applied both in suspension and film states. Surprisingly, on CD signals were observed in suspension before and after annealing, while in film state, the strong mirror images of CD signals were observed even without annealing. In suspension, no CD or apparent CD is reproducible, and also step 2 shows small CD signals which are not interesting for further study. Next, the film state of PNCs-silica helical ribbons would be more interesting for further study and discussion.

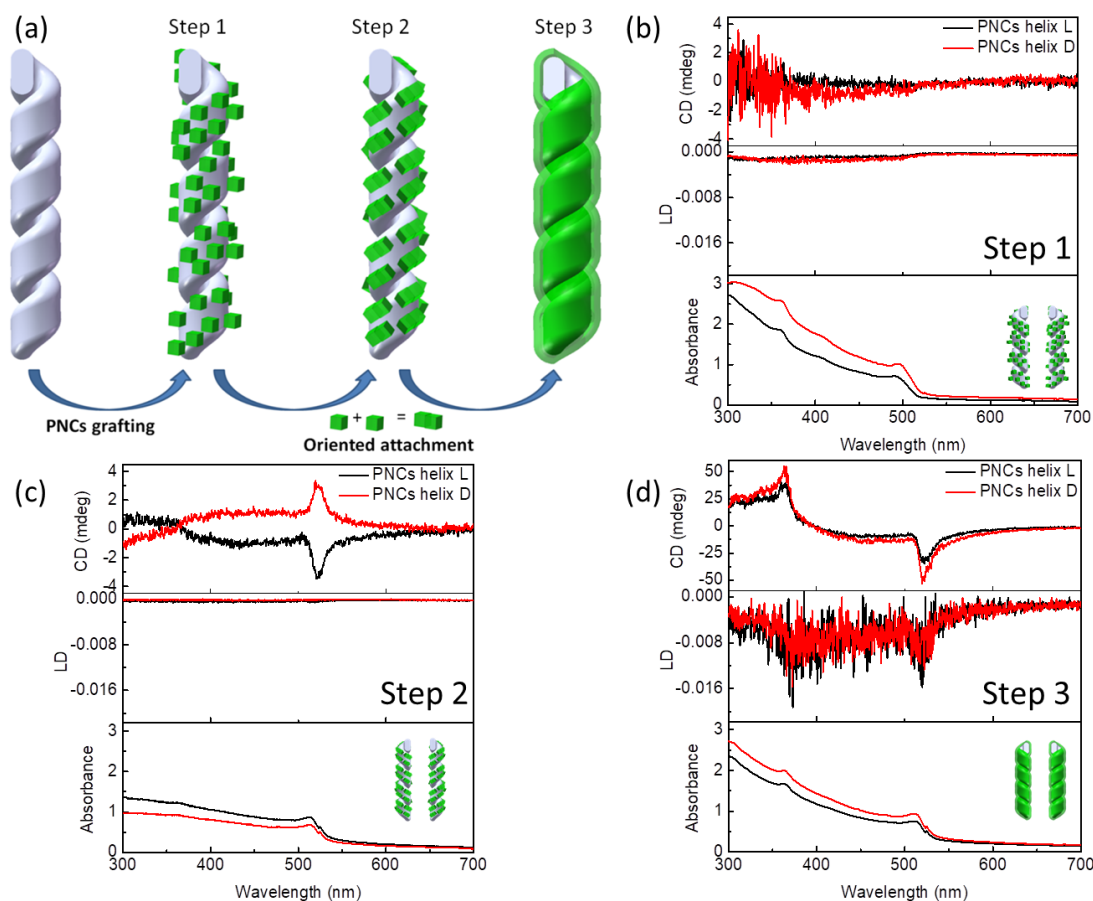


Figure 4-16. The schematic of PNCs anisotropic growth with silica helix (a) and different CD, LD, and absorption results (b), (c), and (d)

4.2 Results in drying state

Generally in suspension, no CD or CPL signals were observed for the PNCs-silica helical ribbons without PNCs oriented attachment as shown in Figures 4-17 (c) and (d). While after drying as film state, strong CD and CPL signals are observed indicates the different morphology of PNCs-silica helical ribbons in the solvated and drying state as shown in Figures 4-18 (b) and (c). The TEM images only show the sample in a drying state which is not the real morphology of PNCs-silica helical ribbons in suspension. The cryo-EM image of solvated PNCs-L-silica helical ribbons in toluene has been measured as shown in Figure 4-17 (a). The cryo-EM images of PNCs-silica helical ribbons show different morphology compared with TEM images of the sample (Figure 4-17 (b)). For the films dried at 4 °C, the PNCs-R-silica helical

ribbons show a positive CD signal with the maximum $g_{\text{abs}} \sim 6.2 \times 10^{-3}$ at around 367.5 nm whereas the PNCs-L-silica helical ribbons show a negative CD signal with $g_{\text{abs}} \sim -6.4 \times 10^{-3}$. The CPL spectra also show mirror images and the maximum g_{lum} at 517.5 nm are 6.9×10^{-3} for PNCs-R-silica helical ribbons and -5.7×10^{-3} for PNCs-L-silica helical ribbons respectively. Tomography TEM image with the 3D reconstruction of the dried (@20 °C) sample is shown in Figure 4-18 (a). It is observed that compared with the solvated cryo-EM image, the grafted PNCs of the dried sample are closer to the surface of silica helices and the reconstituted images (framed in red and yellow) clearly show a helical arrangement of the PNCs along with the helical ribbons. This is likely due to the ligands' collapse while solvent evaporation and alignment of the PNCs during the drying process. These PNCs probably have much stronger local interaction and organization with the small surface area on the silica helical ribbons. The PNCs self-organization during solvent evaporation is very important for chirality induction.

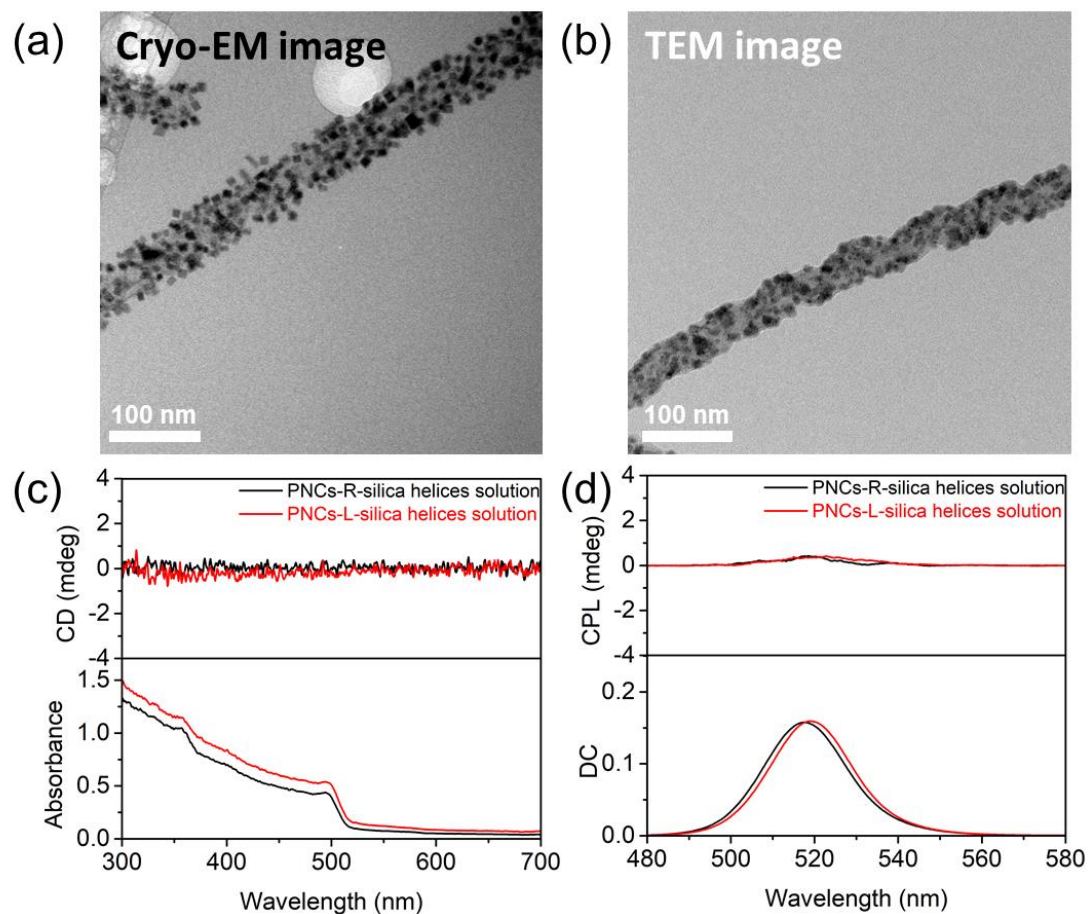


Figure 4-17. (a) Cryo-EM image and (b) TEM image of PNCs-L-silica helical ribbons, (c) UV-Vis absorbance and CD spectra and (d) fluorescence (Ex@ 365 nm) and CPL spectra of PNCs-R-silica helical ribbons (black) and PNCs-L-silica helical ribbons (red)

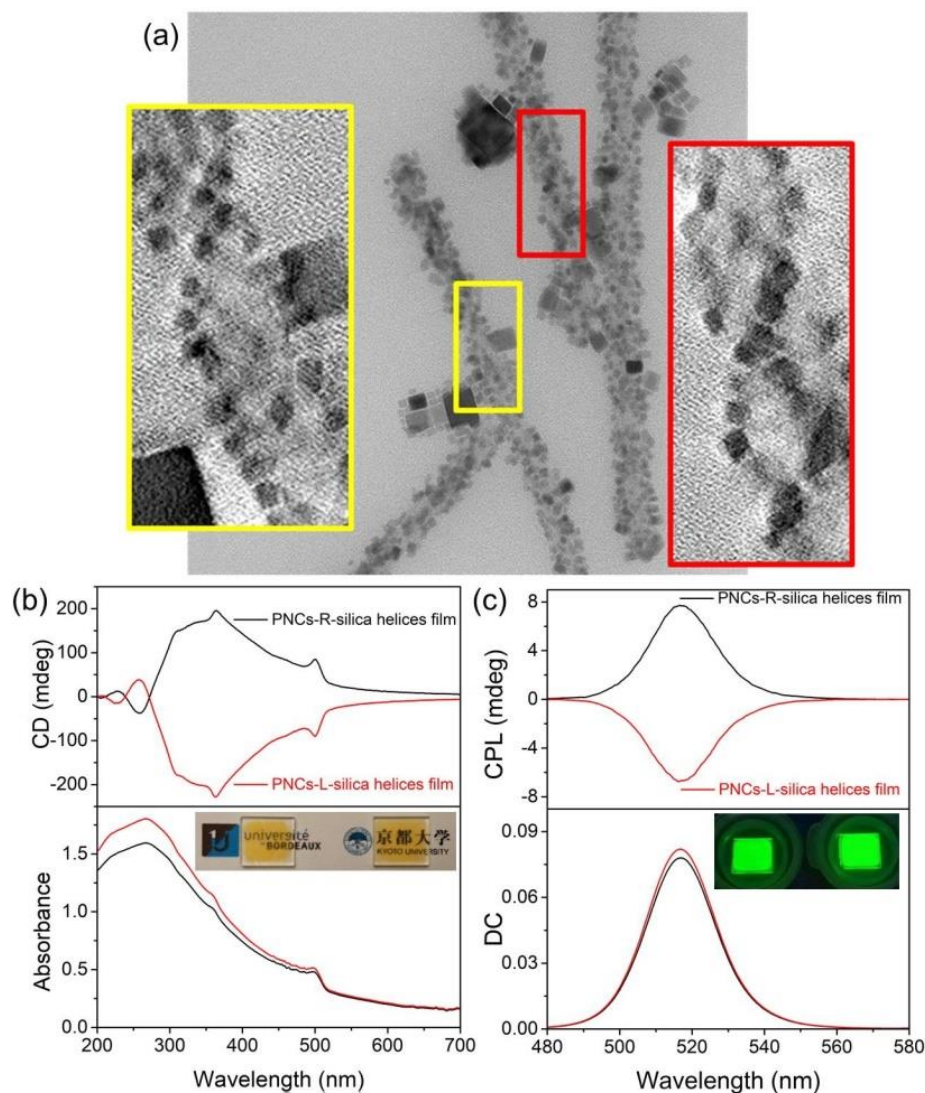


Figure 4-18. (a) TEM image of helical ribbons@PNCs and the cross-sections obtained with the tomography 3D reconstructions (framed in red and yellow) for the dried film. (b) Absorbance and CD spectra and (c) DC and CPL spectra of PNCs-R-silica helical ribbons (black) and PNCs-L-silica helical ribbons film (red) dried at 4 °C. The inset picture in (b) shows the drop-caste film from right-handed and left-handed samples under natural light. The inset picture in (c) shows the drop-cast films from right-handed and left-handed samples irradiated under a UV lamp at 365 nm. The mean values of data measured at 0° and 90° are shown to eliminate the contribution of linear dichroism. The dissymmetric factors for PNCs-L/R-silica helices are $g_{\text{abs}} (\text{abs}367.5 \text{ nm}) \sim 6.2 \cdot 10^{-3} / -6.4 \cdot 10^{-3}$ and $g_{\text{lum}} (\text{em}517.5 \text{ nm}) \sim 6.9 \cdot 10^{-3} / -5.7 \cdot 10^{-3}$.

Before discussing the optically active properties of PNCs-R/L-silica helical ribbons film, the PNCs toluene solution was drop-casted on the surface of the quartz. After drying, the CD and CPL of the PNCs film were measured with different angles as shown in Figure 4-19 (f). Interestingly, the PNCs film show strong LD with the magnitude of 10^{-2} and related angle-dependent CD and CPL signals as shown in Figures 4-19 (a-e). The strong LD indicates the alignment of PNCs after drying which is also indicated by the TEM images (Figure 4-11 (a-b)). PNCs in suspension, no alignment, and no CD observed, while after drying, alignment and apparent angle-dependent CD and CPL were observed. This indicates the self-organization of PNCs happened during the solvent evaporation process.⁵⁴

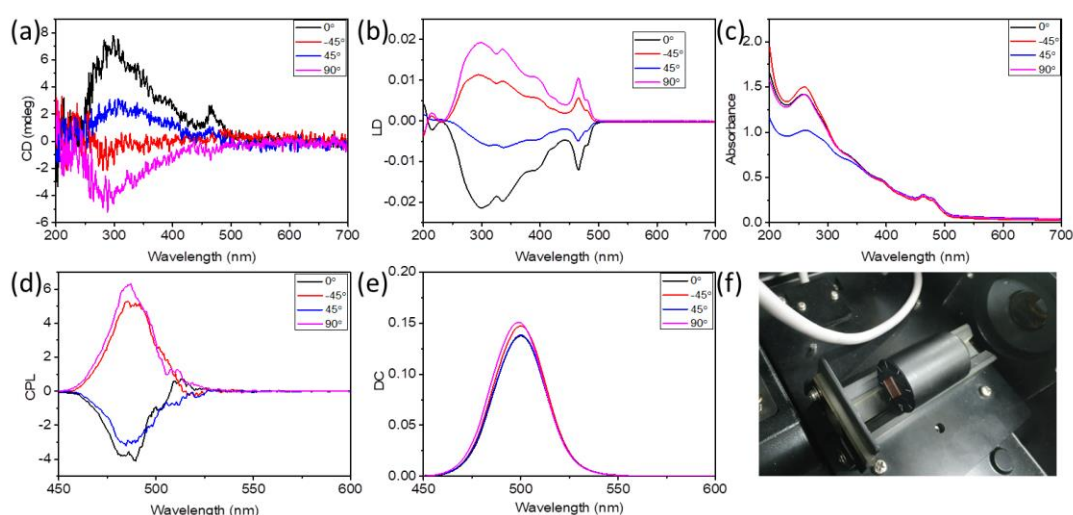


Figure 4-19. (a) CD, (b) LD, (c) absorbance, (d) CPL, and (e) DC spectra of PNC films measured with different angles as realized with (f) the rotational holder for the film angle-dependent measurements.

4.2.1 Solvent evaporation temperature effect

The PNCs-R/L-silica helical ribbons films were made by drop-casting PNCs-R/L-silica helical ribbons suspension (50 μ l of 20 mg/ml suspension) on the surface of quartz and drying them at 4 $^{\circ}$ C or 20 $^{\circ}$ C. Four groups of PNCs-R/L-silica helical ribbons films were prepared by evaporation at 20 $^{\circ}$ C and 4 $^{\circ}$ C labeled as R sample 1-2 and L sample 1-2, and CD, LD, and CPL data are shown in Figures 4-20

and 4-21. All samples were measured with vertical (0°) and horizontal (90°) angles. The dissymmetric g-factor spectra were directly obtained by the CD and CPL machine ($g_{\text{abs}} = \text{CD}/(32980 \cdot A)$; $g_{\text{lum}} = [\text{CPL}/(32980/\ln 10)]/\text{DC}$). And the detailed dissymmetric g-factors were shown in Table 1.

For the film dried at 20°C , the dissymmetric g-factor of CD and CPL (around $3\text{-}4 \cdot 10^{-3}$) are smaller (Figures 4-20 and 4-21) than the film dried at 4°C . Previously, Bodnarchuk *et al.* reported that the temperature had an important effect on the NCs' self-organization.⁵⁵ Recently, Momper *et al.* also reported that the solvent evaporation speed controls the perovskite nanoplatelets' orientation (edge-up or face-down).⁵⁶ Therefore, the difference of the dissymmetric g-factor of CD and CPL at different drying temperatures can be attributed to these effects.

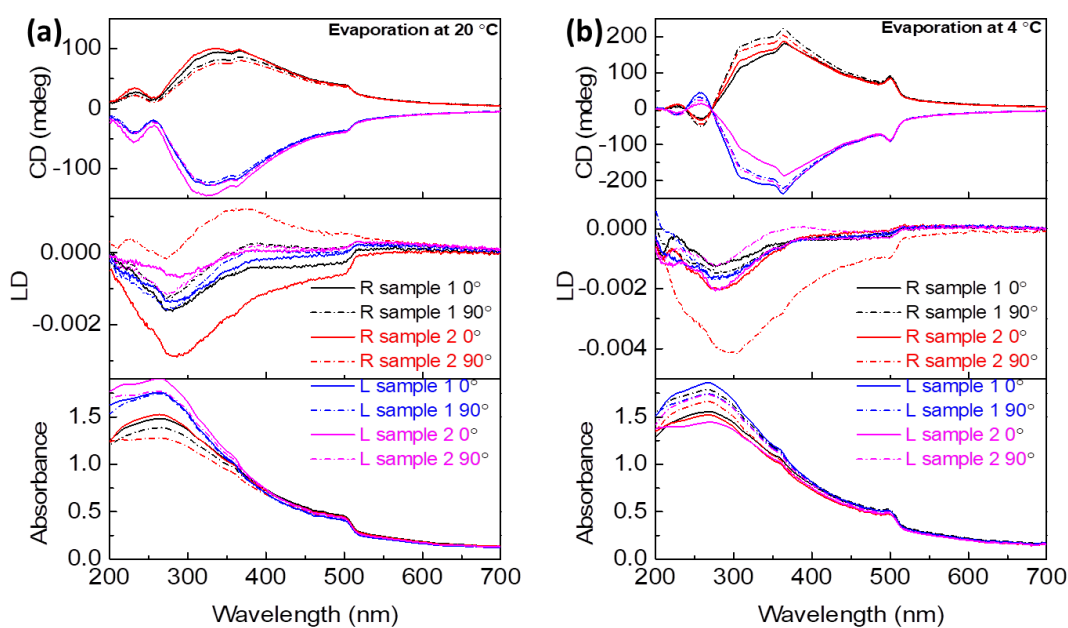


Figure 4-20. CD, LD and absorbance spectra measured at two angles (0° and 90°) of simultaneously prepared PNCs-R/L-silica helical ribbons films evaporated at (a) 20°C and (b) 4°C .

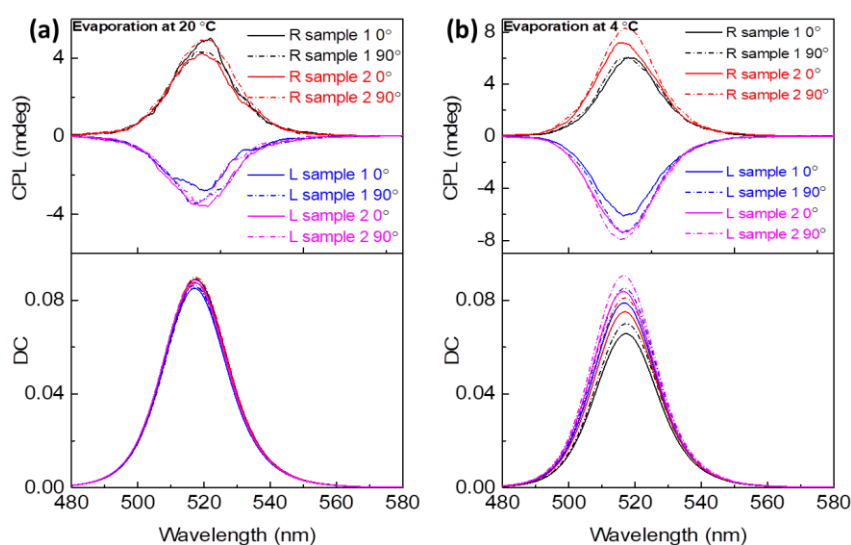


Figure 4-21. CPL and DC spectra measured at two angles (0° and 90°) of simultaneously prepared PNCs-R/L-silica helical ribbons films evaporated at (a) 20°C and (b) 4°C .

Table 1. Dissymmetric g-factors of PNCs-R/L-silica helical ribbons films.

Evaporation temperature	Samples name	g_{abs} at 367.5 nm ($0^\circ/90^\circ$)	Mean g_{abs} at 367.5 nm	g_{lum} at 517.5 nm ($0^\circ/90^\circ$)	Mean g_{lum} at 517.5 nm
20°C	R sample 1	$3.1 \times 10^{-3}/$ 3.0×10^{-3}	3.0×10^{-3}	$3.5 \times 10^{-3}/$ 3.5×10^{-3}	3.5×10^{-3}
	R sample 2	$3.3 \times 10^{-3}/$ 2.9×10^{-3}	3.1×10^{-3}	$3.2 \times 10^{-3}/$ 3.6×10^{-3}	3.4×10^{-3}
	L sample 1	$-3.8 \times 10^{-3}/$ -3.7×10^{-3}	-3.8×10^{-3}	$-2.1 \times 10^{-3}/$ -2.8×10^{-3}	-2.5×10^{-3}
	L sample 2	$-3.9 \times 10^{-3}/$ -3.7×10^{-3}	-3.8×10^{-3}	$-2.8 \times 10^{-3}/$ -2.6×10^{-3}	-2.7×10^{-3}
4°C	R sample 1	$5.5 \times 10^{-3}/$ 6.2×10^{-3}	5.9×10^{-3}	$6.4 \times 10^{-3}/$ 6.00×10^{-3}	6.2×10^{-3}
	R sample 2	$6.0 \times 10^{-3}/$ 6.3×10^{-3}	6.2×10^{-3}	$6.6 \times 10^{-3}/$ 7.1×10^{-3}	6.9×10^{-3}
	L sample 1	$-6.5 \times 10^{-3}/$ -6.3×10^{-3}	-6.4×10^{-3}	$-5.4 \times 10^{-3}/$ -6.0×10^{-3}	-5.7×10^{-3}
	L sample 2	$-5.9 \times 10^{-3}/$ -6.6×10^{-3}	-6.3×10^{-3}	$-6.2 \times 10^{-3}/$ -6.0×10^{-3}	-6.1×10^{-3}

The local organization of PNCs grafted on the silica helical ribbons in the dried

samples is investigated with grazing-incidence small-angle X-ray scattering (GISAXS). Samples which were dried at 4 °C and 20 °C, are compared mainly based on the horizontal line-cut analysis as shown in Figure 4-22. These data are analyzed with modeling as described in Figure 4-23 and Table 2. The modeling results indicate that the 4 °C dried film has a smaller inter-particle distance (11 ± 2 nm) than the dried ones (12 ± 2 nm), which suggests the PNCs coupling in the dried films at 4 °C is stronger than that at 20 °C. Moreover, the GISAXS line-cut of the film dried at 20 °C exhibits a prominent shoulder at a large q_y range, which is attributed to the presence of PNCs clusters (or aggregates). Solvent evaporation at 20 °C shortens the self-organization time of the PNCs as comparing with the time available in the 4 °C conditions, thereby leading to the formation of the PNCs aggregates. The as-formed aggregates are likely to cause an inhomogeneous coupling to the remaining PNCs ensemble.⁵⁷ The intensity contribution from the aggregates in the case of drying at 4 °C is relatively weak indicating a homogeneous PNCs arrangement. Consequently, a uniform PNCs-coupling is expected for the films dried at 4 °C. Notably, the effective 3D substrate by the silica helical ribbons, as shown in Figure 4-22 (d), leads to a smeared feature of the PNCs inter-particle distance.

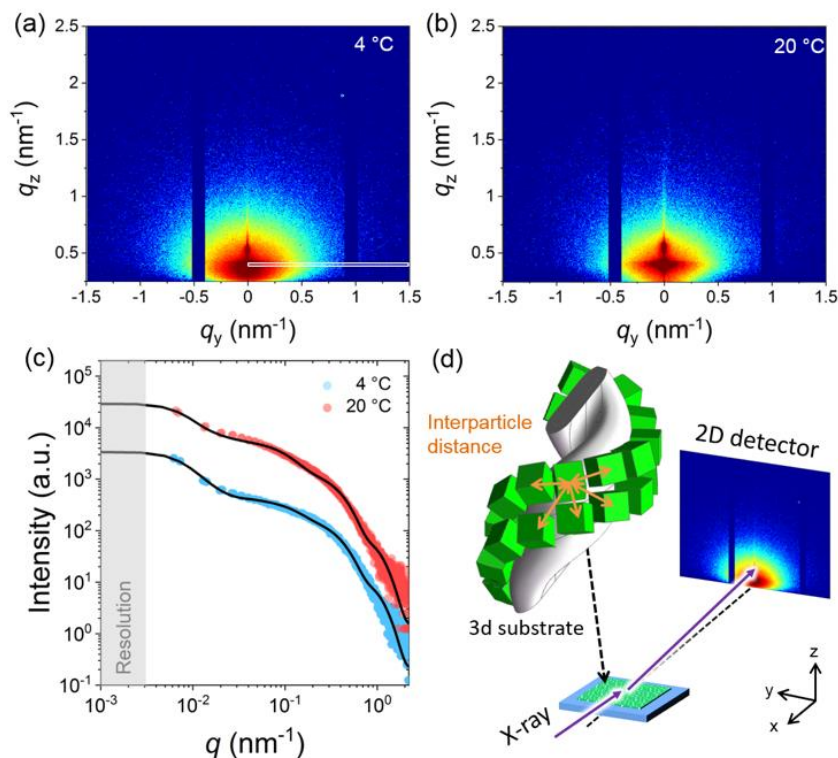


Figure 4-22. 2 D GISAXS data of PNCs-R-silica helical ribbons films dried at 4 °C (a) and 20 °C (b). (c) Horizontal line cut data of films dried at 4 °C (blue) and 20 °C (red) shown with the fit (solid lines) based on a model as explained. (d) Schematic of the GIXS experiment for analysis of the imprinting on PNCs-silica helical ribbons, in which the silica helical ribbons act as an effective 3D substrate leading to a smeared scattering feature of the PNCs inter-particle distance.

GISAXS line-cuts were studied *via* the modeling based on spherical models, by which the size and the interparticle distances of structures containing PNC and silica-helices were approximated. The intensity contributions are shown in Figure 4-23 and the respective modeling parameters are shown in Table 2.

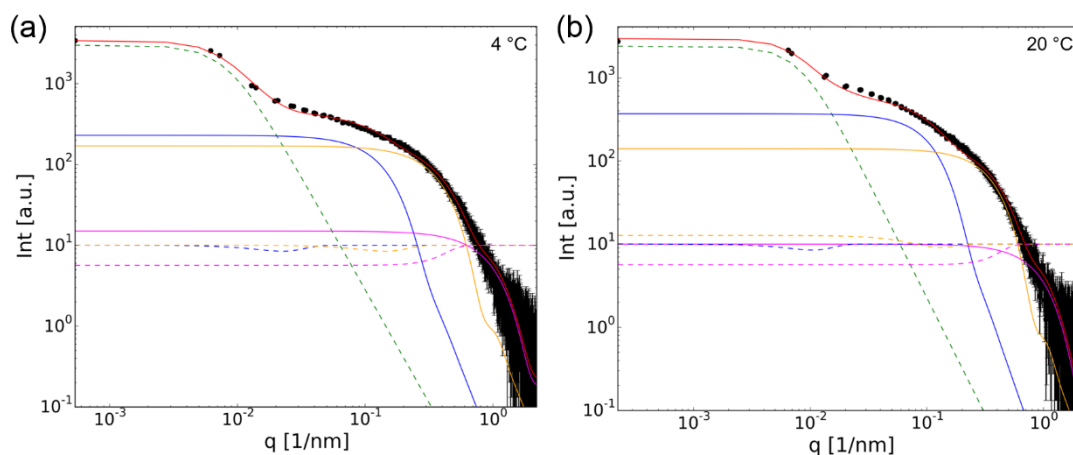


Figure 4-23. Horizontal line cuts of the 2D GISAXS data (symbols) with model fits based on parameters as listed in Table S2 for PNCs-R-silica helices films dried at (a) 4 °C and (b) 20 °C.

Table 2. GISAXS modeling parameters based on different sized sphere-model using the effective interface approximation, in which R denotes the sphere radius and D the distance between adjacent spheres.

Sample	R_1 (nm)	D_1 (nm)	R_2 (nm)	D_2 (nm)	R_3 (nm)	D_3 (nm)
	blue		yellow		pink	
4 °C	10.3 ± 0.2	70 ± 6	4.8 ± 0.1	11.0 ± 2.0	1.7 ± 0.2	6.5 ± 0.4
20 °C	12.8 ± 0.2	150 ± 10	4.8 ± 0.1	12.0 ± 2.0	1.7 ± 0.2	6.5 ± 0.4

Such observations are in very good agreement with the effect of drying vs solvated samples as well as the effect of the drying temperature on the g-factors. The comparison between cryo-EM (solvated) and tomography TEM (dried) show clearly that PNCs are closely attached to the silica helical ribbons and also are close with each other probably due to the collapse of the ligands when dried. SAXS measurements (Figure 4-24) show that there is no inter-particle correlation when the helical ribbons are solvated whilst for the dried samples, correlation distances with the particle-to-particle distances of 1-2 nm (drying temperature of 4 °C and 20 °C

respectively) are observed. The variation of the simulated g-factor is in good agreement with the measured ones during the drying process. We conclude that having no correlation distance (no self-organization) and an increasing inter-particle distance of the PNCs are likely the origin of the disappearance of the CD signals for the solvated samples. This result is in contrast with our previous report on gold nanoparticles (GNPs) grafted on silica helical ribbons which showed induced CD even when suspended in water. Indeed, the difference comes from the range of induced electromagnetic fields between GNPs and PNCs.

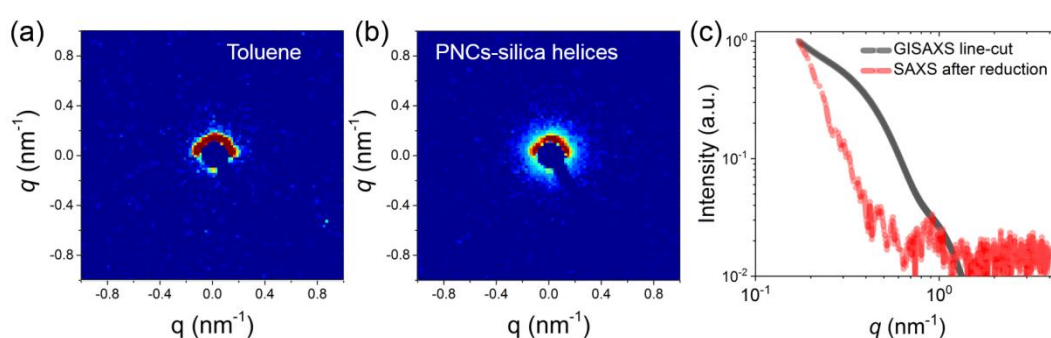


Figure 4-24. 2D SAXS data of (a) toluene and (b) PNC-silica helical ribbons in toluene. (c) Comparison of the GISAXS line cut data of PNCs-silica helices film and SAXS data of PNCs-silica helices in toluene after background subtraction (pure toluene).

In addition, the local organization of PNCs and PNCs grafted on the silica helical ribbons in the dried samples are investigated with grazing incidence wide-angle X-ray scattering (GIWAXS) as shown in Figure 4-25. The 2D GIWAXS of PNCs film shows arcs and spots graph which means the partial alignment of PNCs as shown in Figure 4-25 (d). Also, the 2D GISAXS data of PNCs film indicates a featured superstructure scattering as shown in Figure 4-26. The alignment result consists of the TEM and LD results of PNCs after drying. The GIWAXS of PNCs-silica helical ribbons dried at 4 and 20 °C show perfect rings in different lattice planes indicates a 3D grafting of PNCs on the 3D chiral silica helical ribbons.

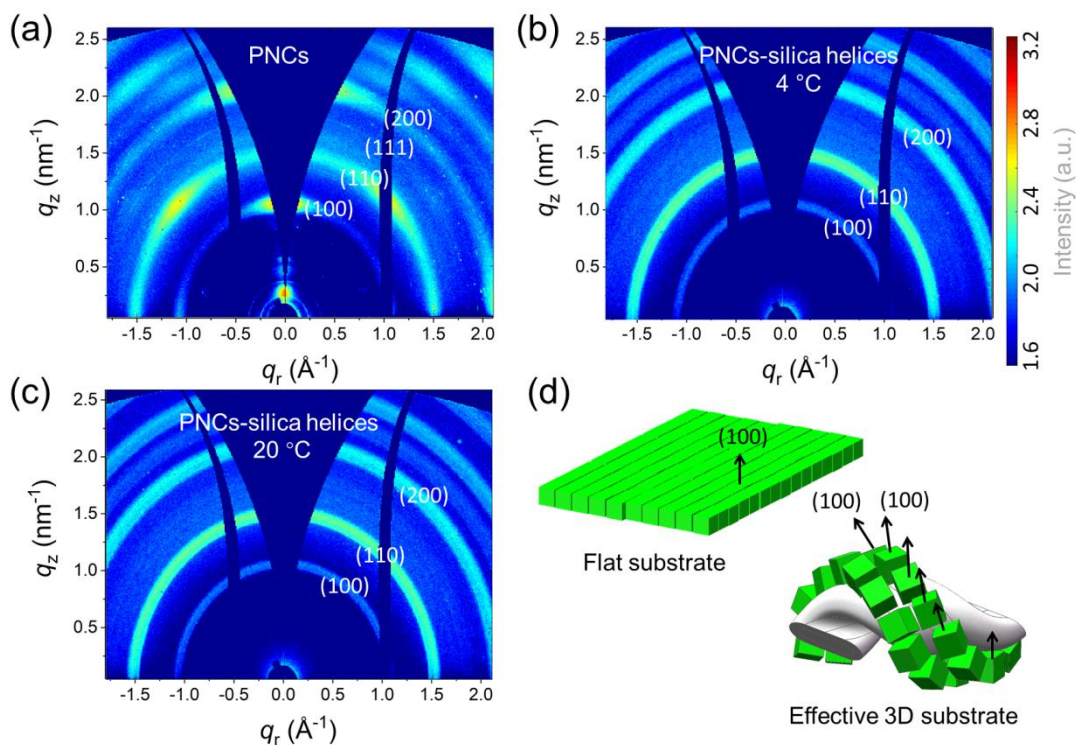


Figure 4-25. 2D GIWAXS data of (a) PNCs on a glass substrate and PNCs-R-silica helices films dried at (b) 4 °C and (c) 20 °C. (d) Schematic of the effective 3D substrate effect introduced by the silica helical ribbons.

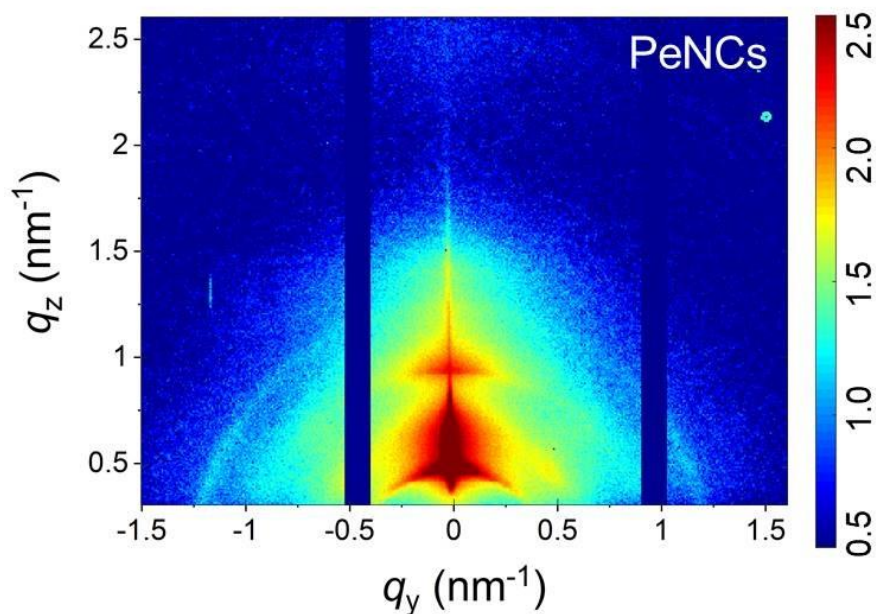


Figure 4-26. 2D GISAXS data of PNCs self-assembled on a flat glass substrate with a featured superstructure scattering

4.2.2 The kinetic drying effect of the PNCs-silica helical ribbons

The evolution of the CD or CPL signals during the drying process is investigated as follows: First PNCs-R/L-silica helical ribbons suspension was dried on a quartz substrate at 20 °C to prepare films. Then 10 µL toluene was dropped on the surface of the film to penetrate the PNCs-R/L-silica helical ribbons. The CD and LD spectra of such wetted film are measured at 502 nm during drying at various temperatures (0 – 80 °C) as shown in Figures 4-27. Upon soaking with toluene and drying at 0 °C for the PNCs-L-silica helical ribbons film, the CD value decreased from initial -41 mdeg (measure as dried film) to -7 mdeg (measured at t=0). Here it should be noted that once a dried film is formed, adding toluene to wet the film does not transform all the sample back to the suspension state. That is why the CD value@502 nm does not go down to ~0 mdeg. While drying at 0 °C, during the initial stage (0-10 min) of toluene evaporation, the CD values slightly increased. Then from 10 min, a sudden increase of the CD value is observed, followed by reaching a plateau with -39 mdeg at 11.5 min. The absorbance and LD values changed also during the drying process. The absorbance decreased slightly during the initial drying followed by a jump just before the complete dryness, finally reaching a similar value at the complete dried state and in the wet state. The CPL signal has also shown a similar kinetic curve as CD (Figure 4-28). Weidman, Tisdale *et al.* reported that the drying of a free nanocrystals suspension in toluene to a solid-state PbS nanocrystal film resulted in self-organization as observed by *in-situ* Grazing Incidence X-ray Scattering.⁵⁸ The free nanocrystals go from 5 to 95% of their maximum alignment only takes 1.2 minutes during the drying process which is similar to the CD and CPL signals drastic change time. It should be noted that the XRD patterns didn't show any change for the dried PNCs, PNCs-silica helical ribbons in suspension, and dried PNCs-silica helical ribbons as shown in Figure 4-29. So the signals' drastic change indicates the self-organization of PNCs on the surface of silica helical ribbons.

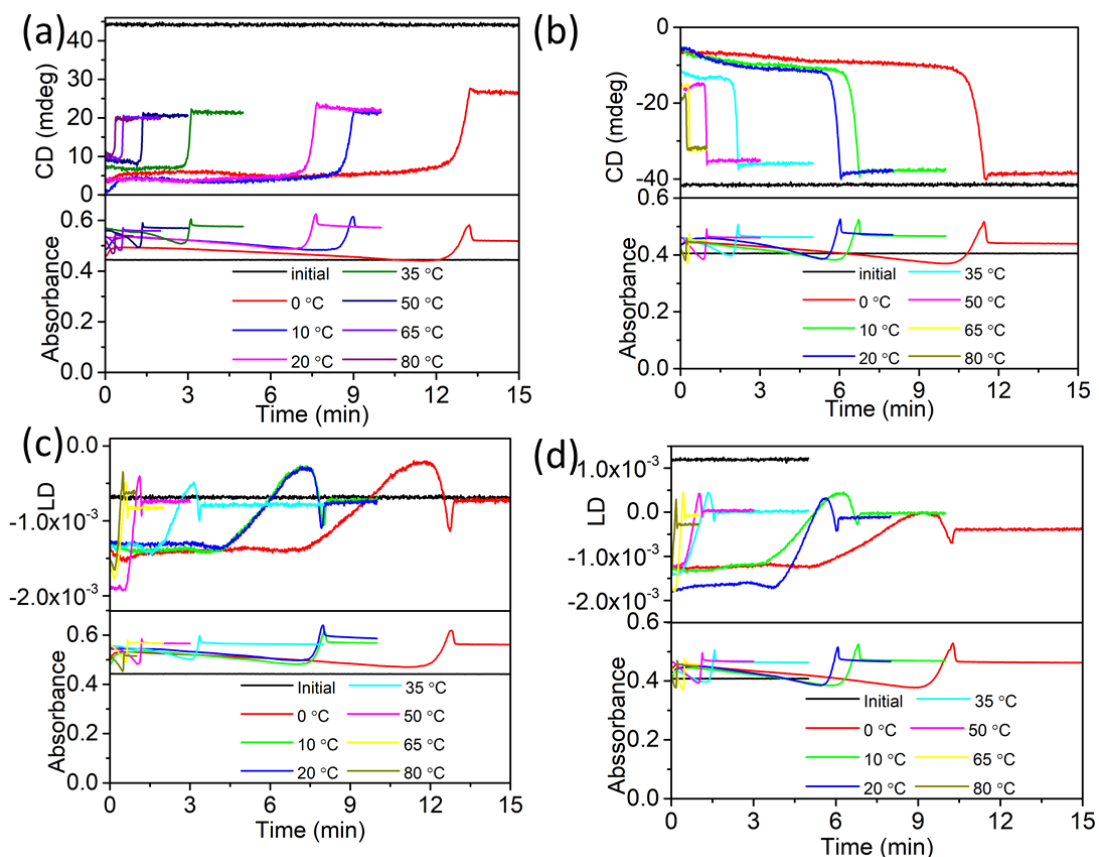


Figure 4-27. (a,b) CD and absorbance at 502 nm as well as (c,d) LD and absorbance of (a,c) PNCs-R-silica helical ribbons and (b,d) PNCs-L-silica helical ribbons films with toluene soaking (initial) and drying at different temperatures as indicated.

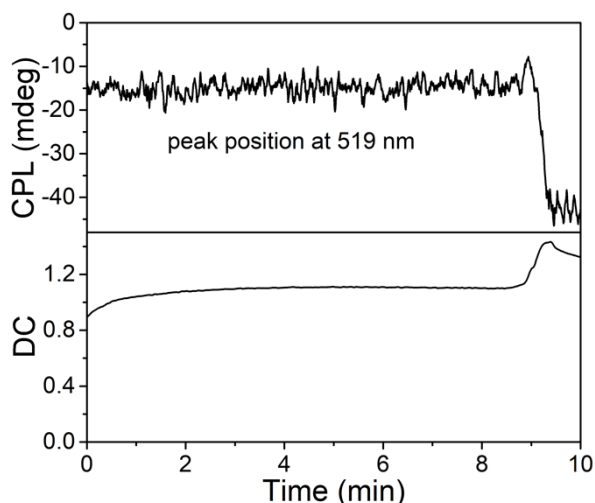


Figure 4-28. Temporal evolution of DC and CPL at wavelength 519 nm of a PNCs-L-silica helical ribbons film with toluene soaking and drying processes. PNCs-L-silica helical ribbons suspension was dried on quartz at 20 °C to create films. Then

10 μL toluene was added to the surface of the film to soak the silica helical ribbons. The DC and CPL spectra of such wetted film are measured at 519 nm during drying at 4 $^{\circ}\text{C}$.

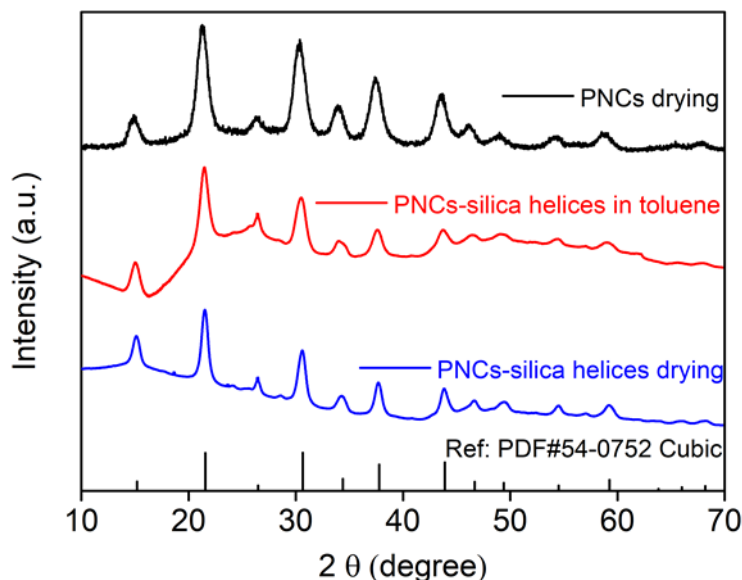


Figure 4-29. XRD spectra of dried PNCs and PNCs-silica helical ribbons (solvated and dried). Curves are shifted along the y axis for clarity of the presentation. For all samples, no modification in the lattice spacing is observed.

4.2.3 Temperature stability

The temperature stability of the chiroptical properties of the PNCs-R/L-silica helical ribbons films has been evaluated. The g_{abs} and g_{lum} spectra of PNCs-R/L-silica helices in the temperature ranging between 0 $^{\circ}\text{C}$ and 90 $^{\circ}\text{C}$ (g_{abs}) and -10 to 80 $^{\circ}\text{C}$ (g_{lum}) are as shown in Figures 4-30 (a-d). The spectra of PNCs-L-silica helices are shown in Figure 4-31. While the g_{abs} show almost no variation with temperature upon heating and cooling, g_{lum} is less stable upon heating as the emission intensity decreased to less than 10% of the initial intensity. Upon cooling, the emission intensity recovered a little (~35% of the initial intensity) as shown in Figure 4-32, probably due to the thermal photoluminescence quenching, as previously reported.⁵⁹ The g_{lum} first decreased slowly upon heating to 50 $^{\circ}\text{C}$ (~88% of the initial value), then decreased

fast upon heating to 80 °C (~69% of the initial value). While upon cooling, the g_{lum} didn't recover (-10 °C with 73% of the initial value) due to the thermal degradation of luminescence. However, there is no doubt that the PNCs chiral self-organization assisted by inorganic silica helical ribbons is still robust than soft templates which will facilitate future application.

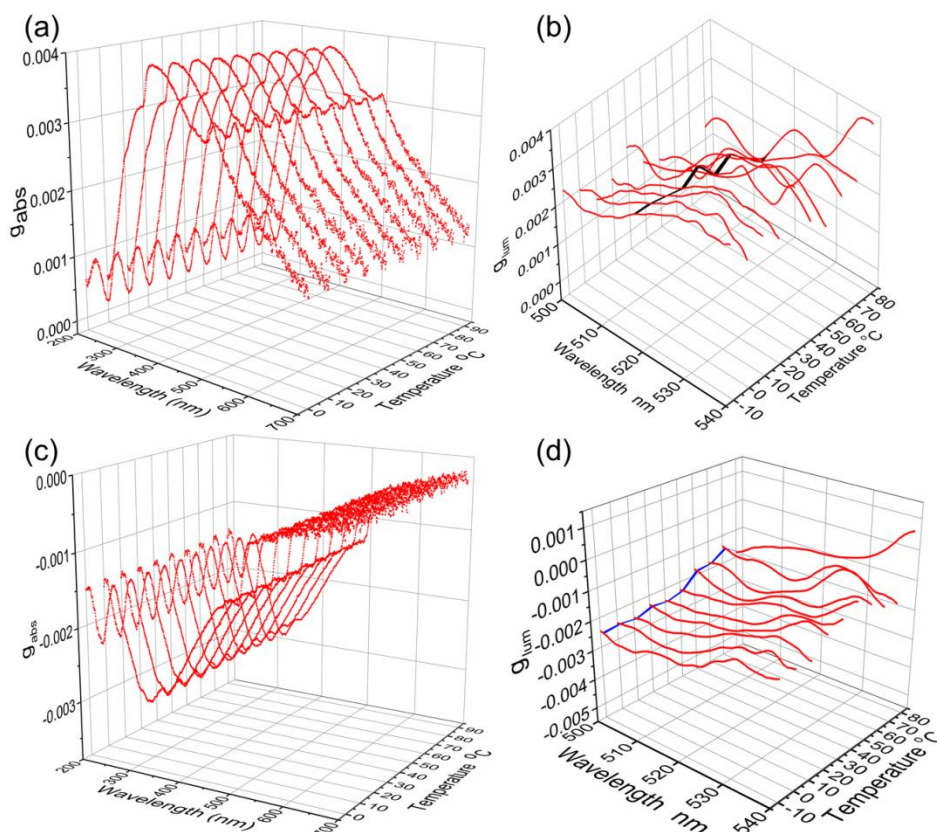


Figure 4-30. (a,c) g_{abs} and (b,d) g_{lum} spectra of (a,b) PNCs-R- silica helical ribbons and (c,d) PNCs-L-silica helical ribbons at different temperatures.

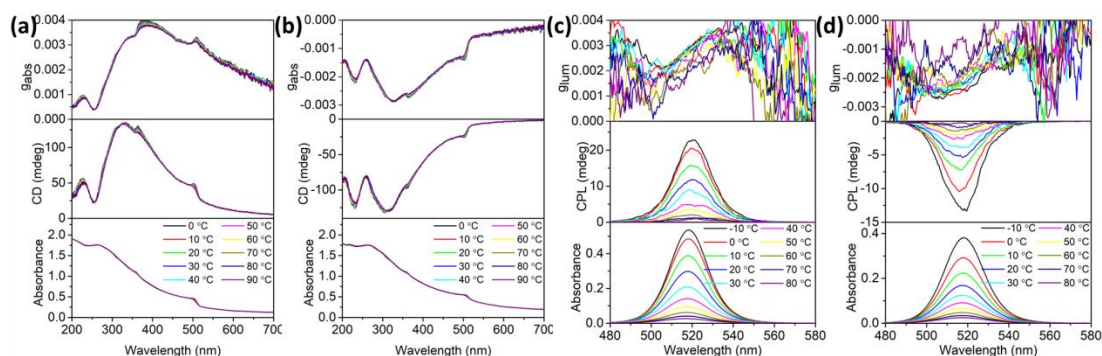


Figure 4-31. Absorbance, CD, and g_{abs} of PNCs-R-silica helical ribbons (a) and

PNCs-L-silica helical ribbons (b) measured with different temperature (0-90 °C); DC, CPL and g_{lum} of PNCs-R-silica helical ribbons (c) and PNCs-L-silica helical ribbons (d) measured with different temperature (-10-80 °C)

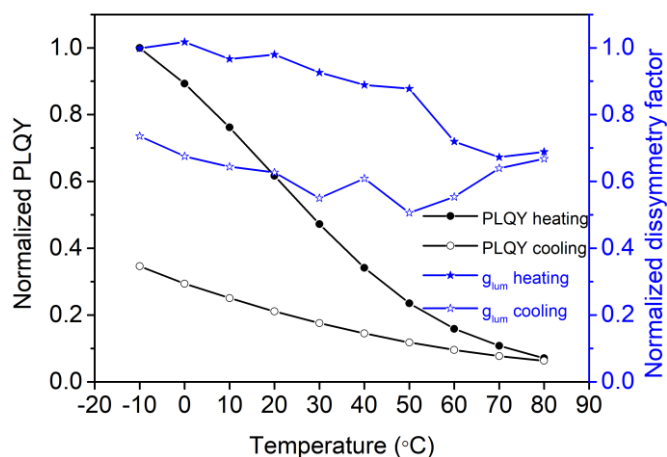


Figure 4-32. Normalized PLQY (black) and g_{lum} (blue) of PNCs-R-silica helical ribbons measured in a heating and cooling cycle.

4.2.4 Theoretical simulation

The optical properties of PNCs-silica helical ribbons are simulated by using the coupled dipole method (CDM) as described in the experiment section. Figure 4-33 (a) shows a schematic representation of the models used for the simulation, which consist of helically ordered PNCs. Figure 4-33 (b) shows the influence of the density of the PNCs by removing various percentages of PNCs from the perfect alignment. As is shown, simulated CD spectra exhibit the same spectral variations as the measured ones, suggesting that the CD signal comes from the interaction between the induced dipoles. The amplitude of the CD and g-factor spectra decreases as the number of removed PNC increases. As it can be observed with tomography TEM, the organization of the PNCs are not exactly as it is in the model. There are some domains where observed closely packed and helically arranged PNCs, but there are other areas where the arrangement is not that perfect. Therefore, the effect of the defect by removing randomly various percentages of PNCs was evaluated. The g-factors calculated from these plots show that the observed g-factor @516 nm

simulates the best match when around 30% of PNCs are removed with the interparticle 1 nm. The CD is negligible for a higher wavelength than 550 nm, while it progressively increases as the wavelength decreases. The CD reaches its maximum value at 325 nm. According to simulations proposed by Kovalenko *et al.*,² the bands located at 516 nm and 325 nm can be related to the lowest-energy excitonic transition at the R point of the first Brillion zone (BZ) and the second-lowest energy transition at the M point of BZ, respectively. The inset in Figure 4-33 (b) illustrates the influence of the interparticle distance on the CD and g-factor of a single NPC-silica nanohelix. The CD signal and g-factor decrease as the interparticle distance increases. Indeed, the g-factor decreases by half when the interparticle distance is increased from 1 to 2 nm, then continues to decrease. Beyond 4 nm, it is less than 10 % of the initial value. It is observed that the amplitude of the scattered field decreases with the distance from the PNC dipole source. Therefore, the interaction between PNCs and the CD becomes negligible for large interparticle distances.

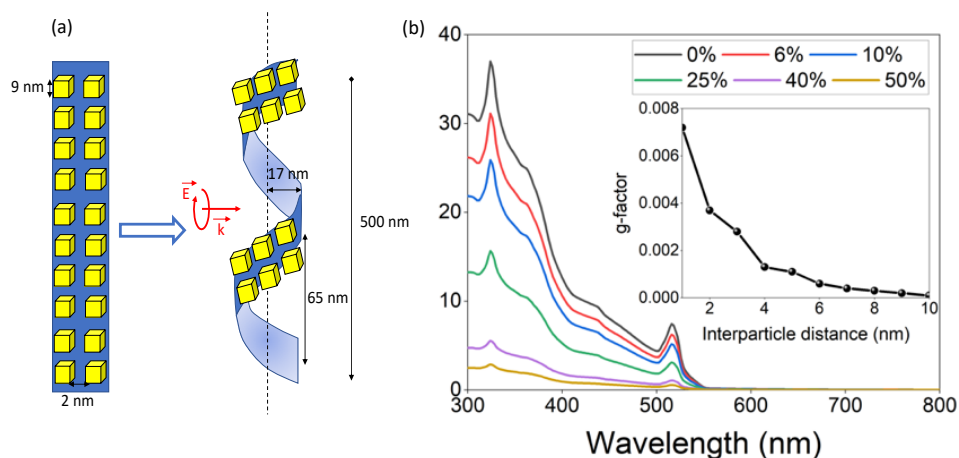


Figure 4-33. (a) Schematic representation of helically ordered PNCs. All simulations are performed by considering an NCs size of 9 nm. Two rows of PNCs are perfectly aligned around the helix, the radius of the helix is 34 nm, and the pitch is 65 nm (b) Simulated CD of a PNC-silica helix for several amounts of randomly removed NPCs. In the inset of (b), the evolution of the g-factor at a 516 nm wavelength with the interparticle distance (1-10 nm) is simulated by removing 30% of NPCs (which gives the g-factor as observed experimentally in dried sample).

5. CONCLUSION

Perovskite CsPbBr₃ nanocrystals could be grafted on the surface of silica helical ribbons by an in-situ growth method or ligand exchange method. PNCs grafted by in-situ growth method, no chirality induction observed in suspension. While PNCs were grafted by the ligand exchange method, three different results could be observed in suspension. When PNCs were isolated and randomly grafted on the surface of left- and right-handed silica helical ribbons, no CD was observed in suspension. After the grafted PNCs oriented attachment, PNCs grow along with the silica helical ribbons, mirror-image CD signals were observed from PNCs-R/L-silica helical ribbons in suspension. Further growth of PNCs for full coverage on the silica surface results in partial alignment of PNCs-R/L-silica helical ribbons, strong apparent CD signals were observed due to the LD and vortex flow.

Even though PNCs grafted silica helical ribbons do not show any observable optical activity in suspension. After drying on substrates to form films, strong CD and CPL signals are observed with the dissymmetric factor of $> 6 \times 10^{-3}$. Solvated and dried TEM images both show densely attached PNCs on the surface of the helical ribbons. However, for the solvated helical ribbons, the PNCs show a thicker and swollen layer around the silica helical ribbons without detectable helical organization probably with strongly solvated ligands. In contrast, for the dried helical ribbons, the PNCs are closely attached on the surface, suggesting ligands collapse and a higher interaction between the both, which may induce higher self-organization with a 3-dimensional spiral arrangement of the PNCs along with the inorganic chiral silica helical ribbons. GISAXS confirms a correlation between PNCs for the dried samples, which does not exist for solvated samples. CDM simulation confirms that for the dielectric nanoparticles such as PNCs, the correlation between the particles to “feel” the chirality, the inter-particle distances need to be very close to each other with good alignment, which is likely why solvated samples with larger particle distances with much less ordered organization do not show any detectable CD. The samples dried at

4 °C (with slower drying) show stronger ICD signals than those dried at 20 °C (faster drying), which is probably due to the closer packing originating from the slower film drying. The films show excellent photostability in their absorbance and CD properties, however, lose emissivity significantly upon heating up to 80 °C.

6. Experimental section

6.1 Materials and instruments

All the chemical reagents were purchased from Sigma Company. The chemicals reagents Cs₂CO₃ (99.995%), CsBr (99.999%), PbBr₂ (99.999%), octadecene (ODE, 90%), oleic acid (OA, 90%), oleylamine (OLA, 70%), dimethylformamide (DMF, 99.8%, anhydrous) toluene (>99.3%), ethyl acetate (>99.5%), acetonitrile (>99.8%) were chosen to prepare perovskite nanocrystals.

Transmission electron microscopy (TEM) was performed with CM 120 (Philips) at 120 kV. Cryogenic electron microscopy (cryo-EM) was performed with Tecnai F20 (FEI). Circular dichroism (CD), linear dichroism (LD), and UV-vis spectrums were measured by J-815 (JASCO). Circularly polarized luminescence (CPL) and emission spectra were obtained by CPL-300 (JASCO).

XRD

XRD diffraction patterns were recorded on a Rigaku FRX rotating anode X-Ray generator equipped with high flux Osmic Varimax HF mirrors and a hybrid Dectris Pilatus 300K detector. The source is operating at the copper K α wavelength (1.54178 Å) with a partial chi goniometer that decreases blind areas and enables automatic axial adjustment. Data were processed with the CrysAlisPro suite version 1.171.38.43⁶⁰ and WinPLOTR⁶¹. Dry powder samples were mounted on cryoloops, solvated samples were kept in sealed capillaries during data collection. Each

diffraction pattern corresponds to a 360 ° rotation along the phi axis (perpendicular to the direct beam) with an exposure time of 360 sec.

SAXS, GISAXS, and GIWAXS

Small-angle X-ray scattering (SAXS), grazing incidence small and wide-angle X-ray scattering (GISAXS and GIWAXS) was measured with an in-house Ganesha 300XL SAXS-WAXS instrument. The X-ray photon energy was 8 keV (Cu-K α X-ray source) and the detector was a Pilatus 300k. The sample-detector distance was set to 1045 mm for SAXS and GISAXS and 95.7 mm for GIWAXS. The X-ray incidence angle was 0.4 ° for GISAXS and GIWAXS measurements. The GIWAXS data were corrected according to standard procedure.

6.2 CsPbBr₃ perovskites nanocrystals (PNCs) prepared at room temperature

The preparation of PNCs at room temperature was modified based on the previous report.¹ Typically, 0.4 mmol CsBr and 0.4 mmol PbBr₂ dissolved into 10 ml DMF solution to obtain Cs⁺, Pb²⁺, and Br⁻ transparent ions precursors. Then 1 ml oleic acid (OA) and 0.5 ml oleylamine (OLA) was added and sonication for 5 min. Then 1 ml of the mixed solution was added into 10 ml toluene with magneton stirring. Then PNCs are synthesized by supersaturated recrystallization.

Purification of CsPbBr₃: the crude PNCs solution and 3 equal volumes of ethyl acetate were mixed: 7000 g centrifugation for 4 min, then remove all the supernatant, 5 ml toluene was added to disperse the PNCs, then 5 ml acetonitrile was added, 5000 rpm centrifugation for 3 min, remove all the supernatant, 5 ml toluene was added to disperse the PNCs, 7000 g centrifugation for 4 min, the supernatant was collected and keep it in the fridge at 4 °C.

6.3 In-situ growth of CsPbBr₃ on the surface of silica helical ribbons

Typically, 100 ug amine-modified silica helical ribbons were dispersed into 100 uL

Chapter 4. Optically active perovskite nanocrystals helically arranged on inorganic silica helical ribbons

Cs^+ , Pb^{2+} , and Br^- ions precursors. Then 10 μL OA was added as carboxyl acid ligand and different amount of extra amine ligands APTES or OLA was added as amine ligand as table 3 and 4 shown. Then the solution was injected into 1 mL toluene. The crude solution was washed with toluene twice by centrifugation (9800 g for 10 min) to remove the free PNCs. Finally, the precipitate was re-dispersed into 1 mL toluene.

Table 3. PNCs in-situ grow on silica helical ribbons with different extra APTES

1	100 μg silica helical ribbons with amine modification	100 μL Cs^+ , Pb^{2+} , Br^- DMF solution	10 μL OA	0 μL APTES	1 mL toluene
2	100 μg silica helical ribbons with amine modification	100 μL Cs^+ , Pb^{2+} , Br^- DMF solution	10 μL OA	1 μL APTES	1 mL toluene
3	100 μg silica helical ribbons with amine modification	100 μL Cs^+ , Pb^{2+} , Br^- DMF solution	10 μL OA	2 μL APTES	1 mL toluene
4	100 μg silica helical ribbons with amine modification	100 μL Cs^+ , Pb^{2+} , Br^- DMF solution	10 μL OA	5 μL APTES	1 mL toluene
5	100 μg silica helical ribbons with amine modification	100 μL Cs^+ , Pb^{2+} , Br^- DMF solution	10 μL OA	10 μL APTES	1 mL toluene

Table 4. PNCs in-situ grow on silica helical ribbons with different extra OLA

1	100 μg silica helical ribbons with amine modification	100 μL Cs^+ , Pb^{2+} , Br^- DMF solution	10 μL OA	1 μL OLA	1 mL toluene
2	100 μg silica helical ribbons with amine modification	100 μL Cs^+ , Pb^{2+} , Br^- DMF solution	10 μL OA	2 μL APTES	1 mL toluene
3	100 μg silica helical ribbons with amine modification	100 μL Cs^+ , Pb^{2+} , Br^- DMF solution	10 μL OA	3 μL APTES	1 mL toluene
4	100 μg silica helical ribbons with amine modification	100 μL Cs^+ , Pb^{2+} , Br^- DMF solution	10 μL OA	4 μL APTES	1 mL toluene
5	100 μg silica helical ribbons with amine modification	100 μL Cs^+ , Pb^{2+} , Br^- DMF solution	10 μL OA	5 μL APTES	1 mL toluene
6	100 μg silica helical ribbons with amine modification	100 μL Cs^+ , Pb^{2+} , Br^- DMF solution	10 μL OA	6 μL APTES	1 mL toluene
7	100 μg silica helical ribbons with amine modification	100 μL Cs^+ , Pb^{2+} , Br^- DMF solution	10 μL OA	7 μL APTES	1 mL toluene
8	100 μg silica helical ribbons with amine modification	100 μL Cs^+ , Pb^{2+} , Br^- DMF solution	10 μL OA	8 μL APTES	1 mL toluene

6.4 CsPbBr_3 perovskites nanocrystals (PNCs) prepared at high temperature

The preparation of CsPbBr₃ PNCs was similar to the previous report.² First, the mixture of 0.0814 g Cs₂CO₃, 0.25 mL OA, and 4 mL ODE was degassed at 120 °C for 1 h, the temperature was increased to 150 °C to get a clear CsOA precursor solution. In parallel, the mixture of 0.138 g PbBr₂, 1 mL OA, 1 mL OLA and 10 mL ODE was degassed at 120 °C for 1 h, the temperature was then increased to 180 °C, 0.8 mL CsOA (maintained at 80 °C before injection) was injected immediately. 5 s later, the mixture was removed from the heat and cooled down to room temperature by an ice water bath.

CsPbBr₃ PNCs purification

The mixture was mixed with 30 mL ethyl acetate and centrifuged at 10000 g for 6 min, the supernatant was removed and the precipitate was dispersed into 10 mL toluene, then centrifuged again at 8000 g for 4 min to precipitate the large particles and the supernatant was collected.

6.5 Grafting of CsPbBr₃ PNCs on the surface of silica helical ribbons by ligand exchange methods

5 mL APTES modified silica ribbons ethanol solution (1 mg/mL) was centrifuged at 9800 g for 10 min, the supernatant was removed, and 5 mL toluene was added to the precipitate to disperse the silica ribbons. The dispersion was centrifuged again at 9800 g for 10 min, the supernatant was removed and 5 mL toluene was added to disperse the silica ribbons. Finally, the silica ribbons were dispersed into a 5 mL toluene solution. Then the silica ribbons toluene mass concentration was calculated measuring the mass of dried silica ribbons in a certain volume solution.

0.5 mL purified PNCs has added 0.5 mL acetonitrile and centrifuged at 3000 g for 3 min, the supernatant was removed and the precipitate was re-dispersed into 0.5 mL toluene solution. Repeat this process and the PNCs were finally dispersed into 0.5 mL toluene.

Silica helical ribbons and purified PNCs were mixed and sonication for 10 min, then

the mixture was shaken at 4 °C for 3 days (roller mixer). After that, to separate the PNCs-silica helical ribbons and free PNCs, the mixture was centrifuged at 9800 g for 10 min, the supernatant was discarded and 1 mL toluene was added to disperse the precipitate. Centrifugation again and the precipitate PNCs-silica helical ribbons were re-dispersed into 0.5 mL toluene.

PNCs-silica helical ribbons film preparation

The quartz was cut to 1 * 1 cm plates. Then the prepared PNCs-silica helical ribbons toluene solution 50 uL was drop cast on the quartz surface and dried at 4 °C or 20 °C. Two films were prepared in parallel under the same conditions for each sample. After drying, CD and CPL were measured with different parameters.

6.6 Coupled dipole method simulation

The optical properties of a PNCs-silica helix were simulated by using the coupled dipole method (CDM). Each PNC grafted on the helix has a sufficiently small size to be considered as a point dipole. The CDM took into account the dipolar interaction between PNC in the same helix. The polarizability of cubic PNC was given by previous reports.⁶²

$$\alpha = \frac{3.6442}{4\pi} a^3 (\tau - 1) \frac{\tau^3 + 4.83981\tau^2 + 5.54742\tau + 1.6383}{\tau^4 + 8.0341\tau^3 + 19.3534\tau^2 + 15.4349\tau + 3.6442}, \quad (1)$$

where a is the PNC size and $\tau = \frac{\epsilon_{PNC}}{\epsilon_m}$, the ratio between the dielectric function of PNC (ϵ_{PNC}) and the dielectric function of the matrix (ϵ_m). By neglecting the quantum confinement effect, the dielectric function of bulk CsPbBr₃^{63, 64} was used as the dielectric function of PNC. This simulation considered that the PNC was located in a homogeneous matrix composed of silica and void. The dielectric function of the matrix was set to 1.5, which corresponded to the average value of the dielectric function of silica and air. By neglecting, the size distribution of PNC, the parameter a was set to 9 nm. The local electric field $\vec{E}_{loc,m}$ view by the m^{th} PNC located at the

position \vec{r}_m induced a dipole moment \vec{P}_m given by:

$$\vec{P}_m = \alpha \vec{E}_{loc,m}, \quad (2)$$

$\vec{E}_{loc,m}$ is the sum of the incident electric field $\vec{E}_{0,m}$ and the field scattered by the other PNC l:

$$\alpha^{-1} \vec{P}_m = \vec{E}_{0,m} - \sum_{l \neq m}^N A_{ml} \vec{P}_l. \quad (3A)$$

N is the number of grafted PNC on the helix. The second term of this equation, which described the electromagnetic interactions between the induced dipole, was expressed as:

$$A_{ml} \vec{P}_l = \frac{e^{jkr_{ml}}}{r_{ml}^3} \left\{ k^2 \vec{r}_{ml} \wedge \vec{r}_{ml} \wedge \vec{P}_l + \frac{1-jkr_{ml}}{r_{ml}^2} (r_{ml}^2 \vec{P}_l - 3\vec{r}_{ml} \cdot (\vec{r}_{ml} \cdot \vec{P}_l)) \right\}. \quad (3B)$$

k and r_{ml} are the norms of the vectors \vec{k} and $\vec{r}_{ml} = \vec{r}_m - \vec{r}_l$, respectively. In the following, we considered that \vec{k} was normal to the PNC-helix. By using the same procedure for all nanoparticles, we obtained a set of 3N linear equations which were rewritten into the form:

$$E_0 = AP. \quad (3C)$$

E_0 and P are the 3N incident field and dipole moment vectors. The matrix A was deduced from equations (3A) and (3B).

The vector P was obtained by solving equation (3C) by using the generalized minimal residual method (GMRES). The extinction cross-section σ of PNC-helix was then calculated for a given polarization by using the following equations:

$$\sigma = \frac{4\pi}{|E_0|^2} \sum_{m=1}^N \text{Im}(\vec{E}_{0,m} \cdot \vec{P}_m^*). \quad (4)$$

The CD of the PNC-helix was then deduced from the extinction cross-section calculated for a right- σ_R and left σ_L handed circular polarization:

$$CD = \sigma_L - \sigma_R. \quad (5)$$

The g-factor was also given by:

$$g = 2 \frac{\sigma_L - \sigma_R}{\sigma_L + \sigma_R}. \quad (6)$$

The position \vec{r}_m of PNC, which was a crucial parameter for CDM, was calculated as follows: First, the PNCs were perfectly organized, on a flat ribbon, into a

Chapter 4. Optically active perovskite nanocrystals helically arranged on inorganic silica helical ribbons

two-dimensional square lattice. The gap distance between two adjacent PNCs was denoted d . The width of the ribbon contained 2 PNCs. Then, the ribbon was twisted into a helix. The pitch and the radius of the helix as determined by TEM were 65 nm and 17 nm, respectively. The length of the helix was 520 nm.

7. Reference

1. Li, X.; Wu, Y.; Zhang, S.; Cai, B.; Gu, Y.; Song, J.; Zeng, H., CsPbX₃ Quantum Dots for Lighting and Displays: Room-Temperature Synthesis, Photoluminescence Superiorities, Underlying Origins and White Light-Emitting Diodes. *Advanced Functional Materials* **2016**, *26* (15), 2435-2445.
2. Protesescu, L.; Yakunin, S.; Bodnarchuk, M. I.; Krieg, F.; Caputo, R.; Hendon, C. H.; Yang, R. X.; Walsh, A.; Kovalenko, M. V., Nanocrystals of Cesium Lead Halide Perovskites (CsPbX₃, X = Cl, Br, and I): Novel Optoelectronic Materials Showing Bright Emission with Wide Color Gamut. *Nano Letters* **2015**, *15* (6), 3692-3696.
3. Liu, P.; Chen, W.; Wang, W.; Xu, B.; Wu, D.; Hao, J.; Cao, W.; Fang, F.; Li, Y.; Zeng, Y.; Pan, R.; Chen, S.; Cao, W.; Sun, X. W.; Wang, K., Halide-Rich Synthesized Cesium Lead Bromide Perovskite Nanocrystals for Light-Emitting Diodes with Improved Performance. *Chemistry of Materials* **2017**, *29* (12), 5168-5173.
4. Lin, K.; Xing, J.; Quan, L. N.; de Arquer, F. P. G.; Gong, X.; Lu, J.; Xie, L.; Zhao, W.; Zhang, D.; Yan, C.; Li, W.; Liu, X.; Lu, Y.; Kirman, J.; Sargent, E. H.; Xiong, Q.; Wei, Z., Perovskite light-emitting diodes with external quantum efficiency exceeding 20 per cent. *Nature* **2018**, *562* (7726), 245-248.
5. Zhang, J.; Hodes, G.; Jin, Z.; Liu, S. F., All-Inorganic CsPbX₃ Perovskite Solar Cells: Progress and Prospects. *Angew Chem Int Ed Engl* **2019**, *58* (44), 15596-15618.
6. Ma, T.; Wang, S.; Zhang, Y.; Zhang, K.; Yi, L., The development of all-inorganic CsPbX₃ perovskite solar cells. *Journal of Materials Science* **2019**, *55* (2), 464-479.
7. Gao, X.; Han, B.; Yang, X.; Tang, Z., Perspective of Chiral Colloidal Semiconductor Nanocrystals: Opportunity and Challenge. *J Am Chem Soc* **2019**, *141* (35), 13700-13707.
8. Chen, C.; Gao, L.; Gao, W.; Ge, C.; Du, X.; Li, Z.; Yang, Y.; Niu, G.; Tang, J., Circularly polarized light detection using chiral hybrid perovskite. *Nat Commun* **2019**, *10* (1), 1927.
9. Long, G.; Sabatini, R.; Saidaminov, M. I.; Lakhwani, G.; Rasmita, A.; Liu, X.; Sargent, E. H.; Gao, W., Chiral-perovskite optoelectronics. *Nature Reviews Materials* **2020**, *5* (6), 423-439.
10. Ben Moshe, A.; Szwarcman, D.; Markovich, G., Size dependence of chiroptical activity in colloidal quantum dots. *ACS nano* **2011**, *5* (11), 9034-9043.
11. Zhou, Y.; Zhu, Z.; Huang, W.; Liu, W.; Wu, S.; Liu, X.; Gao, Y.; Zhang, W.; Tang, Z., Optical coupling between chiral biomolecules and semiconductor nanoparticles: size - dependent circular dichroism absorption. *Angewandte Chemie International Edition* **2011**, *50* (48), 11456-11459.
12. Ben-Moshe, A.; Wolf, S. G.; Bar Sadan, M.; Houben, L.; Fan, Z.; Govorov, A. O.; Markovich, G., Enantioselective control of lattice and shape chirality in inorganic nanostructures using chiral biomolecules. *Nat Commun* **2014**, *5*, 4302.
13. Ben - Moshe, A.; Govorov, A. O.; Markovich, G., Enantioselective synthesis of intrinsically chiral mercury sulfide nanocrystals. *Angewandte Chemie International Edition* **2013**, *52* (4), 1275-1279.
14. Shi, Y.; Duan, P.; Huo, S.; Li, Y.; Liu, M., Endowing Perovskite Nanocrystals with Circularly Polarized Luminescence. *Adv Mater* **2018**, *30* (12), e1705011.
15. Huo, S.; Duan, P.; Jiao, T.; Peng, Q.; Liu, M., Self-Assembled Luminescent Quantum Dots To Generate Full-Color and White Circularly Polarized Light. *Angewandte Chemie International Edition* **2017**, *56* (40), 12174-12178.
16. Choi, J. K.; Haynie, B. E.; Tohgha, U.; Pap, L.; Elliott, K. W.; Leonard, B. M.; Dzyuba, S. V.; Varga, K.; Kubelka, J.; Balaz, M., Chirality Inversion of CdSe and CdS Quantum Dots without Changing the Stereochemistry of the Capping Ligand. *ACS Nano* **2016**, *10* (3), 3809-15.

Chapter 4. Optically active perovskite nanocrystals helically arranged on inorganic silica helical ribbons

17. Gao, X.; Zhang, X.; Deng, K.; Han, B.; Zhao, L.; Wu, M.; Shi, L.; Lv, J.; Tang, Z., Excitonic Circular Dichroism of Chiral Quantum Rods. *J Am Chem Soc* **2017**, *139* (25), 8734-8739.
18. Gao, X.; Zhang, X.; Zhao, L.; Huang, P.; Han, B.; Lv, J.; Qiu, X.; Wei, S. H.; Tang, Z., Distinct Excitonic Circular Dichroism between Wurtzite and Zincblende CdSe Nanoplatelets. *Nano Lett* **2018**, *18* (11), 6665-6671.
19. Govorov, A. O.; Fan, Z.; Hernandez, P.; Slocik, J. M.; Naik, R. R., Theory of circular dichroism of nanomaterials comprising chiral molecules and nanocrystals: plasmon enhancement, dipole interactions, and dielectric effects. *Nano Lett* **2010**, *10* (4), 1374-82.
20. Cheng, J.; Hao, J.; Liu, H.; Li, J.; Li, J.; Zhu, X.; Lin, X.; Wang, K.; He, T., Optically Active CdSe-Dot/CdS-Rod Nanocrystals with Induced Chirality and Circularly Polarized Luminescence. *ACS Nano* **2018**, *12* (6), 5341-5350.
21. Tohgha, U.; Deol, K. K.; Porter, A. G.; Bartko, S. G.; Choi, J. K.; Leonard, B. M.; Varga, K.; Kubelka, J.; Muller, G.; Balaz, M., Ligand induced circular dichroism and circularly polarized luminescence in CdSe quantum dots. *ACS nano* **2013**, *7* (12), 11094-11102.
22. Gao, X.; Chan, W. C.; Nie, S., Quantum-dot nanocrystals for ultrasensitive biological labeling and multicolor optical encoding. *Journal of biomedical optics* **2002**, *7* (4), 532-538.
23. Osaki, F.; Kanamori, T.; Sando, S.; Sera, T.; Aoyama, Y., A quantum dot conjugated sugar ball and its cellular uptake. On the size effects of endocytosis in the subviral region. *Journal of the American Chemical Society* **2004**, *126* (21), 6520-6521.
24. William, W. Y.; Chang, E.; Drezek, R.; Colvin, V. L., Water-soluble quantum dots for biomedical applications. *Biochemical and biophysical research communications* **2006**, *348* (3), 781-786.
25. Purcell-Milton, F.; Visheratina, A. K.; Kuznetsova, V. A.; Ryan, A.; Orlova, A. O.; Gun'ko, Y. K., Impact of Shell Thickness on Photoluminescence and Optical Activity in Chiral CdSe/CdS Core/Shell Quantum Dots. *ACS Nano* **2017**, *11* (9), 9207-9214.
26. Wang, P. P.; Yu, S. J.; Govorov, A. O.; Ouyang, M., Cooperative expression of atomic chirality in inorganic nanostructures. *Nat Commun* **2017**, *8*, 14312.
27. Zhou, Y.; Marson, R. L.; van Anders, G.; Zhu, J.; Ma, G.; Ercius, P.; Sun, K.; Yeom, B.; Glotzer, S. C.; Kotov, N. A., Biomimetic Hierarchical Assembly of Helical Supraparticles from Chiral Nanoparticles. *ACS Nano* **2016**, *10* (3), 3248-56.
28. Yeom, J.; Yeom, B.; Chan, H.; Smith, K. W.; Dominguez-Medina, S.; Bahng, J. H.; Zhao, G.; Chang, W.-S.; Chang, S.-J.; Chuvilin, A., Chiral templating of self-assembling nanostructures by circularly polarized light. *Nature materials* **2015**, *14* (1), 66-72.
29. Feng, W.; Kim, J.-Y.; Wang, X.; Calcaterra, H. A.; Qu, Z.; Meshi, L.; Kotov, N. A., Assembly of mesoscale helices with near-unity enantiomeric excess and light-matter interactions for chiral semiconductors. *Science advances* **2017**, *3* (3), e1601159.
30. Duan, Y.; Che, S., Electron transition-based optical activity (ETOA) of achiral metal oxides derived from chiral mesoporous silica. *Chemistry* **2013**, *19* (32), 10468-72.
31. Cheng, J.; Le Saux, G.; Gao, J.; Buffeteau, T.; Battie, Y.; Barois, P.; Ponsinet, V.; Delville, M. H.; Ersen, O.; Pouget, E.; Oda, R., GoldHelix: Gold Nanoparticles Forming 3D Helical Superstructures with Controlled Morphology and Strong Chiroptical Property. *ACS Nano* **2017**, *11* (4), 3806-3818.
32. Gao, J.; Wu, W.; Lemaire, V.; Carvalho, A.; Nlate, S.; Buffeteau, T.; Oda, R.; Battie, Y.; Pauly, M.; Pouget, E., Tuning the Chiroptical Properties of Elongated Nano-objects via Hierarchical Organization. *ACS Nano* **2020**, *14* (4), 4111-4121.
33. Protesescu, L.; Yakunin, S.; Nazarenko, O.; Dirin, D. N.; Kovalenko, M. V., Low-Cost Synthesis of

Chapter 4. Optically active perovskite nanocrystals helically arranged on inorganic silica helical ribbons

Highly Luminescent Colloidal Lead Halide Perovskite Nanocrystals by Wet Ball Milling. *ACS Appl Nano Mater* **2018**, *1* (3), 1300-1308.

34. Hintermayr, V. A.; Richter, A. F.; Ehrat, F.; Doblinger, M.; Vanderlinden, W.; Sichert, J. A.; Tong, Y.; Polavarapu, L.; Feldmann, J.; Urban, A. S., Tuning the Optical Properties of Perovskite Nanoplatelets through Composition and Thickness by Ligand-Assisted Exfoliation. *Adv Mater* **2016**, *28* (43), 9478-9485.
35. Wang, N.; Liu, W.; Zhang, Q., Perovskite-Based Nanocrystals: Synthesis and Applications beyond Solar Cells. *Small Methods* **2018**, *2* (6).
36. Shamsi, J.; Urban, A. S.; Imran, M.; De Trizio, L.; Manna, L., Metal Halide Perovskite Nanocrystals: Synthesis, Post-Synthesis Modifications, and Their Optical Properties. *Chem Rev* **2019**, *119* (5), 3296-3348.
37. Sun, C.; Zhang, Y.; Ruan, C.; Yin, C.; Wang, X.; Wang, Y.; Yu, W. W., Efficient and Stable White LEDs with Silica-Coated Inorganic Perovskite Quantum Dots. *Adv Mater* **2016**, *28* (45), 10088-10094.
38. Luo, B.; Pu, Y. C.; Lindley, S. A.; Yang, Y.; Lu, L.; Li, Y.; Li, X.; Zhang, J. Z., Organolead Halide Perovskite Nanocrystals: Branched Capping Ligands Control Crystal Size and Stability. *Angew Chem Int Ed Engl* **2016**, *55* (31), 8864-8.
39. Xue, X.; Penn, R. L.; Leite, E. R.; Huang, F.; Lin, Z., Crystal growth by oriented attachment: kinetic models and control factors. *CrystEngComm* **2014**, *16* (8), 1419.
40. Cho, K. S.; Talapin, D. V.; Gaschler, W.; Murray, C. B., Designing PbSe nanowires and nanorings through oriented attachment of nanoparticles. *J Am Chem Soc* **2005**, *127* (19), 7140-7.
41. Ivanov, V. K.; Fedorov, P. P.; Baranchikov, A. Y.; Osiko, V. V., Oriented attachment of particles: 100 years of investigations of non-classical crystal growth. *Russian Chemical Reviews* **2014**, *83* (12), 1204-1222.
42. van Huis, M. A.; Kunneman, L. T.; Overgaag, K.; Xu, Q.; Pandraud, G.; Zandbergen, H. W.; Vanmaekelbergh, D., Low-temperature nanocrystal unification through rotations and relaxations probed by in situ transmission electron microscopy. *Nano Lett* **2008**, *8* (11), 3959-63.
43. De Yoreo, J. J.; Gilbert, P. U.; Sommerdijk, N. A.; Penn, R. L.; Whitlam, S.; Joester, D.; Zhang, H.; Rimer, J. D.; Navrotsky, A.; Banfield, J. F.; Wallace, A. F.; Michel, F. M.; Meldrum, F. C.; Colfen, H.; Dove, P. M., CRYSTAL GROWTH. Crystallization by particle attachment in synthetic, biogenic, and geologic environments. *Science* **2015**, *349* (6247), aaa6760.
44. Liu, L.; Huang, S.; Pan, L.; Shi, L. J.; Zou, B.; Deng, L.; Zhong, H., Colloidal Synthesis of CH₃ NH₃ PbBr₃ Nanoplatelets with Polarized Emission through Self-Organization. *Angew Chem Int Ed Engl* **2017**, *56* (7), 1780-1783.
45. Tong, Y.; Bohn, B. J.; Bladt, E.; Wang, K.; Muller-Buschbaum, P.; Bals, S.; Urban, A. S.; Polavarapu, L.; Feldmann, J., From Precursor Powders to CsPbX₃ Perovskite Nanowires: One-Pot Synthesis, Growth Mechanism, and Oriented Self-Assembly. *Angew Chem Int Ed Engl* **2017**, *56* (44), 13887-13892.
46. Li, X.; Yu, D.; Cao, F.; Gu, Y.; Wei, Y.; Wu, Y.; Song, J.; Zeng, H., Healing All-Inorganic Perovskite Films via Recyclable Dissolution-Recrystallization for Compact and Smooth Carrier Channels of Optoelectronic Devices with High Stability. *Advanced Functional Materials* **2016**, *26* (32), 5903-5912.
47. Ji, X.; Copenhaver, D.; Sichmeller, C.; Peng, X., Ligand bonding and dynamics on colloidal nanocrystals at room temperature: the case of alkylamines on CdSe nanocrystals. *Journal of the American Chemical Society* **2008**, *130* (17), 5726-5735.
48. Yu, W. W.; Qu, L.; Guo, W.; Peng, X., Experimental determination of the extinction coefficient of CdTe, CdSe, and CdS nanocrystals. *Chemistry of Materials* **2003**, *15* (14), 2854-2860.

Chapter 4. Optically active perovskite nanocrystals helically arranged on inorganic silica helical ribbons

49. De Roo, J.; Ibanez, M.; Geiregat, P.; Nedelcu, G.; Walravens, W.; Maes, J.; Martins, J. C.; Van Driessche, I.; Koyalenko, M. V.; Hens, Z., Highly Dynamic Ligand Binding and Light Absorption Coefficient of Cesium Lead Bromide Perovskite Nanocrystals. *Acs Nano* **2016**, *10* (2), 2071-2081.
50. Yang, T.; Zhang, Z.; Ding, Y.; Yin, N.; Liu, X. J. J. o. N. R., Nondestructive purification process for inorganic perovskite quantum dot solar cells. **2019**, *21* (5), 1-8.
51. Chiba, T.; Hoshi, K.; Pu, Y. J.; Takeda, Y.; Hayashi, Y.; Ohisa, S.; Kawata, S.; Kido, J., High-Efficiency Perovskite Quantum-Dot Light-Emitting Devices by Effective Washing Process and Interfacial Energy Level Alignment. *ACS Appl Mater Interfaces* **2017**, *9* (21), 18054-18060.
52. Spada, G. P., Alignment by the convective and vortex flow of achiral self-assembled fibers induces strong circular dichroism effects. *Angew Chem Int Ed Engl* **2008**, *47* (4), 636-8.
53. Wolffs, M.; George, S. J.; Tomovic, Z.; Meskers, S. C.; Schenning, A. P.; Meijer, E. W., Macroscopic origin of circular dichroism effects by alignment of self-assembled fibers in solution. *Angew Chem Int Ed Engl* **2007**, *46* (43), 8203-5.
54. Raino, G.; Becker, M. A.; Bodnarchuk, M. I.; Mahrt, R. F.; Kovalenko, M. V.; Stoferle, T., Superfluorescence from lead halide perovskite quantum dot superlattices. *Nature* **2018**.
55. Bodnarchuk, M. I.; Kovalenko, M. V.; Heiss, W.; Talapin, D. V., Energetic and entropic contributions to self-assembly of binary nanocrystal superlattices: temperature as the structure-directing factor. *Journal of the American Chemical Society* **2010**, *132* (34), 11967-11977.
56. Momper, R.; Zhang, H.; Chen, S.; Halim, H.; Johannes, E.; Yordanov, S.; Braga, D.; Blulle, B.; Doblas, D.; Kraus, T.; Bonn, M.; Wang, H. I.; Riedinger, A., Kinetic Control over Self-Assembly of Semiconductor Nanoplatelets. *Nano Lett* **2020**.
57. Gilmore, R. H.; Liu, Y.; Shcherbakov-Wu, W.; Dahod, N. S.; Lee, E. M.; Weidman, M. C.; Li, H.; Jean, J.; Bulović, V.; Willard, A. P., Epitaxial dimers and Auger-assisted detrapping in PbS quantum Dot solids. *Matter* **2019**, *1* (1), 250-265.
58. Weidman, M. C.; Smilgies, D. M.; Tisdale, W. A., Kinetics of the self-assembly of nanocrystal superlattices measured by real-time in situ X-ray scattering. *Nat Mater* **2016**, *15* (7), 775-81.
59. Yuan, X.; Hou, X.; Li, J.; Qu, C.; Zhang, W.; Zhao, J.; Li, H., Thermal degradation of luminescence in inorganic perovskite CsPbBr₃ nanocrystals. *Phys Chem Chem Phys* **2017**, *19* (13), 8934-8940.
60. CrysAlisPRO, O. D. J. Y., England, Agilent Technologies UK Ltd. **2014**, *1* (39.34).
61. Roisnel, T.; Rodríguez-Carvajal, J. In *WinPLOTR: a windows tool for powder diffraction pattern analysis*, Materials Science Forum, Transtec Publications; 1999: 2001; pp 118-123.
62. Sihvola, A.; Ylä-Oijala, P.; Jarvenpää, S.; Avelin, J. J. I. t. o. a.; propagation, Polarizabilities of platonic solids. **2004**, *52* (9), 2226-2233.
63. Zhao, M.; Shi, Y.; Dai, J.; Lian, J. J. J. o. M. C. C., Ellipsometric study of the complex optical constants of a CsPbBr₃ perovskite thin film. **2018**, *6* (39), 10450-10455.
64. Yan, W.; Mao, L.; Zhao, P.; Mertens, A.; Dottermusch, S.; Hu, H.; Jin, Z.; Richards, B. S. J. O. e., Determination of complex optical constants and photovoltaic device design of all-inorganic CsPbBr₃ perovskite thin films. **2020**, *28* (10), 15706-15717.

Chapter 5. Chirality induction to CdSe nanocrystals self-organization on silica nanoribbons tuning chiroptical properties

Chapter 5. Chirality induction to CdSe nanocrystals self-organized on silica nanoribbons tuning chiroptical properties

1. Introduction.....	133
2. Quantum dots size and molar concentration calculations.....	135
3. Result and discussion.....	138
3.1 Grafting density effects.....	139
3.2 Concentration, temperature, and solvent effect.....	143
3.3 CdSe-silica helical ribbons annealing.....	145
3.4 CdSe-silica helical ribbons PMMA film.....	146
3.5 Size and crystal structure effect.....	147
3.6 The effect of the chiral morphologies: Helical vs twisted ribbons.....	153
3.7 Core-shell structured QDs with silica helical ribbons.....	158
3.8 Quantum rods shape effect.....	160
4. Conclusion.....	167
5. Experiment section.....	168
5.1 Chemical and reagents.....	168
5.2 Cubic crystal structured CdSe QDs synthesise and purification.....	168
5.3 Hexagonal crystal structured CdSe QDs synthesise and purification.....	169
5.4 CdSe/CdS quantum rods (QRs) synthesise and purification.....	169
5.5 Grafting of QDs and QRs on the surface of silica helices by ligand exchange methods.....	170
5.6 Optical properties simulations by CDM.....	171
6. Reference.....	173

Chapter 5. Chirality induction to CdSe nanocrystals self-organized on silica nanoribbons tuning chiroptical properties

1. Introduction

Semiconductor nanocrystals (SNCs) exhibit excellent photoelectric properties which have been widely studied in solar cells, light-emitting diodes (LED), and display.^{1,2} Recently, chirality induction to SNCs has attracted lots of attention due to their chiral-induced spin selectivity (CISS) effect which has shown prospective applications in biological electron transfer, enantioselective separation, and asymmetric catalysis as well as spintronics.³⁻⁶ Optical activity of SNCs induced by chiral ligands are most widely studied since 2007⁷, the first reported optical activity of CdS quantum dots (QDs) capped with D- or L-penicillamine. In 2009⁸, Nakashima reported the chirality memory effects on CdTe QDs where the chiral nature of the QDs was maintained after the ligands were exchanged with achiral ones. The magnetic, electrical, and optical properties of SNCs depend on their size, shape, and crystals structure. In 2011, Tang⁹ and Markovich¹⁰ simultaneously reported that the CdSe QDs combined with chiral ligands show the optical activity which depends on the QDs' size (dissymmetry factor or g-factor decreased with increasing the QDs size) likely due to the decreasing surface-to-volume ratio. Meanwhile, more factors play roles in determining the g-factor, such as the types of chiral ligand, chiral ligand density, chiral ligands binding mode, and the dipole moment of the QDs.¹¹ In 2013¹², Balaz *et al.* showed that the CdSe QDs combined with L/D cysteine show that the g-factor increased with the increasing QD size. In 2019¹¹, Gun'ko reported that the chiral ligand concentration and binding mode have an important effect on the g-factor with a 10 times difference. In 2018¹³, Tang reported that the CdSe nanoplatelets with wurtzite (hexagonal) and zinblende (cubic) crystal structure combined with L/D cysteine shown different chirality induction. CdSe NPLs with hexagonal crystal structure showed 10 times larger CD signal compared to those having cubic crystal structure. This was explained as the results of their different dipole moment and polarization. In 2017¹⁴, Tang reported that the CdSe rods with different aspect ratio

having L/D cysteine ligands show different g-factor. The g-factor increases with the increasing aspect ratio (sphere to rod) and reaches a plateau when the aspect ratio is about 4. In general, the CdSe QDs combined with chiral ligands suffer lower photoluminescence quantum yield (PLQY) and seldom circularly polarized luminescence (CPL) was reported. Core-shell structured QDs would boost the PLQY, however, it hampered the chirality induction.¹⁵ Recently, core-shell structured CdSe/CdS with various morphologies such as quantum rods¹⁶, tadpoles¹⁷ also have been reported which could enhance the chirality induction compared to core-shell QDs.

Chirality induction by chiral building block system has been widely studied in recent decades, especially for all organic self-assembly,^{18, 19} organic and inorganic hybrid self-organization such as plasmonic gold nanoparticles and nanorods.²⁰⁻²⁴ While the self-organization with organic molecules suffers limited organization stability with external parameters such as temperature, solvent, salinity or pH,^{25, 26} the alternative inorganic chiral self-organization system is still at an emerging point to get stable self-organization system. Recently, our group reported that gold nanoparticles electrostatically or covalently bonded on the surface of nanometric inorganic silica helical ribbons show plasmonic induced CD mirror images in suspension.^{27, 28} More recently, we reported that semiconductor nanocrystals CsPbBr₃ can also be helically grafted on inorganic silica helical nanoribbons templates. Interestingly, they do not show any optically active properties in suspension, while when they are drop-casted on a substrate and dried, which show large g-factor (6×10^{-3}) of CD and CPL.²⁹ The CsPbBr₃ QDs on the chiral inorganic platform show good helical arrangement and are stable against temperature variation. In the present study, we have investigated achiral CdSe quantum dots with different sizes, crystal structures along with CdSe/CdS quantum rods (QRs) with different lengths grafted around the inorganic silica nanoribbons to obtain the helical arrangement. Their chiral optical properties have been studied by experiment and compared with theoretical simulations. Similar to our previous report on CsPbBr₃ on silica nanoribbons, CdSe-silica helical nanoribbons do not show CD signals in suspension but show large signals when dried as a film. The

g-factor increased with the increasing grafting density as well as the size of the crystals. The effect of morphological differences between helical (cylindrical curvature) and twisted (saddle-like curvature) ribbons on their chiroptical properties was also studied. The g-factor of QDs-silica helical ribbons is larger than that of the QDs-silica twisted ribbons. Finally, rod-like QDs (QR), with different aspect ratios were grafted on silica twisted ribbons. Their grafting direction concerning the helix surface changed from side-grafting for short QR to tip-grafting for long rods and the corresponding CD spectra switched signs. All these results were compared with the simulation performed using coupled dipole method (CDM). This simulation reveals that the CD comes from the dipolar interaction between QDs organized in chiral structure.

2. Quantum dots size and molar concentration calculations

Quantum dots synthesis methods were described in the experiment section. The as-prepared cubic and hexagonal crystal structured CdSe QDs size and molar concentration were calculated based on Peng's method.³⁰ Typically, the purified QDs toluene solution was diluted 40 times and measured by a UV-vis spectrophotometer. The first absorption peak position (λ) and absorbance (A) were recorded. Based on the formula below, the size and molar concentration could be calculated.

$$A = \epsilon * c * l$$

$$D = (1.6122 * 10^{-9}) \lambda^4 - (2.6575 * 10^{-6}) \lambda^3 + (1.6242 * 10^{-3}) \lambda^2 - (0.4277) \lambda + 41.57$$

$$\epsilon = 5857(D)^{2.65}$$

Where A , ϵ , c , l , λ , and D are absorbance, molar absorptivity ($L / (mol * cm)$), CdSe QDs concentration (mol/L), cuvette path length (cm), first absorption peak wavelength, and diameter of QDs, respectively.

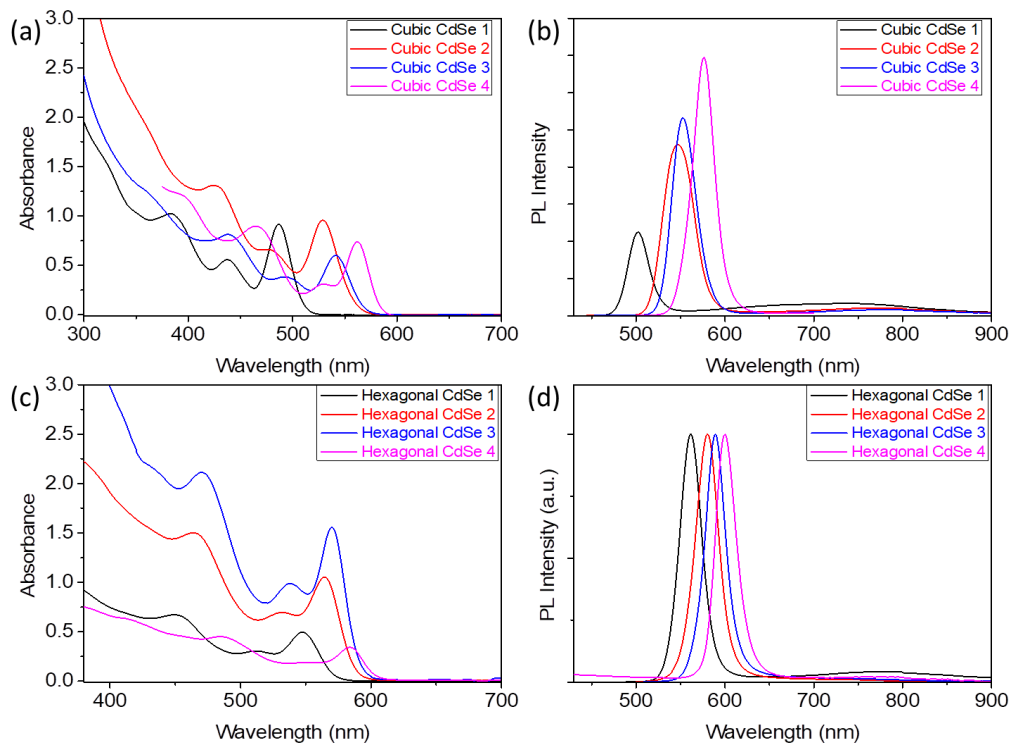


Figure 5-1. the absorption and emission spectra of size depended cubic crystal structured CdSe (a) and (b), and hexagonal crystal structured CdSe (c) and (d).

The as-prepared cubic crystal structured CdSe QDs with different sizes shows tunable absorption and emission spectra as shown in Figures 5-1 (a-b). All the QDs showed a strong first absorption peak which can be used for the size and molar concentration calculations. The detailed information is shown in Table 5-1, the QDs average diameters are tunned from 2.22 nm to 3.31 nm labeled as C1-4. The absorption and emission spectra of as-prepared hexagonal crystal structured CdSe with tunable sizes are shown in Figures 5-1 (c-d). The hexagonal crystal structured CdSe were prepared at a higher temperature (370 °C) which shows a bigger size. The sizes are varied from 2.99 to 3.94 nm. The detailed information is shown in Table 5-2. The typical XRD data of C4 CdSe and H1 CdSe confirm that they have the cubic and hexagonal crystal structure separately as shown in Figures 5-2 (a-b).

Table 5-1. The parameters of cubic crystal structured QDs with different sizes.

Chapter 5. Chirality induction to CdSe nanocrystals self-organization on silica nanoribbons tuning chiroptical properties

Cubic QDs	CdSe	The first exciton absorption peak	Absorbance	Diameter of QDs	of Molar concentration	PL peak	FWHM
C1		486.5 nm	0.9145	2.22 nm	18.82 uM	502 nm	28 nm
C2		529.0 nm	0.9568	2.68 nm	11.96 uM	547 nm	40 nm
C3		541.5 nm	0.5996	2.88 nm	6.20 uM	553 nm	32 nm
C4		562.0 nm	0.7388	3.31 nm	5.30 uM	576 nm	29 nm

Table 5-2. The parameters of hexagonal crystal structured QDs with different sizes.

Hexagonal CdSe QDs	The first exciton absorption peak	Absorbance	Diameter of QDs	of Molar concentration	PL peak	FWHM
H1	547.5 nm	0.49472	2.99 nm	4.63 uM	561 nm	28 nm
H2	564.5 nm	1.05207	3.37 nm	7.18 uM	580 nm	40 nm
H3	570.0 nm	1.55849	3.52 nm	9.49 uM	589 nm	32 nm
H4	583.5 nm	0.34207	3.94 nm	1.54 uM	600 nm	29 nm

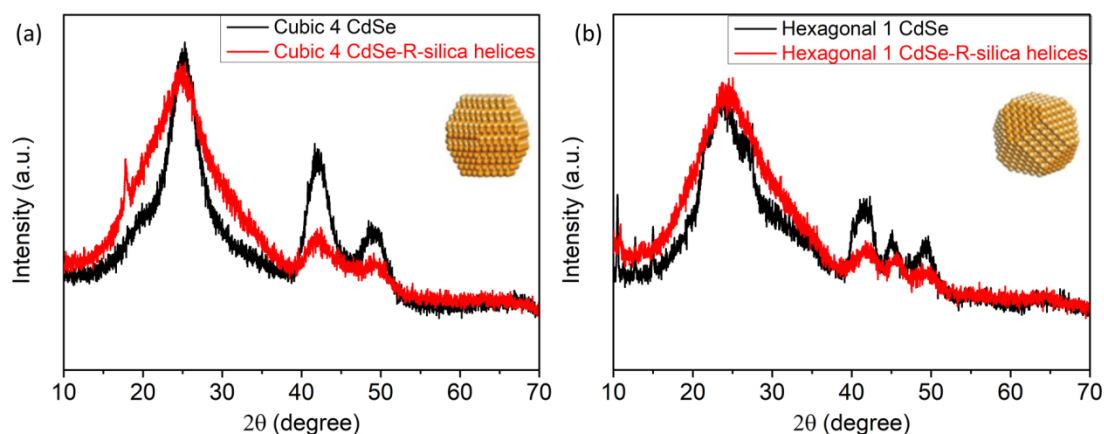


Figure 5-2. XRD of cubic crystal structured CdSe QDs and after grafted with silica helical ribbons (a), XRD of hexagonal crystal structured CdSe QDs and after grafted with silica helical ribbons (b).

The as-prepared cubic and hexagonal crystal structured QDs were measured with CD and CPL as shown in Figure 5-3. No CD and CPL signals were observed indicate that all the as-prepared QDs are nonchiral QDs.

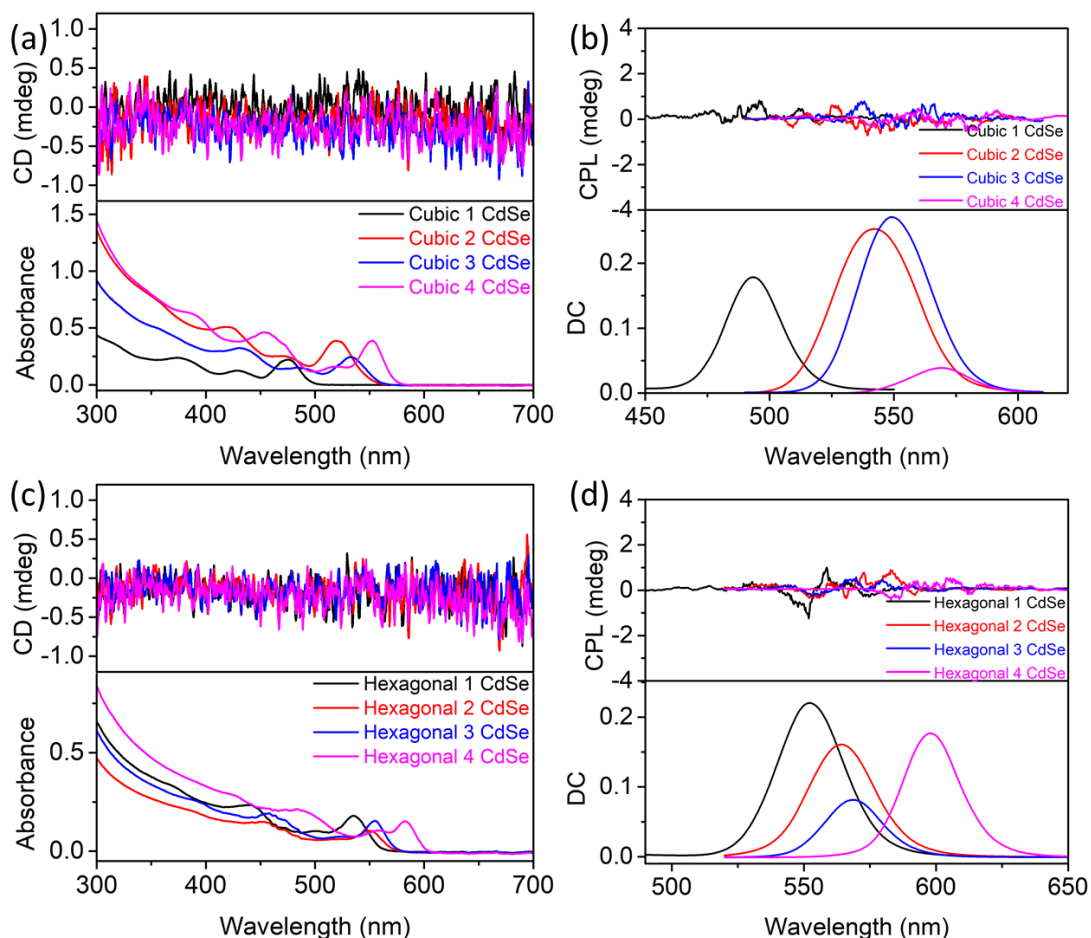


Figure 5-3. Size-dependent CD, absorption, CPL, and emission (DC) spectra of cubic crystals structured CdSe QDs (a) and (b), hexagonal crystal structured CdSe QDs (c) and (d) in toluene solution.

3. Result and discussion

Before evaluating the size effect of the QDs-silica ribbons system, it is necessary to ensure the maximum grafting density with different sizes of QDs. Based on the TEM images of silica helical ribbons and twisted ribbons, the basic approximate parameters are shown in chapter 2 Figure 2-4, and Table 2-1. For the silica helical ribbons, the efficient surface area for QDs grafting is around 4210 nm^2 for 1 pitch and $7.59 \times 10^{16} \text{ nm}^2$ for 0.5 mg silica helical ribbons. For the CdSe QDs with a diameter of 3.3 nm, in solution, the expended surface ligands length is around 2 nm which means the total diameter of QDs in suspension is around 7.3 nm. If the QDs in solution are closely

packed, the minimum area of QDs occupied on the surface of silica is around 44 nm^2 . So the maximum grafting numbers are around 96 for 1 pitch and 1.73×10^{15} for 0.5 mg silica helical ribbons theoretically. The ligand exchange method is used for all the QDs grafting as shown in the experiment section.

3.1 Grafting density effects

The as-prepared C4 QDs were used for the grafting density studying. Different number of QDs (I) 8.7×10^{14} , (II) 8.7×10^{15} , (III) 1.7×10^{16} , (VI) 8.7×10^{16} , and (V) 1.7×10^{17} were mixed with 0.5 mg silica helical nanoribbons. The approximate surface area of silica helical and twisted nanoribbons is calculated as shown in chapter 2. For the helical ribbons and twisted ribbons, their surface areas are around 8400 nm^2 and 6040 nm^2 respectively, for 1 pitch of the helix. For helical ribbons, the only outer surface is accessible for QD grafting, and for twisted ribbons, both sides are equally accessible, (7.6×10^{16} or $7.93 \times 10^{16} \text{ nm}^2$ for 0.5 mg of silica helical or twisted nanoribbons respectively). After grafting, the un-grafted QDs were removed by washing with toluene, and the silica helices @CdSe QDs were dispersed into 0.5 mL toluene. Then 50 μL of this suspension was drop-casted on the surface of quartz plate (around $1 \times 1 \text{ cm}$) at $4 \text{ }^\circ\text{C}$. The CD spectra were recorded based on the mean spectra of silica helices @QDs film measured at 0° and 90° . Figures 5-4 (a-c) show the TEM images of drop-casted silica helices @CdSe QDs for the samples (I), (II), and (VI). Figure 5-4 (d) shows the solvated cryo-electron microscopy (cryo-EM) image of the sample (VI). Based on both types of TEM images, grafted QD numbers per pitch are approximate, (I) 18, (II) 39, (III) 59, (VI) 65, and (V) 60. This indicates that the grafting density reaches a plateau at around 60-65 QDs /pitch. In agreement with our previous report on perovskite nanocrystals on silica helices,²⁹ the silica helices @CdSe QDs in suspension do not show CD signals as shown in Figure 5-13. However, once deposited on the substrates and formed dried films, they show large CD signals as shown in Figure 5-4 (e). It is important to note that these observed CD signals are composed of two factors, scattering from the hybrid nanoobjects and

Chapter 5. Chirality induction to CdSe nanocrystals self-organization on silica nanoribbons tuning chiroptical properties

absorption. As it is difficult to separate these two factors experimentally, two methods to calculate the g-factor $g_{\text{abs}} = \Delta\epsilon/\epsilon = \theta(\text{mdeg}) / (32980 * A)$ were used, one is by using the raw data (which includes the scattering) and the second is by only taking into account the first exciton absorption peak at around 546 nm. In the latter case, the absorption peak of QDs at around 546 nm which originates from the first exciton absorption peak due to the transition between the valence band and conduction band of QDs as shown in Figure 5-5 (a). Indeed, the CD peak at around 546 nm is attributed to the exciton absorption peak which means the ΔCD is attributed to the ΔAbs as shown in Figures 5-5 (b) and Table 5-3. In this case, the g-factor of electronic circular dichroism could be calculated as $g_{\text{electronic-abs}} = \Delta\theta(\text{mdeg}) / (32980 * \Delta A)$ approximately. As shown in Figure 5-4 (f), the g-factors increased strongly with the QDs grafting density. Below 20 QDs/pitch, no detectable CD signal was observed, however beyond 40 QDs/pitch, they increase until about 2.75×10^{-3} for the grafting density of ~ 70 /pitch.

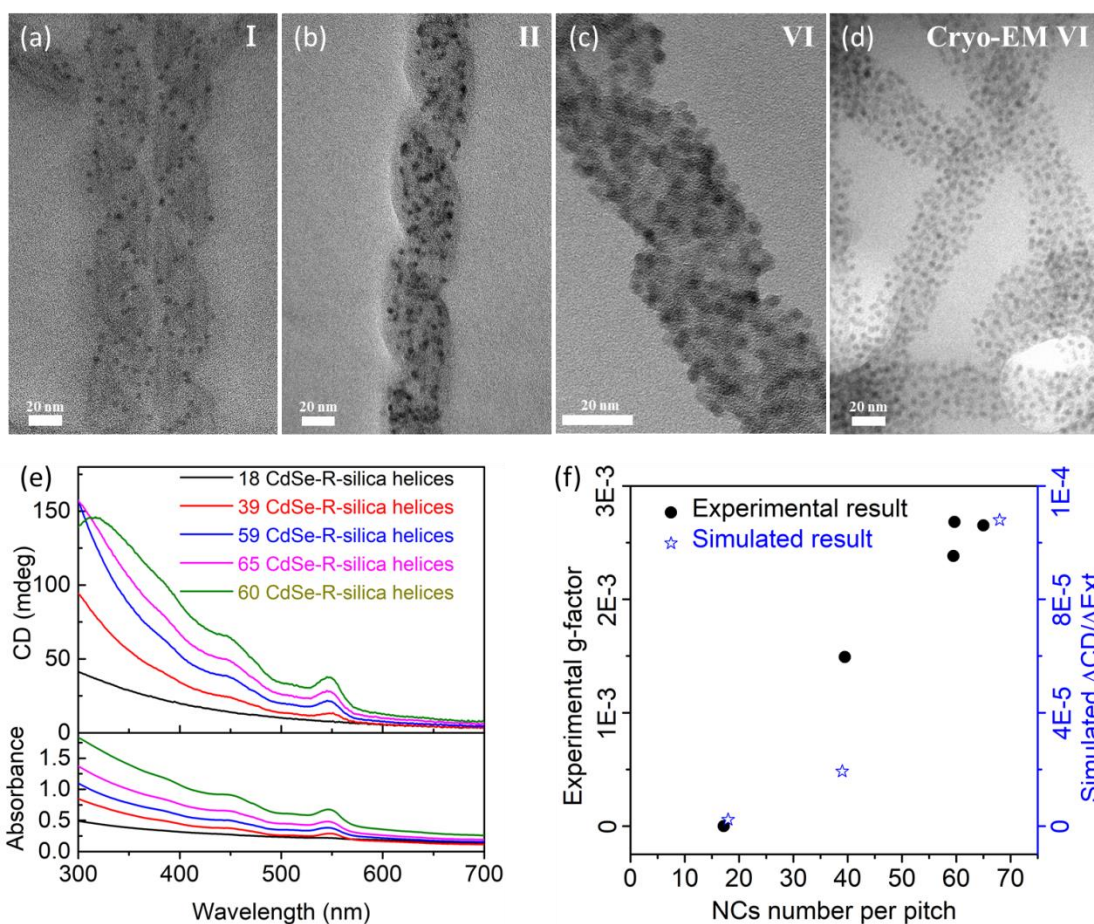


Figure 5-4. (a-c) The TEM images of R-silica helices@QDs with different ratio (I), (II) and (VI); (d) The cryo-EM image of QDs-R-silica helical nanoribbons (VI); (e) CD and absorption spectra of QDs-R-silica helical nanoribbons film with different ratio; (f) Experimental calculated electronic g-factor at first exciton absorption peak and simulated CD/Ext at first exciton absorption peak of the model helix with 18, 39, and 68 particles /pitch.

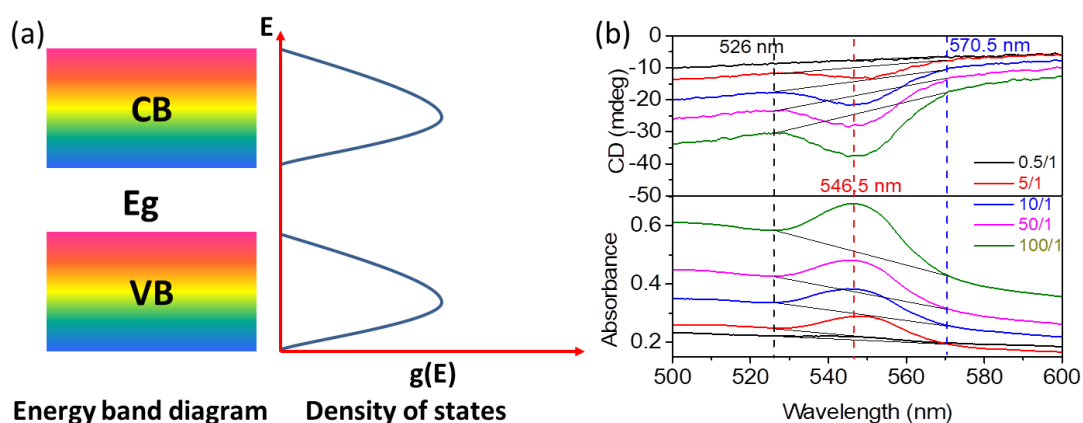


Figure 5-5. QDs energy band and density of states diagram (a), and the way to calculate the g-factor without scattering (b).

Table 5-3. The detailed parameters of the g-factor calculations.

	0.5/1	5/1	10/1	50/1	100/1
A1(546.5 nm)	0.2217	0.2874	0.3821	0.4848	0.6741
A2(546.5 nm)	0.2093	0.2217	0.2998	0.3738	0.5137
ΔA	0.0124	0.0657	0.0823	0.1110	0.1604
CD1(546.5 nm)	-7.80	-9.76	-14.31	-18.80	-24.56
CD2(546.5 nm)	-7.80	-13.13	-21.42	-28.14	-37.49
ΔCD	0	-3.37	-7.11	-9.34	-12.93
$\Delta CD/(32980 * \Delta A)$	0	$-1.56 * 10^{-3}$	$-2.62 * 10^{-3}$	$-2.55 * 10^{-3}$	$-2.44 * 10^{-3}$

The impact of the QDs density is also investigated through simulations based on

CDM as shown in simulation section. Each QD is represented as a point dipole. Their diameter was set to 3.3 nm. The QDs were organized into a square lattice on a ribbon with a 30 nm width. The gap distance between two adjacent QDs was adjusted to control their density. Then, the ribbon was wound around into helix. The pitch and the diameter of the helix as determined by TEM were 65 nm and 35 nm, respectively. The length of the helix was 500 nm. As illustrated in Figure 5-6 the simulation globally reproduced the measurements. Indeed, extinction and CD spectra are dominated by an excitonic band located at 560 nm. Some bands associated with to critical point in the joint density of the state of QDs are also observed at 460 nm, 480nm, and 530 nm. The CD of right-handed and left-handed QDs helices are opposite in sign. Contrary to measurement, the extinction cross-section of QDs helix is equal to 0 above the bandgap located at 592 nm. Indeed, our simulations do not take into account the scattering losses induced by silica helices. As expected, the extinction cross-section, the CD, and the g-factor (Figure 5-4 (f)) increase with the density of QDs in the helices. Indeed, the interaction between QDs is enhanced when the gap between QDs decreases. Inversely, below a certain grafting density ~ 20 QDs/pitch, no CD signal was observed. These results confirm that the CD signal comes from two contributions: i) the dipolar interaction between QDs organized into the chiral structure, which requires their grafting density to be beyond 20 QDs/pitch and ii) the scattering from silica helices QDs.

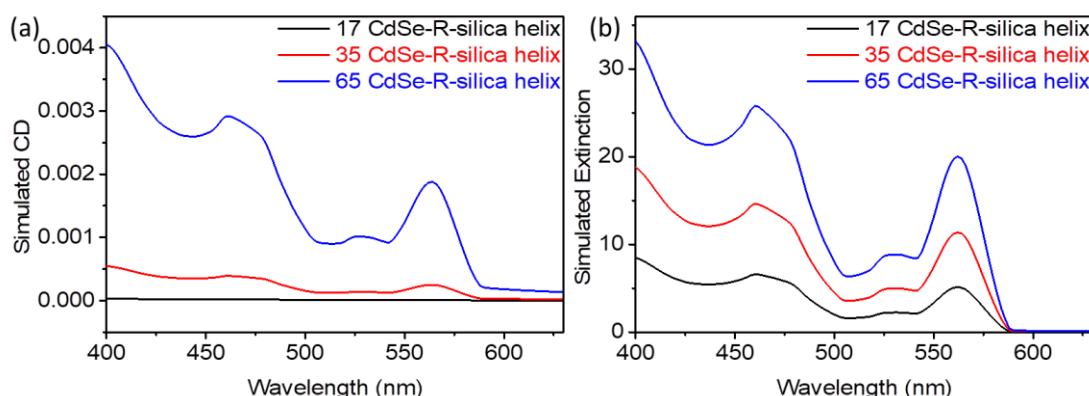


Figure 5-6. Simulated CD (a) and extinction (b) spectra of CdSe-R-silica helix with different QDs grafting density.

3.2 Concentration, temperature, and solvent effect

In our previous study of gold helical ribbons film²⁸, the higher concentration of gold helical ribbons results in gold nanoparticles coupling between different helical ribbons which quench the chirality. In here, different concentration of CdSe-R-silica helical ribbons films was prepared, and the CD and absorption spectra were measured as shown in Figure 5-7 (a). The CD signals and absorbance at absorption peak increased with concentration increasing. In the absorption peak, unlike the result of gold nanoparticles grafted on the surface of silica helical ribbons that the g-factor decreased with multiple layers, the g-factor almost keep the same with different concentrations as shown in Figure 5-7 (b).

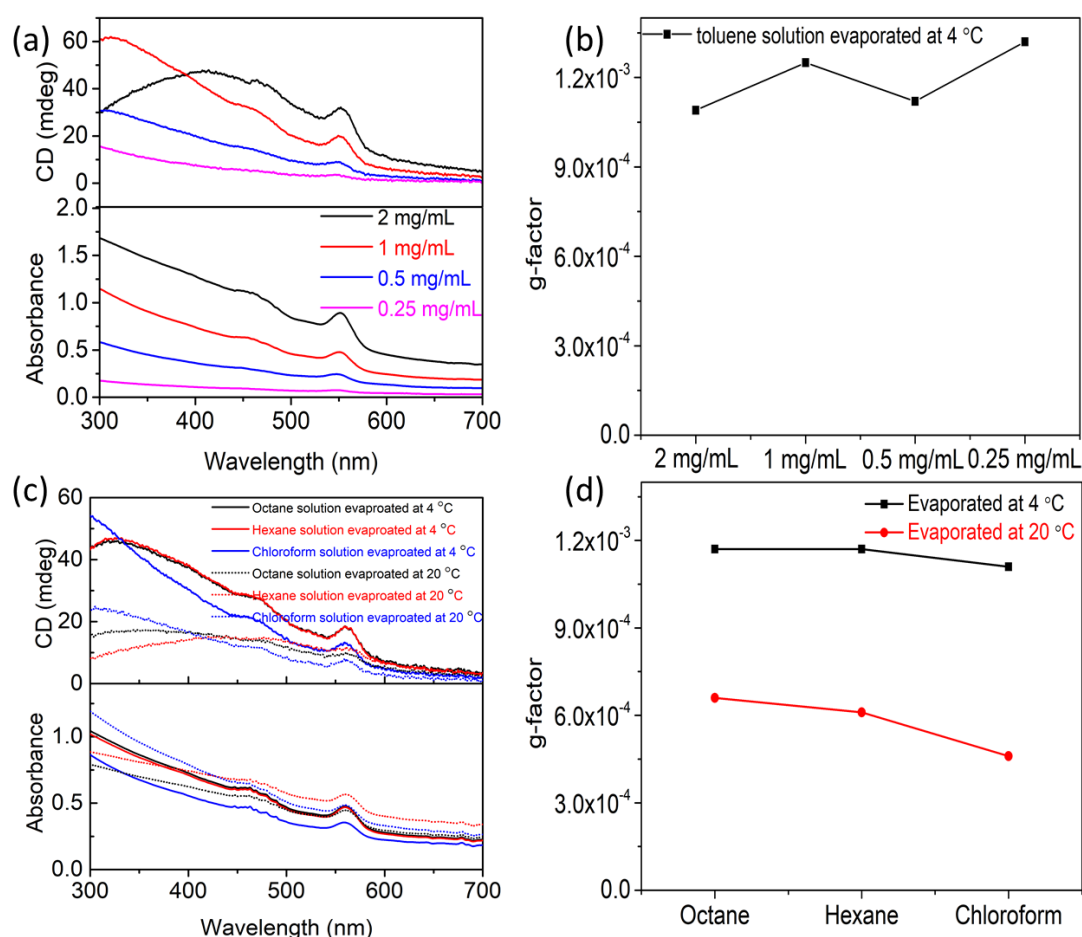


Figure 5-7. CD and absorption spectra of CdSe-R-silica helical ribbons film with different concentrations (a) and different solvents and evaporated at different temperatures (c); g-factor at absorption peak involved with different concentrations (b)

and different solvent and evaporated at different temperature (d).

In the previous work²⁹ of CsPbBr₃-silica helical ribbons films, the drying temperature affects the self-organization of QDs which influences the chirality of QDs-silica helical ribbons. Also, solvent vapor pressure plays a role in nanocrystals' evaporative self-assembly.³¹ Different solvents with different vapor pressure such as octane, hexane, and chloroform were chosen as QDs-R-silica helical ribbons solvent and the films were dried at 4 and 20 °C separately. As shown in Figure 5-7 (c), all the films show positive CD spectra, and it is obvious that the films dried at 20 °C show smaller CD than those dried at 4 °C. As shown in Figure 5-7 (d), the films dried at 4 °C show g-factor around 1.1×10^{-3} , while the films dried at 20 °C show g-factor around 6×10^{-4} . Also, the vapor pressure of chloroform is bigger than hexane and octane at the same temperature, the g-factor is slightly smaller as shown in Figures 5-7 (d). This concludes that the lower temperature and lower solvent vapor pressure showed better QDs self-organization resulting in a higher g-factor. After the solvent exchange, there is no grafting difference and no free QDs observed from the TEM images as shown in Figure 5-8.

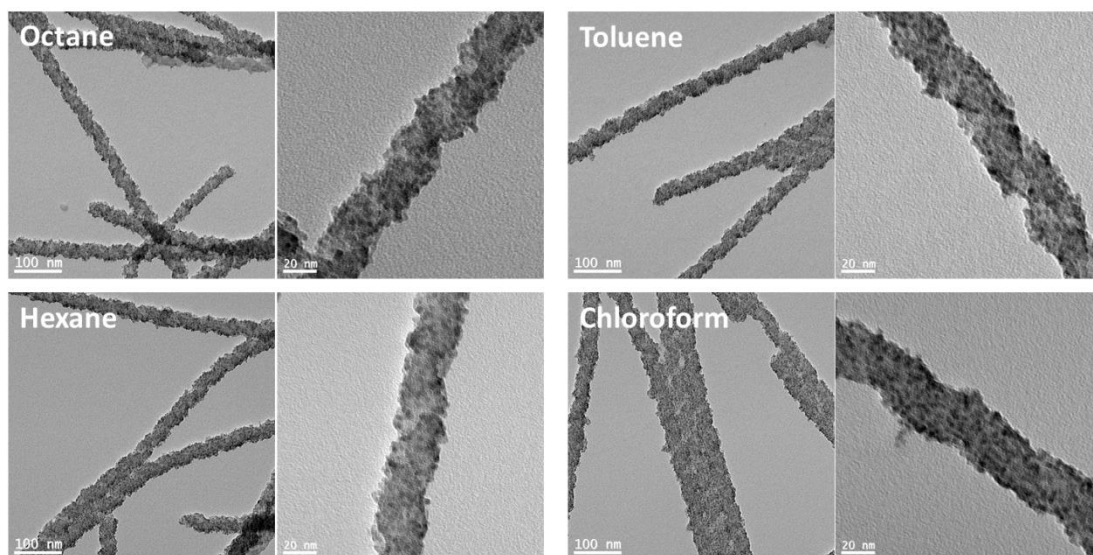


Figure 5-8. TEM images of CdSe-R-silica helical ribbons in different solvents evaporated at 20 °C.

3.3 CdSe-silica helical ribbons annealing

Nanocrystals alignment by oriented attachment has been widely studied.^{32, 33} The oriented attachment could be driven by heat annealing.³⁴ To enhance the chirality of QDs-R/L-silica helical ribbons, the oriented attachment might be a good option.

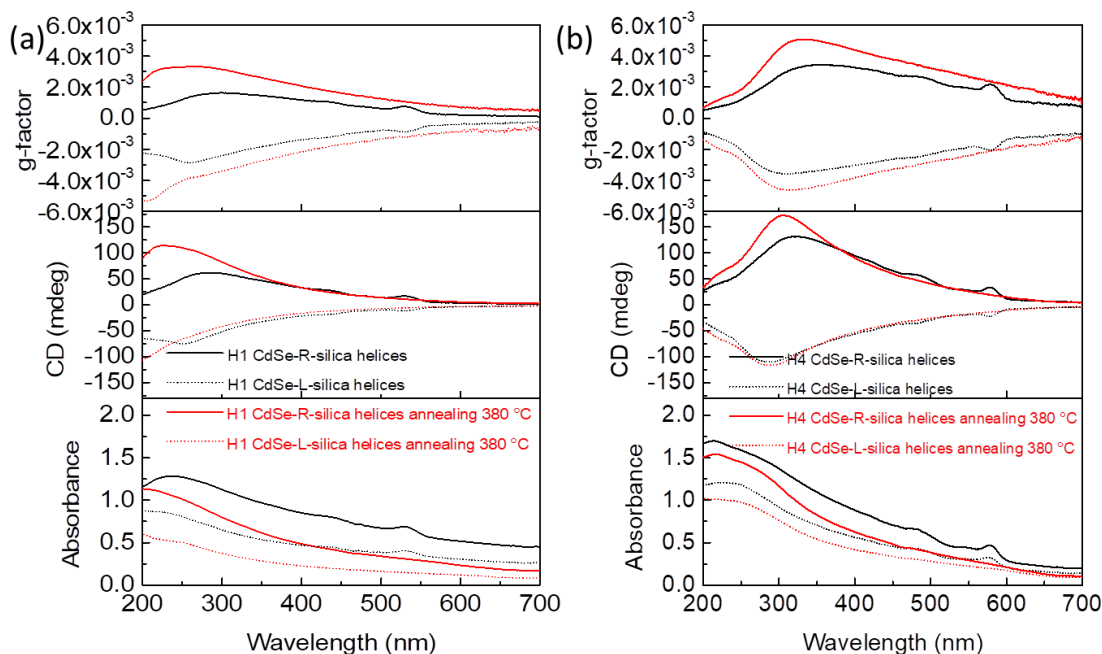


Figure 5-9. g-factor, CD, absorption spectra of H1 (a) and H2 (b) CdSe-R/L-silica helical ribbons before annealing and after annealing at 380 °C.

To make QDs oriented attached on the surface of silica helical ribbons, the H1 and H4 QDs-R/L-silica helical ribbons films were heated to 380 °C for 0.5 h, then the CD was recorded before and after annealing as shown in Figures 5-9 (a) and (b). After annealing, the oriented attachment results in increased QDs size and broad size distribution. As shown in Figure 5-9, the first absorption peak dispersed due to the broad size distribution, and the decreased absorbance is due to the lower concentration of QDs after the oriented attachment of QDs. Even though the absorbance decreased a lot, the CD didn't decrease except the absorption peak position. For the final g-factor, it increased dramatically for the full wavelength. Before annealing, the isolated QDs could be observed, while the QDs are merged after annealing as shown in Figures 5-10 (a-b).

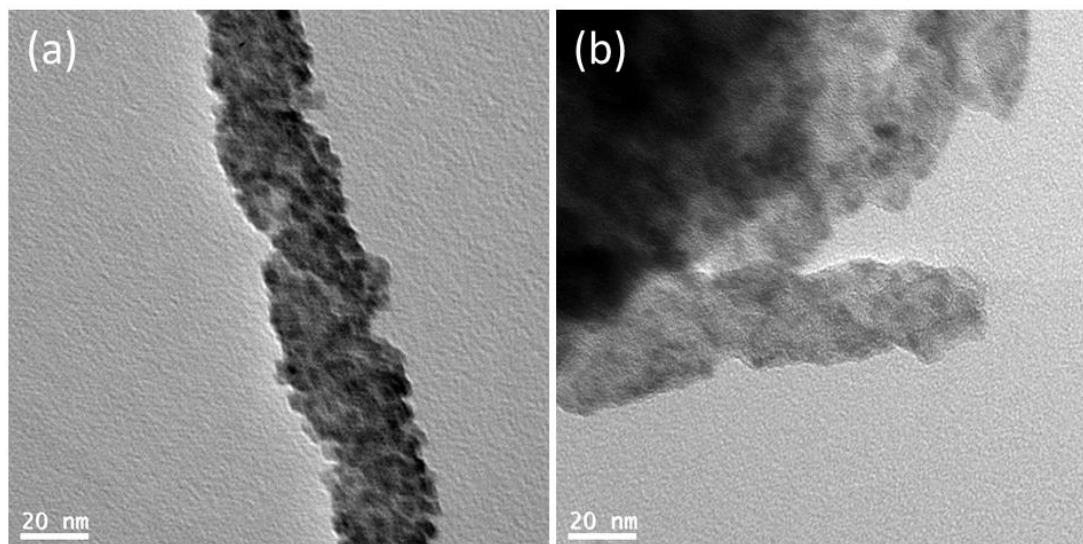


Figure 5-10. TEM images of CdSe-R-silica helical ribbons before (a) and after (b) annealing.

3.4 CdSe-silica helical ribbons PMMA film

To emphasize the importance of the QDs self-organization on the surface of silica helical nanoribbons during the drying process, how the presence of polymer in the suspension can affect/hinder the QDs self-assembly was investigated. Poly(methyl methacrylate) (PMMA) is chosen due to their excellent optical properties and good dispersity in toluene. Interestingly, in the presence of PMMA with a higher concentration than 10 mg/mL, the CD signals disappeared as shown in Figures 5-11 (c-d). The TEM images of silica helix @CdSe QDs with PMMA show clear swelling of the helices from ~35 nm without PMMA to ~40 nm with PMMA (Figures 5-11 (a-b)). Along with the disappearance of the CD signal, this indicates that the presence of PMMA disturbs the close contact and self-organization of the QDs.

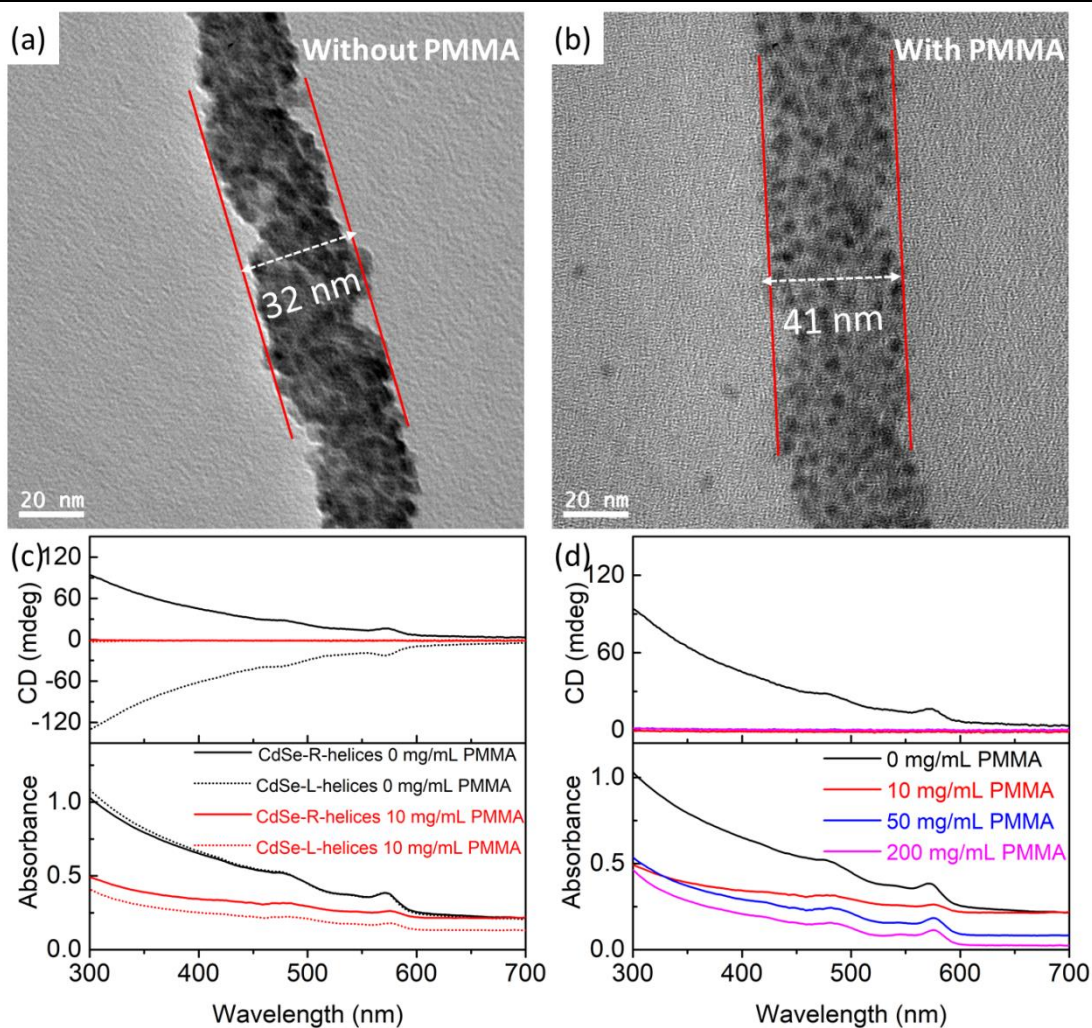


Figure 5-11. TEM images of CdSe-R-silica helical ribbons without PMMA (a), with PMMA (b); CD and absorption spectra of CdSe-R/L-silica helical ribbons without or with 10 mg/mL PMMA film (c) and CdSe-L-silica helical ribbons with different concentration PMMA film (d).

3.5 Size and crystal structure effect

The effect of different crystal structures and sizes of QDs were detailed discussed. The cubic and hexagonal crystal structured QDs with different sizes are labeled as C1-4 and H1-4 respectively. The QDs show size-tunable absorption and emission spectra as shown in Figure 5-1. The QDs size is calculated based on the first exciton absorption peak as shown in Figure 5-1 and Table 5-1 and 5-2. The QDs C1-4 size varied from 2.2, 2.7, 2.9, and 3.3 nm, while the QDs' H1-4 size varied from 3.0, 3.4, 3.5, and 3.9 nm. The QDs alone in suspension do not show any CD and CPL signals

Chapter 5. Chirality induction to CdSe nanocrystals self-organization on silica nanoribbons tuning chiroptical properties

as shown in Figure 5-3. They were then grafted on silica helical nanoribbons (Figures 5-12) and ungrafted QDs were washed away. The QDs before and after grafting on silica don't change their crystal structures as shown in Figure 5-2. Still, in suspension, no CD and CPL were observed as shown in Figures 5-13.

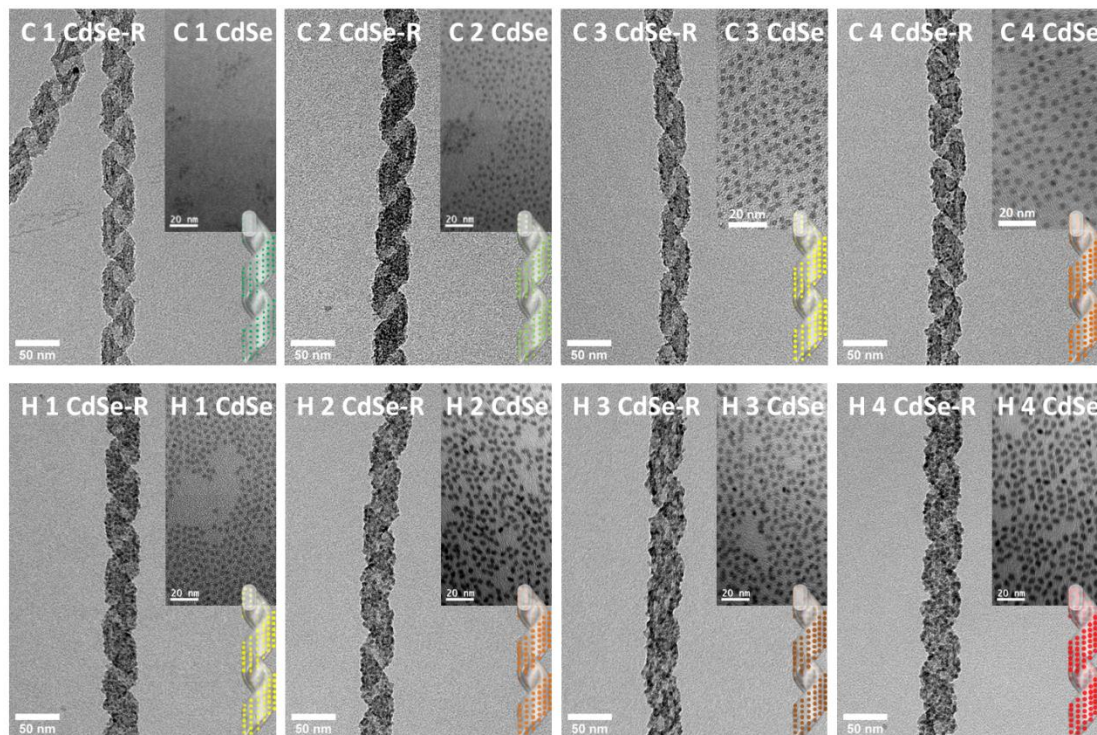


Figure 5-12. TEM images of cubic and hexagonal crystal structured (C1-4 and H1-4) R-silica helices@CdSe QDs.

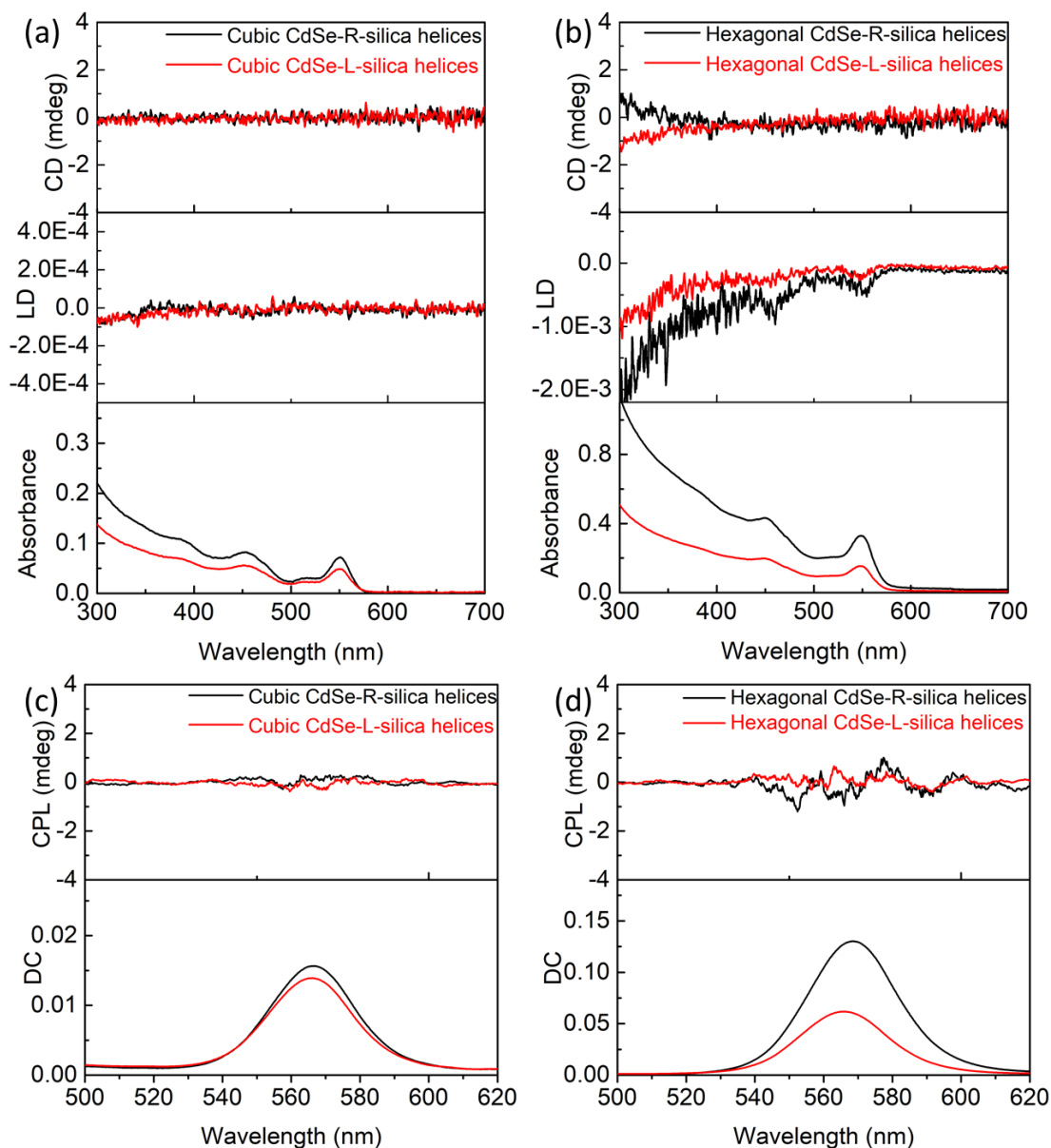


Figure 5-13. CD, LD, absorption spectra of C4 (a) and H2 (b) CdSe-R/L-silica helical ribbons in toluene solution. CPL and DC spectra of C4 (c) and H2 (b) CdSe-R/L-silica helical ribbons in toluene solution.

These silica helices@QDs are drop-casted and dried on the quartz substrate at 4 °C, and the CD signals were measured. Figure 5-14 shows the experimental and simulated CD spectra of C1-4 and H1-4 R-silica helices@QDs. All the QDs with right-handed silica helical nanoribbons show positive CD signals while all the QDs with left-handed silica helical nanoribbons show negative CD signals as shown in Figure 5-15. The absorption spectra, CD spectra as well as g-factors taking into account the

scattering effect are shown in Figure 5-16 (a).

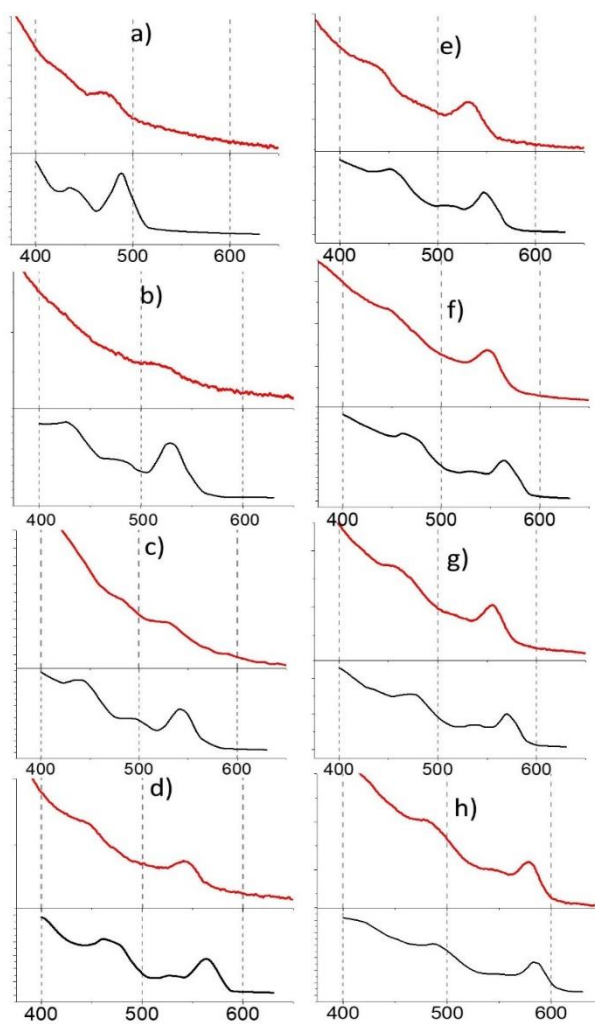


Figure 5-14. Experimental (red curves) and simulated (black curves) CD spectra of C1-4 (a-d) and H1-4 (e-h) QDs-R-silica helical nanoribbons.

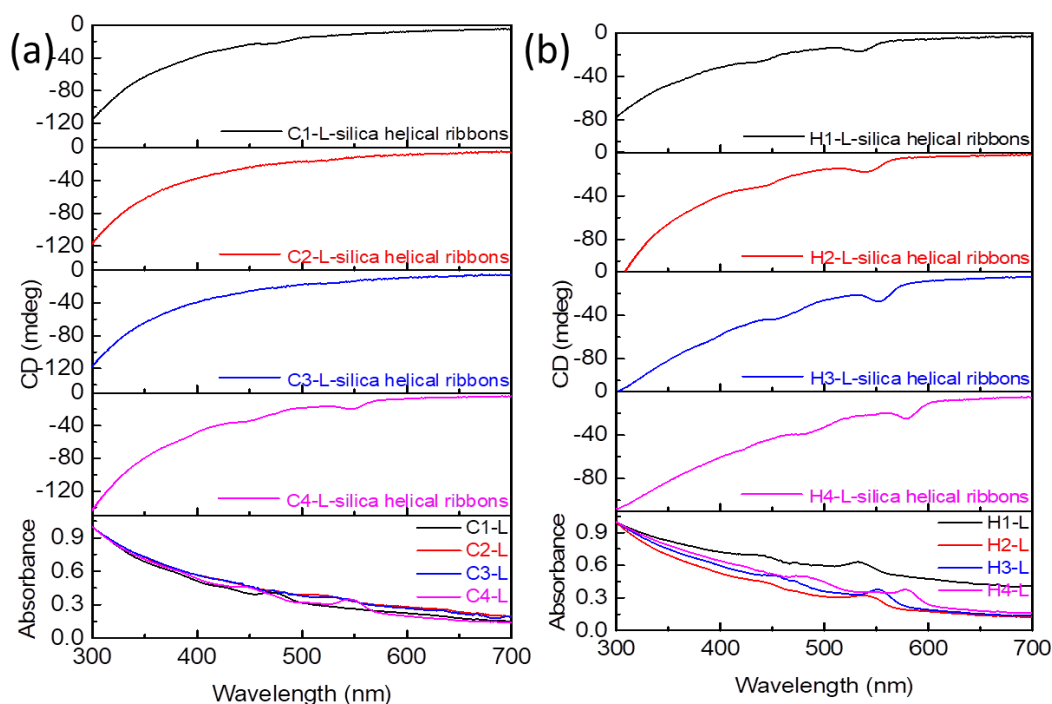


Figure 5-15. CD and absorption spectra of different sizes of crystal structured (a) silica L-helice@ C1-4CdSe and (b) silica L-helice@ H1-4CdSe.

Then the performed simulations with the CDM to elucidate the impact of the QDs size and crystal on the CD were discussed. The QDs sizes are equal to those measured by TEM. The same procedure as presented in the previous section is used to organized QDs into a helical structure. The distance between adjacent QDs is equal to 6.5 nm. The pitch and the diameter of the helix as determined by TEM were 65 nm and 35 nm, respectively. The length of the helix is equal to 500 nm.

The spectral variations observed in the measured spectra are globally well reproduced by the simulations. Indeed, the excitonic band observed in the extinction cross-section and CD spectra are blue-shifted as the QDs size decreased. This behavior is attributed to the confinement effect. The amplitude of the CD and extinction cross-section increases with the quantum dot size. Indeed, the extinction cross-section and the magnitude of the scattered field of a dipole are proportional to its volume. To evaluate the impact of crystallinity, the g-factor of each QDs helix were calculated (Figure

5-16). No discontinuity between the data obtained for cubic and hexagonal crystal structured QDs is observed. Thus, the magnitude and position of the excitonic band are mainly governed by the QDs' size. On the contrary, the crystal structure plays a minor role in the optical properties of QDs helices.

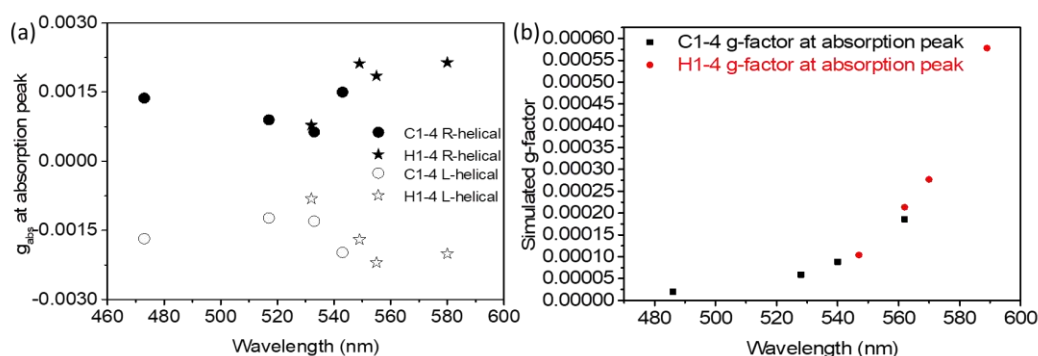


Figure 5-16. (a) g factors calculated at the absorption peak at 550 nm for right-handed and left-handed helices for silica L-helice@ C1-4 and H1-4CdSe QDs. (b) simulated g -factors calculated for silica R-helice@ C1-4 and H1-4CdSe QDs. Black symbols show C1-4 and Red symbols show H1-4 CdSe QDs.

It should be noted that the right-handed samples show positive CPL signals and the left-handed samples show negative CPL signals. However, the bare CdSe suffers lower fluorescence and poor photochemical stability.^{35, 36} CPL were measured with two angles horizontal (0°) and vertical (90°) with excitation wavelength at 365 nm. Due to the lower fluorescence of bare CdSe QDs, high PMT voltage was applied which result in larger noisy signals. Several decades times measurements and final accumulation were necessary to get smooth signals. However, due to the poor photochemical stability of bare CdSe QDs, the DC (fluorescence) signals, as well as CPL signals, increased with light illumination due to the photoactivation effect.³⁵ With a longer time of CPL measurement, the light illumination etches the surface of QDs and reduces the size of QDs which result in little blue shift emission of samples. All those factors make it hard to obtain the exact CPL signals. The typical CPL measurements of C4/H4 QDs-R/L-silica helical ribbons are shown in Figures 5-17.

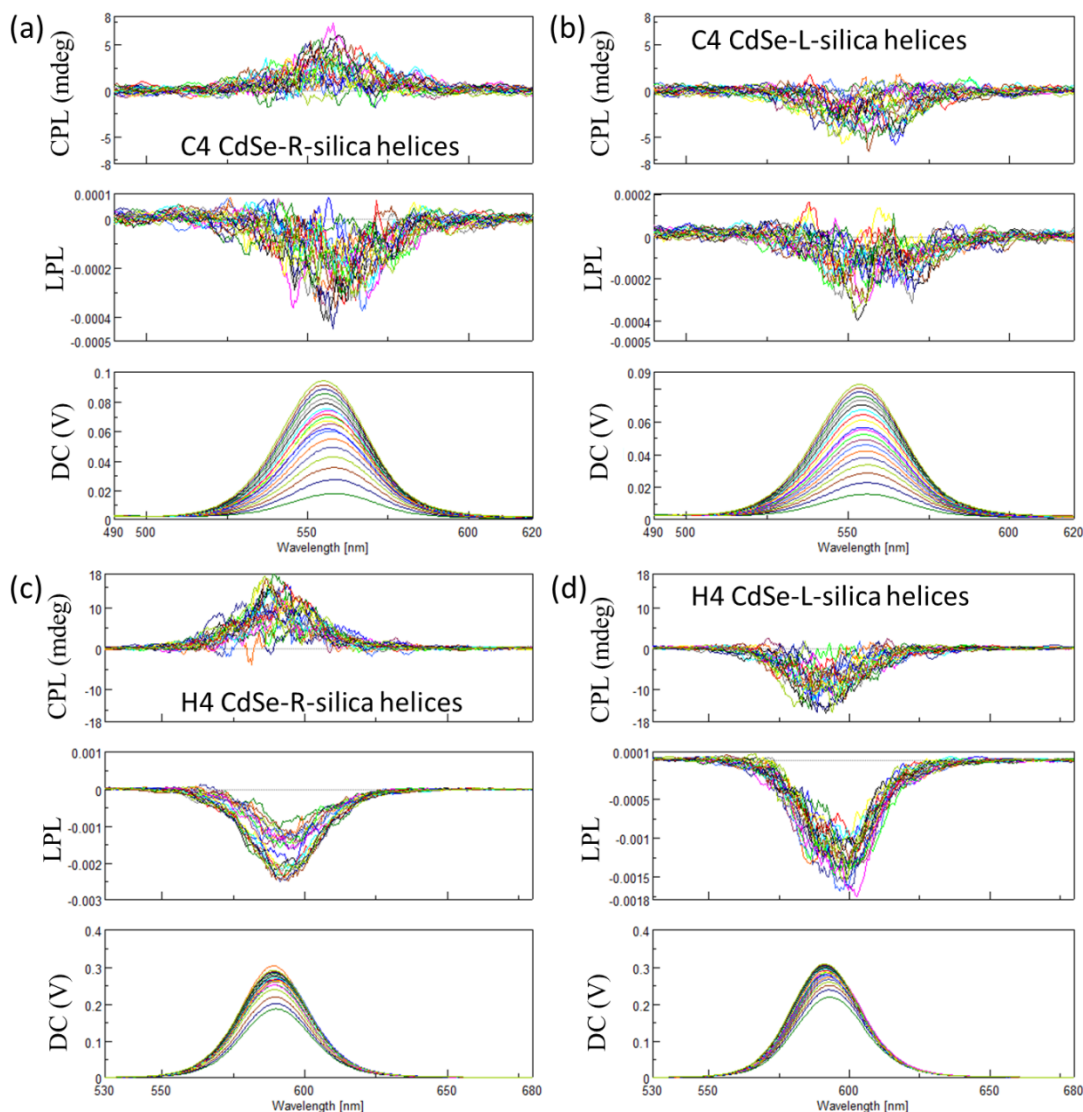


Figure 5-17. CPL, linearly polarized luminescence (LPL), and DC spectra measured with 10 times vertical and 10 times horizontal directions of C4 CdSe-R-silica helical ribbons (a), C4 CdSe-L-silica helical ribbons (b), H4 CdSe-R-silica helical ribbons (c), and H4 CdSe-L-silica helical ribbons (d).

3.6 The effect of the chiral morphologies: Helical vs twisted ribbons

The effect of the chiral morphologies of the silica ribbons, having twisted shape *vs* helical shape was compared. As we have previously reported, depending on the aging time of the Gemini surfactant self-assembly, twisted or helical Gemini tartrate bilayers can be obtained, which then can be transcribed to silica to obtain twisted or helical silica nanoribbons. The helical ribbons and twisted ribbons show the different chiral

shapes and different widths and pitches.

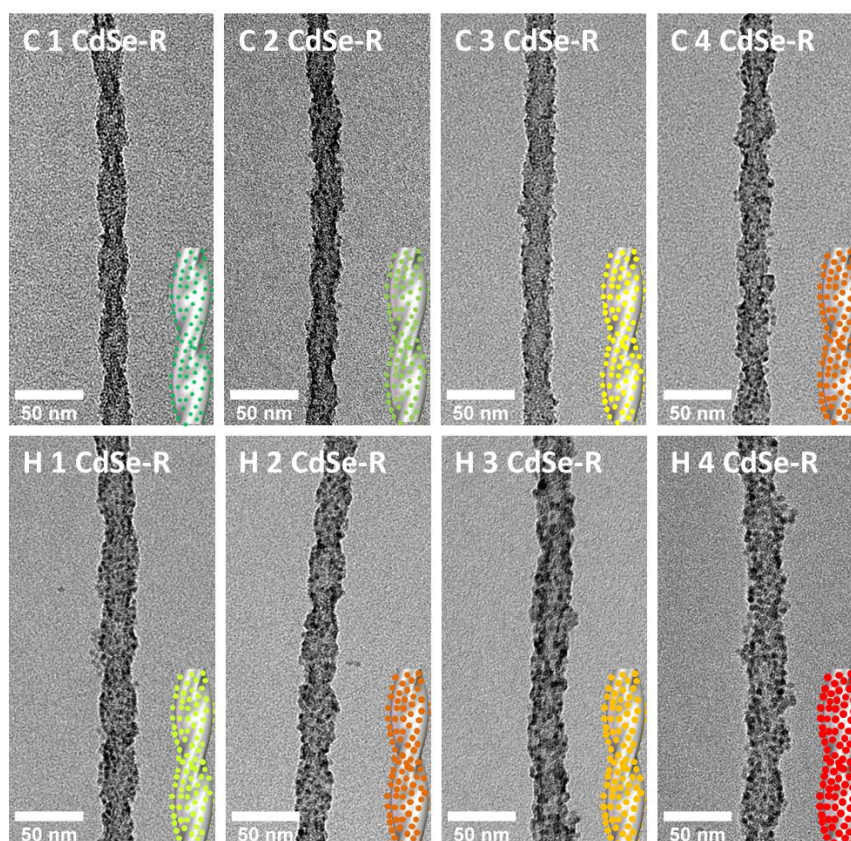


Figure 5-18. TEM images of different sizes of cubic and hexagonal crystal structured QDs (C1-4 and H1-4) CdSe-R -silica twisted ribbons.

As shown in Figures 5-18, QDs are also grafted on the surface of these twisted silica ribbons. In the case of twisted ribbons, both sides of the ribbons are equivalent, and QDs are grafted on both sides. While in suspension, large LD and apparent positive CD signals were observed for both right-handed and left-handed samples as shown in Figures 5-19. When drop-casted on the surface of the quartz, mirror CD images were observed as indicated in Figure 5-20. Here also, the right-handed samples show positive CD signals while the left-handed samples show negative CD signals. However, the CD signals are weaker than the helical samples.

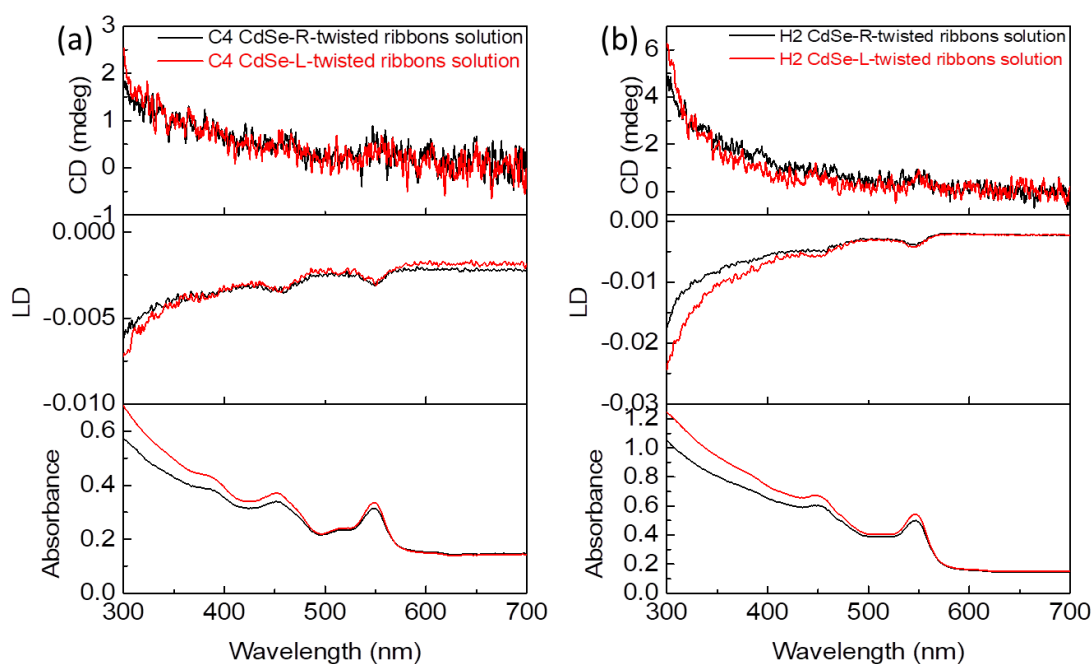


Figure 5-19. CD, LD, absorption spectra of C4 (a) and H2 (b) CdSe-R/L-silica twisted ribbons in toluene solution.

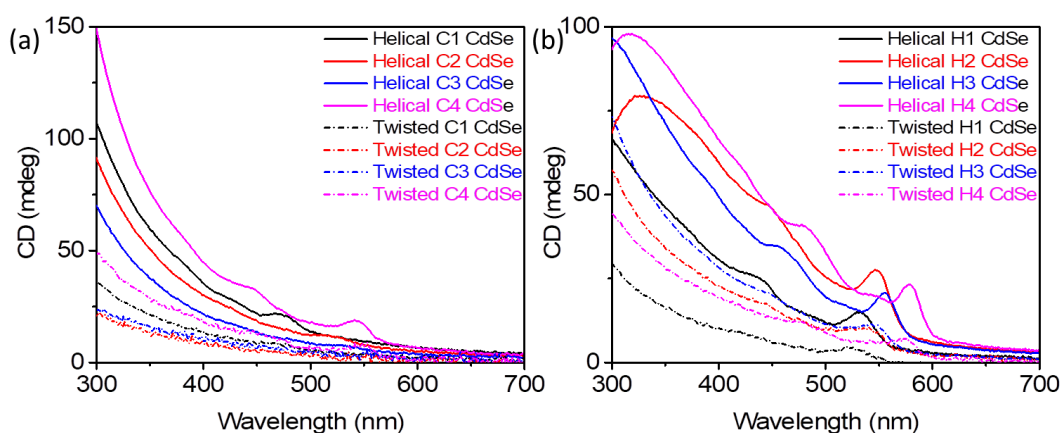


Figure 5-20. CD spectra of (a) R-helical silica@C1-4 QDs and R-twisted silica@C1-4 QDs, (b) R-helical silica@H1-4 QDs and R-twisted silica@H1-4 QDs,

To understand and compare how the twist vs helical platforms for QD grafting affect the CD signal, simplified models were made for which 4 nm QDs are organized on helical vs twisted platforms (based on the observed dimensions) keeping the adjacent QD distance (diameter 4 nm, center to center is 5 nm, therefore inter-particle distance is 1 nm) organized parallel to the long axis of the ribbon (not helix) (Figure 5-21).

When considering this model, for the QD grafted around *helical* silica ribbons, all the QDs are positioned at the same distance (20.5 nm) from the center of the helices, whilst for the QDs grafted around *twisted* silica ribbons, QDs have different distances from the center of the helices, *i.e.* the pink QDs is the farthest (12 nm), then the blue QDs (9 nm). The gray QDs are the closest (7 nm). Not only these three types of QDs have different helical routes to make one pitch, as the inter QD distances are fixed, but there are also different numbers of QDs per pitch. The details of the models are described in Figures 5-22.

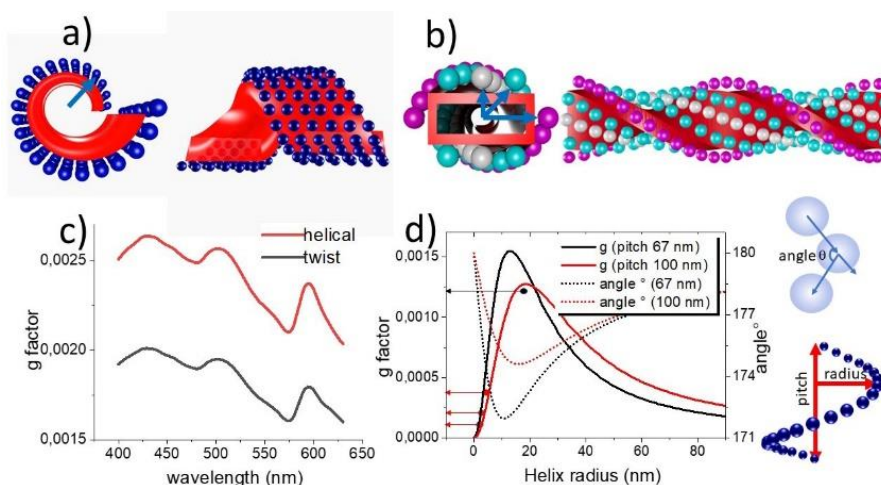


Figure 5-21. Models of QDs grafted on helical (a) or twisted ribbon (b) based on the relative dimensions of QD and silica helices (shown in red). (c) Simulated g-factors for QDs grafted around the twisted ribbon (black) and helical ribbon (red). (d) Simulated g-factor versus helix pitch and QDs-helix center radius.

The CDM simulation on the model shows indeed that the QDs organized around twisted ribbon show lower g-factor (normalized by the number of QDs) than that for helical ribbon. Looking more in detail into the results of a simplified simulation for which at a helically arranged QDs with a fixed interparticle distance (1 nm), The g-factors depend strongly both on the radius and the pitch of the helical arrangement of the QDs (Figure 5-21 (d) and 5-22). For a given pitch, the g-factor is enhanced for a helix radius r_H which minimized the angle between 3 adjacent QDs:

$$r_H = \frac{p}{2\pi}$$

with p the pitch of helical arrangement. This result suggests that the chiroptical properties of QDs helices can be optimized by controlling their geometrical parameters. For this optimal configuration, the curvature of the helical arrangement and the misalignment between three adjacent QDs are maximized.

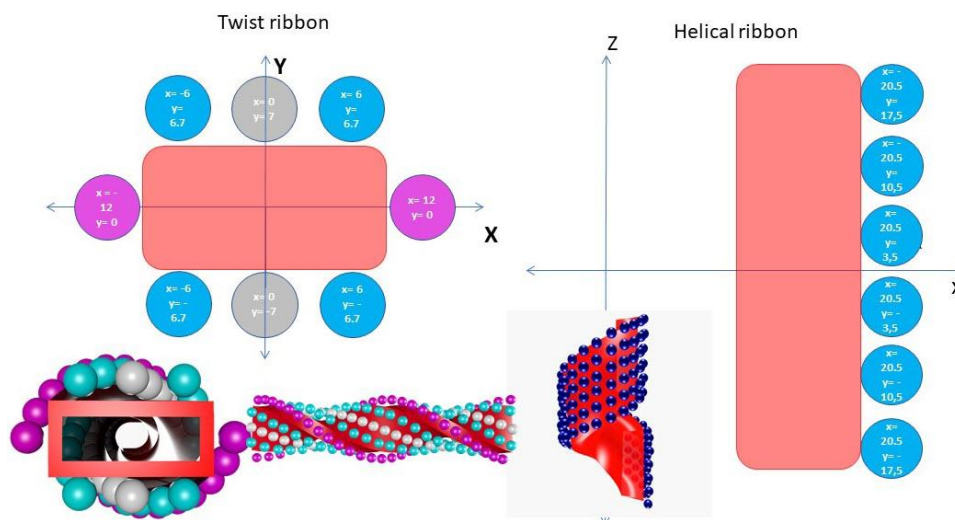


Figure 5-22. Models created for the QDs arranged around twisted or helical ribbons taking into account the real dimensions of the ribbons and QDs (4 nm diameter) and keeping inter QDs distance to be $5 = 4+1$ nm.

Interestingly, the g -factor of the QDs on the helical ribbons (pitch 67 nm and radius 20.5 nm) is close to the maximum of the curve (~ 0.0013) whereas for those on the twisted ribbons, (pitch 100 nm radius 7 (gray), 9 (blue) and 12 (pink) nm QDs) they are all much lower (0.00057, 0.0008 and 0.0011 respectively). This explains why helical ribbons show higher g -factors. In Figure 5-23, the simulated results on the variation of g -factors as well as the angles formed by three consecutive QDs in the direction tangent to the helix as a function of the helix radius for various pitches. A very interesting agreement between the g -factor and the angle variation was observed. Indeed, 1) g -factor is the highest when the curvature formed by the consecutive QDs are the highest (lowest angles), 2) longer the pitches, the maximum of g -factors are observed for the larger helix radius, and 3) the maximum of the g -factor decreases with the pitches.

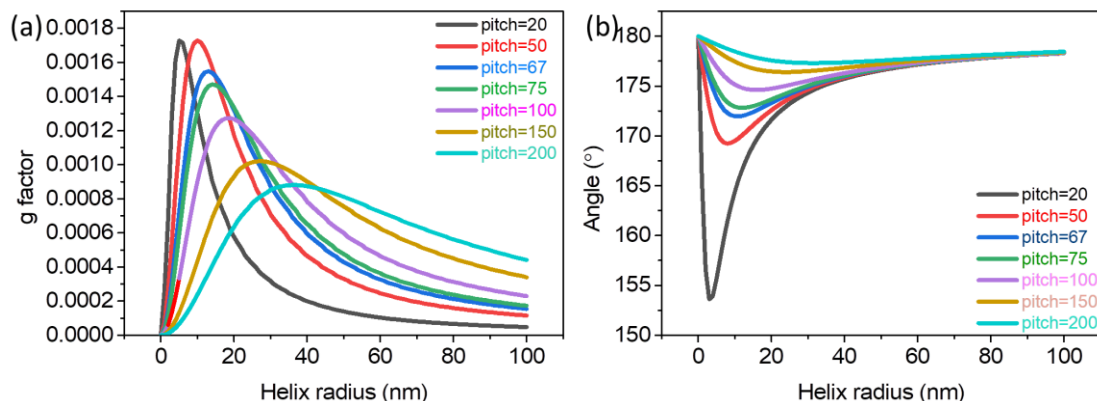


Figure 5-23. Simulated g factor (a) and angle (b) versus with helix pitch for CdSe-R-silica twisted ribbons.

3.7 Core-shell structured QDs with silica helical ribbons

As it is well known, the bare CdSe QDs suffer lower PLQY and poor stability which limit their application such as Vivo imaging, light, and display. Core-shell structured QDs such as CdSe/ZnS QDs exhibit high PLQY and good stability than bare CdSe QDs. Here, core-shell CdSe/ZnS QDs with green (G-QDs-530) and red (R-QDs-620) emission grafted on the surface of silica helical ribbons as shown in Figure 5-24. The core-shell structured QDs are well grafted on the surface of silica helical ribbons due to the larger size and high contrast compared with bare CdSe QDs as shown in Figure 5-25.

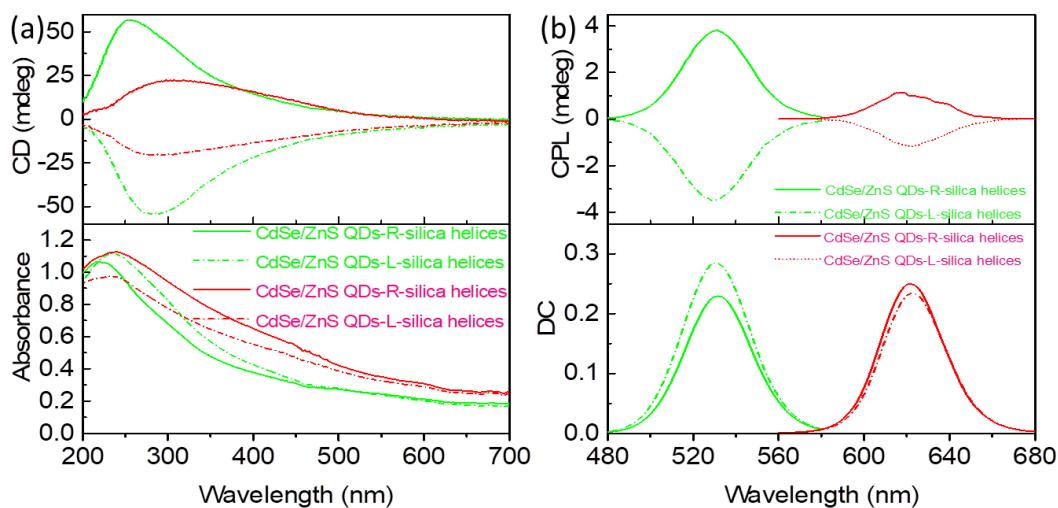


Figure 5-24. CD, absorption spectra (a) and CPL, DC spectra (b) of green and red emission of CdSe/ZnS core-shell QDs-R/L-silica helical ribbons

The right-handed samples show positive CD and CPL signals while left-handed samples show negative CD and CPL signals for the core-shell structured QDs-R/L-silica helical ribbons respectively as shown in Figure 5-24. The core-shell structured QDs show smaller CD and CPL signals compared with the bare CdSe grafted on the surface of silica helical ribbons. The g_{abs} at 365 nm of G-QDs-530-R/L-silica helical are 1.46×10^{-3} for the right-handed sample and -1.77×10^{-3} for the left-handed sample separately. While the g_{lum} at 530 nm is 1.16×10^{-3} and -0.86×10^{-3} which are smaller than the g_{abs} . The g_{abs} at 365 nm of R-QDs-620-R/L-silica helical are 0.79×10^{-3} and -0.78×10^{-3} separately. While the g_{lum} at 620 nm is 0.30×10^{-3} and -0.34×10^{-3} which are also smaller than the g_{abs} . The g_{abs} are based on the electron transition from the valence band of both CdSe core and ZnS shell to the conduction band of core and shell materials. While the g_{lum} are only based on the electron transition from the conduction band of CdSe core to the valence band of core material which might result in different g-factor of absorption and emission.

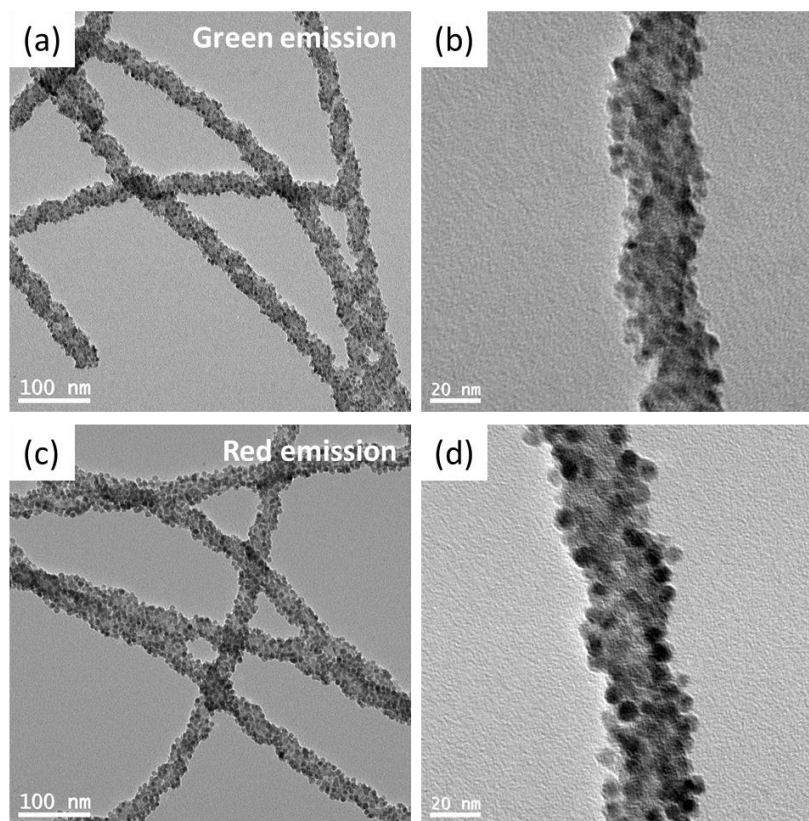


Figure 5-25. TEM images of green emission core-shell QDs-L-silica helical ribbons (a) and red emission core-shell QDs-L-silica helical ribbons (b) with different magnification.

3.8 Quantum rods shape effect

The effect of the shape of NCs on their chiral arrangement and the resulting chiroptical properties were detailed investigated. Here, CdSe/CdS core-shell structured quantum rods (QRs) were used to combine with silica twisted nanoribbons. As shown in Figures 5-26 and 5-27, the synthesized QRs show different lengths labeled as R1-6, the length of which are 9.5 nm, 13 nm, 18 nm, 23 nm, 27 nm, and 32 nm with size distribution (Figure 5-27).

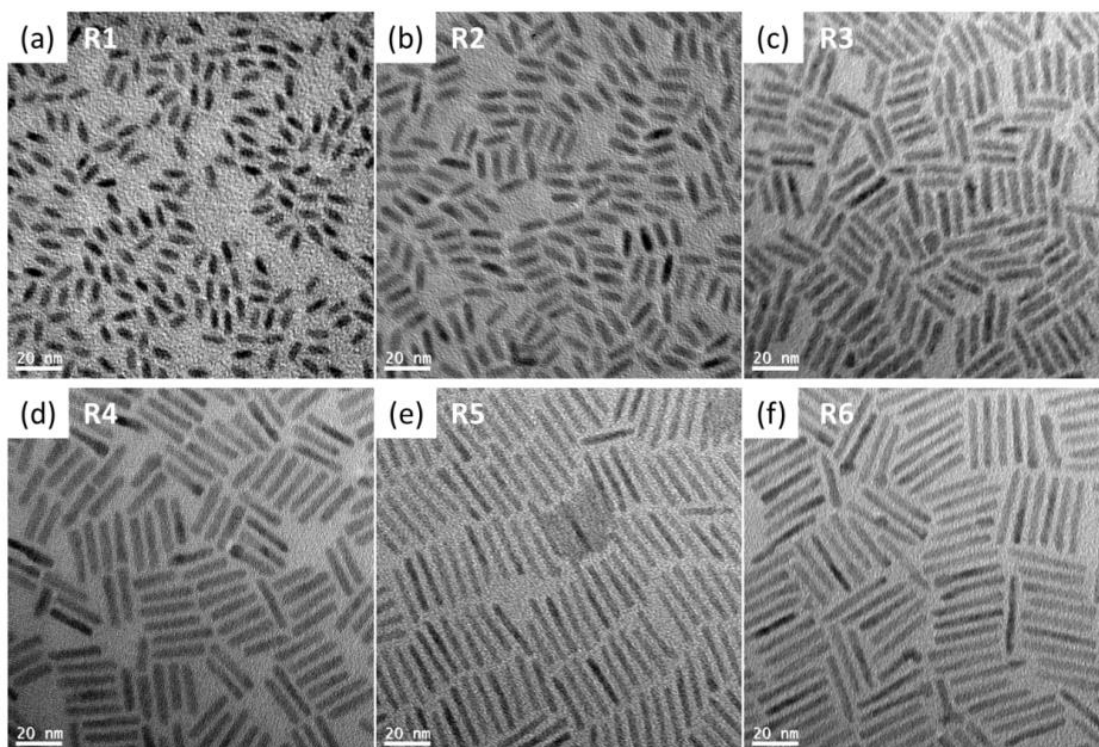


Figure 5-26. TEM images of quantum rods R1-6 with different length

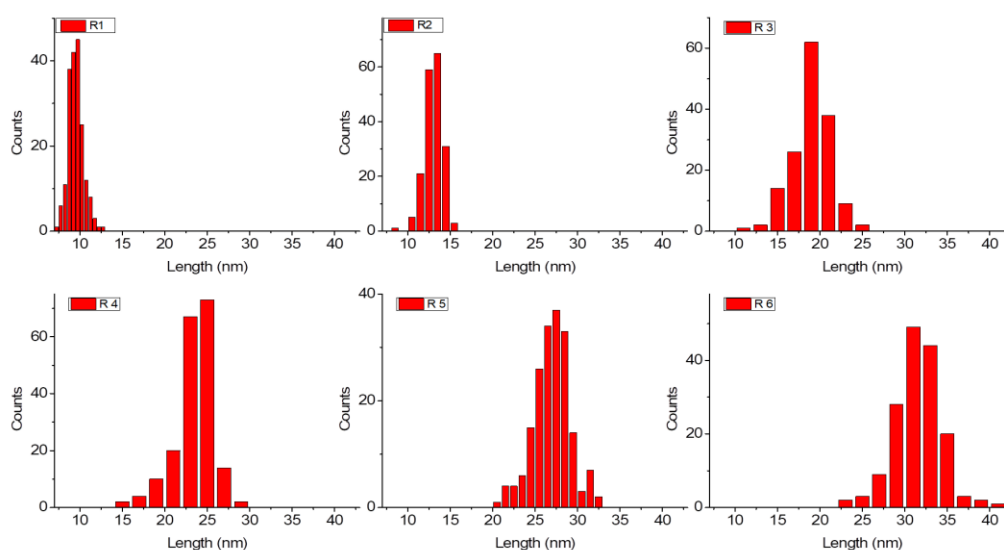


Figure 5-27. Quantum rods length distribution of R1-6

R1-6 CdSe/CdS QRs were then grafted on the surface of silica twisted nanoribbons as shown in Figure 5-28. The rods R1 and R2 are mainly attached to silica ribbons by their side whereas R5 and R6 are mainly attached by their tips. For the R3 and R4, both orientations are observed. When compared with the cryo-EM images of the same samples in suspension, interestingly, not only they show more swollen organization as

observed with QDs, but they are also attached with helices with their tips disregarded their length. This grafting model is consisted of the ligand exchange grafting methods as shown in the experiment section. The ligands on the tip side of QRs have higher activity³⁷ than the side part which is easier to be combined with the surface amine of silica twisted ribbons.

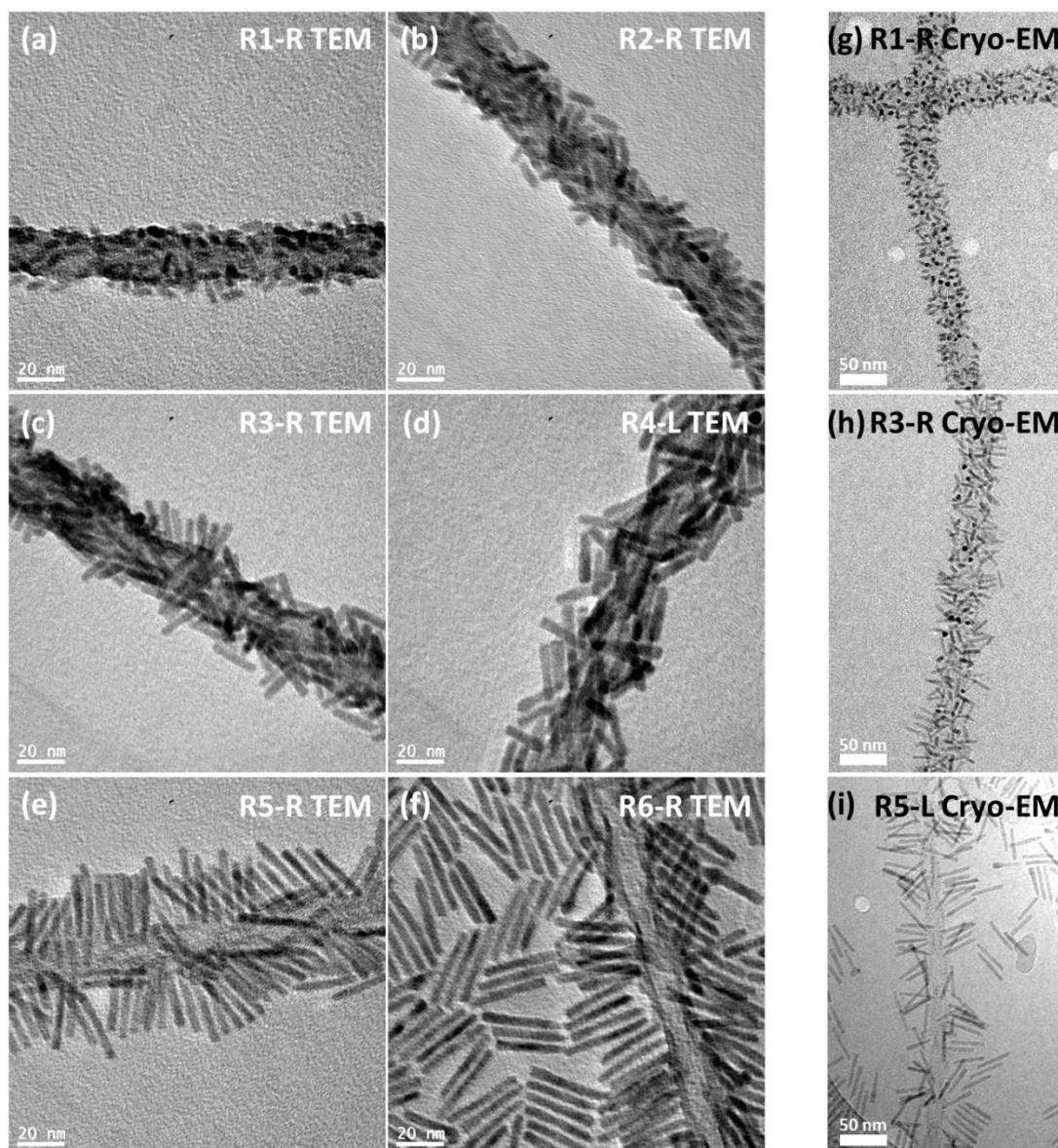


Figure 5-28. (a-f) TEM images of dried silica helices@R1-6 QRs and (g-i) cryo TEM images of solvated silica helices@R1,3,5 QRs. When dried, R1 and R2 are organized parallel to the silica surface, R5 and R6 QRs are tip grafted. R3 and R4 show intermediate orientation. When solvated, all of them show tip grafting orientation.

Once again, these silica helices @QRs in suspension do not show any CD signals as shown in Figure 5-29. When dried on the substrates, clear CD signals are observed as shown in Figure 5-30. The R1 and R2 QRs with left-handed (L-) silica helices show negative signals in the wavelength range of 300-500 nm while with right-handed helices, they show positive CD signals (Figure 5-30). Interestingly, for the sample with R3-6 QRs, the CD signals switch their signs, and L-silica helices@R3-6 QR show positive CD signals.

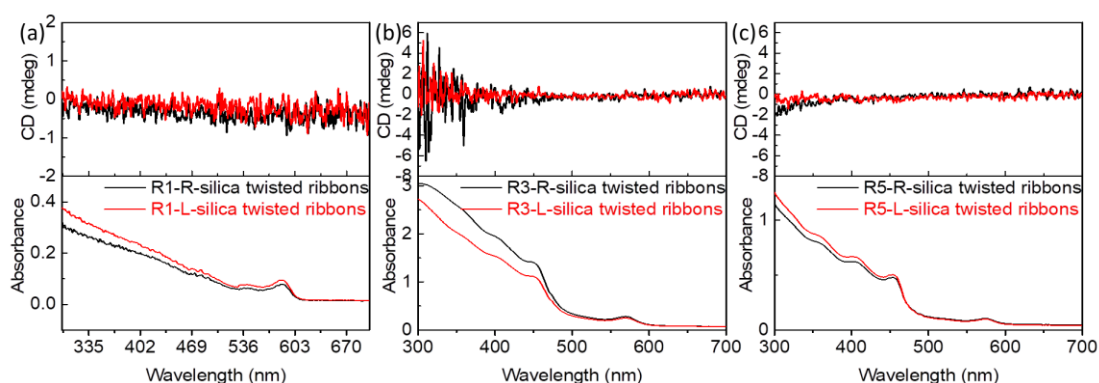


Figure 5-29. CD and absorption spectra of R1 (a), R3 (b), and R5 (c) grafted on the surface of silica twisted ribbons in suspension.

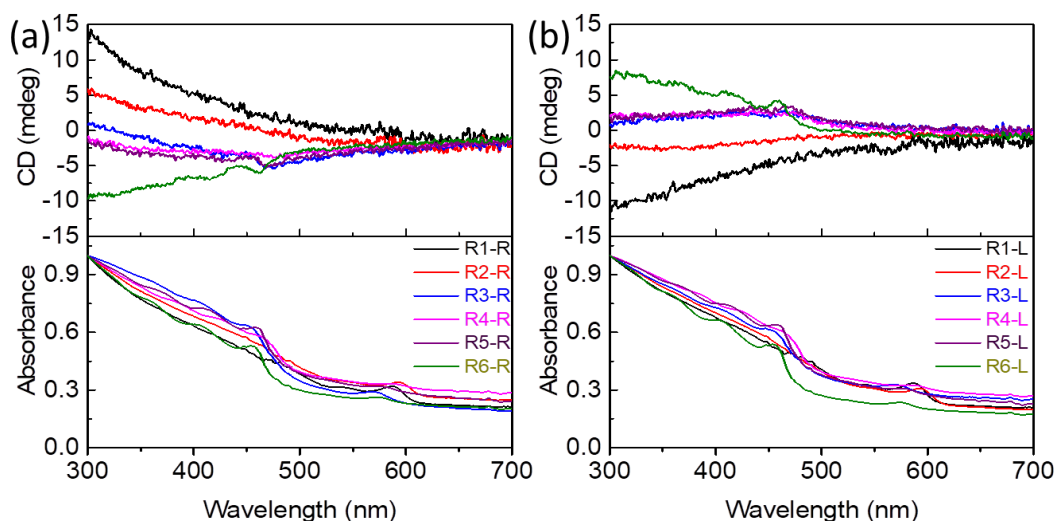


Figure 5-30. CD and absorption spectra of R1-6-R-silica twisted ribbons (a) and R1-6-L-silica twisted ribbons (b).

To investigate this switching of the CD signals, the simulation of QRs grafted on twisted ribbons with different orientations has been performed. In Figure 5-31 (b), four different types of grafting are shown, 1) QR are oriented parallel to the axis of the helix, 2) they have oriented perpendicular to the axis and the surface of the helix (tip grafting), 3) they are tangent to the helix, and 4) they are perpendicular to the tangent of the helix. The respective simulated CD signals for each orientation are shown in Figure 5-31 (b). These simulations are performed by considering CdSe nanorods with 25 nm length and 5 nm width. The CdSe nanorods are organized into helical structures. The helix pitch, radius, and length are 70 nm, 35 nm, and 500 nm. The distance between 2 adjacent rods is 25.2 nm. The incident wave vector of light is perpendicular to the helix axis.

Interestingly, while the orientation of nanorods has a negligible impact on the extinction cross-section, the sign of the CD spectra depends strongly on their orientation. Indeed, the CD is positive for configurations 1 and 2 while it becomes negative for configurations 3 and 4. The highest amplitudes of CD signal are observed for configurations 3 and 4. Although it is not easy to clearly define the orientation of the QR from the TEM images, it seems clear that the tip grafted QRs as seen in R3-R6 (Figure 5-28) agree with case 2, which shows positive signals in the wavelength range of 300-500 nm. For the sample L helices@R1-2 QRs, they show negative CD signals, which is in agreement with either 3 or 4 orientation in Figure 5-31 (b).

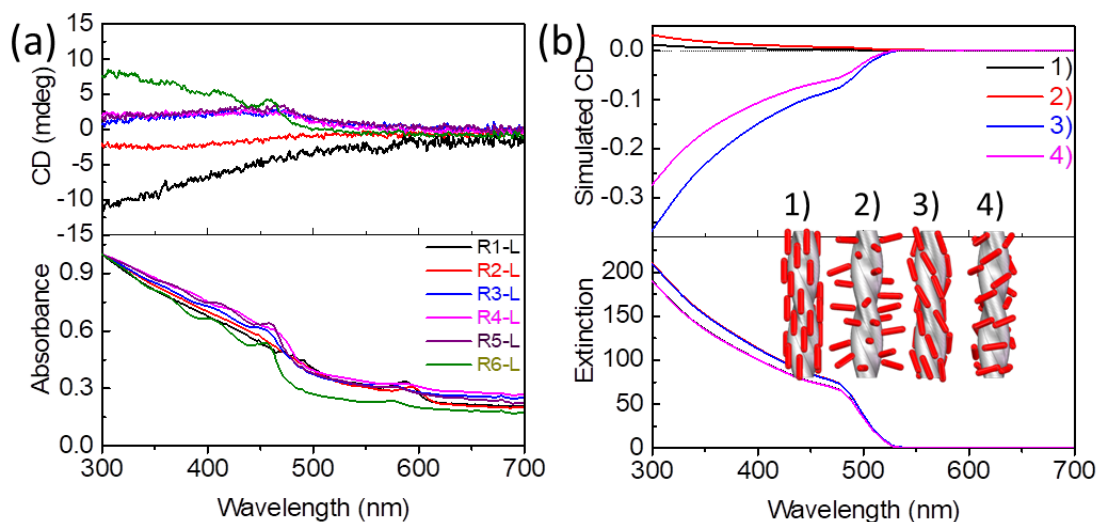


Figure 5-31. (a) CD and absorption spectra of L-silica helices@R1-6 QRs. (b)

simulated CD and absorption spectra of L-silica helix@QRs with 4 different orientations with respect to the helix.

Compared with QDs, QRs exhibit stronger linear absorption and linear emission. The QDs films show negligible linear dichroism (LD) and zero CD signals, however, the rods film shows strong angle-dependent LD as well as apparent angle-dependent CD signals as shown in Figure 5-32 (a). Also from the TEM image of R5, nematic alignment of R5 was observed as shown in Figure 5-32 (b). The LD of the QRs-silica twisted ribbons film was measured with different angles as shown in Figure 5-33. With the rod's length increasing, the R3-6-silica twisted ribbons show strong LD between 200 to 400 nm. As shown in Figures 3-34, rods 1 and 2 with silica twisted ribbons show mirror CPL images, but rods 3-6 with silica twisted ribbons do not show mirror CPL images due to their strong LD.

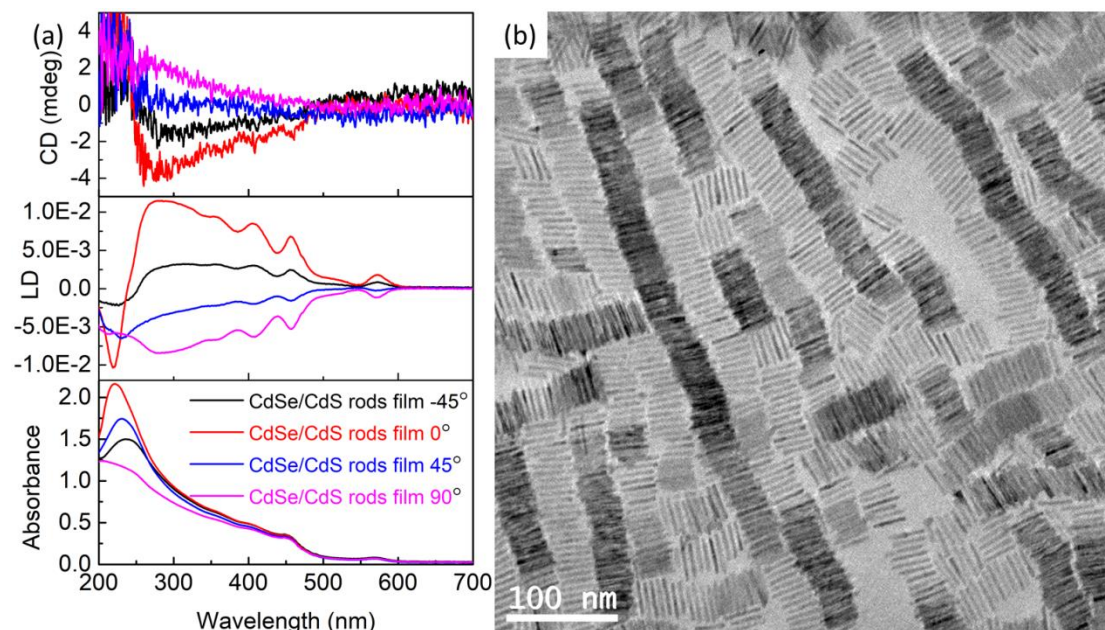


Figure 5-32. (a) CD, LD, and absorption spectra of QRs-R/L-silica twisted ribbons film measured with different angles. (b) TEM image of high concentrated R5 with the nematic arrangement.

Chapter 5. Chirality induction to CdSe nanocrystals self-organization on silica nanoribbons tuning chiroptical properties

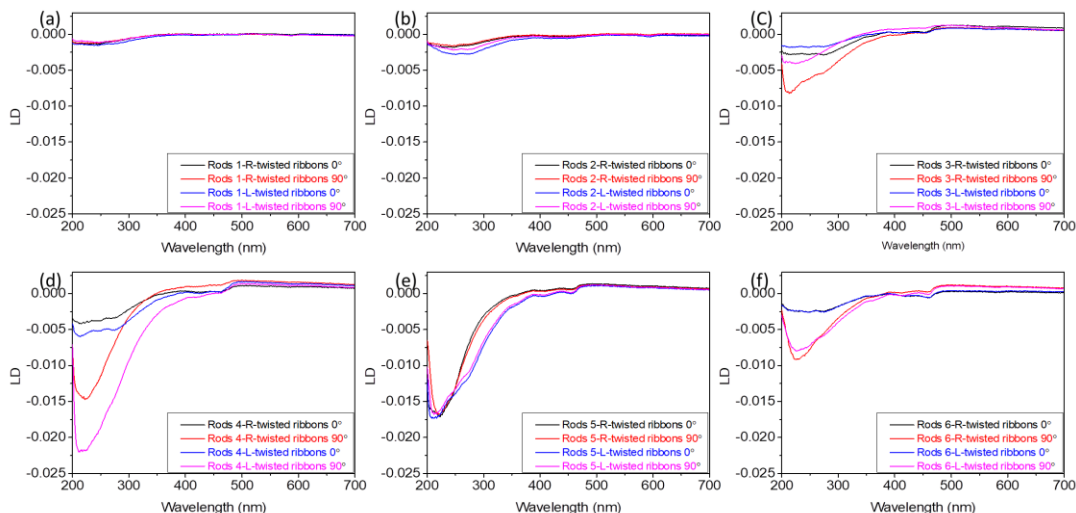


Figure 5-33. LD spectra of QRs (1-6)-R/L-twisted ribbons measured with vertical and horizontal angles.

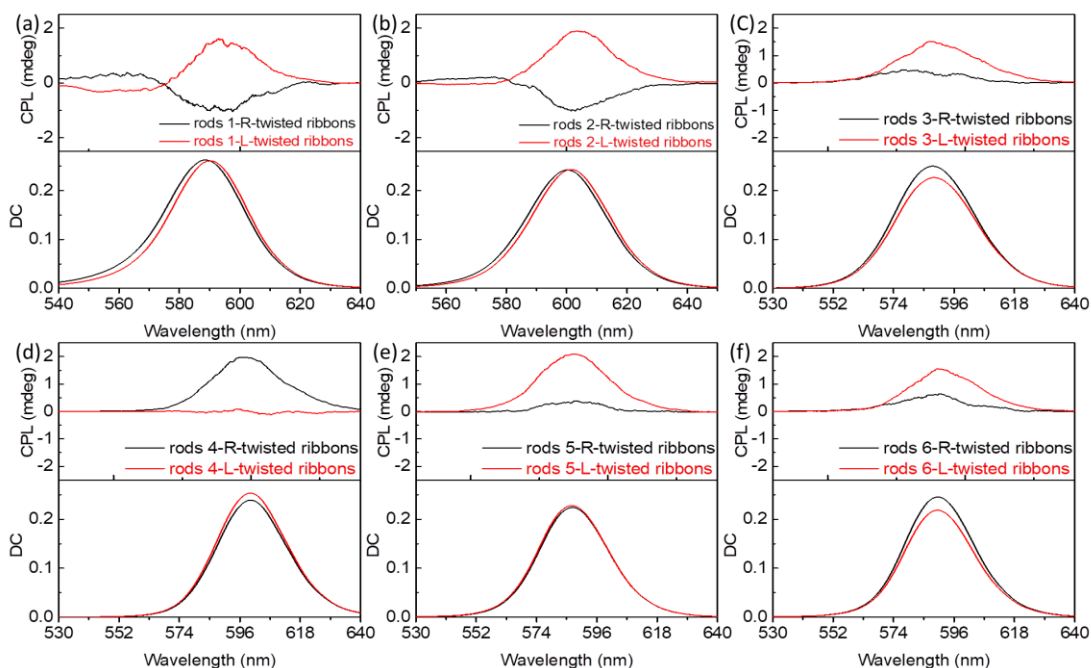


Figure 5-34. CPL and DC spectra of QRs (1-6)-R/L-twisted ribbons

4. Conclusion

This chapter systematically studied how chirality is induced to QDs or QRs which are chirally arranged around the chiral inorganic platform by looking into the effect of

various parameters and comparing the experimental observations and the simulation. The helices@QDs in suspension do not show CD signals, whereas they are dried on a substrate, clear CD signals were observed. The g-factor of the induced CD increased strongly with the grafting density. Interestingly, the QDs self-organization is hindered by co-drying with PMMA polymer, and no CD was observed in the latter case. The QDs with different sizes and different crystal structures have been grafted on the silica helical/twisted nanoribbons for which the CD signals were mainly controlled by the size of the QDs. By comparing QDs grafted on helical ribbons and twisted ribbons, for which the former showed stronger CD signals, and by analyzing the system by simulation, the chiroptical signals of the helically arranged QDs are strongly dependent both on the helical pitch and the radius which in turn depends on the angles formed by the three consecutive QDs in the helical arrangement. Finally, elongated QRs grafted around the twisted ribbons showed grafting orientation-dependent sign inversion of the optical activity. The QRs with a lower aspect ratio showed the orientation tangent to the helix and negative CD signals for the left-hand helix whereas those with a higher aspect ratio show tip-grafting (perpendicular to the helix axis) and show positive CD signals. The ensemble of the observation gives us powerful hints for designing efficient chiroptical nano-systems based on inorganic silica-QD components.

5. Experiment section

5.1 Chemical and reagents

Se powder (100 mesh, 99.99%), CdO (99.99%), S powder (100 mesh, 99.998%), 1-Octadecene (90%), Tri-n-octylphosphine (97%), Trioctylphosphine oxide (99%), Tetradecylphosphonic acid (97%), Oleylamine (70%), Oleic acid (90%), toluene were purchased from Sigma Company.

5.2 Cubic crystal structured CdSe QDs synthesise and purification

The different sizes of cubic crystal structured CdSe were synthesized according to Peng's method³⁸. The size of QDs was controlled by the growth temperature and concentration of precursors. The typical synthesis protocol is as below:

Se-ODE precursor: 0.1 mmol Se powder (100 mesh) mixed with 2 mL 1-octadecene (ODE) and sonication for 5 mins before injection.

0.0256 g (0.2 mmol) CdO, 0.2 mL oleic acid (OA), and 8 ml ODE were loaded into a 50 mL three-neck flask, bubbling with nitrogen for 30 min at 100 °C. Then increasing the temperature at 250 °C, 2 mL Se-ODE suspension solution was injected quickly and set the temperature at 220 °C, growth for 5 min. Then remove the heating source and cool down to room temperature.

CdSe quantum dots purification:

10 mL hexane and 10 mL ethanol were added into the crude CdSe solution, stirring and sonication for 10 min until the solution stratification, the bottom white part solution was discarded. Repeat this step twice. 10 mL ethanol was added and centrifuged at 9000 g. All the supernatant was removed and 2 mL toluene was added to disperse the precipitate. 7000 g centrifuged again and the supernatant was collected and kept in a refrigerator for further use and characterization.

5.3 Hexagonal crystal structured CdSe QDs synthesise and purification

The different sizes of hexagonal crystal structured CdSe were synthesized according to the previous report³⁹. The size was controlled by the growth time and the typical synthesis protocol is as below:

Se-TOP precursor: 0.789 g Se powder dissolved into 10 mL tri-n-octyl phosphine (TOP) with stirring.

54 mg CdO, 224 mg Tetradecylphosphonic acid (TDPA), 3 g trioctylphosphine oxide (TOPO) in 100 ml three-necked flask, degassed for 60 min at 150 °C. The temperature was increased to 330 °C, the flask was shaken manually to let the CdO dissolved quickly. After the CdO was dissolved, the temperature was increased to 350 °C, 1.5 ml TOP was injected. Then the temperature was increased to 370 °C, 0.63 ml Se-TOP

was injected quickly. 10 seconds later, the heating source was removed and the CdSe crude solution was cooled down to room temperature

Purification: 6 ml chloroform was added to the crude solution, centrifuged for 3 min at 9000 g. The supernatant was collected and 12 ml ethanol was added, centrifuged for 3 min at 9000 g, the supernatant was removed and 12 ml toluene was added to disperse the precipitate, then 12 ml ethanol was added, centrifuged for 3 min at 9000 g again. The supernatant was removed and around 2 ml toluene was added to disperse the precipitate. The solution was kept in the refrigerator for further use.

5.4 CdSe/CdS quantum rods (QRs) synthesis and purification

CdSe core seeds: the CdSe seeds were prepared with the same step of hexagonal crystal structured CdSe QDs. The purified CdSe was dispersed into 4 mL TOP instead of a toluene solution and the CdSe TOP solution was used to prepare the CdSe/CdS QRs. Then the molar concentration was calculated by Peng's methods³⁰.

S-TOP precursor: 1.202 g S powder dissolved into 15 mL TOP solution by heating to 100 °C with stirring,

CdSe/CdS QRs synthesis according to previous report³⁹: 40 mg CdO, 52 mg hexyl phosphonic acid (HPA), 200 mg TDPA, 2 g TOPO in the three-necked flask, degassed for 60 min at 150 °C, then the temperature was increased to 300 °C to dissolve the CdO. After the CdO was completely dissolved, 1 ml TOP was injected. The temperature was increased to 320 °C, the mixture of 53.3 nmol CdSe TOP QDs and 1 ml S-TOP was injected, keep its growth at 320 °C for 8 min, then the heating source was removed and cool down to room temperature.

The length of CdSe/CdS rods was controlled by the mass of CdO and the number of CdSe-TOP seeds.

5.5 Grafting of QDs and QRs on the surface of silica helices by ligand exchange methods

5 mL APTES modified silica ribbons ethanol solution (1 mg/mL) was centrifuged at 9800 g for 10 min, the supernatant was removed, and 5 mL toluene was added to the precipitate to disperse the silica ribbons. The dispersion was centrifuged again at 9800

g for 10 min, the supernatant was removed and 5 mL toluene was added to disperse the silica ribbons. Finally, the silica ribbons were dispersed into a 5 mL toluene solution. Then the silica ribbons toluene mass concentration was calculated measuring the mass of dried silica ribbons in a certain volume solution.

The as-prepared QDs and QRs were washed with acetonitrile once to decrease the surface of ligands by centrifugation. 10 times more QDs/QRs numbers than theoretical maximum grafting number were mixed with silica ribbons and sonication for 10 min. The mixture was shaken at 4 °C for 3 days (roller mixer). After that, to separate the QDs/QRs-silica ribbons and free QDs/QRs, the mixture was centrifuged at 9800 g for 10 min, the supernatant was discarded and 1 mL toluene was added to disperse the precipitate. Centrifugation again and the precipitate QDs/QRs-silica ribbons were re-dispersed into 0.5 mL toluene.

QDs/QRs-silica helices film preparation

The quartz was cut to 1 * 1 cm plates. Then the prepared QDs/QRs-silica ribbons toluene solution 50 uL was drop cast on the quartz surface and dried at 4 °C or 20 °C. Two films were prepared in parallel under the same conditions for each sample. After drying, CD and CPL were measured with different parameters.

5.6 Optical properties simulations by CDM

The optical properties of QDs helices are simulated by using the coupled dipole method (CDM). Each QDs m located at a position \vec{r}_m is considered as a point dipole which has a polarizability tensor α . For spherical NPs with radius R , the polarizability tensor is defined as following:

$$\alpha = R^3 \frac{\varepsilon_{QD} - \varepsilon_h}{\varepsilon_{QD} + 2\varepsilon_h} I_3, (1)$$

with I_3 the 3x3 identity matrix. ε_{QD} and ε_h are the dielectric function of the QD and the host matrix. As QDs are located on the surface of SiO₂ helices, ε_h is set to 1.5 i.e. the average value of the dielectric function of silica and air. The dielectric function of QDs is deduced for each crystal structure by analyzing the absorption spectroscopy measurements shown in Figure S1 with the Maxwell Garnett effective

medium approximation. In the case of nanorods, we assume that the polarizability tensor is given by those of prolate ellipsoid. This latter, expressed in the local frame of the ellipsoid is given by:

$$\alpha = \frac{Dd^2}{8} \begin{pmatrix} \frac{\varepsilon_{QD}-\varepsilon_h}{\varepsilon_{QD}+\frac{1-L_1}{L_1}\varepsilon_h} & 0 & 0 \\ 0 & \frac{\varepsilon_{QD}-\varepsilon_h}{\varepsilon_{QD}+\frac{1-L_2}{L_2}\varepsilon_h} & 0 \\ 0 & 0 & \frac{\varepsilon_{QD}-\varepsilon_h}{\varepsilon_{QD}+\frac{1-L_2}{L_2}\varepsilon_h} \end{pmatrix}, (2)$$

with $L_1 = \frac{a^2}{1-a^2} \left(-1 + \frac{0.5}{\sqrt{1-a^2}} \ln\left(\frac{1+\sqrt{1-a^2}}{1-\sqrt{1-a^2}}\right)\right)$ and $L_2 = 0.5(1-L_1)$. a , D and d are the aspect ratio, the length, and the width of nanorods, respectively. Exposed to a local field $\vec{E}_{loc,m}$, the QD m acquires a dipole moment \vec{P}_m expressed as:

$$\vec{P}_m = \alpha \vec{E}_{loc,m}. (3)$$

By considering that the local electric field is the sum of the incident field $\vec{E}_{inc,m}$ and the field radiated by the other dipoles l , equation (3) can be rewritten as follows:

$$\alpha^{-1} \vec{P}_m = \vec{E}_{inc,m} - \sum_{l \neq m} A_{ml} \vec{P}_l. (4)$$

The second term of equation (4) which describes the dipolar interaction between QDs is given by:

$$A_{ml} \vec{P}_l = \frac{e^{jkr_{ml}}}{r_{ml}^3} \left\{ k^2 \vec{r}_{ml} \wedge \vec{r}_{ml} \wedge \vec{P}_l + \frac{1-jkr_{ml}}{r_{ml}^2} (r_{ml}^2 \vec{P}_l - 3\vec{r}_{ml} \cdot (\vec{r}_{ml} \cdot \vec{P}_l)) \right\}, (5)$$

where k the norm of the wavevector and $\vec{r}_{ml} = \vec{r}_m - \vec{r}_l$. By applying equation (4) for all QDs in the helix, we obtain a set of linear equations which can be solved by using the generalized minimal residual method. The extinction cross-section of the QDs helix is then calculated, for a given polarization by:

$$\sigma_{ext} = \frac{4\pi k}{|E_0|^2} \sum_{m=1} Im(\vec{E}_{inc,m} \cdot \vec{P}_m). (6)$$

$|E_0|$ is the amplitude of the incident electric field. The CD of the QDs helix was then deduced from the extinction cross-section calculated for a right $\sigma_{ext,R}$ and left $\sigma_{ext,L}$ handed circular polarization:

$$CD = \sigma_{ext,L} - \sigma_{ext,R}. \quad (7)$$

The g-factor is deduced from the following equation:

$$g = 2 \frac{\sigma_{ext,L} - \sigma_{ext,R}}{\sigma_{ext,L} + \sigma_{ext,R}} \quad (8)$$

6. Reference

1. Bera, D.; Qian, L.; Tseng, T.-K.; Holloway, P. H., Quantum Dots and Their Multimodal Applications: A Review. *Materials* **2010**, *3* (4), 2260-2345.
2. Dai, X.; Deng, Y.; Peng, X.; Jin, Y., Quantum-Dot Light-Emitting Diodes for Large-Area Displays: Towards the Dawn of Commercialization. *Adv Mater* **2017**, *29* (14).
3. Chen, C.; Gao, L.; Gao, W.; Ge, C.; Du, X.; Li, Z.; Yang, Y.; Niu, G.; Tang, J., Circularly polarized light detection using chiral hybrid perovskite. *Nat Commun* **2019**, *10* (1), 1927.
4. Kim, Y. H.; Zhai, Y.; Lu, H.; Pan, X.; Xiao, C.; Gaubing, E. A.; Harvey, S. P.; Berry, J. J.; Vardeny, Z. V.; Luther, J. M.; Beard, M. C., Chiral-induced spin selectivity enables a room-temperature spin light-emitting diode. *Science* **2021**, *371* (6534), 1129-1133.
5. Michaeli, K.; Kantor-Uriel, N.; Naaman, R.; Waldeck, D. H., The electron's spin and molecular chirality - how are they related and how do they affect life processes? *Chem Soc Rev* **2016**, *45* (23), 6478-6487.
6. Naaman, R.; Paltiel, Y.; Waldeck, D. H., Chiral molecules and the electron spin. *Nature Reviews Chemistry* **2019**.
7. Moloney, M. P.; Gun'ko, Y. K.; Kelly, J. M., Chiral highly luminescent CdS quantum dots. *Chem Commun (Camb)* **2007**, (38), 3900-2.
8. Nakashima, T.; Kobayashi, Y.; Kawai, T., Optical activity and chiral memory of thiol-capped CdTe nanocrystals. *J Am Chem Soc* **2009**, *131* (30), 10342-3.
9. Zhou, Y.; Zhu, Z.; Huang, W.; Liu, W.; Wu, S.; Liu, X.; Gao, Y.; Zhang, W.; Tang, Z., Optical coupling between chiral biomolecules and semiconductor nanoparticles: size-dependent circular dichroism absorption. *Angew Chem Int Ed Engl* **2011**, *50* (48), 11456-9.
10. Moshe, A. B.; Szwarcman, D.; Markovich, G., Size dependence of chiroptical activity in colloidal quantum dots. *ACS Nano* **2011**, *5* (11), 9034-43.
11. Kuznetsova, V. A.; Mates-Torres, E.; Prochukhan, N.; Marcaste, M.; Purcell-Milton, F.; O'Brien, J.; Visheratina, A. K.; Martinez-Carmona, M.; Grornova, Y.; Garcia-Melchor, M.; Gun'ko, Y. K., Effect of Chiral Ligand Concentration and Binding Mode on Chiroptical Activity of CdSe/CdS Quantum Dots. *ACS Nano* **2019**, *13* (11), 13560-13572.
12. Tohgha, U.; Deol, K. K.; Porter, A. G.; Bartko, S. G.; Choi, J. K.; Leonard, B. M.; Varga, K.; Kubelka, J.; Muller, G.; Balaz, M., Ligand induced circular dichroism and circularly polarized luminescence in CdSe quantum dots. *ACS Nano* **2013**, *7* (12), 11094-102.
13. Gao, X.; Zhang, X.; Zhao, L.; Huang, P.; Han, B.; Lv, J.; Qiu, X.; Wei, S. H.; Tang, Z., Distinct Excitonic Circular Dichroism between Wurtzite and Zincblende CdSe Nanoplatelets. *Nano Lett* **2018**, *18* (11), 6665-6671.
14. Gao, X.; Zhang, X.; Deng, K.; Han, B.; Zhao, L.; Wu, M.; Shi, L.; Lv, J.; Tang, Z., Excitonic Circular Dichroism of Chiral Quantum Rods. *J Am Chem Soc* **2017**, *139* (25), 8734-8739.
15. Purcell-Milton, F.; Visheratina, A. K.; Kuznetsova, V. A.; Ryan, A.; Orlova, A. O.; Gun'ko, Y. K., Impact of Shell Thickness on Photoluminescence and Optical Activity in Chiral CdSe/CdS Core/Shell Quantum Dots. *ACS Nano* **2017**, *11* (9), 9207-9214.
16. Cheng, J.; Hao, J.; Liu, H.; Li, J.; Li, J.; Zhu, X.; Lin, X.; Wang, K.; He, T., Optically Active CdSe-Dot/CdS-Rod Nanocrystals with Induced Chirality and Circularly Polarized Luminescence. *ACS Nano* **2018**, *12* (6), 5341-5350.
17. Hao, J.; Li, Y.; Miao, J.; Liu, R.; Li, J.; Liu, H.; Wang, Q.; Liu, H.; Delville, M.-H.; He, T.; Wang, K.; Zhu,

Chapter 5. Chirality induction to CdSe nanocrystals self-organization on silica nanoribbons tuning chiroptical properties

X.; Cheng, J., Ligand-Induced Chirality in Asymmetric CdSe/CdS Nanostructures: A Close Look at Chiral Tadpoles. *ACS Nano* **2020**, *14* (8), 10346-10358.

18. Liu, M.; Zhang, L.; Wang, T., Supramolecular Chirality in Self-Assembled Systems. *Chem Rev* **2015**, *115* (15), 7304-97.

19. Mateos-Timoneda, M. A.; Crego-Calama, M.; Reinhoudt, D. N., Supramolecular chirality of self-assembled systems in solution. *Chem Soc Rev* **2004**, *33* (6), 363-72.

20. Baginski, M.; Tupikowska, M.; Gonzalez-Rubio, G.; Wojcik, M.; Lewandowski, W., Shaping Liquid Crystals with Gold Nanoparticles: Helical Assemblies with Tunable and Hierarchical Structures Via Thin-Film Cooperative Interactions. *Adv Mater* **2020**, *32* (1), e1904581.

21. Guerrero-Martinez, A.; Auguie, B.; Alonso-Gomez, J. L.; Dzolic, Z.; Gomez-Grana, S.; Zinic, M.; Cid, M. M.; Liz-Marzan, L. M., Intense optical activity from three-dimensional chiral ordering of plasmonic nanoantennas. *Angew Chem Int Ed Engl* **2011**, *50* (24), 5499-503.

22. Szustakiewicz, P.; Kowalska, N.; Grzelak, D.; Narushima, T.; Gora, M.; Baginski, M.; Pocięcha, D.; Okamoto, H.; Liz-Marzan, L. M.; Lewandowski, W., Supramolecular Chirality Synchronization in Thin Films of Plasmonic Nanocomposites. *ACS Nano* **2020**, *14* (10), 12918-12928.

23. Hentschel, M.; Schaferling, M.; Duan, X.; Giessen, H.; Liu, N., Chiral plasmonics. *Sci Adv* **2017**, *3* (5), e1602735.

24. Schreiber, R.; Luong, N.; Fan, Z.; Kuzyk, A.; Nickels, P. C.; Zhang, T.; Smith, D. M.; Yurke, B.; Kuang, W.; Govorov, A. O.; Liedl, T., Chiral plasmonic DNA nanostructures with switchable circular dichroism. *Nat Commun* **2013**, *4*, 2948.

25. Huo, S.; Duan, P.; Jiao, T.; Peng, Q.; Liu, M., Self-Assembled Luminescent Quantum Dots To Generate Full-Color and White Circularly Polarized Light. *Angewandte Chemie International Edition* **2017**, *56* (40), 12174-12178.

26. Shi, Y.; Duan, P.; Huo, S.; Li, Y.; Liu, M., Endowing perovskite nanocrystals with circularly polarized luminescence. *Advanced Materials* **2018**, *30* (12), 1705011.

27. Cheng, J.; Le Saux, G.; Gao, J.; Buffeteau, T.; Battie, Y.; Barois, P.; Ponsinet, V.; Delville, M. H.; Ersen, O.; Pouget, E.; Oda, R., GoldHelix: Gold Nanoparticles Forming 3D Helical Superstructures with Controlled Morphology and Strong Chiroptical Property. *ACS Nano* **2017**, *11* (4), 3806-3818.

28. Gao, J.; Wu, W.; Lemaire, V.; Carvalho, A.; Nlate, S.; Buffeteau, T.; Oda, R.; Battie, Y.; Pauly, M.; Pouget, E., Tuning the Chiroptical Properties of Elongated Nano-objects via Hierarchical Organization. *ACS Nano* **2020**, *14* (4), 4111-4121.

29. Liu, P.; Chen, W.; Okazaki, Y.; Battie, Y.; Brocard, L.; Decossas, M.; Pouget, E.; Muller-Buschbaum, P.; Kauffmann, B.; Pathan, S.; Sagawa, T.; Oda, R., Optically Active Perovskite CsPbBr₃ Nanocrystals Helically Arranged on Inorganic Silica Nanohelices. *Nano Lett* **2020**, *20* (12), 8453-8460.

30. Yu, W. W.; Qu, L.; Guo, W.; Peng, X., Experimental determination of the extinction coefficient of CdTe, CdSe, and CdS nanocrystals. *Chemistry of Materials* **2003**, *15* (14), 2854-2860.

31. Boles, M. A.; Engel, M.; Talapin, D. V., Self-Assembly of Colloidal Nanocrystals: From Intricate Structures to Functional Materials. *Chem Rev* **2016**, *116* (18), 11220-89.

32. Xue, X.; Penn, R. L.; Leite, E. R.; Huang, F.; Lin, Z., Crystal growth by oriented attachment: kinetic models and control factors. *CrystEngComm* **2014**, *16* (8), 1419.

33. Ivanov, V. K.; Fedorov, P. P.; Baranchikov, A. Y.; Osiko, V. V., Oriented attachment of particles: 100 years of investigations of non-classical crystal growth. *Russian Chemical Reviews* **2014**, *83* (12), 1204-1222.

34. van Huis, M. A.; Kunneman, L. T.; Overgaag, K.; Xu, Q.; Pandraud, G.; Zandbergen, H. W.;

Chapter 5. Chirality induction to CdSe nanocrystals self-organization on silica nanoribbons tuning chiroptical properties

Vanmaekelbergh, D., Low-temperature nanocrystal unification through rotations and relaxations probed by in situ transmission electron microscopy. *Nano Lett* **2008**, *8* (11), 3959-63.

35. Carrillo-Carrion, C.; Cardenas, S.; Simonet, B. M.; Valcarcel, M., Quantum dots luminescence enhancement due to illumination with UV/Vis light. *Chem Commun (Camb)* **2009**, (35), 5214-26.

36. Galian, R. E.; de la Guardia, M.; Perez-Prieto, J., Size reduction of CdSe/ZnS core-shell quantum dots photosensitized by benzophenone: where does the Cd(0) go? *Langmuir* **2011**, *27* (5), 1942-5.

37. Talapin, D. V.; Nelson, J. H.; Shevchenko, E. V.; Aloni, S.; Sadtler, B.; Alivisatos, A. P., Seeded growth of highly luminescent CdSe/CdS nanoheterostructures with rod and tetrapod morphologies. *Nano Lett* **2007**, *7* (10), 2951-9.

38. Pu, C.; Zhou, J.; Lai, R.; Niu, Y.; Nan, W.; Peng, X., Highly reactive, flexible yet green Se precursor for metal selenide nanocrystals: Se-octadecene suspension (Se-SUS). *Nano Research* **2013**, *6* (9), 652-670.

39. Carbone, L.; Nobile, C.; De Giorgi, M.; Sala, F. D.; Morello, G.; Pompa, P.; Hytch, M.; Snoeck, E.; Fiore, A.; Franchini, I. R.; Nadasan, M.; Silvestre, A. F.; Chiodo, L.; Kudera, S.; Cingolani, R.; Krahn, R.; Manna, L., Synthesis and micrometer-scale assembly of colloidal CdSe/CdS nanorods prepared by a seeded growth approach. *Nano Lett* **2007**, *7* (10), 2942-50.

Chapter 6. Chiral shaped perovskite nanocrystals growth inside chiral hollow silica nanoribbons

1. Introduction.....	177
2. Result and discussion.....	178
2.1 One-step method.....	180
2.1.1 Effect of concentration.....	180
2.1.2 Effect of annealing condition.....	182
2.2 Two-step method.....	183
2.2.1 Effect of concentration.....	183
2.2.2 Effect of solvent evaporation temperature.....	184
2.2.3 Effect of annealing condition.....	185
2.2.4 Effect of halide composition.....	186
3. Conclusion.....	187
4. Experiment section.....	188
4.1 Materials and instruments.....	188
4.2 Silica ribbons and ions precursors.....	188
5. Reference.....	190

Chapter 6. Chiral shaped perovskite nanocrystals growth inside chiral hollow silica nanoribbons

1. Introduction

Perovskite materials attract lots of attention due to their outstanding optoelectronic properties and promising applications, such as solar cells and light-emitting diodes (LEDs). The lower trap densities¹ and long carrier-diffusion length² have led to the solar cells with efficiency up to 20%³; the higher photoluminescence quantum yields and tunable emission have enabled with high-performance LEDs.⁴ Chiral materials can exhibit special properties, such as circular dichroism (CD) and circularly polarized luminescence (CPL),⁵ second-harmonic generation (SHG),⁶ piezoelectricity, pyroelectricity,⁷ ferroelectricity⁸ and topological quantum properties.⁹ The distinctive properties result in many potential and promising applications in chirophoelectronics, such as CPL detector,¹⁰ circularly polarized LEDs,¹¹ 3 D display,¹² quantum computing,¹³ quantum communication,¹⁴ and spintronics.¹⁵⁻¹⁹ Recently, the preparation of chiral perovskite materials and their applications have been emerging topics; many review papers have given well introduces on the ways to endow chirality to perovskites materials and their potential and promising applications.^{16, 20-22} In general, chirality generation in nanocrystals (NCs) can be roughly classified into four approaches, such as a) coordination of chiral ligands;²³⁻²⁵ b) chiral self-organization;²⁶⁻²⁸ c) chiral lattice;^{29, 30} and d) chiral shape.³¹⁻³³ The chirality of perovskite materials endowed by chiral ligands has been widely reported. The chiral ligands coordinated to the perovskites materials can induce chiral inorganic structure, chiral distortion of the inorganic surface, chiral patterning of the surface ligands, and electronic coupling between the chiral organic molecules and the inorganic structure which result in optically active properties.¹⁶ Also the chirality endowed to perovskite NCs by organic templates²⁸ or inorganic templates²⁶ have also been reported. While up to now, there is no report on the helical/twisted shape of perovskite NCs at all. One mechanism of chiral shape materials formation is attributed to the differential growth rates of chiral facets which possibly mediated by the presence of chiral ligands³³⁻³⁶ or

the intrinsic chiral crystal structure.^{37, 38} Another mechanism of chiral shaped materials formation is that the nuclei of the crystals contain screw dislocations can grow further because these dislocations create a more reactive crystal growth front.³⁹⁻⁴³ Such screw-dislocation-mediated growth yields helical or twisted shape materials. Moreover, nanomaterials can grow inside of hollow structure materials⁴⁴⁻⁴⁶, such as CdSe⁴⁷, CdS^{48, 49}, InP⁵⁰. And recently, perovskite NCs such as hybrid CH₃NH₃PbBr₃⁵¹ and all inorganic CsPbX₃ (X=Cl, Br, I or their mixture)⁵²⁻⁵⁴ are successful to grow inside the hollow materials with high luminescence due to their halide self-passivation⁵⁵ and defect tolerance⁵³. It would be very interesting to grow perovskite NCs inside the chiral hollow materials with a chiral shape, which can show strong CD and as well as CPL.

Here, the chiral shaped PNCs assisted by the hollow silica ribbons *via* supersaturated recrystallization methods were prepared. First, the left-/right-handed hollow silica ribbons were prepared, and then the precursor ions of perovskite mixed with the chiral hollow silica. After the solvent evaporation, the perovskite NCs grow with a left- or right-handed chiral shape and the handedness is dependent on the handedness of chiral hollow silica. The left- and right-handed PNCs show strong CD and CPL mirror images and the dissymmetric g-factor is up to 2×10^{-2} . It should be noted that in the whole process, there is no chiral ligand used. The chiral shaped PNCs would origin from the screw-dislocation and the confinement of the hollow silica ribbons.

2. Result and discussion

The silica helical ribbons were prepared by sol-gel transcription of self-assembled Gemini surfactants and their handedness can be controlled by the counterions of Gemini-L-tartrate form right-handed helices, while D-tartrate form left-handed helices as presented in chapter 2. After washed with methanol at 60 °C, the organic template Gemini-L/D-tartrate can be removed and the hollow silica ribbons were obtained. The hollow structure replicated the shape of the organic template Gemini-L/D-tartrate. The chiral shaped PNCs were synthesized as shown in Figure 6-1, the hollow silica helical

Chapter 6. Chiral shaped perovskite nanocrystals growth inside chiral hollow silica nanoribbons

ribbons were mixed with the precursor of ions such as Cs^+ , Pb^{2+} , and Br^- in DMF. Through the increased concentration of the mixture by the solvent evaporation, the CsPbBr_3 NCs grew inside of the hollow silica helical ribbons with helical shape due to the supersaturated recrystallization. In this process, the PNCs replicated the shape of the organic template and the handedness, which is decided by the L- or D-tartrate. The thickness and width of the organic ribbons are around 6.5 nm and 23 nm, respectively.⁵⁶ Molar concentration of the Cs^+ , Pb^{2+} , and Br^- ions as the precursor were 0.04 M and the mass concentration of ions was 0.023 g/mL, while the obtained CsPbBr_3 PNCs density was 4.42 g/mL. For 1 mg silica helical ribbons, the hollow volume is $2.84 \times 10^{-4} \text{ cm}^3$ which means that 1.25 mg CsPbBr_3 PNCs (54.35 μL precursor ions) can grow inside the silica helical ribbons with 1 mg theoretically.

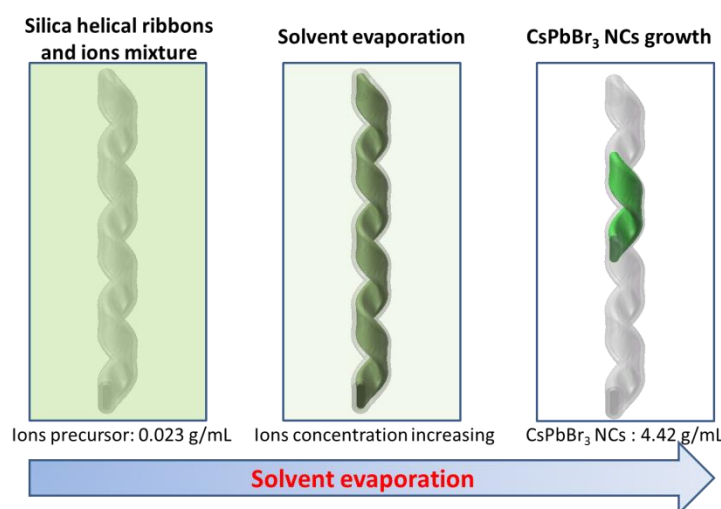


Figure 6-1. Scheme of the chiral PNCs growth inside the hollow silica helical ribbons.

Two ways were described in this chapter to prepare the chiral shaped PNCs inside the silica ribbons, one-step method and two-step method as shown in Figure 6-2. The one-step method is just to drop-cast the mixture of hollow silica helical ribbons and precursor ions, the PNCs can grow inside the silica helical ribbons after the solvent evaporation. The two-step method is to drop-cast the hollow silica helical ribbons first

followed by the dryness of them, then the precursor ions is infiltrated into the void of the hollow silica helical ribbons, thereafter the PNCs can be formed by the solvent evaporation. Both two methods inevitably result in some part of PNCs growth outside the silica ribbons confirmed by the TEM observation. However, the outside PNCs with achiral shape result in non-chiral absorption (non-CD contribution) and emission which (non-CPL contribution) weaken the dissymmetric g-factor of absorption and luminescence. It is necessary to change the ratio of silica ribbons to precursor ions to optimize the dissymmetric g-factor.

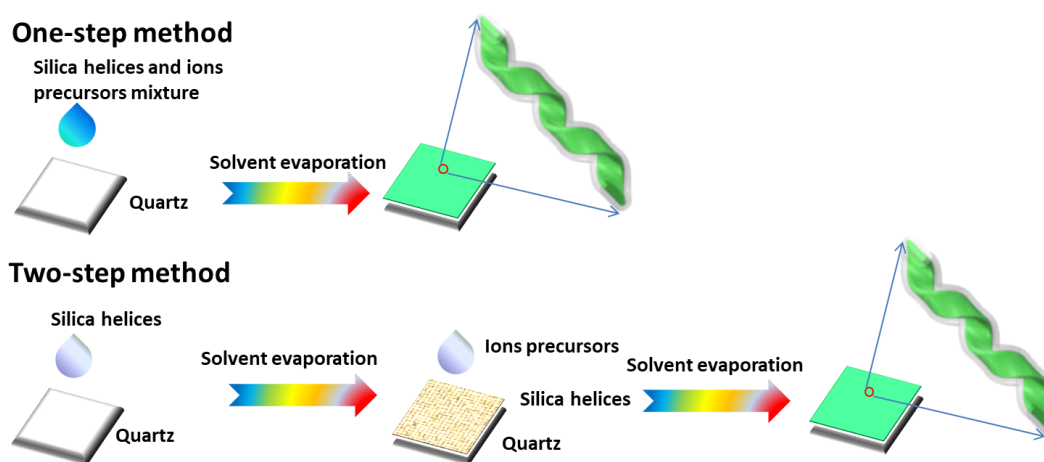


Figure 6-2. Scheme of the chiral shaped PNCs synthesis inside the silica helical ribbons by one-step method and two-step method.

2.1 One-step method

2.1.1 Effect of concentration

The 0.04 M (23 mg/mL) of ions precursor were mixed with different amount of silica helical ribbons with concentration of 1 mg/mL, 2 mg/mL, 3 mg/mL, 4 mg/mL, respectively. Then 50 μ L of each solution was drop-casted on the surface of quartz slides (1 cm*1 cm) and dry at room temperature. The CD and CPL were measured with two angles at 0° and 90° respectively and accumulated to eliminate the LD effect. Based on the theoretical calculation of the ratio of silica helical ribbons and ions precursor (1 mg/1.25 mg), the ions are excess for the full in-situ inside growth which means lots of ions unreacted or recrystallized outside the silica helical ribbons. As

shown in Figures 6-3, the PNCs growth inside left-handed silica helical ribbons shows negative CD and CPL signals. The g-CPL decreased with the increment of the concentration of silica helical ribbons, while the g-CD increased. This might due to the different ratio of the achiral PNCs outside recrystallized and the chiral PNCs inside. It should be noted that the PNCs growth outside the silica helical ribbons show weaker luminescence (DC) as compared with the PNCs growth inside the silica helical ribbons due to the different surface passivation. Generally, $g\text{-CPL} \propto \frac{\text{CPL}_{\text{chiral PNCs}}}{\text{DC}_{\text{chiral PNCs}} + \text{DC}_{\text{achiral PNCs}}} \approx \frac{\text{CPL}_{\text{chiral PNCs}}}{\text{DC}_{\text{chiral PNCs}}}$ (outside achiral PNCs show weak luminescence) and $g\text{-CD} \propto \frac{\text{CD}_{\text{chiral PNCs}}}{\text{Abs}_{\text{chiral PNCs}} + \text{Abs}_{\text{achiral PNCs}}}$. With increasing the concentration of the hollow silica helical ribbons, more PNCs grow inside the hollow silica while fewer PNCs grow outside, which enhances the g-CD and causes little effect on the g-CPL due to weak luminescence of outside achiral PNCs. Interestingly, the chiral PNCs growth inside the hollow silica ribbons showed decreased size from helical CsPbBr₃ ribbons to small CsPbBr₃ nanocrystals (Figure 6-3 (d-g)) with increasing concentration of the hollow silica. The decreased size weakens the dissymmetric of the chiral PNCs, which results in smaller g-factor of CD and CPL. While the g-CD ($1.1\text{-}1.8 \times 10^{-3}$) at absorption peak 508 nm is smaller than the g-CPL ($8.2\text{-}13.9 \times 10^{-3}$) at emission peak 514 nm, which is attributed to the large amount of outside achiral PNCs. The decreased g-CPL is due to the decreased size of the chiral PNCs inside, while the increased g-CD is due to the fewer amounts of the recrystallized achiral PNCs outside.

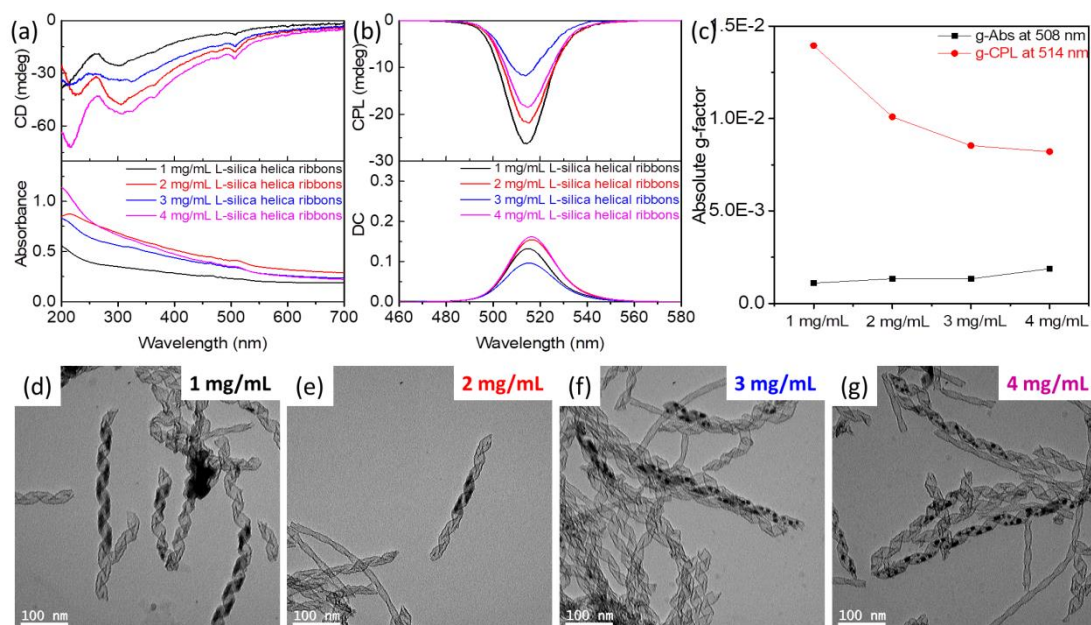


Figure 6-3. CD (a), CPL (b), absolute g-factor of absorption, and luminescence (c) spectra of chiral PNCs growth with different concentrations of the silica helical ribbons. TEM images (d-g) of chiral PNCs grow inside the silica helical ribbons with 1-4 mg/mL, respectively.

2.1.2 Effect of annealing condition

Surface of the silica helical ribbons has hydroxyl group, which is a benefit for infiltration of the perovskite precursor ions in DMF. The silica helical ribbons were calcined at 900 °C for 2 h to remove the hydroxyl group on the surface, the mixture of the calcined silica helical ribbons and the ions precursor in DMF was drop-casted on the surface of the quartz. After drying at room temperature, they show smaller CD ($g\text{-CD} \approx 1 \times 10^{-4}$) and CPL ($g\text{-CPL} \approx 1 \times 10^{-3}$) signals as shown in Figure 6-4 (a-b). The TEM image (Figure 6-4 (c)) shows the small size of PNCs growth inside the calcined silica helical ribbons which result in smaller CD and CPL signals. The calcination makes silica helical ribbons shrinkage and removes the surface hydroxyl group which hinders the infiltration of precursor ions in DMF into the calcined silica helical ribbons.

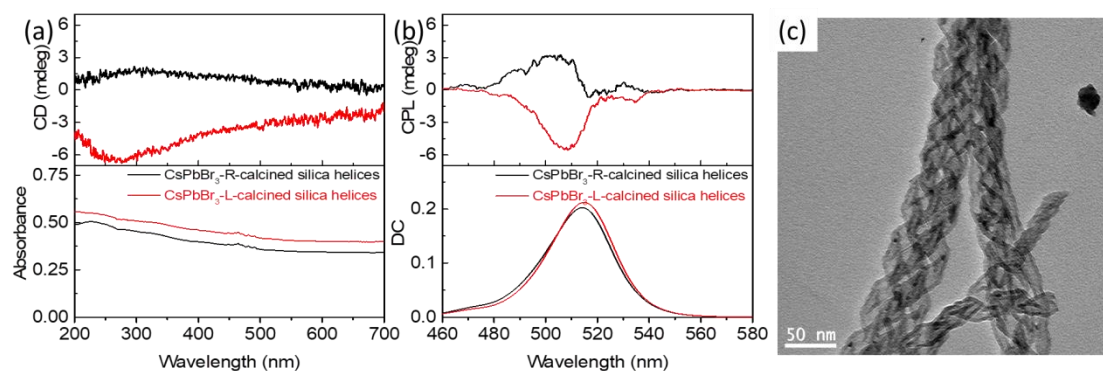


Figure 6-4. CD, absorption (a), CPL, DC (b) spectra, and TEM image (c) of chiral PNCs growth inside the 900 °C calcined silica helical ribbons prepared by the one-step method.

2.2 Two-step method

2.2.1 Effect of concentration

Different amount of silica helical ribbons (10 ug, 20 ug, 50 ug, 100 ug, 150 ug, and 200 ug) were drop-casted on the surface of the quartz slide and drying at room temperature. Then 10 uL of ions precursor was drop-casted on the silica helical ribbons quartz film and drying at room temperature. As shown in Figures 6-5, the right-handed samples show positive CD and CPL signals, while the left-handed samples show negative CD and CPL signals. The absorbance, CD, DC, and CPL signals increased with the increment of the amount of the silica helical ribbons. The CD g-factor at the absorption peak of 506 nm increased with the increasing mass of silica helical ribbons, which is similar to the one-step method. The mass ratios of the silica helical ribbons and the ions were 1/23, 1/11.5, 1/4.6, 1/1.5, 1/1.15 for the two-step method and 1/23, 1/11.5, 1/7.7, 1/5.8 for the one-step method respectively. Both methods show relatively large g-factor. While the two-step method also shows relatively large CPL g-factor ($> 2 \times 10^{-2}$) and the ratio of silica and ions is easier to optimize in terms of larger g-CD and g-CPL. Theoretically, if the amount of ions is excess against the hollow silica helical ribbons, the extent parts of PNCs growth outside the silica helical ribbons will be enhanced.

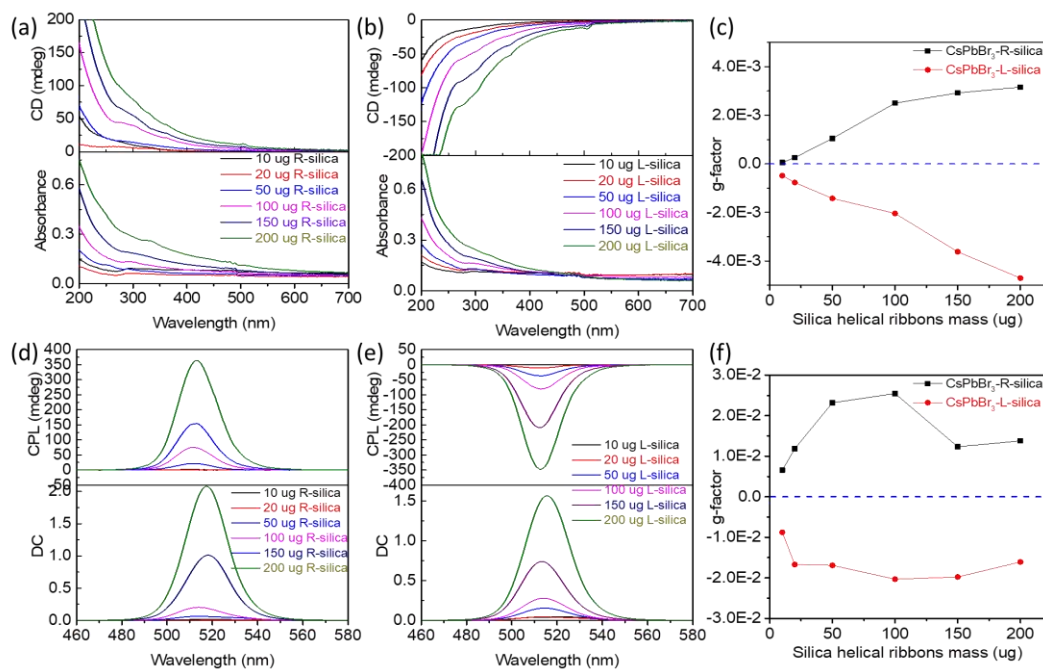


Figure 6-5. CD (a-b) and g-factor (c) spectra of PNCs grow inside the different amounts of R/L-silica helical ribbons. CPL (d-e) and g-factor (f) spectra of PNCs grow inside the different amounts of R/L-silica helical ribbons.

2.2.2 Effect of solvent evaporation

Supersaturated recrystallization of the PNCs inside the hollow silica helical ribbons can be affected by the solvent evaporation speed. Firstly, thin film made of 50 ug of silica helical ribbons on the quartz substrate were prepared, then 10 uL of precursor ions were drop-casted on the surface of the silica film and heated to dryness at 6.8, 20, 35, and 50 °C, respectively. Then the CD and CPL were measured as shown in Figures 6-6 (a-b). The PNCs growth at 6.8 and 20 °C show lower scattering absorption and the values of the g-CD are higher than those of 35 and 50 °C. Also, the values of the g-CD of PNCs growth at 6.8 and 20 °C are slightly higher than those of 35 and 50 °C. The full width at half maximum (FWHM) of the emission spectra (DC) increased with higher temperature and the redshifted shoulder peak (yellow circle) might be ascribed to the PNCs growth outside the hollow silica ribbons. The CPL peak position (514 nm) corresponds to the emission of PNCs growth inside the hollow silica ribbons (Figure 6-6 (c) red circle) with a thickness of 6.5 nm and width 22 nm,

respectively. While the broad emission spectra correspond to the weak emission of larger size of PNCs growth outside the hollow silica ribbons as shown in Figures 6-6 (b-c) (yellow circles).

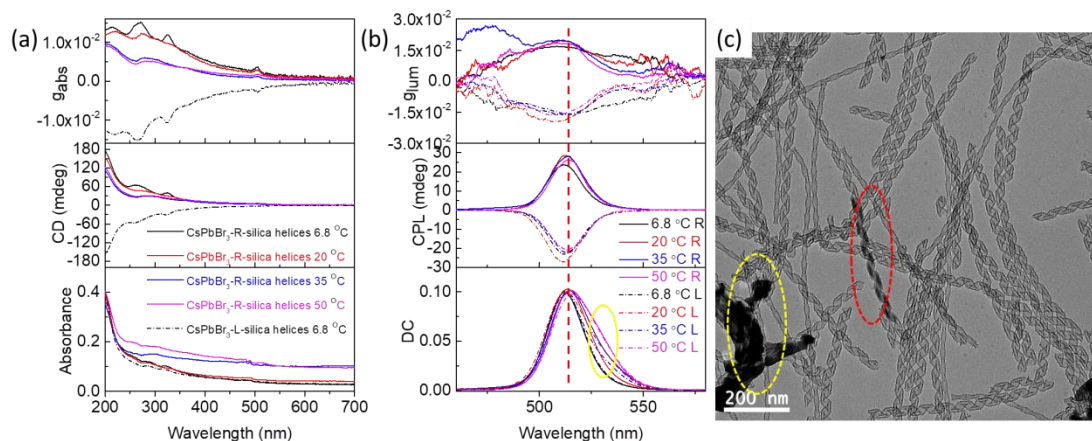


Figure 6-6. g_{abs} , CD, absorption (a) and g_{lum} , CPL, DC (b) spectra of CsPbBr₃-R/L-silica helices growth at different evaporation temperatures. (c) TEM image of CsPbBr₃-R-silica helices at 50 °C.

The lower magnification TEM images of PNCs growth inside silica helical ribbons at different temperatures were observed as shown in Figures 6-7 (a-d). More and more PNCs grow outside the silica helical ribbons with increasing the temperature. This means the precursor solvent evaporated too fast to go inside the hollow silica helical ribbons and results in more PNCs grow outside the silica helical ribbons.

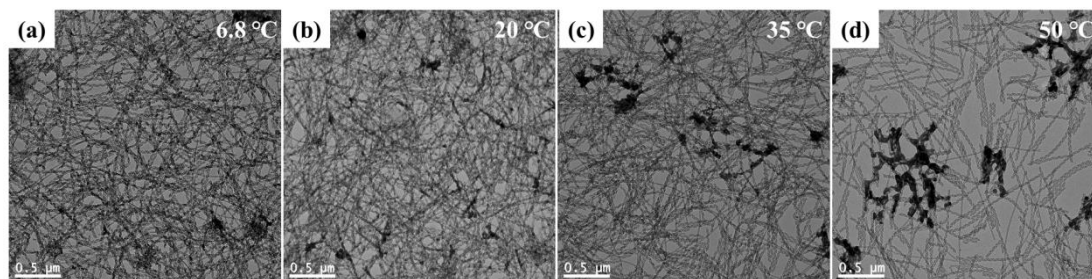


Figure 6-7. Lower magnification of TEM images of PNCs grow at 6.8 °C (a), 20 °C (b), 35 °C (c) and 50 °C (d), respectively.

2.2.3 Effect of annealing condition

50 μg of silica helical ribbons were drop-casted on the surface of quartz slides and made them to dryness at room temperature. Then the silica helical ribbons quartz film were calcined at 900 °C for 2 h. 10 μL of precursor ions were drop-casted on the surface of the calcined silica helical ribbons quartz film and dried at room temperature. As compared with the one-step method, the two-step method shows larger CD and CPL signals. The wavelength of the CPL peaks is at around 502 nm and the value of the g-CPL is around 6×10^{-3} which is one-third of the sample before the calcination.

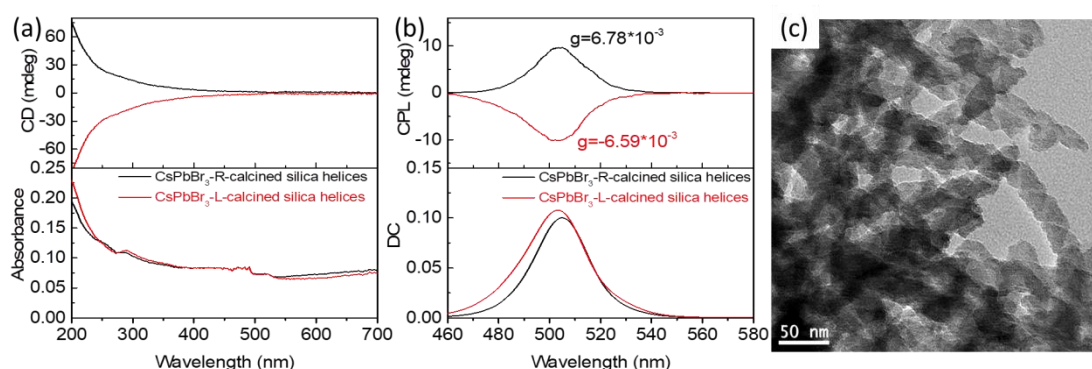


Figure 6-8. CD, absorption (a), CPL, DC (b) spectra, and TEM image (c) of CsPbBr₃-R/L-silica helices growth inside the 900 °C calcined silica helical ribbons prepared by two-step method.

2.2.4 Effect of halide composition

The PNCs growth inside the silica helical ribbons replicates the organic template of self-assembled Gemini tartrate. In this context, the emission wavelength of those materials is limited by their size. To expand their range of optical response, the halide compositions were tuned in terms of tuning the optical bandgap. The precursor ions were prepared by dispersing CsBr, CsI, PbBr₂, and PbI₂ in DMF with different ratios of Br and I. For the mixed halide precursor ions, the in-situ growth of PNCs showed strong CD signals as shown in Figure 6-9. The right-handed samples show positive signals while left-handed samples show negative signals. The absorption spectra were expected to show a red shift with increasing the ratios of I ions, while the absorption peak shows a blue shift to 420 nm which results from the yellow nonperovskite polymorph.^{57, 58} The film showed yellow color under the natural light and no emission

were observed by CPL measurement. The TEM images with the mixed halide ions in-situ growth show different images as compared with that of the single-component Br ions as shown in Figures 6-10 (a-c).

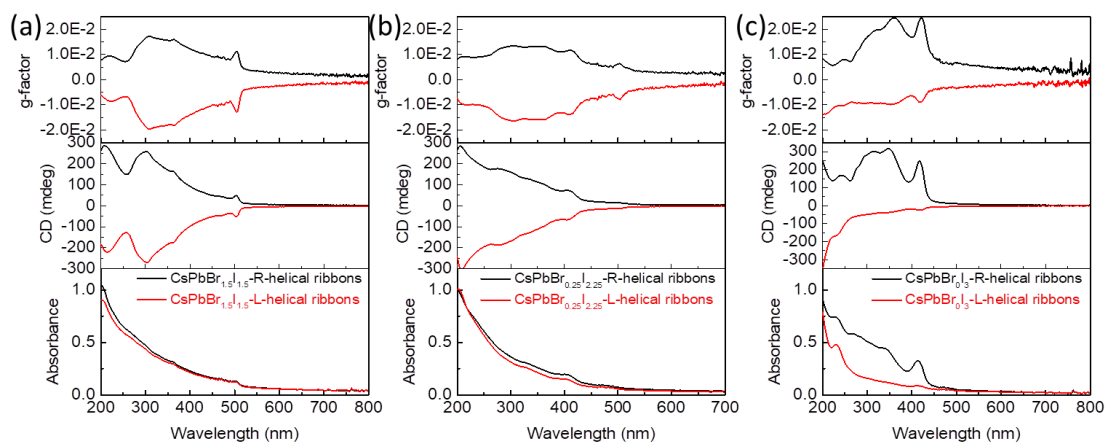


Figure 6-9. g-factor, CD, and absorption spectra of CsPbBr_{1.5}I_{1.5} (a), CsPbBr_{0.25}I_{2.75} (b), and CsPbBr₀I₃ (c).

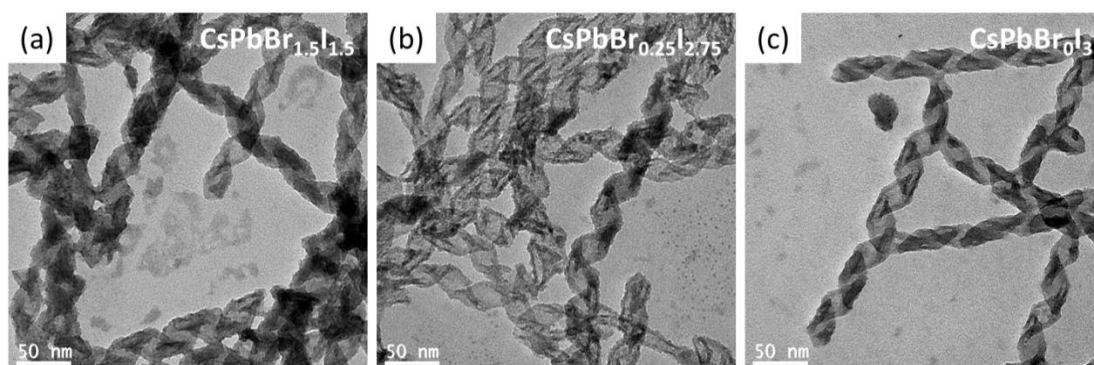


Figure 6-10. TEM images of CsPbBr_{1.5}I_{1.5} (a), CsPbBr_{0.25}I_{2.75} (b), and CsPbBr₀I₃ (c).

3. Conclusion

The chiral shape of PNCs assisted by the hollow silica ribbons *via* supersaturated recrystallization methods have been successfully prepared by two methods. Both of the one-step method and the two-step method show promising optical activities. The two-step method shows a larger g-factor and easier control of the ratio of silica and precursor ions as compared with the one-step method. The two-step method prepared left- and right-handed PNCs show strong CD and CPL mirror images and the

dissymmetric g-factor is up to 2×10^{-2} . Both of the ratios of the silica ribbons and precursor ions and the solvent evaporation temperature show significant effect on the PNCs growth inside and outside the hollow silica ribbons. The g-factor decreased a lot when the hollow silica ribbons was calcined at 900 °C due to the modification of the silica surface which hinders the penetration of the precursor ions into the hollow silica ribbons. For the mixed halide ions, yellow nonperovskite nanocrystal growth inside the hollow silica helical ribbons were confirmed and that materials showed strong CD while no emission was observed. The tremendous g-factor of the chiral shaped PNCs prepared inside the hollow silica ribbons would enrich the chiral group of PNCs for their further applications.

4. Experiment section

4.1 Materials and instruments

Chemical reagents CsBr (99.999%), CsI (99.999%), PbBr₂ (99.999%), PbI₂ (99.999%), dimethylformamide (DMF, 99.8%, anhydrous), were purchased from Sigma Company.

Transmission electron microscopy (TEM) was performed with CM 120 (Philips) at 120 kV. Cryogenic electron microscopy (Cryo-EM) was performed with Tecnai F20 (FEI). Circular dichroism (CD), linear dichroism (LD), and UV-vis spectrums were measured by J-815 (JASCO). Circularly polarized luminescence (CPL) and emission spectra were obtained by CPL-300 (JASCO).

4.2 Silica ribbons and ions precursors

Silica ribbons were prepared according to the procedures as described in Chapter 2; the silica ribbons powder was obtained by lyophilizing for overnight.

CsPbBr_xI_(3-x) ($0 \leq x \leq 3$) precursor mixture of: $0.4/3 \times x$ mmol CsBr and $0.4/3 \times (3-x)$ mmol CsI and mixture of $0.4/3 \times x$ mmol PbBr₂ and $0.4/3 \times (3-x)$ mmol PbI₂ mixture dissolved in 10 ml DMF. Precursor for CsPbBr₃ NCs in-situ growth: 0.4 mmol of CsBr and 0.4 mmol of PbBr₂ were dissolved in 10 ml of DMF to obtain transparent precursors containing Cs⁺, Pb²⁺, and Br⁻.

One-step preparation:

Silica ribbons (0.5 mg-2 mg) were added into 0.5 mL precursor ions DMF solution and the mixture was tip-sonicated for 10 min to get a homogenous solution. Then 50 uL mixture was drop-casted on the surface of quartz slides (1 cm*1cm) and dried at different temperatures.

Two-step preparation:

Silica ribbons (50 ug or 100 ug) were drop-casted on the surface of quartz slides and dried at room temperature, then 10 uL of precursor ions was drop-casted on the surface of silica ribbons quartz slides and dried at different temperatures.

5. Reference

1. Shi, D.; Adinolfi, V.; Comin, R.; Yuan, M.; Alarousu, E.; Buin, A.; Chen, Y.; Hoogland, S.; Rothenberger, A.; Katsiev, K.; Losovyj, Y.; Zhang, X.; Dowben, P. A.; Mohammed, O. F.; Sargent, E. H.; Bakr, O. M., Solar cells. Low trap-state density and long carrier diffusion in organolead trihalide perovskite single crystals. *Science* **2015**, *347* (6221), 519-22.
2. Dong, Q.; Fang, Y.; Shao, Y.; Mulligan, P.; Qiu, J.; Cao, L.; Huang, J., Solar cells. Electron-hole diffusion lengths > 175 μm in solution-grown $\text{CH}_3\text{NH}_3\text{PbI}_3$ single crystals. *Science* **2015**, *347* (6225), 967-70.
3. Kim, J. Y.; Lee, J. W.; Jung, H. S.; Shin, H.; Park, N. G., High-Efficiency Perovskite Solar Cells. *Chem Rev* **2020**, *120* (15), 7867-7918.
4. Du, P.; Gao, L.; Tang, J., Focus on performance of perovskite light-emitting diodes. *Frontiers of Optoelectronics* **2020**, *13* (3), 235-245.
5. Chen, W.; Zhang, S.; Zhou, M.; Zhao, T.; Qin, X.; Liu, X.; Liu, M.; Duan, P., Two-Photon Absorption-Based Upconverted Circularly Polarized Luminescence Generated in Chiral Perovskite Nanocrystals. *J Phys Chem Lett* **2019**, *10* (12), 3290-3295.
6. Yuan, C.; Li, X.; Semin, S.; Feng, Y.; Rasing, T.; Xu, J., Chiral Lead Halide Perovskite Nanowires for Second-Order Nonlinear Optics. *Nano Lett* **2018**, *18* (9), 5411-5417.
7. Naciri, J.; Shenoy, D. K.; Keller, P.; Gray, S.; Crandall, K.; Shashidhar, R., Synthesis and Pyroelectric Properties of Novel Ferroelectric Organosiloxane Liquid Crystalline Materials. *Chemistry of Materials* **2002**, *14* (12), 5134-5139.
8. Zhang, H. Y.; Tang, Y. Y.; Shi, P. P.; Xiong, R. G., Toward the Targeted Design of Molecular Ferroelectrics: Modifying Molecular Symmetries and Homochirality. *Acc Chem Res* **2019**, *52* (7), 1928-1938.
9. Sanchez, D. S.; Belopolski, I.; Cochran, T. A.; Xu, X.; Yin, J. X.; Chang, G.; Xie, W.; Manna, K.; Suss, V.; Huang, C. Y.; Alidoust, N.; Multer, D.; Zhang, S. S.; Shumiya, N.; Wang, X.; Wang, G. Q.; Chang, T. R.; Felser, C.; Xu, S. Y.; Jia, S.; Lin, H.; Hasan, M. Z., Topological chiral crystals with helicoid-arc quantum states. *Nature* **2019**, *567* (7749), 500-505.
10. Chen, C.; Gao, L.; Gao, W.; Ge, C.; Du, X.; Li, Z.; Yang, Y.; Niu, G.; Tang, J., Circularly polarized light detection using chiral hybrid perovskite. *Nat Commun* **2019**, *10* (1), 1927.
11. Kim, Y. H.; Zhai, Y.; Lu, H.; Pan, X.; Xiao, C.; Gaubling, E. A.; Harvey, S. P.; Berry, J. J.; Vardeny, Z. V.; Luther, J. M.; Beard, M. C., Chiral-induced spin selectivity enables a room-temperature spin light-emitting diode. *Science* **2021**, *371* (6534), 1129-1133.
12. Bisoyi, H. K.; Li, Q., Light-Directing Chiral Liquid Crystal Nanostructures: From 1D to 3D. *Accounts of Chemical Research* **2014**, *47* (10), 3184-3195.
13. Service, R. F. J. S., Ultrafast Lasers. Lighting the Way to a Quantum Computer. **2001**, *292* (5526), 2412-2413.
14. Humphreys, P. C.; Kalb, N.; Morits, J. P. J.; Schouten, R. N.; Vermeulen, R. F. L.; Twitchen, D. J.; Markham, M.; Hanson, R., Deterministic delivery of remote entanglement on a quantum network. *Nature* **2018**, *558* (7709), 268-273.
15. Michaeli, K.; Kantor-Uriel, N.; Naaman, R.; Waldeck, D. H., The electron's spin and molecular chirality - how are they related and how do they affect life processes? *Chem Soc Rev* **2016**, *45* (23), 6478-6487.
16. Long, G.; Sabatini, R.; Saidaminov, M. I.; Lakhwani, G.; Rasmita, A.; Liu, X.; Sargent, E. H.; Gao, W.,

Chapter 6. Chiral shaped perovskite nanocrystals growth inside chiral hollow silica nanoribbons

Chiral-perovskite optoelectronics. *Nature Reviews Materials* **2020**, 5 (6), 423-439.

17. Naaman, R.; Paltiel, Y.; Waldeck, D. H., Chiral Induced Spin Selectivity Gives a New Twist on Spin-Control in Chemistry. *Acc Chem Res* **2020**, 53 (11), 2659-2667.
18. Naaman, R.; Waldeck, D. H., Chiral-Induced Spin Selectivity Effect. *J Phys Chem Lett* **2012**, 3 (16), 2178-87.
19. Abendroth, J. M.; Stemer, D. M.; Bloom, B. P.; Roy, P.; Naaman, R.; Waldeck, D. H.; Weiss, P. S.; Mondal, P. C., Spin Selectivity in Photoinduced Charge-Transfer Mediated by Chiral Molecules. *ACS Nano* **2019**, 13 (5), 4928-4946.
20. Dong, Y.; Zhang, Y.; Li, X.; Feng, Y.; Zhang, H.; Xu, J., Chiral Perovskites: Promising Materials toward Next-Generation Optoelectronics. *Small* **2019**, 15 (39), e1902237.
21. Ma, J.; Wang, H.; Li, D., Recent Progress of Chiral Perovskites: Materials, Synthesis, and Properties. *Adv Mater* **2021**, e2008785.
22. Dang, Y.; Liu, X.; Cao, B.; Tao, X. J. M., Chiral halide perovskite crystals for optoelectronic applications. **2021**.
23. Gao, X.; Zhang, X.; Deng, K.; Han, B.; Zhao, L.; Wu, M.; Shi, L.; Lv, J.; Tang, Z., Excitonic Circular Dichroism of Chiral Quantum Rods. *J Am Chem Soc* **2017**, 139 (25), 8734-8739.
24. Gao, X.; Zhang, X.; Zhao, L.; Huang, P.; Han, B.; Lv, J.; Qiu, X.; Wei, S. H.; Tang, Z., Distinct Excitonic Circular Dichroism between Wurtzite and Zincblende CdSe Nanoplatelets. *Nano Lett* **2018**, 18 (11), 6665-6671.
25. Kuno, J.; Imamura, Y.; Katouda, M.; Tashiro, M.; Kawai, T.; Nakashima, T., Inversion of Optical Activity in the Synthesis of Mercury Sulfide Nanoparticles: Role of Ligand Coordination. *Angew Chem Int Ed Engl* **2018**, 57 (37), 12022-12026.
26. Liu, P.; Chen, W.; Okazaki, Y.; Battie, Y.; Brocard, L.; Decossas, M.; Pouget, E.; Muller-Buschbaum, P.; Kauffmann, B.; Pathan, S.; Sagawa, T.; Oda, R., Optically Active Perovskite CsPbBr₃ Nanocrystals Helically Arranged on Inorganic Silica Nanohelices. *Nano Lett* **2020**, 20 (12), 8453-8460.
27. Guerrero-Martinez, A.; Auguie, B.; Alonso-Gomez, J. L.; Dzolic, Z.; Gomez-Grana, S.; Zinic, M.; Cid, M. M.; Liz-Marzan, L. M., Intense optical activity from three-dimensional chiral ordering of plasmonic nanoantennas. *Angew Chem Int Ed Engl* **2011**, 50 (24), 5499-503.
28. Shi, Y.; Duan, P.; Huo, S.; Li, Y.; Liu, M., Endowing Perovskite Nanocrystals with Circularly Polarized Luminescence. *Adv Mater* **2018**, 30 (12), e1705011.
29. Ben-Moshe, A.; Govorov, A. O.; Markovich, G., Enantioselective synthesis of intrinsically chiral mercury sulfide nanocrystals. *Angew Chem Int Ed Engl* **2013**, 52 (4), 1275-9.
30. Flack, H. D., Chiral and Achiral Crystal Structures. *Helvetica Chimica Acta* **2003**, 86 (4), 905-921.
31. Wang, P. P.; Yu, S. J.; Ouyang, M., Assembled Suprastructures of Inorganic Chiral Nanocrystals and Hierarchical Chirality. *J Am Chem Soc* **2017**, 139 (17), 6070-6073.
32. Ben-Moshe, A.; Wolf, S. G.; Bar Sadan, M.; Houben, L.; Fan, Z.; Govorov, A. O.; Markovich, G., Enantioselective control of lattice and shape chirality in inorganic nanostructures using chiral biomolecules. *Nat Commun* **2014**, 5, 4302.
33. Wang, P. P.; Yu, S. J.; Govorov, A. O.; Ouyang, M., Cooperative expression of atomic chirality in inorganic nanostructures. *Nat Commun* **2017**, 8, 14312.
34. Orme, C. A.; Noy, A.; Wierzbicki, A.; McBride, M. T.; Grantham, M.; Teng, H. H.; Dove, P. M.; DeYoreo, J. J., Formation of chiral morphologies through selective binding of amino acids to calcite surface steps. *Nature* **2001**, 411 (6839), 775-9.
35. Lee, H. E.; Ahn, H. Y.; Mun, J.; Lee, Y. Y.; Kim, M.; Cho, N. H.; Chang, K.; Kim, W. S.; Rho, J.; Nam, K.

Chapter 6. Chiral shaped perovskite nanocrystals growth inside chiral hollow silica nanoribbons

- T., Amino-acid- and peptide-directed synthesis of chiral plasmonic gold nanoparticles. *Nature* **2018**, 556 (7701), 360-365.
36. Duan, Y.; Liu, X.; Han, L.; Asahina, S.; Xu, D.; Cao, Y.; Yao, Y.; Che, S., Optically active chiral CuO "nanoflowers". *J Am Chem Soc* **2014**, 136 (20), 7193-6.
37. Hazen, R. M.; Sholl, D. S., Chiral selection on inorganic crystalline surfaces. *Nat Mater* **2003**, 2 (6), 367-74.
38. Ernst, K.-H., Molecular chirality in surface science. *Surface Science* **2013**, 613, 1-5.
39. Shtukenberg, A. G.; Punin, Y. O.; Gujral, A.; Kahr, B., Growth actuated bending and twisting of single crystals. *Angew Chem Int Ed Engl* **2014**, 53 (3), 672-99.
40. Liu, Y.; Wang, J.; Kim, S.; Sun, H.; Yang, F.; Fang, Z.; Tamura, N.; Zhang, R.; Song, X.; Wen, J.; Xu, B. Z.; Wang, M.; Lin, S.; Yu, Q.; Tom, K. B.; Deng, Y.; Turner, J.; Chan, E.; Jin, D.; Ritchie, R. O.; Minor, A. M.; Chrzan, D. C.; Scott, M. C.; Yao, J., Helical van der Waals crystals with discretized Eshelby twist. *Nature* **2019**, 570 (7761), 358-362.
41. Bierman, M. J.; Lau, Y. K.; Kvit, A. V.; Schmitt, A. L.; Jin, S., Dislocation-driven nanowire growth and Eshelby twist. *Science* **2008**, 320 (5879), 1060-3.
42. Ben-Moshe, A.; da Silva, A.; Muller, A.; Abu-Odeh, A.; Harrison, P.; Waelder, J.; Niroui, F.; Ophus, C.; Minor, A. M.; Asta, M.; Theis, W.; Ercius, P.; Alivisatos, A. P., The chain of chirality transfer in tellurium nanocrystals. *Science* **2021**, 372 (6543), 729-733.
43. Meng, F.; Morin, S. A.; Forticaux, A.; Jin, S., Screw dislocation driven growth of nanomaterials. *Acc Chem Res* **2013**, 46 (7), 1616-26.
44. Martin, C. R., Nanomaterials: a membrane-based synthetic approach. *Science* **1994**, 266 (5193), 1961-6.
45. Lu, A. H.; Schüth, F., Nanocasting: A Versatile Strategy for Creating Nanostructured Porous Materials. *Advanced Materials* **2006**, 18 (14), 1793-1805.
46. Zhang, L.; Jin, L.; Liu, B.; He, J., Templated Growth of Crystalline Mesoporous Materials: From Soft/Hard Templates to Colloidal Templates. *Front Chem* **2019**, 7, 22.
47. Parala, H.; Winkler, H.; Kolbe, M.; Wohlfart, A.; Fischer, R. A.; Schmechel, R.; Seggern, H. v., Confinement of CdSe Nanoparticles Inside MCM-41. *Advanced Materials* **2000**, 12 (14), 1050-1055.
48. Li, Y.; Xu, D.; Zhang, Q.; Chen, D.; Huang, F.; Xu, Y.; Guo, G.; Gu, Z., Preparation of Cadmium Sulfide Nanowire Arrays in Anodic Aluminum Oxide Templates. *Chemistry of Materials* **1999**, 11 (12), 3433-3435.
49. Hirai, T.; Okubo, H.; Komasa, I., Size-Selective Incorporation of CdS Nanoparticles into Mesoporous Silica. *The Journal of Physical Chemistry B* **1999**, 103 (21), 4228-4230.
50. Agger, J. R.; Anderson, M. W.; Pemble, M. E.; Terasaki, O.; Nozue, Y., Growth of Quantum-Confined Indium Phosphide inside MCM-41. *The Journal of Physical Chemistry B* **1998**, 102 (18), 3345-3353.
51. Longo, G.; Pertegás, A.; Martínez-Sarti, L.; Sessolo, M.; Bolink, H. J., Highly luminescent perovskite-aluminum oxide composites. *Journal of Materials Chemistry C* **2015**, 3 (43), 11286-11289.
52. Zong, Y.; Yang, T.; Hao, P.; Shan, B.; Peng, B.; Hu, X.; Tao, R.; Chen, X.; Wu, P.; Zhang, K., Spatial and chemical confined ultra-small CsPbBr₃ perovskites in dendritic mesoporous silica nanospheres with enhanced stability. *Microporous and Mesoporous Materials* **2020**, 302.
53. Dirin, D. N.; Protesescu, L.; Trummer, D.; Kochetygov, I. V.; Yakunin, S.; Krumeich, F.; Stadie, N. P.; Kovalenko, M. V., Harnessing Defect-Tolerance at the Nanoscale: Highly Luminescent Lead Halide Perovskite Nanocrystals in Mesoporous Silica Matrixes. *Nano Lett* **2016**, 16 (9), 5866-74.

Chapter 6. Chiral shaped perovskite nanocrystals growth inside chiral hollow silica nanoribbons

54. Zhang, Q.; Wang, B.; Zheng, W.; Kong, L.; Wan, Q.; Zhang, C.; Li, Z.; Cao, X.; Liu, M.; Li, L., Ceramic-like stable CsPbBr₃ nanocrystals encapsulated in silica derived from molecular sieve templates. *Nat Commun* **2020**, *11* (1), 31.
55. Liu, P.; Chen, W.; Wang, W.; Xu, B.; Wu, D.; Hao, J.; Cao, W.; Fang, F.; Li, Y.; Zeng, Y.; Pan, R.; Chen, S.; Cao, W.; Sun, X. W.; Wang, K., Halide-Rich Synthesized Cesium Lead Bromide Perovskite Nanocrystals for Light-Emitting Diodes with Improved Performance. *Chemistry of Materials* **2017**, *29* (12), 5168-5173.
56. Oda, R.; Artzner, F.; Laguerre, M.; Huc, I., Molecular Structure of Self-Assembled Chiral Nanoribbons and Nanotubules Revealed in the Hydrated State. *Journal of the American Chemical Society* **2008**, *130* (44), 14705-14712.
57. Eperon, G. E.; Paternò, G. M.; Sutton, R. J.; Zampetti, A.; Haghighirad, A. A.; Cacialli, F.; Snaith, H. J., Inorganic caesium lead iodide perovskite solar cells. *Journal of Materials Chemistry A* **2015**, *3* (39), 19688-19695.
58. Sutton, R. J.; Filip, M. R.; Haghighirad, A. A.; Sakai, N.; Wenger, B.; Giustino, F.; Snaith, H. J., Cubic or Orthorhombic? Revealing the Crystal Structure of Metastable Black-Phase CsPbI₃ by Theory and Experiment. *ACS Energy Letters* **2018**, *3* (8), 1787-1794

Chapter 7. Conclusion and perspectives

In Chapter 1, the developments and origins of chiral organic materials and inorganic materials were surveyed and compared. Similar to the origins of chiral organic materials, the chiral inorganic materials can replicate the origins of the organic chiral materials, like intrinsic chirality, chiral material self-assembly, and achiral materials chiral self-assembly. The importance of chirality in our life has been presented based on their advanced applications such as chiral catalysis, chiral recognition, and separation, 3D display, spintronics, *etc.* Inorganic nanocrystals (NCs) exhibit more excellent optoelectronic properties as compared with organic materials. In particular, the inorganic NCs show more advanced applications if chirality is induced. The general strategies and developments of endowing chirality to NCs have been discussed in detail which is a benefit for the project design and understanding. The chirality of NCs can be induced by the chiral ligands, chiral lattice, chiral shape, and chiral self-organization or their cooperative chirality. Among the various ways of the chirality induction, endowing chirality to achiral NCs through their chiral self-organization or chiral shape assisted by hollow chiral silica ribbons would be convenient and promising methods. It is very important to understand the surface state of the NCs and silica ribbons for their complexation. Indeed, classification and exchange rules of the surface ligands of NCs, and surface modification of the silica ribbons have been discussed which inspired us several strategies to graft NCs on the surface of silica ribbons.

In Chapter 2, the strategies of the materials designs are described based on the background of endowing chirality to NCs. The silica ribbons replicate the organic helical Gemini tartrate shape, which has chiral helical and hollow structure. The helical and hollow structures offer the opportunity to endow chirality by chiral self-organization or chiral shape formation of NCs. The synthetic processes of the helical and twisted silica ribbons are elucidated. Also, surface modification of the silica ribbons and related parameters are discussed for the preparation of optically

active NCs by complexed with silica ribbons. Three possible methods for grafting NCs on the surface of silica ribbons are discussed in detail based on the backgrounds. Also, a general way to grow the NCs inside the hollow silica ribbons has also been presented.

In Chapter 3, scattering CD of the silica ribbons film was presented. Since the silica helical/twisted ribbons have a chiral shaped structure, which might have different interaction on different handedness of circularly polarized light. Silica show big band gap which have no absorbance and emission in UV-vis range. While it has absorbance in IR range and scattering in UV range. The VCD of silica ribbons has been studied before, but the scattering CD is still lack. In here the right-handed silica ribbons show positive scattering CD signals, while left-handed silica ribbons show negative scattering CD signals. Silica helical ribbons show larger scattering CD than the silica twisted ribbons. It should be noted that, the film composed of the silica ribbons and the NCs mixture (without grafting) does not show any CD signals in the NCs absorption range, while the scattering CD signals decreased due to the impregnation of the NCs and weaken the chiral structure of the silica ribbons. If the silica ribbons and NCs are separated, it does not show any changes in the scattering CD signals. That valuable information would be useful for the related materials design.

In Chapter 4, the perovskite CsPbBr_3 nanocrystals were grafted on the surface of silica helical ribbons by an in-situ growth method or ligand exchange method. In the case of PNCs grafted by in-situ growth method, no chirality induction observed in suspension. When PNCs were grafted by the ligand exchange method, three different results were observed in suspension as follows: 1) When isolated PNCs were grafted randomly on the surface of left- and right-handed silica helical ribbons, no CD was observed in suspension; 2) When PNCs were grafted with oriented attachment, PNCs grew along with the silica helical ribbons, and mirror-image CD signals were observed from PNCs-R/L-silica helical ribbons in suspension. When further growth of PNCs for full coverage on the silica surface was performed, partial alignment of

PNCs-R/L-silica helical ribbons was confirmed, and strong apparent CD signals were observed due to the LD and vortex flow.

Even though PNCs grafted silica helical ribbons do not show any observable optical activity in suspension. After drying on the substrates to form films, strong CD and CPL signals are observed with the dissymmetric factor of $> 6 \times 10^{-3}$. Both of solvated and dried TEM images show densely attached PNCs on the surface of the helical ribbons. However, for the solvated helical ribbons, the PNCs show a thicker and swollen layer around the silica helical ribbons without detectable helical organization probably with strongly solvated ligands. On the other hand, for the dried helical ribbons, the PNCs are closely attached on the surface, suggesting ligands collapse and a higher interaction between the adjacent NCs, which may induce higher self-organization with a 3D spiral arrangement of the PNCs along with the inorganic chiral silica helical ribbons. GISAXS confirms a correlation between PNCs for the dried samples, which does not exist for solvated samples. CDM simulation confirms that for the dielectric nanoparticles such as PNCs, the correlation between the particles to “feel” the chirality, the inter-particle distances need to be very close to each other with good alignment, which is likely why solvated samples with larger particle distances with much less ordered organization do not show any detectable CD. The samples dried at 4 °C (with slower drying) show stronger CD signals than those dried at 20 °C (faster drying), which is probably due to the closer packing originating from the slower film drying. The films show excellent photostability in their absorbance and CD properties, however, lose significantly their emissivity upon heating up to 80 °C. Consequently, this Chapter confirms that the self-organization of NCs on the surface of silica helical ribbons is the key for the chirality induction.

In Chapter 5, a full view of the chirality induction by QDs or QRs chiral arrangement on the inorganic silica ribbons was described. The QDs-silica helical ribbons film was optimized in terms of the QDs grafting density. The g-factor is increased with the QDs grafting density. The QDs-silica helical ribbons drying temperature effect and solvent effect on the optical activity of the obtained materials have been studied. Lower

temperature and lower vapor pressure solvent result in remarkable optical activities with dissymmetric g-factor 1.2×10^{-3} (Octane as solvent and evaporated at 4 °C) and 0.65×10^{-3} (Octane as solvent and evaporated at 20 °C). It was also found that the QDs self-organization would be hindered by applied PMMA or enhanced by annealing. The QDs with different sizes and different crystal structures have also been grafted on the silica helical/twisted ribbons. QDs with helical arrays show stronger optical activities than the twisted array. Also high fluorescence core-shell QDs and QRs have been grafted on the silica helical or twisted ribbons. The core-shell structured QDs and QRs also show optically active properties though they have smaller g-factor as compared with those of bare CdSe QDs. The QRs trend to tip grafting on the surface of silica twisted ribbons in suspension. While after drying in a film state, the QRs grafting models are modified depending on the length of QRs due to the drying effect. QRs with tip grafting or side grafting show reversed CD spectra. While with QRs length increasing, the QRs-silica twisted ribbons show strong LD which affects the CPL measurement. The chirality induction by chiral self-organization with solvent evaporation technology would be very promising in the future commercial photoelectric application to address some energy issues, such as chiral catalysis and spintronics.

In Chapter 6, the chiral shape of PNCs assisted by the hollow silica ribbons *via* supersaturated recrystallization methods has been successfully prepared by two ways. Both of the one-step method and two-step method show remarkable optically active properties. While the two-step method shows a larger g-factor and easier control of the ratio of the silica and the precursor ions as compared with those of the one-step method. The left- and right-handed PNCs prepared by two-step method show strong CD and CPL mirror images and the dissymmetric g-factor is up to 2×10^{-2} . Both of the ratios of the silica and the precursor ions and the temperature for the solvent evaporation affect crucially for the PNCs growth inside and outside the hollow silica ribbons. The g-factor decreased a lot when the hollow silica ribbons was calcined at 900 °C due to the modification of the silica surface state which hinders the penetration

of the precursor ions into the hollow silica ribbons. For the mixed halide precursor ions, yellow nonperovskite nanocrystal growth inside the hollow silica helical ribbons was confirmed and those materials show strong CD while no emission was observed. The relative larger g-factor of chiral shaped PNCs prepared inside the hollow silica ribbons would enrich the chiral group of PNCs which can be beneficial to their applications.

For the NCs self-organization on the surface of silica ribbons, the whole process can be generally described as below: NCs preparation, silica ribbons preparation, NCs combined with silica ribbons, NCs-silica ribbons in suspension without chirality induction, solvent evaporation to promote the NCs self-organization on the surface of the silica ribbons, and the preparation of the NCs-silica ribbons film with strong chirality induction. In order to understand the chirality induction process systematically, each process such as the preparation of the NCs, preparation of the silica ribbons, combination of them, and the drying conditions of them can be modified. 1) NCs with different sizes, shapes, crystal structures, and core-shell structures have been discussed. The dissymmetric g-factor increased with increasing the size of spherical NCs, while the crystal structures have small effect on the chirality induction. NCs with core-shell structure show smaller g-factor as compared with bare NCs. Nanorods with different lengths show smaller g-factor due to the bad self-organization on the surface of the silica ribbons. Also, the CD signals turned to the opposite along with increasing the length of the nanorods in the two different types of the combination systems (tip-grafting and side grafting). 2) The silica ribbons with different morphology (silica helical ribbons and twisted ribbons) have been discussed, the silica helical ribbons with NCs show stronger chirality induction as compared with the silica twisted ribbons. Since the pitch and the width of the silica helical and the twisted ribbons are difficult to adjust, it is hard to optimize the chirality induction by the pitch and width of the silica ribbons templates. 3) The g-factor increased with the increment of the grafting density of the NCs. The NCs grafting density is decided by the diameter of the NCs and the surface ligands. Based

on the simulation, the g-factor increased exponentially with decreasing the NCs inter-particle distance. Promising g-factor ($> 10^{-2}$) might be obtained when the NCs surface ligands were changed to have short ligands. 4) For the drying process, the solvent, environment temperature have been discussed, the solvent with a higher boiling point and lower temperature results in a relatively larger g-factor. If the PMMA was added to the solution with a higher concentration than 10 mg/mL, no CD signals was detected after drying as a film state. Still, some other parameters for preparation are not discussed in this thesis, such as humidity.

For preparation of the chiral shaped NCs, the crucial steps are the preparation of precursor ions and silica ribbons followed by the solvent evaporation. The chiral shaped NCs can be prepared by two ways, which are one-step or two-step methods. The one-step method is to drop-cast the mixture of ions and silica ribbons as the precursor followed by the dryness of them, while the two-step method is to drop-cast the silica ribbons initially followed by the dryness as the first step. In the second step, the precursor ions are drop-casted and made them to dryness. Obtained chiral PNCs through two step method show relatively larger g-factor and easier to control the ratio of silica and precursor ions as compared with those by the one-step method. The concentration effect of the silica ribbons is discussed in this thesis, though the concentration of precursor ions is hard to adjust for the CsPbBr₃ growth. For the drying effect, the temperature effect has been discussed, while the solvent and humidity haven't been discussed yet. Also the hollow silica ribbons with tunable pitch and width have not yet been discussed. In this context, further investigation to optimize the preparation conditions for chiral shaped PNCs is still required

It would also be very interesting to use the NCs with their chiral self-organization or their chiral shaped structures for some applications, such as chiral catalysts, spintronics, *etc.*

List of publication

- Oda, R., Liu, P., Hillard, E., Rosa, P., Nlate, S., Okazaki, Y., Pouget, E., Sagawa, T., Battie, Y., Butteteau, T., *Chirogenesis in Solid State and Spontaneous Resolution*, “*Chirogenesis in Chemical Science*” World Scientific, London, Chapter 9, (Accepted)
- Liu, P., Battie, Y., Okazaki, Y., Ryu, N., Pouget, E., Nlate, S., Sagawa, T,*. Oda, R.*, *Optically active scattering from helical and twisted silica nanoribbons*, **Chemical communication**, 2021, (Accepted)
- Liu, P., Battie, Y., Decossas, M., Tan, S., Pouget, E., Okazaki, Y., Sagawa, T,*. Oda, R.*, *Chirality induction to CdSe nanocrystals self-organized on silica nanohelices-tuning chiroptical properties*, **ACS Nano**, 2021, (Accepted) DOI: org/10.1021/acsnano.1c05819.
- Liu, P., Chen, W., Okazaki, Y., Battie, Y., Brocard, L., Decossas, M., Pouget, E., Müller-Buschbaum, P., Kauffmann, B., Pathan, S., Sagawa, T,*. Oda, R.*, *Optically active perovskite CsPbBr₃ nanocrystals helically arranged on inorganic silica nanohelices*, **Nano Letters**, 2020, 20, 8453–8460.

List of presentation

- Liu, P., *et al.*, “*Optical Activity Endowed to Inorganic Semiconductor Nanocrystals engaged with Inorganic Silica Ribbons*”, Soft Matter for Functional Materials School, Bordeaux, France, June 14-18, 2021;
- Liu, P., *et al.*, “*Optically Active Inorganic Semiconductor Nanocrystals Helical Arranged on Inorganic Silica Nanohelices*”, GDR ChiraFun, Bordeaux, France, Online, April 19-21, 2021,;
- Liu, P., *et al.*, “*Anisotropic Optical Properties of Perovskites Nanocrystals via Growth on Surface of Silica Helices*”, Tohoku University Summer School, Sendai Japan, August 27-29, 2019;

-
- Liu, P., *et al.*, “*Asymmetric Optical Properties of Perovskites CsPbBr₃ Nanocrystals after Oriented Attachment on the Surface of Silica Nanohelices*”, The Society of Polymer Science, Osaka Japan, May 28-31, 2019;
 - Liu, P., *et al.*, “*Perovskites Quantum Dots Self-Assembly on the Silica Helix with Chiral Optical Properties*”, The 4th Annual Meeting of LIA-CNPA, Bordeaux, France, September 20-21, 2018;

Acknowledgment

This work was performed under the guidance of Professor Reiko Oda at the Institute of Chemistry and Biology of Membranes and Nano-objects, University of Bordeaux, France, and Professor Takashi Sagawa at the Department of Fundamental Energy Science, Graduate School of Energy Science, Kyoto University, Japan. I would like to thank the funding support from China Scholarship Council (CSC) during my Ph.D. study in France and Japan. Also, I really appreciate all the jury members, especially Prof. Hirotaka Ihara (Kumamoto University) and Prof. Thomas Buergi (University of Geneva) who spent their precious time reviewing this manuscript.

I would like to express most sincere gratitude to my supervisors Prof. Reiko Oda and Prof. Takashi Sagawa, who whose countless guidance in both academic and life constituted my achievement in Bordeaux and Kyoto. I believe no matter where I will be and what I will do, their invaluable way of thinking and experience will always be my lighthouse. In the past four years, I found that the ways of thinking, communication, and behavior are very important for both science and life. At beginning, I always behaved with a jump thinking which lacks logical mind. These result in inefficient communication and misunderstanding. I really appreciate their patient and tolerance for my poor communication and let me learn and grow. I remember many times that Prof. Reiko Oda and Prof. Takashi Sagawa guide me how to explain clearly and logically.

Of course, I cannot have my thesis like this without all the collaborations. I would like to thank Prof. Yann Battie whom provided his expertise in theoretical simulations analysis. I also would like to thank Prof. Peter Müller-Buschbaum and Dr Wei Chen for the GISAXS and GIWAXS measurement and analysis.

This thesis is consisted by numerous helps, and there are a number of people who shared their knowledge, kindness and expertise with me. I would like to thank all of them in particular: Dr. Marion Decossas and Dr. Sisareuth Tan who helped and trained me with TEM characterization and cryo-EM measurement; Miss Laetitia Minder who trained and helped me with CD spectra characterization; Dr. Lysiane

Brocard who helped for the Tomography measurement; Dr. Brice Kauffman who help for the XRD measurement.

I would like to thank my lovely colleagues in our two groups: In particular, I would like to thank Assoc. Prof. Yutaka Okazaki who helped me in science and life in Bordeaux and Kyoto; Dr. Emilie Pouget who helped me in science and life in Bordeaux. I also would like to thank the group members in University of Bordeaux: Dr. Sylvain Nlate, Dr. Jie Gao, Dr. Antoine Scalabre, Dr. Simon Poly, Dr. Jianqiao Jiang, Dr. Rahul Nag, Dr. Zakaria Anfar, Dr. Antoine Amestoy, Dr. Balamurgugan Kuppan, Dr. Kyohei Yoshida, Dr. Shaheen Pathan, Dr. Wijak Yospanya. Gautier Duroux, Piyannan Pranee, Lucas Robin. And I also would like to thank the group members in Kyoto University: Assoc. Prof. Hachiya Kan, Dr. Chen Qu, Dr. Kaewprajak Anusit, Masahiro Nakaya, Boyang Zhou, Ege Mutlu Altun, Takaki Kimura, Yangwon Kang, Jaewang Park, Yiting Li, Yishuo Cui, Yohei Okawada, Rei Akasegawa, Tokuma Takeuchi, Yoshiki Kihara, Ryoji Yamada, Takahiro Hayashi, Oji Sato, Sakai Yusuke.

And I would like to thank all my friends in Bordeaux, who shared the impressive moments: Dr. Jinhua Wang, Dr. Junjie Hao, Dr. Chenhao Yao, Dr. Qilei Song, Dr. Wencan He, Dr. Jinglian Zhang, Dr. Bo Li, Fujing Ma, Fenghuan Zhao, Jiaming Huang,

Last but not least, the unconditional love from my family support to go through all the unfavorable conditions.